eman ta zabal zazu

Universidad del País Vasco

Euskal Herriko Unibertsitatea

Crystallization and self-assembly of ferroelectric/piezoelectric materials designed for organic electronic devices

Nicolás María Muñoz

Supervisors:

Prof. Alejandro J. Müller

Dr. Jon Maiz

Department of Polymers and Advanced Materials: Physics, Chemistry and Technology, University of Basque country (UPV/EHU)

Donostia-San Sebastián, 2022

Agradecimientos

En primer lugar, me gustaría agradecer a mis directores de tesis, tanto al Dr. Jon Maiz como al Prof. Alejandro J. Müller, por todo el trabajo de supervisión y todos los consejos y enseñanzas que me han dado durante este tiempo. También me gustaría agradecer a mi tutora la Dra. Agurtzane Múgica por la ayuda que me ha ofrecido durante mi trabajo en la tesis.

También me gustaría agradecer a todas esas personas que han colaborado para que este trabajo haya visto la luz y que han ayudado a mejorar la calidad de esta tesis. Así pues, me gustaría mencionar al Prof. Nikos Hadjichristidis (KAUST, Arabia Saudí), a la Prof. Alba González (UPV/EHU, Donostia-San Sebastián) a la Dra. Agnieszka Tercjak (UPV/EHU, Donostia-San Sebastián), Dr. Daniel Enrique Tong (CFM, Donostia-San Sebastián) y a Maite Miranda y la Dra. Ana Martinez (UPV/EHU, Donostia-San Sebastián).

In addition, I would like to thank Prof. Go Matsuba and his research group at the University of Yamagata in Japan for the opportunity that gave me to work with them. Thanks to the support that they gave to me during those months, I learnt new characterization techniques and they showed to me how to work in a different and new environment. Moreover, all the help received during that days made me feel as I was at home and I could enjoy a new culture in all the possible aspects.

Agradezco a la Universidad del País Vasco/Euskal Herriko Unibertsitatea y a POLYMAT Basque Center for Macromolecular Design and Engineering, al Gobierno del País Vasco (Grupos consolidados IT1309-19 y IT1503-22), a MINECO (MAT2017-83014-C2-1-P), a la fundación IBERDROLA y al proyecto RISE BIODEST (GA 778092) por la financiación recibida durante este tiempo, sin la cual este trabajo no podría haber sido llevado a cabo.

Por supuesto tengo que agradecer a toda la gente que ha estado conmigo durante este tiempo en San Sebastián, tanto los que han pasado por el laboratorio como a los que he conocido fuera de él. Sin ellos todo este tiempo fuera de casa habría sido muy complicado, gracias a ellos no solo me llevo un doctorado,

también me llevo muy buenos recuerdos y momentos y también muy buenas amistades. A parte también he podido aprender mucho sobre la cultura vasca (con la cual he acabado encantado) y que solo pueda tener buenas palabras hacia la gente de aquí.

Tengo muchísimo que agradecer a mi familia, sobre todo a mis padres y a mi hermano, por todo el apoyo que me han dado durante este tiempo, tanto en los buenos como en los malos momentos, y por estar ahí siempre que les he necesitado. Al final este doctorado es también parte suya por todos los sacrificios que han hecho por mí a lo largo de los años.

Por último, también me gustaría agradecer a mis amigos de toda la vida todo el apoyo y las fuerzas que me han dado durante este tiempo. A algunos de ellos incluso les hace más ilusión que a mí que ahora en el grupo haya un doctor. Siempre da gusto estar con gente que, aunque estemos casi todos en sitios distintos y cada vez sea más difícil vernos, por mucho que pase el tiempo nunca se pierde esa amistad que es como la del primer día.

Index

Chapter 5:

Phase Transitions in Poly(vinylidene fluoride)/Polymethylene-Based Diblock Copolymers and Blends

Chapter 6:

Morphology and crystallization of PVDF-based PM-*b*-PS-*b*-PVDF triblock terpolymers and their precursors

List of abbreviations

AA	Acid acrylic
AFM	Atomic Force Microscopy
ATR	Attenuated Total Reflectance
BDS	Broadband Dielectric Spectroscopy
CO_2	Carbon dioxide
CTA	Chain Transfer Agent
CTFE	Clorotrifluoroethylene
d	Distance between planes
d^*	Long period
δ	Solubility parameter
$Đ$ *or* PDI	Polydispersivity index
DMF	Dimethylformamide
DMP	Dimethyl phthalate
DSC	Differential Scanning Calorimetry
ΔG^*	Free energy barrier
ΔH_c	Crystallization enthalpy
ΔH_m^0	Equilibrium melting enthalpy
ΔT	Supercooling
E	Electric field
ε^*	Complex dielectric permittivity
FTIR	Fourier Transform Infrared Spectroscopy
G	Gauche
G (T)	Crystal growth rate
HFP	Hexafluoropropylene
HH	Head to head
HT	Head to tail
ITP	Iodine Transfer Polymerization
K	Overall crystallization rate constant
K_g	Nucleation parameter
l	Lamellar thickness
M_n	Nominal average molecular weight
M_w	Weight average molecular weight

n	Avrami index
P	Polarization
P_r	Remnant polarization
P2VP	Poly 2-vynilpyridine
PANI	Polyaniline
PBAT	Poly butylene adipate terephthalate
PBSA	Poly butylene succinate-*co*-adipate
PBS	Poly butylene succinate
PDMAEMA	Poly 2-(dimethylamino ethylmethacrylate
PE	Poly ethylene
PEDOT	Poly ethylene dioxytiophene
PEG	Polyethylene glycol
PEO	Poly ethylene oxide
PET	Poly ethylene terephthalate
PHA	Poly hydroxy alkanoate
PLA	Poly lactic acid
PLOM	Polarized Light Optical Microscopy
PM	Poly methylene
PMMA	Poly methyl methacrylate
PNIPAM	Poly n-isopropylacrylamide
PP	Poly propylene
PPO	Poly propylene oxide
PPV	Poly p-phenylene vinylene
PPy	Poly pyrrole
PS	Poly styrene
PSF	Polysulfone
PSS	Poly styrene sulfonate
PtBA	Poly (tert-butyl acrylate)
PTh	Poly thiophene
PVA	Poly vinyl alcohol
PVC	Poly vinylidene chloride
PVDF	Poly vinylidene fluoride
RAF	Rigid amorphous fraction

RAFT	Reversible Addition Fragmentation Transfer
SAXS	Small Angle X-ray Scattering
SN	Self-nucleation
SSA	Successive self-nucleation and annealing
T	Trans
TT	Tail to tail
t_0	Induction time
$\tau_{50\%}$	Half crystallization time
τ_{max}	Relaxation time
T_c	Crystallization temperature
T_{cc}	Cold crystallization temperature
$T_{c,min}$	Minimum isothermal crystallization temperature
T_{Curie}	Curie transition temperature
TEM	Transmission Electron Microscopy
T_g	Glass transition temperature
T_m	Melting temperature
T_m^0	Equilibrium melting temperature
T_s	Self-nucleation temperature
TrFE	Trifluoroethylene
WAXS	Wide Angle X-ray Scattering
χ_{12}	Interaction parameter
χ_c	Crystallinity degree
χN	Segregation strength
XRD	X-Ray Diffraction

Chapter 1

General Introduction and Objectives

1.1 Polymers as alternative materials

Synthetic polymeric materials have been studied since 1909, when the Bakelite, the first synthetic polymer, was fabricated. Polymers are materials with a wide range of possible applications as packaging and wrapping, surfaces, electronic devices, adhesives and coatings, batteries, etc.[1-7] Nowadays the importance to the sustainability of the environment, the employment of renewal energies and the use of recycled materials are a mandatory topic to deal with due to the climatic change and the environment situation that we find in our society. The evolution of the technologies applied in these fields tend to the reduction of the combustions of fuel in order to avoid the emission of CO_2 to the atmosphere.[8] In addition, for the development of new technologies it is necessary the employment of electrical micro- or nanodevices. Up to now, these devices were mainly made with inorganic metallic compounds, where light rare earths (e.g., lanthanides) are used in the chips preparation as semiconductor materials. Moreover, in renewable energies some metallic compounds as magnesium, niobium, scandium or some borates are usually employed. The main drawback of the inorganic devices is the design process, where a lot of mineral compounds that are difficult to find in the nature are involved. Moreover, their extraction requires a lot of energy and generates pollution for the environment.[9, 10] Polymers can play an important role in order to avoid the employment of these inorganic materials and make the new "green technologies" cleaner and more efficient.[11, 12]

The renewable energy where the polymers are being more useful currently is the solar energy; in this case polymers can be a good substitute of some inorganic compounds in solar cells. The need to reduce the costs and the environmental impact promotes the study of organic solar cells.[13-15] Solar cells are normally made by different layers of metallic or inorganic compounds, in the case of polymer solar cells some of these layers can be substituted by a polymer layer with a good efficiency and low cost.[16-18] One of the most employed polymer in solar cells is the poly (eth-

ylenedioxytiophene) (PEDOT) and poly (styrene sulfonate) (PSS) and their derivatives.[19-21] These semiconductor materials have good flexibility, high conductivity, low cost and good thermal stabilities, so they can act as charge injectors. In the case of perovskites solar cells, the PEDOT:PSS layer is used as a hole transport layer.[20, 22, 23]

The lithium batteries employed for energy storage or in electric/hybrid vehicles have become increasingly important in the last decade due to the technological development. The main drawbacks of the batteries are the accidents created by explosion or combustion and the few environment tolerance of the electrolytes employed.[24, 25] In the design of the batteries, the electrolyte has an important role, where it should have great electromechanical and thermal properties and a good voltage stability. Normally the electrolytes employed are lithium hexafluorophosphate, ethylene carbonate or propylene carbonate, with the high environment impact and the risk of explosions that all of them involve. From the use of polymer electrolytes, these problems have been fixed and a great yield have been maintained. Poly (propylene oxide) (PPO)[26] or poly (methyl methacrylate) (PMMA)[27] are some of the polymers employed as new electrolytes, but the most extended is the poly (ethylene oxide) (PEO) due to its high dielectric constant.[28-30]

Conducting organic polymers can be used as the structure of electronic devices or as the selective part of chemical sensors. Currently conducting polymers have been applied in electronics,[31] optoelectronics[32] or electrochemical sensors[33] and even in mechanical transduction mechanisms.[34] For instance, polyaniline (PANI), polypyrrole (PPy), polythiophene (PTh) and the previous mentioned PEDOT, are among the well-studied electroactive materials for the construction of stretchable supercapacitors.[35] Another example of polymers in electronic devices is the random copolymers based on poly (vinylidene fluoride)/trifluoroehtylene P(VDF-*co*-TrFE) applied in pressure sensors, thanks to their piezoelectric properties.[36] Polymer capacitors use solid polymers as electrolytes with a better yield due to their longer lifetime and higher stability. Another advantage of these solid conductor capacitors

against the electrolytic capacitors, that are always in liquid or gel form, is that it is possible to avoid the drying effect and it is not necessary to charge the electrolyte. In addition, for all these mentioned applications, ferroelectric polymers can be really useful because these semi-crystalline polymers can maintain a permanent electric polarization that can be switched or converted in an external electric field. Moreover, piezoelectric polymers have been also studied with the aim to apply them in electrical circuits, these materials change its electrical polarization in response to a mechanical stress.[37] The most studied polymer with these both characteristics is the PVDF, which will be explained in detail in the following section.

Polymers are also widely used in clinical medicine and healthcare fields. Due to its carbon based chemistry, polymers are similar to biological tissues instead of inorganic compounds. Polymers are useful in healthcare thanks to its structural and mechanical properties[38, 39] and also to its specific functional characteristics.[40] One of the most employed polymers in biomedical applications are biodegradable polymers. These type of polymers are used in vascular stents, in ligaments and orthopaedic fixations and now they are used as coatings in the delivery of drugs in specific places in the organism.[41-44]

Apart from the applications mentioned above, polymers are an alternative to the inorganic compounds due to their recyclability and they can be re-used again in the same or different applications. Moreover, polymers can be extracted from biological sources with less environmental impact than inorganic elements. The possibility of reusing the materials made with polymers solve the problem of the huge amount of waste that produces ecological and social impact.[45, 46] Recycling a polymer can be a long process depending of the type of polymer and the final use in the industry. Although there are several polymers that can be recycled by a primary mechanical method as the thermoplastics poly propylene (PP), poly ethylene (PE), poly ethylene terephthalate (PET) and poly (vinylidene chloride) (PVC), and normally the recycled process has several steps. First, it is necessary to separate the materials, wash them in order to remove the pollution and dry them. After it, a melting and extruding

procedure is carried out obtaining a new homogeneous polymer. The term bioplastic is used for those plastics that have a biological source and/or are biodegradable, they are commonly differentiated in three main groups. Biobased non-biodegradable plastics such as PE, PP, or PET, plastics that are both biobased and biodegradable, as for example poly lactic acid (PLA),poly hydroxy alkanoate (PHA) or poly butylene succinate (PBS), and plastics that are based on fossil resources and are biodegradable, as for instance poly butylene adipate terephthalate (PBAT).[47]

In this PhD work we have focused in the field of polymers that can be applied in electronic devices and renewal energies. For this work materials with ferroelectric and piezoelectric properties are required, and the most suitable polymer to reach the established objectives is PVDF. In the following section a detailed description of PVDF and the main works and applications found in the literature will be presented.

1.2 State of the art. Poly (vinylidene fluoride) (PVDF)

PVDF is a semi-crystalline fluoropolymer with good mechanical properties such as a good flexibility, low cost, high chemical resistance and good biocompatibility with other polymers.[48] Apart from these properties, the reason of the wide employment of the PVDF in the industry is its ferroelectric, piezoelectric and pyroelectric properties, that arises from the strong $–CF_2$ dipole.[49] The structure of PVDF (Figure 1.1), with two fluorides in the repeating unit, make possible the polarization of the material depending on the phase crystallized.

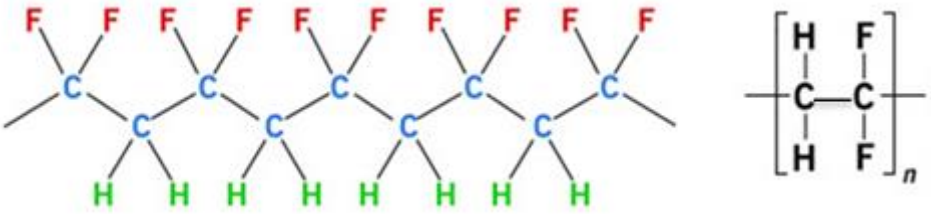

Figure 1. 1. *Structure of the chain and the repeating unit of the PVDF.*

Materials are ferroelectrics when, due to the effect of an external electrical field, the dipoles suffer spontaneous and reversible alignment in the same direction of the applied electrical field. When the electrical field is removed, not all the dipoles return to the same energy state, and some of them remain in the same direction.[50] Piezoelectricity consists in the increase of the electrical potential in the material when an external mechanical stress is applied.[51] Finally, pyroelectricity can be explained as the change in the polarization when the material suffers a change in the temperature and this promotes an electric field inside the material.[52]

PVDF is a polymorphic polymer that can crystallize in at least four different crystalline phases, denoted as α, β, γ and δ phases.[37, 53] The most stable phase when the crystallization is from the melt is the α-phase, where molecules in the crystal lattice have a $TG^+TG^-TG^+TG^-$ chain conformation, where ‘‘T’’ refers to a trans bond

conformation and ‘‘G’’ to a gauche bond conformation.[54] This α-phase is paraelectric, and the formation of oriented dipoles is not possible. The α-phase is commonly found when commercial PVDF is cooled from the melt, as when parts are extruded or injection moulded. On the other hand, PVDF’s most polar phase is the β-phase, which has chains within the crystal with a TTTT conformation.[55] The β-phase has the highest dipole moment perpendicular to the chain axis and shows the highest piezoelectric effect of the overall crystalline phases.[56] This β-phase is not easy to obtain; however, reports indicate that when certain processing conditions are applied (i.e., ultrafast cooling, addition of nucleating agents, mechanical stretching, etc.), crystallization into this more desirable β-phase is obtained.[57] In the case of the γ-phase, the crystal chain conformation is $TTTG^{+}TTTG^{-}$ [58] and the δ-phase is the polar version of the α-phase; both phases have the same lattice constants and chain conformation ($TG^{+}TG^{-}$). However, in δ-PVDF, every second chain is rotated 180º around the chain axis and the macromolecules are shifted by half of the c-axis lattice constant.[59-61] Therefore, all the fluorides are oriented in the same direction between chains. In the Figure 1.2 are shown all the conformations explained above for the four possible crystalline phases found in PVDF.

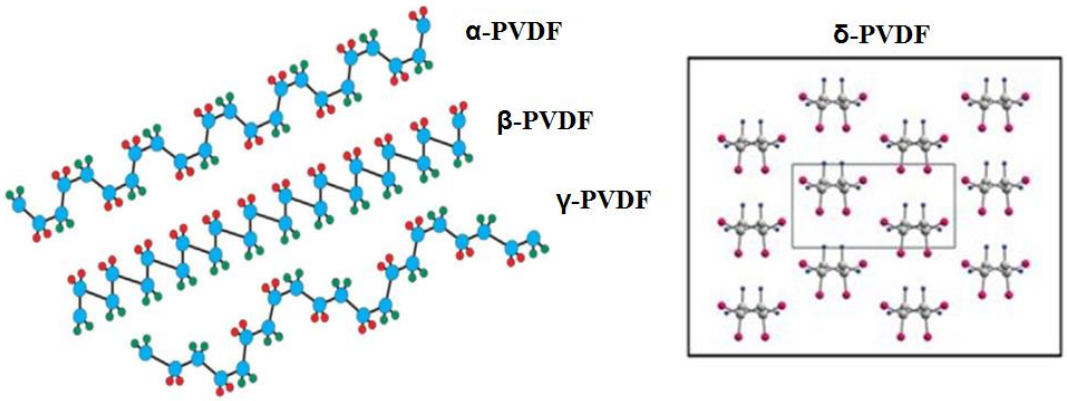

Figure 1. 2. *Scheme of the possible chain conformations within the crystalline phases studied in PVDF.*[62, 63]

Since piezoelectric properties were discovered in PVDF, many studies have been published to correlate its semi-crystalline properties with its piezoelectricity.[64] The β-phase has been the most studied phase due to its large spontaneous polarization, which promotes ferroelectric and piezoelectric applications.[65-68] To induce β-phase formation in PVDF materials, different ways have been proposed in the literature during the last few years. One of the most employed method to obtain the β-phase in PVDF films is stretching, where mechanical stress is applied to transform polymer crystals from an α-phase to β-phase.[69] In this process, the stretching temperature is one of the most important parameter and has to be considered.[70] The inconvenient of the conversion from α- to β-phase obtained by this method is that is not a complete transition, and both phases coexist simultaneously in the PVDF stretched films.[71] The stretching process promotes the elongation of the amorphous tie chains, followed by the slip and tilt of the crystalline lamellar chains, where the orientation of the crystals occurs. The α- to β-phase transformation by stretching begins with the transformation of the spherulites into a microfibrillar structure, where some blocks of lamellae are excluded from the original lamellar structure to convert them into a fibrillar structure of crystallites.[72] This mechanism promotes the all trans conformation.[53]

The preparation of PVDF based blends is another method to achieve the polar β-phase in PVDF directly.[73] PVDF blended with PMMA for example, crystallizes directly in the β-phase when the crystallization process occurs from the melt.[74, 75] These blends of PVDF and PMMA can be used as solid polymer electrolyte when they are mixed with different concentrations of lithium salt ($LiClO_4$). This blend has the highest ionic conductivity when the concentration of salt is at 8% and the amount of PVDF is two times more than PMMA. In addition, this material shows a good thermal stability, making it really useful as electrolyte in batteries.[76] In order to employ this material in batteries, it is also necessary the use of dimethylpthalate (DMP) as plasticizer to make the system more stable.[77] Other examples of blended PVDF are also well-studied in literature, e.g., with poly vinyl alcohol (PVA), where the

particle size and the thickness have a big relevance in order to achieve good thermal conductivities and thermal diffusivities.[78]

Another option to obtain ferroelectric phases in PVDF based systems is the random copolymers, e.g., VDF and trifluoroethylene, P(VDF-*co*-TrFE), that it is a well-known copolymer that preferentially crystallizes with all trans conformation.[79-85] This system can be applied in the tactile sensor field due to its good flexibility, biocompatibility and its excellent sensitivity in biological environments.[85] It has been demonstrated that the presence of TrFE increases the crystallization of the all trans conformation when the composition of TrFE is among a range of 0.15-0.4 approximately, being the P(VDF_{75}-*co*-$TrFE_{25}$) the one with the highest ferroelectric response.[86] Another option studied in the literature but free of TrFE are the random P(VDF-*co*-CTFE) (CTFE: clorotrifluoroethylene) copolymers. In this case the random copolymers have not any ferroelectric behaviour due to the large size of the CTFE, and this molecule is excluded from the crystalline phase of the PVDF, which remarks the importance of the size in the copolymerization processes of PVDF to achieve ferroelectric phases.[87] In addition, P(VDF-*co*-TrFE-*co*-CTFE) terpolymers are also employed as relaxators, actuators or transducers due to its excellent electromechanical performance.[88-90] One of the inconvenient of the ferroelectric phases of the PVDF is the relative high dielectric loss observed in the compound. To avoid this problem random PVDF hexafluoropropylene (HFP) copolymers were synthesized to confine the ferroelectric domains in nanodomains.[91, 92]

Other alternatives to achieve the desired β-phase are to produce PVDF-based graft or block copolymers.[93] Graft copolymers based on PVDF were studied in order to improve the crystallization of the β-phase. Synthesis of PVDF grafted with poly (butylene succinate-*co*-adipate) (PVDF-*g*-PBSA) or poly (methyl methacrylate-*co*-acrylic acid) [PVDF-*g*-(PMMA-*co*-AA)] with previous ozonation of the PVDF induces the crystallization of the β-phase in almost 100%, thanks to the covalent links formed in the PVDF-OH groups.[94] The most studied PVDF graft copolymers are the (P(VDF-*co*-CTFE)-*g*-PS), and their potential application as high energy density and

low loss capacitor films. After the crystallization process a microphase separation is induced, the PS chains are segregated in the periphery of the PVDF crystals, forming a confined interfacial layer. Due to the low polarizability of this confined PS layer at the amorphous–crystalline interface observed, the compensation polarization is decreased resulting in a novel confined ferroelectric behaviour in these materials. At the end, both dielectric and ferroelectric losses are significantly reduced.[95]

In a recent study, it has been shown that the β-phase can be obtained in self-assembled linear P2VP-*b*-P(VDF_{70}-*co*-$TrFE_{30}$)-*b*-P2VP (P2VP: poly (2-vynilpyridine) ABA triblock copolymers.[96] This linear triblock copolymer can crystallize directly in the β-phase using the P2VP blocks to preserve the ferroelectricity inside both components. The choice of the block strongly influences the value of the compensational polarization at the amorphous crystalline interface, responsible for the dipole reversal. Furthermore, the main parameter that affects the switching nature of block copolymers is the polarity of the amorphous phase. Moreover, in the case of amphiphilic PVDF-*b*-PDMAEMA (PDMAEMA: poly (2-(dimethylamino)ethylmethacrylate) copolymers depending on the pH employed during the synthesis method different morphologies can be obtained, independently to the crystalline phase observed in the final systems.[97]

Block copolymer morphology has been employed in PVDF with the objective to enhance the properties of this polymer. For instance, polysulfone-*b*-PVDF (PSF-*b*-PVDF) diblock copolymer is an interesting material in the proton exchange membranes fuel cells field.[98] Another example of the employment of PVDF based diblock copolymers is the poly (vinyl alcohol)-*b*-PVDF (PVA-*b*-PVDF), which is an amphiphilic fluorinated material that opens new opportunities in the fluorinated colloids field.[99, 100] In this work, the poly methylene-*b*-PVDF (PM-*b*-PVDF) diblock copolymers will be studied and compared against blends of the same materials with the same proportion in order to appreciate the differences in the properties due to the structure and morphology.

PVDF triblock copolymers also has been prepared, normally in this type of morphology there are two blocks of the same polymer forming an A-*b*-B-*b*-A structure, as for example, polyethylene glycol/PVDF (PVDF-*b*-PEG-*b*-PVDF) triblock copolymers employed in membranes[101] or more examples with polystyrene (PS-*b*-PVDF-*b*-PVDF) or poly (*tert*-butyl acrylate) (PtBa-*b*-PVDF-*b*-PtBA).[102] In the present work, the addition of a PVDF block to the PM-*b*-PS segregated system will be studied in different compositions and compared with the respective precursors.

Novel PVDF miktoarm block copolymers have been synthetized by the group of professor Nikos Hadjichristidis in KAUST. Poly (*n*-isopropylacrylamide) blocks joined to the PVDF blocks and to a benzene ring as a center have been synthetized with a different number of arms (PNIPAM-*b*-PVDF).[103] In the current manuscript, a novel miktoarm star block copolymer structure with two arms of PVDF and two arms of poly (ethylene oxide) (PVDF-*b*-PEO) will be studied in order to understand how can affect this new morphology in the crystallization of the PVDF.

As it was mentioned above, the materials composed by PVDF and their blends or copolymers are useful in electronic devices (as sensors), in data storage devices or even in renewal energies when the crystalline phase is the appropriate or the most convenient one.[104, 105] There are many applications for this kind of materials. For instance, Sharma et al., used P(VDF-*co*-TrFE) thin films in piezoelectric sensors for measurements of highly dynamic pressures in intravascular surgery in hospitals, where TrFE helps PVDF to avoid the $TG^{+}TG^{-}$ conformation below the Curie temperature and encourages β-phase formation independently of the composition.[106, 107] The e-textile is another field where PVDF is used for potential applications. In this case the PVDF is employed in fibres from granules, where the granules are melt extruded and poled in a continuous process in order to achieve the all trans conformation and its sensorial characteristics.[108]

1.3 Objectives

The main objective of this PhD work is the study of the morphology and the crystallization kinetics of different PVDF-based systems as homopolymers, blends, random copolymers and block copolymers (diblock and triblock) and the correlation between these properties with their ferroelectric response. In order to achieve these goals several experimental techniques were employed to investigate the processing-structure-function relationships, in order to find the best final conditions that result in optimum materials for energy applications.

Related with the experimental techniques used during the work, the specific objectives are designed to fulfill the main objective of this PhD work:

- Study the non-isothermal and isothermal crystallization processes by Differential Scanning Calorimetry (DSC).
- Analyze the crystalline structure and texture by Wide Angle X-ray Scattering (WAXS) and Fourier Transform Infrared Spectroscopy (FTIR).
- Study the polymorphism and how the cooling rate affects the different crystalline phases.
- Analyze the crystallization morphology and the growth kinetics by Polarized Light Optical Microscopy (PLOM).
- Study of the crystallization kinetics, mainly nucleation and growth, (comparison by theory and experimental data).
- Perform self-nucleation (SN) and successive self-nucleation and annealing studies (SSA).
- Study the miscibility of the polymers in the molten state.
- Correlation between structure and ferroelectric response.

1.4 References

1. Nemani, S. K.; Annavarapu, R. K.; Mohammadian, B.; Raiyan, A.; Heil, J.; Haque, M. A.; Abdelaal, A.; Sojoudi, H., Surface Modification of Polymers: Methods and Applications. *Advanced Materials Interfaces* 2018, 5, (24), 1801247.

2. Allen, J., Review of polymers in the prevention of thermal runaway in lithium-ion batteries. *Energy Reports* 2020, 6, 217-224.

3. Siracusa, V.; Rocculi, P.; Romani, S.; Rosa, M. D., Biodegradable polymers for food packaging: a review. *Trends in Food Science & Technology* 2008, 19, (12), 634-643.

4. Bunker, S. P.; Wool, R. P., Synthesis and characterization of monomers and polymers for adhesives from methyl oleate. *Journal of Polymer Science Part A: Polymer Chemistry* 2002, 40, (4), 451-458.

5. Feig, V. R.; Tran, H.; Bao, Z., Biodegradable Polymeric Materials in Degradable Electronic Devices. *ACS Central Science* 2018, 4, (3), 337-348.

6. Hohnholz, D.; Okuzaki, H.; MacDiarmid, A. G., Plastic Electronic Devices Through Line Patterning of Conducting Polymers. *Advanced Functional Materials* 2005, 15, (1), 51-56.

7. Zoveidavianpoor, M.; Gharibi, A., Application of polymers for coating of proppant in hydraulic fracturing of subterraneous formations: A comprehensive review. *Journal of Natural Gas Science and Engineering* 2015, 24, 197-209.

8. Painuly, J. P., Barriers to renewable energy penetration; a framework for analysis. *Renewable Energy* 2001, 24, (1), 73-89.

9. Ali, S. H., Social and Environmental Impact of the Rare Earth Industries. *Resources* 2014, 3, (1).

10. Lèbre, É.; Stringer, M.; Svobodova, K.; Owen, J. R.; Kemp, D.; Côte, C.; Arratia-Solar, A.; Valenta, R. K., The social and environmental complexities of extracting energy transition metals. *Nature Communications* 2020, 11, (1), 4823.

11. Carvalho, A. P. A. d.; Conte Junior, C. A., Green strategies for active food packagings: A systematic review on active properties of graphene-based nanomaterials and biodegradable polymers. *Trends in Food Science & Technology* 2020, 103, 130-143.

12. Mülhaupt, R., Green Polymer Chemistry and Bio-based Plastics: Dreams and Reality. *Macromolecular Chemistry and Physics* 2013, 214, (2), 159-174.

13. Kanicki, J.; Skotheim, T., Handbook of conducting polymers. *Dekkker, New York* 1986, 543.

14. Glenis, S.; Horowitz, G.; Tourillon, G.; Garnier, F., Electrochemically grown polythiophene and poly(3-methylthiophene) organic photovoltaic cells. *Thin Solid Films* 1984, 111, (2), 93-103.

15. Yu, G.; Gao, J.; Hummelen, J. C.; Wudl, F.; Heeger, A. J., Polymer Photovoltaic Cells: Enhanced Efficiencies via a Network of Internal Donor-Acceptor Heterojunctions. *Science* 1995, 270, (5243), 1789-1791.

16. Li, G.; Shrotriya, V.; Huang, J.; Yao, Y. A. N.; Moriarty, T. O. M.; Emery, K.; Yang, Y., High-efficiency solution processable polymer photovoltaic cells by self-organization of polymer blends. In *Materials for Sustainable Energy*, Co-Published with Macmillan Publishers Ltd, UK: 2010; pp 80-84.

17. Jhang, R.-X.; Chen, G.-L.; Raja, R.; Chen, P.-T.; Hayashi, M.; Rwei, S.-P.; Hsu, S.-h.; Wang, L., Difluoroterthiophene as promising block to build highly planar conjugated polymer for polymer photovoltaic cells. *Dyes and Pigments* 2021, 188, 109206.

18. Xu, Y.; Yao, H.; Ma, L.; Wu, Z.; Cui, Y.; Hong, L.; Zu, Y.; Wang, J.; Woo, H. Y.; Hou, J., Organic photovoltaic cells with high efficiencies for both indoor and outdoor applications. *Materials Chemistry Frontiers* 2021, 5, (2), 893-900.

19. Zhang, F.; Johansson, M.; Andersson, M. R.; Hummelen, J. C.; Inganäs, O., Polymer Photovoltaic Cells with Conducting Polymer Anodes. *Advanced Materials* 2002, 14, (9), 662-665.

20. Xia, Y.; Dai, S., Review on applications of PEDOTs and PEDOT:PSS in perovskite solar cells. *Journal of Materials Science: Materials in Electronics* 2021, 32, (10), 12746-12757.

21. Kim, Y.; Ballantyne, A. M.; Nelson, J.; Bradley, D. D. C., Effects of thickness and thermal annealing of the PEDOT:PSS layer on the performance of polymer solar cells. *Organic Electronics* 2009, 10, (1), 205-209.

22. Kang, Q.; Liao, Q.; Yang, C.; Yang, Y.; Xu, B.; Hou, J., A New PEDOT Derivative for Efficient Organic Solar Cell with a Fill Factor of 0.80. *Advanced Energy Materials* 2022, 12, (15), 2103892.

23. Sun, Y.; Yang, Z.; Gao, P.; He, J.; Yang, X.; Sheng, J.; Wu, S.; Xiang, Y.; Ye, J., Si/PEDOT:PSS Hybrid Solar Cells with Advanced Antireflection and Back Surface Field Designs. *Nanoscale Research Letters* 2016, 11, (1), 356.

24. Ren, D.; Liu, X.; Feng, X.; Lu, L.; Ouyang, M.; Li, J.; He, X., Model-based thermal runaway prediction of lithium-ion batteries from kinetics analysis of cell components. *Applied Energy* 2018, 228, 633-644.

25. Chen, Z.; Xiong, R.; Lu, J.; Li, X., Temperature rise prediction of lithium-ion battery suffering external short circuit for all-climate electric vehicles application. *Applied Energy* 2018, 213, 375-383.

26. LaFollette, T. A.; Walker, L. M., Structural and Mechanical Hysteresis at the Order-Order Transition of Block Copolymer Micellar Crystals. *Polymers* 2011, 3, (1).

27. Manuel Stephan, A.; Nahm, K. S., Review on composite polymer electrolytes for lithium batteries. *Polymer* 2006, 47, (16), 5952-5964.

28. Ahn, J. H.; Wang, G. X.; Liu, H. K.; Dou, S. X., Nanoparticle-dispersed PEO polymer electrolytes for Li batteries. *Journal of Power Sources* 2003, 119-121, 422-426.

29. Mathew, D. E.; Gopi, S.; Kathiresan, M.; Stephan, A. M.; Thomas, S., Influence of MOF ligands on the electrochemical and interfacial properties of PEO-based electrolytes for all-solid- state lithium batteries. *Electrochimica Acta* 2019, 319, 189-200.

30. Li, C.; Xue, P.; Chen, L.; Liu, J.; Wang, Z., Reducing the crystallinity of PEO-based composite electrolyte for high performance lithium batteries. *Composites Part B: Engineering* 2022, 234, 109729.

31. Angelopoulos, M., Conducting polymers in microelectronics. *IBM Journal of Research and Development* 2001, 45, (1), 57-75.

32. Gazotti, W. A.; Nogueira, A. F.; Girotto, E. M.; Micaroni, L.; Martini, M.; das Neves, S.; De Paoli, M. A., Chapter 2 - Optical devices based on conductive polymers. In *Handbook of Advanced Electronic and Photonic Materials and Devices*, Singh Nalwa, H., Ed. Academic Press: Burlington, 2001; pp 53-98.

33. Otero, T. F., Electrochemomechanical Devices Based on Conducting Polymers. In *Polymer Sensors and Actuators*, Osada, Y.; De Rossi, D. E., Eds. Springer Berlin Heidelberg: Berlin, Heidelberg, 2000; pp 295-323.

34. Bailey, R. A.; Persaud, K. C., Sensing Volatile Chemicals Using Conducting Polymer Arrays. In *Polymer Sensors and Actuators*, Osada, Y.; De Rossi, D. E., Eds. Springer Berlin Heidelberg: Berlin, Heidelberg, 2000; pp 149-181.

35. Wang, Y.; Ding, Y.; Guo, X.; Yu, G., Conductive polymers for stretchable supercapacitors. *Nano Research* 2019, 12, (9), 1978-1987.

36. Zhu, M.; Chng, S. S.; Cai, W.; Liu, C.; Du, Z., Piezoelectric polymer nanofibers for pressure sensors and their applications in human activity monitoring. *RSC Advances* 2020, 10, (37), 21887-21894.

37. Lovinger, A. J., Ferroelectric Polymers. *Science* 1983, 220, (4602), 1115.

38. Lendlein, A.; Behl, M.; Hiebl, B.; Wischke, C., Shape-memory polymers as a technology platform for biomedical applications. *Expert Review of Medical Devices* 2010, 7, (3), 357-379.

39. Serrano, M. C.; Ameer, G. A., Recent Insights Into the Biomedical Applications of Shape-memory Polymers. *Macromolecular Bioscience* 2012, 12, (9), 1156-1171.

40. Stamatialis, D. F.; Papenburg, B. J.; Gironés, M.; Saiful, S.; Bettahalli, S. N. M.; Schmitmeier, S.; Wessling, M., Medical applications of membranes: Drug delivery, artificial organs and tissue engineering. *Journal of Membrane Science* 2008, 308, (1), 1-34.

41. Agrawal, C. M.; Haas, K. F.; Leopold, D. A.; Clark, H. G., Evaluation of poly(L-lactic acid) as a material for intravascular polymeric stents. *Biomaterials* 1992, 13, (3), 176-182.

42. Wiebe, J.; Nef Holger, M.; Hamm Christian, W., Current Status of Bioresorbable Scaffolds in the Treatment of Coronary Artery Disease. *Journal of the American College of Cardiology* 2014, 64, (23), 2541-2551.

43. Gombotz, W. R.; Pettit, D. K., Biodegradable Polymers for Protein and Peptide Drug Delivery. *Bioconjugate Chemistry* 1995, 6, (4), 332-351.

44. Kapoor, D. N.; Bhatia, A.; Kaur, R.; Sharma, R.; Kaur, G.; Dhawan, S., PLGA: a unique polymer for drug delivery. *Therapeutic Delivery* 2015, 6, (1), 41-58.

45. Barnes, D. K. A.; Galgani, F.; Thompson, R. C.; Barlaz, M., Accumulation and fragmentation of plastic debris in global environments. *Philosophical Transactions of the Royal Society B: Biological Sciences* 2009, 364, (1526), 1985-1998.

46. Zia, K. M.; Bhatti, H. N.; Ahmad Bhatti, I., Methods for polyurethane and polyurethane composites, recycling and recovery: A review. *Reactive and Functional Polymers* 2007, 67, (8), 675-692.

47. Calmon-Decriaud, A.; Bellon-Maurel, V.; Silvestre, F., Standard Methods for Testing the Aerobic Biodegradation of Polymeric Materials. Review and Perspectives. In

Blockcopolymers - Polyelectrolytes - Biodegradation, Bellon-Maurel, V.; Calmon-Decriaud, A.; Chandrasekhar, V.; Hadjichristidis, N.; Mays, J. W.; Pispas, S.; Pitsikalis, M.; Silvestre, F., Eds. Springer Berlin Heidelberg: Berlin, Heidelberg, 1998; pp 207-226.

48. Liu, Z. H.; Pan, C. T.; Lin, L. W.; Lai, H. W., Piezoelectric properties of PVDF/MWCNT nanofiber using near-field electrospinning. *Sensors and Actuators A: Physical* 2013, 193, 13-24.

49. Kepler, R. G.; Anderson, R. A., Ferroelectric polymers. *Advances in Physics* 1992, 41, (1), 1-57.

50. Scott, J. F.; Paz de Araujo, C. A., Ferroelectric Memories. *Science* 1989, 246, (4936), 1400.

51. Mason, W. P., Piezoelectricity, its history and applications. *The Journal of the Acoustical Society of America* 1981, 70, (6), 1561-1566.

52. Wada, Y.; Hayakawa, R., Piezoelectricity and Pyroelectricity of Polymers. *Japanese Journal of Applied Physics* 1976, 15, (11), 2041-2057.

53. Lando, J. B.; Doll, W. W., The polymorphism of poly(vinylidene fluoride). I. The effect of head-to-head structure. *Journal of Macromolecular Science, Part B* 1968, 2, (2), 205-218.

54. Cortili, G.; Zerbi, G., Further infra-red data on polyvinylidene fluoride. *Spectrochimica Acta Part A: Molecular Spectroscopy* 1967, 23, (7), 2216-2218.

55. Lando, J. B.; Olf, H. G.; Peterlin, A., Nuclear magnetic resonance and x-ray determination of the structure of poly(vinylidene fluoride). *Journal of Polymer Science Part A-1: Polymer Chemistry* 1966, 4, (4), 941-951.

56. Tashiro, K.; Kobayashi, M.; Tadokoro, H.; Fukada, E., Calculation of Elastic and Piezoelectric Constants of Polymer Crystals by a Point Charge Model: Application to Poly(vinylidene fluoride) Form I. *Macromolecules* 1980, 13, (3), 691-698.

57. Martins, P.; Lopes, A. C.; Lanceros-Mendez, S., Electroactive phases of poly(vinylidene fluoride): Determination, processing and applications. *Progress in Polymer Science* 2014, 39, (4), 683-706.

58. Bachmann, M. A.; Gordon, W. L.; Koenig, J. L.; Lando, J. B., An infrared study of phase-III poly(vinylidene fluoride). *Journal of Applied Physics* 1979, 50, (10), 6106-6112.

59. Bachmann, M.; Gordon, W. L.; Weinhold, S.; Lando, J. B., The crystal structure of phase IV of poly(vinylidene fluoride). *Journal of Applied Physics* 1980, 51, (10), 5095-5099.

60. Li, M.; Wondergem, H. J.; Spijkman, M.-J.; Asadi, K.; Katsouras, I.; Blom, P. W. M.; de Leeuw, D. M., Revisiting the δ-phase of poly(vinylidene fluoride) for solution-processed ferroelectric thin films. *Nature Materials* 2013, 12, 433.

61. Lovinger, A. J., Poly(Vinylidene Fluoride). In *Developments in Crystalline Polymers—1*, Bassett, D. C., Ed. Springer Netherlands: Dordrecht, 1982; pp 195-273.

62. Martín, J.; Zhao, D.; Lenz, T.; Katsouras, I.; De Leeuw, D. M.; Stingelin, N., Solid-state-processing of δ-PVDF. *Materials Horizons* 2017, 4, (3), 408-414.

63. Gusarov, B. PVDF piezoelectric polymers : characterization and application to thermal energy harvesting. 2015.

64. Kawai, H., The Piezoelectricity of Poly (vinylidene Fluoride). *Japanese Journal of Applied Physics* 1969, 8, (7), 975-976.

65. Hasegawa, R.; Kobayashi, M.; Tadokoro, H., Molecular Conformation and Packing of Poly(vinylidene fluoride). Stability of Three Crystalline Forms and the Effect of High Pressure. *Polymer Journal* 1972, 3, (5), 591-599.

66. R. P, V.; Khakhar, D. V.; Misra, A., Studies on α to β phase transformations in mechanically deformed PVDF films. *Journal of Applied Polymer Science* 2010, 117, (6), 3491-3497.

67. Sencadas, V.; Lanceros-Mendez, S.; Filho, R. G.; Chinaglia, D. L.; Pouzada, A. S. In *Influence of the processing conditions and corona poling on the morphology of /spl beta/-PVDF*, 2005 12th International Symposium on Electrets, 11-14 Sept. 2005, 2005; 2005; pp 161-164.

68. Gregorio, R.; Nociti, N. C. P. d. S., Effect of PMMA addition on the solution crystallization of the alpha and beta phases of poly(vinylidene fluoride) (PVDF). *Journal of Physics D: Applied Physics* 1995, 28, (2), 432-436.

69. Gal'perin, Y. L.; Strogalin, Y. V.; Mlenik, M. P., Crystal structure of polyvinylidene fluoride. *Polymer Science U.S.S.R.* 1965, 7, (5), 1031-1039.

70. Li, L.; Zhang, M.; Rong, M.; Ruan, W., Studies on the transformation process of PVDF from α to β phase by stretching. *RSC Advances* 2014, 4, (8), 3938-3943.

71. Du, C.-h.; Zhu, B.-K.; Xu, Y.-Y., Effects of stretching on crystalline phase structure and morphology of hard elastic PVDF fibers. *Journal of Applied Polymer Science* 2007, 104, (4), 2254-2259.

72. Sencadas, V.; Gregorio, R.; Lanceros-Méndez, S., α to β Phase Transformation and Microestructural Changes of PVDF Films Induced by Uniaxial Stretch. *Journal of Macromolecular Science, Part B* 2009, 48, (3), 514-525.

73. Kaempf, G.; Siebourg, W.; Loewer, H.; Lazear, N., Polymeric Data Memories and Polymeric Substrate Materials for Information Storage Devices. In *Polymers in Information Storage Technology*, Mittal, K. L., Ed. Springer US: Boston, MA, 1989; pp 77-104.

74. Li, M.; Stingelin, N.; Michels, J. J.; Spijkman, M.-J.; Asadi, K.; Feldman, K.; Blom, P. W. M.; de Leeuw, D. M., Ferroelectric Phase Diagram of PVDF:PMMA. *Macromolecules* 2012, 45, (18), 7477-7485.

75. Domenici, C.; De Rossi, D.; Nannini, A.; Verni, R., Piezoelectric properties and dielectric losses in PVDF–PMMA blends. *Ferroelectrics* 1984, 60, (1), 61-70.

76. Rajendran, S.; Mahendran, O.; Mahalingam, T., Thermal and ionic conductivity studies of plasticized PMMA/PVdF blend polymer electrolytes. *European Polymer Journal* 2002, 38, (1), 49-55.

77. Rajendran, S.; Kannan, R.; Mahendran, O., An electrochemical investigation on PMMA/PVdF blend-based polymer electrolytes. *Materials Letters* 2001, 49, (3), 172-179.

78. Krishna Bama, G.; Indra Devi, P.; Ramachandran, K., Structural and thermal properties of PVDF/PVA blends. *Journal of Materials Science* 2009, 44, (5), 1302-1307.

79. Meereboer, N. L.; Terzić, I.; van der Steeg, P.; Acuautla, M.; Voet, V. S. D.; Loos, K., Electroactive behavior on demand in Poly(vinylidene fluoride-co-vinyl alcohol) copolymers. *Materials Today Energy* 2019, 11, 83-88.

80. Bhavanasi, V.; Kumar, V.; Parida, K.; Wang, J.; Lee, P. S., Enhanced Piezoelectric Energy Harvesting Performance of Flexible PVDF-TrFE Bilayer Films with Graphene Oxide. *ACS Applied Materials & Interfaces* 2016, 8, (1), 521-529.

81. Pi, Z.; Zhang, J.; Wen, C.; Zhang, Z.-b.; Wu, D., Flexible piezoelectric nanogenerator made of poly(vinylidenefluoride-co-trifluoroethylene) (PVDF-TrFE) thin film. *Nano Energy* 2014, 7, 33-41.

82. Doll, W. W.; Lando, J. B., The polymorphism of poly(vinylidene fluoride) V. The effect of hydrostatic pressure on the melting behavior of copolymers of vinylidene fluoride. *Journal of Macromolecular Science, Part B* 1970, 4, (4), 897-913.

83. Tashiro, K.; Takano, K.; Kobayashi, M.; Chatani, Y.; Tadokoro, H., Structure and ferroelectric phase transition of vinylidene fluoride-trifluoroethylene copolymers: 2. VDF 55% copolymer. *Polymer* 1984, 25, (2), 195-208.

84. Davis, G. T.; Broadhurst, M. G.; Lovinger, A. J.; Furukawa, T., Hysteresis in copolymers of vinylidene fluoride and trifluoroethylene. *Ferroelectrics* 1984, 57, (1), 73-84.

85. Li, C.; Wu, P.; Lee, S.; Gorton, A.; Schulz, M. J.; Ahn, C. H., Flexible Dome and Bump Shape Piezoelectric Tactile Sensors Using PVDF-TrFE Copolymer. *Journal of Microelectromechanical Systems* 2008, 17, (2), 334-341.

86. Furukawa, T., Ferroelectric properties of vinylidene fluoride copolymers. *Phase Transitions* 1989, 18, (3-4), 143-211.

87. Huang, Y.; Xu, J.-Z.; Soulestin, T.; Dos Santos, F. D.; Li, R.; Fukuto, M.; Lei, J.; Zhong, G.-J.; Li, Z.-M.; Li, Y.; Zhu, L., Can Relaxor Ferroelectric Behavior Be Realized for Poly(vinylidene fluoride-co-chlorotrifluoroethylene) [P(VDF–CTFE)] Random Copolymers by Inclusion of CTFE Units in PVDF Crystals? *Macromolecules* 2018, 51, (14), 5460-5472.

88. Kha Tu, N. D.; Noh, M.-S.; Ko, Y.; Kim, J.-H.; Kang, C. Y.; Kim, H., Enhanced electromechanical performance of P(VDF-TrFE-CTFE) thin films hybridized with highly dispersed carbon blacks. *Composites Part B: Engineering* 2018, 152, 133-138.

89. Liu, Q.; Richard, C.; Capsal, J.-F., Control of crystal morphology and its effect on electromechanical performances of electrostrictive P(VDF-TrFE-CTFE) terpolymer. *European Polymer Journal* 2017, 91, 46-60.

90. Cho, Y.; Ahn, D.; Park, J. B.; Pak, S.; Lee, S.; Jun, B. O.; Hong, J.; Lee, S. Y.; Jang, J. E.; Hong, J.; Morris, S. M.; Sohn, J. I.; Cha, S. N.; Kim, J. M., Enhanced Ferroelectric Property of P(VDF-TrFE-CTFE) Film Using Room-Temperature Crystallization for High-Performance Ferroelectric Device Applications. *Advanced Electronic Materials* 2016, 2, (10), 1600225.

91. Guan, F.; Wang, J.; Pan, J.; Wang, Q.; Zhu, L., Effects of Polymorphism and Crystallite Size on Dipole Reorientation in Poly(vinylidene fluoride) and Its Random Copolymers. *Macromolecules* 2010, 43, (16), 6739-6748.

92. Abbrent, S.; Plestil, J.; Hlavata, D.; Lindgren, J.; Tegenfeldt, J.; Wendsjö, Å., Crystallinity and morphology of PVdF–HFP-based gel electrolytes. *Polymer* 2001, 42, (4), 1407-1416.

93. Zapsas, G.; Patil, Y.; Bilalis, P.; Gnanou, Y.; Hadjichristidis, N., Poly(vinylidene fluoride)/Polymethylene-Based Block Copolymers and Terpolymers. *Macromolecules* 2019, 52, (5), 1976-1984.

94. Gebrekrstos, A.; Prasanna Kar, G.; Madras, G.; Misra, A.; Bose, S., Does the nature of chemically grafted polymer onto PVDF decide the extent of electroactive β-polymorph? *Polymer* 2019, 181, 121764.

95. Guan, F.; Yang, L.; Wang, J.; Guan, B.; Han, K.; Wang, Q.; Zhu, L., Confined Ferroelectric Properties in Poly(Vinylidene Fluoride-co-Chlorotrifluoroethylene)-graft-Polystyrene Graft Copolymers for Electric Energy Storage Applications. *Advanced Functional Materials* 2011, 21, (16), 3176-3188.

96. Terzic, I.; Meereboer, N. L.; Acuautla, M.; Portale, G.; Loos, K., Electroactive materials with tunable response based on block copolymer self-assembly. *Nature Communications* 2019, 10, (1), 601.

97. Guerre, M.; Semsarilar, M.; Totée, C.; Silly, G.; Améduri, B.; Ladmiral, V., Self-assembly of poly(vinylidene fluoride)-block-poly(2-(dimethylamino)ethylmethacrylate) block copolymers prepared by CuAAC click coupling. *Polymer Chemistry* 2017, 8, (34), 5203-5211.

98. Yang, Y.; Shi, Z.; Holdcroft, S., Synthesis of Sulfonated Polysulfone-block-PVDF Copolymers: Enhancement of Proton Conductivity in Low Ion Exchange Capacity Membranes. *Macromolecules* 2004, 37, (5), 1678-1681.

99. Guerre, M.; Schmidt, J.; Talmon, Y.; Améduri, B.; Ladmiral, V., An amphiphilic poly(vinylidene fluoride)-b-poly(vinyl alcohol) block copolymer: synthesis and self-assembly in water. *Polymer Chemistry* 2017, 8, (7), 1125-1128.

100. Guerre, M.; Wahidur Rahaman, S. M.; Améduri, B.; Poli, R.; Ladmiral, V., RAFT synthesis of well-defined PVDF-b-PVAc block copolymers. *Polymer Chemistry* 2016, 7, (45), 6918-6933.

101. Folgado, E.; Ladmiral, V.; Semsarilar, M., Towards permanent hydrophilic PVDF membranes. Amphiphilic PVDF-b-PEG-b-PVDF triblock copolymer as membrane additive. *European Polymer Journal* 2020, 131, 109708.

102. Terzic, I.; Meereboer, N. L.; Loos, K., CuAAC click chemistry: a versatile approach towards PVDF-based block copolymers. *Polymer Chemistry* 2018, 9, (27), 3714-3720.

103. Algarni, F.; Musteata, V. E.; Falca, G.; Chisca, S.; Hadjichristidis, N.; Nunes, S. P., Thermo-Responsive Membranes from Blends of PVDF and PNIPAM-b-PVDF Block Copolymers with Linear and Star Architectures. *Macromolecules* 2021, 54, (21), 10235-10250.

104. Guyomar, D.; Pruvost, S.; Sebald, G., Energy harvesting based on FE-FE transition in ferroelectric single crystals. *IEEE Transactions on Ultrasonics, Ferroelectrics, and Frequency Control* 2008, 55, (2), 279-285.

105. Lee, Y.; Park, J.; Cho, S.; Shin, Y.-E.; Lee, H.; Kim, J.; Myoung, J.; Cho, S.; Kang, S.; Baig, C.; Ko, H., Flexible Ferroelectric Sensors with Ultrahigh Pressure Sensitivity and Linear Response over Exceptionally Broad Pressure Range. *ACS Nano* 2018, 12, (4), 4045-4054.

106. Sharma, T.; Je, S.-S.; Gill, B.; Zhang, J. X. J., Patterning piezoelectric thin film PVDF–TrFE based pressure sensor for catheter application. *Sensors and Actuators A: Physical* 2012, 177, 87-92.

107. Dargaville, T. R.; Celina, M.; Chaplya, P. M., Evaluation of piezoelectric poly(vinylidene fluoride) polymers for use in space environments. I. Temperature limitations. *Journal of Polymer Science Part B: Polymer Physics* 2005, 43, (11), 1310-1320.

108. Hadimani, R. L.; Bayramol, D. V.; Sion, N.; Shah, T.; Qian, L.; Shi, S.; Siores, E., Continuous production of piezoelectric PVDF fibre for e-textile applications. *Smart Materials and Structures* 2013, 22, (7), 075017.

Chapter 2

Polymer Crystallization

2.1 Introduction

Crystallization and chain organization in polymers, in general, are important characteristics in order to understand the structure and the final properties of the materials. The crystallization processes in polymers can occur from a solution and/or directly from the molten state; in this work, all the studies are done from the molten state due to its relevance in the industrial protocols.[1-4] For industry, multiphasic polymer materials have been developed with the aim to reach suitable properties for different applications in different fields. To reach this, the most common systems of multiphasic polymers are e. g., polymer blends, polymer composites (or nanocomposites), polymer gels and different types of copolymers.[5]

Crystallization involves the nucleation and the growth of the systems at the same time. The crystallization process cannot occur at temperatures above the melting temperature (T_m), where the mobility of the chains is too high; due to its high-energy state, the nucleation is restricted. In the range of temperatures between T_m and the glass transition temperature (T_g) the semicrystalline polymers can present its chains ordered, forming lamellae with an amorphous interface between them. A crystal can be defined as the regular position of the atoms of a material in the three-dimension space in a periodic pattern.[6] There are several types of crystals, e.g. cubic, tetragonal, orthorhombic, hexagonal, monoclinic and triclinic. These common systems are shown in Figure 2.1 in their simplest way. Although in the Figure 2.1 the orthorhombic and the tetragonal form seem similar the dimensions are different, the tetragonal has a=b≠c unit vector distances whereas the orthorhombic has a≠b≠c. The unit cell is defined as the most repeated period that describes the space lattice of the semicrystalline material in the three dimensional translation.[6]

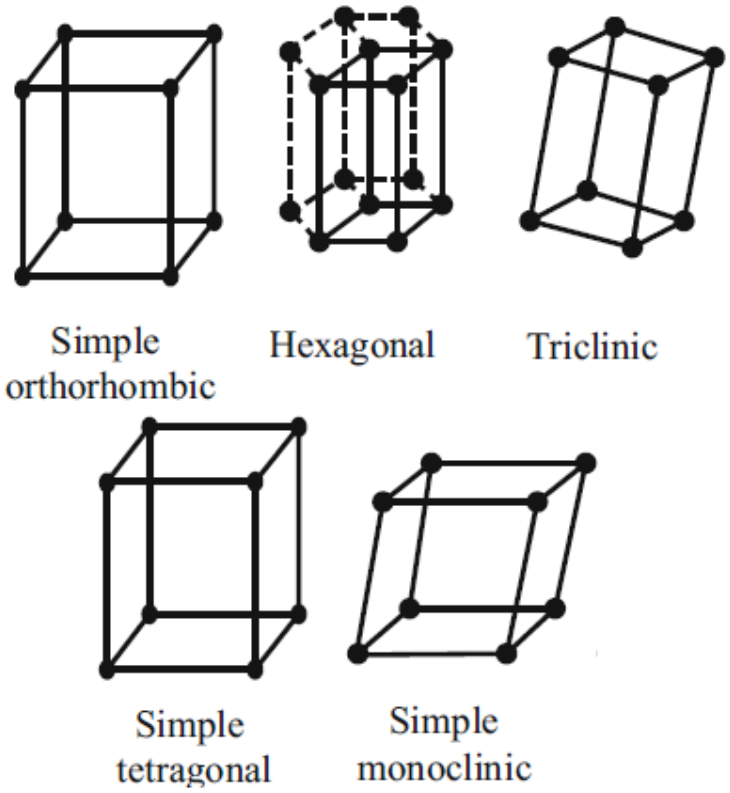

Figure 2. 1. Some of the simplest crystalline structures in polymers.

Two different crystallization processes exist for polymers when the crystallization happens from the molten state. One of them is a non-isothermal crystallization process, where the material is cooled down from the melt at a selected and controlled cooling rate. With this type of crystallization, we can get a global idea of the calorimetric behavior of the material, e.g., its non-isothermal crystallization temperature and its glass transition temperature. The other process for polymer crystallization is the isothermal crystallization procedure; in this case, the material is rapidly cooled down until a previously selected temperature and maintained during a fixed time until saturation. Employing this type of crystallization procedure is possible to study the kinetic parameters involved in these processes such as the nucleation rate or the overall crystallization rate, and also employing some theoretical approximations, e.g., we can predict the morphology or the crystallization kinetics of the system.

2.2 Polymer blends and copolymers

2.2.1 Polymer blends

Polymer blends can be a useful tool in order to tune the final properties of our material and achieve a material with better characteristics. The final properties and the crystallization behavior of the blends depends on the composition of each polymer, the mixing conditions and the miscibility between both polymers. In a homogeneous polymer blend a single-phase structure can be found, both polymers are miscible between them and a single glass transition is observed. This T_g value should be between the T_g of each compound. However, usually the most common type of blends are the heterogeneous polymer blends, where the polymers are segregated and each material shows its correspondent T_g. In addition, a third possibility of polymer blend exists, the so-called compatible polymer blends. In this case, both polymers are not miscible but the blend shows macroscopically uniform physical properties due to the strong interactions between both components.

The crystallization process in polymer blends happens in the range of temperatures between T_g and the equilibrium melting temperature (T_m^0) of the semicrystalline polymer. In the blends with two or more components, if one of them is amorphous, the crystallization kinetics will depend on its T_g. When the components are semicrystalline, the polymer with the highest crystallization temperature (T_c) will crystallize in spherulites in the liquid amorphous phase of the other component promoting the phase segregation between them.

2.2.2 Random/alternating copolymers

The most common type of copolymers are the random or alternating copolymers. Random copolymers are characterized by a statistical order of the repeating units along the backbone of the chain. On the other hand, alternating copolymers are characterized by an alternate order of the repeating units along the chain. This kind of copolymers are unusual due to the specific requirements, e.g. the comonomers need a specific copolymerization reactivity and special reaction conditions.

The main objective of the synthesis of this type of polymers is to achieve a homogeneous system with the properties of the comonomers depending of its composition. In the case of the random copolymers an average in the physical and chemical properties is achieved e.g., T_g. Moreover, random copolymers display a single-phase morphology; the sequences are normally too short to induce a phase separation morphology.

In the Figure 2.2 is showed how can be the distribution of both types of copolymers.

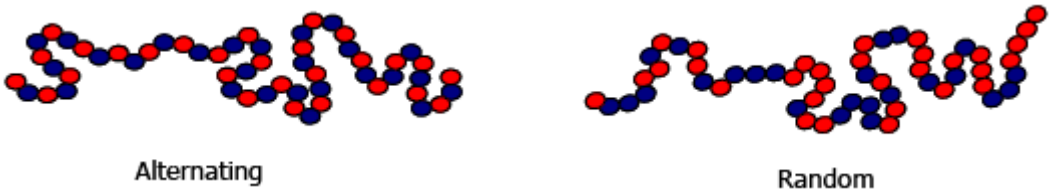

Figure 2. 2. Distribution of the polymers in alternating and random copolymers.

2.2.3 Graft copolymers

Graft copolymers are between polymer blends and random copolymers. There is a main chain basically composed by one polymer and the branches are formed by other polymer. One of the advantage of this type of materials is that they exhibit the main properties of each of the components, instead than an average of their properties. In graft copolymers is possible to observe a single-phase morphology, but the

most common situation is an overall segregated morphology. The morphology depends on the volume fraction of the main backbone component and the grafted component. The compound with the higher concentration forms the continuous phase and has a big influence in the final physical properties of the material.

As in the case of non-compatible polymer blends, the segregated graft copolymers show similar thermal properties and they display two different T_g-s . Another characteristic of the two-phase morphology graft copolymers is that they can blend perfectly with their respective homopolymers, therefore is possible to easily modify the physical properties of the copolymers.

2.2.4 Block copolymers

Block copolymers comprise two or more homopolymer subunits linked by covalent bonds. This type of structure gives to the material some well-defined properties depending on the polymers employed. There are several architectures within the block copolymers, e.g., diblock, triblock (or multiblock), random, alternating, miktoarm or grafted block copolymers as are displayed in Figure 2.3.

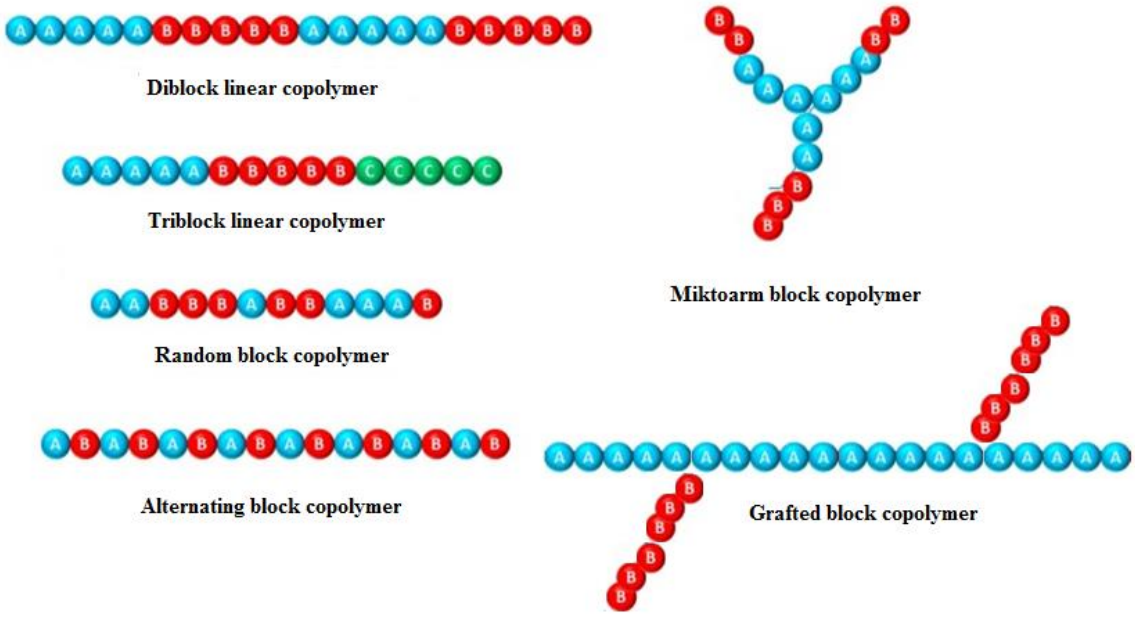

Figure 2. 3. Representation of several types of block copolymers.

The composition, the miscibility in the molten state and the structure are important factors in the crystallization process of this type of block copolymers. The estimation of the miscibility between block copolymers can be calculated using the Flory-Huggins interaction parameter (χ), which contain a significant enthalpic contribution, in order to know the segregation strength. This segregation strength is estimated multiplying the χ parameter by the polymerization degree (N) of the block copolymer.[7-9] If the segregation strength value (χN) is below 10 the blocks are miscible in the melt. If the χN is between 10 and 30 the copolymer is weakly segregated. When χN has a value between 30 and 50 is an indicative of a medium segregation and finally values above 50 show a strong segregation between the components.

When the components are weakly segregated or are miscible between them a break-out crystallization process happens, where the homogeneous molten state is covered by the crystals of the first crystalline polymer, normally in a lamellar way.[10] On the contrary, if there is a strong segregation in the molten state of the system, the morphology of the melt remains during the crystallization process and the crystals grow in confined microdomains forming a crystalline phase separation. When there is a medium segregation, the morphology of the melt can be preserved or the break-out crystallization can occurs.[11-13]

When in the block copolymers there is more than one crystalline block, the crystallization process is even more complex. The final morphology will be determined by the strength of two important factors; the phase segregation and the crystallization process. Depending on the factor that has the biggest influence, and happens before, the morphology of the system will be determined. The two possible options are the break-out of the first crystallizable block due to the crystallization process or the confined crystallization in microdomains due to the phase segregation.

2.3 Crystal morphology

Semicrystalline polymers have a partial regular chain structure, where a part is able to crystallize and another part remains in the amorphous state. Usually the degree of crystallization in semicrystalline polymers is between a range of 10-80 % of conversion. The crystallization process can be carried out from the molten state (employing a cooling process), from a solution when the polymer is dissolved in a good solvent and then well-dried, or using mechanical efforts, e.g. stretching in a thin film. The degree of crystallinity is not the only important factor in the crystallization process; molecular weight, the presence of impurities and/or the orientation of the chains have also a big relevance during this process.

The final properties of the materials and thus the final applications are influenced by the crystal morphology. The morphology depends on the composition of the material and on the conditions of the crystallization process. The main morphology observed in block copolymers is the lamellar structure, but also it is possible to find cylinders, spheres and gyroids.[14-17] The phase diagram with all the possible morphologies in a diblock copolymer is presented in Figure 2.4.

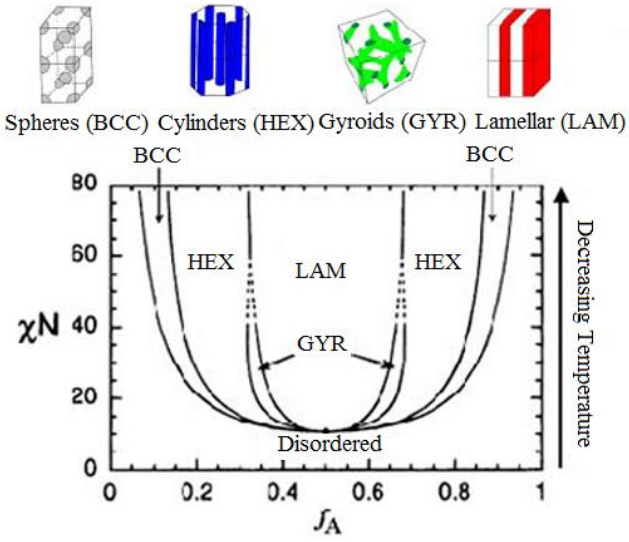

Figure 2. 4. Phase diagram for the diblock copolymer attending to the composition, the strength segregation and the temperature.

The crystallization process from the molten state consists in the reorganization and in the alignment of the long macromolecular chains forming ordered regions called lamellae. The typical mean lamellar thickness value is around 10 nm that means that the polymer chains are folded and stacked searching the most stable energy state. Figure 2.5 shows how are packaging the polymer chains inside the lamellae in a semicrystalline polymer and how the polymer chains are located in the amorphous region.

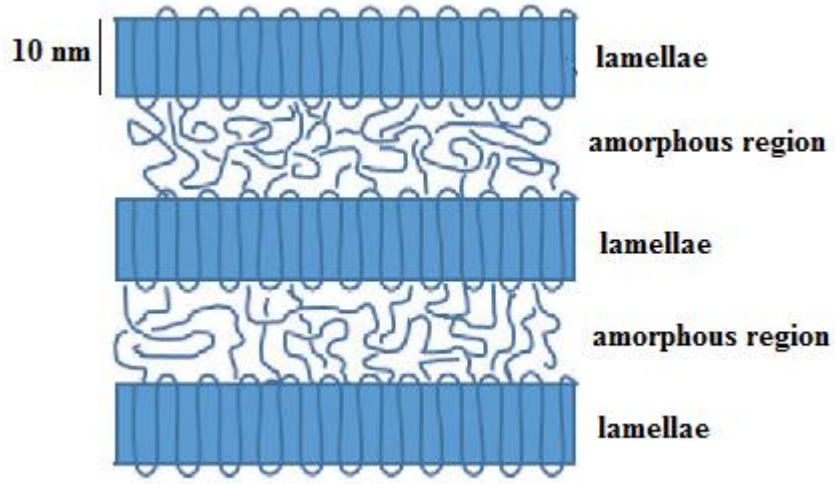

Figure 2. 5. Scheme of the lamellae structure in a semicrystalline polymer, including the amorphous region between the lamellas.

The lamellar thickness is an important factor to measure; this value can be obtained employing mainly microscopic techniques such as Atomic Force Microscopy (AFM), Transmission Electron Microscopy (TEM) or Small Angle X-ray Scattering (SAXS). The T_m of a polymer is influenced by the value of the crystal thickness as is represented in the Thomson-Gibbs equation (see eq. 2.1).[18-20] The Thomson-Gibbs equation predicts a linear relationship between the crystal thickness and the melting temperature, when the crystal thickness increases the melting temperature also increases. That behavior can be explained due to the melting of a thicker crystal that requires more energy, which is translated in more temperature or more time. This equation is given by the following:

$$T_m = T_m^0 - \frac{2\sigma_f T_m^0}{\Delta H_m^0 \rho_c} \times \left(\frac{1}{L_c}\right) \qquad \text{eq. 2.1}$$

where T_m is the melting temperature, T_m^0 is the equilibrium melting temperature, σ_f represents the fold surface free energy, ΔH_m^0 is the equilibrium melting enthalpy, ρ_0 is the density of the crystalline phase and L_c is the lamellar thickness.

Lamellae with folded chains are the fundamental unit of the polymer morphology, which growth can form supramolecular structures as spherulites, axialites or hedrites.[21, 22] One of the most typical superstructure in polymer crystals is the spherulite, which is formed through the symmetric aggregation of the radial lamellae. By Polarized Light Optical Microscopy (PLOM) is possible to observe the spherulites as birefringent spheres with a characteristic extinction pattern called Maltesse cross with a parallel and perpendicular direction regarding to the polarization.[22, 23] TEM technique has demonstrated that the spherulites are constituted by lamellae, with amorphous interlamellar zones, that grow in a radial direction. Figure 2.6 shows how in the growth of one spherulite, the chains are ordered perpendicularly to the horizontal surface and are tangential to the spherulite and the direction of the growth.[24]

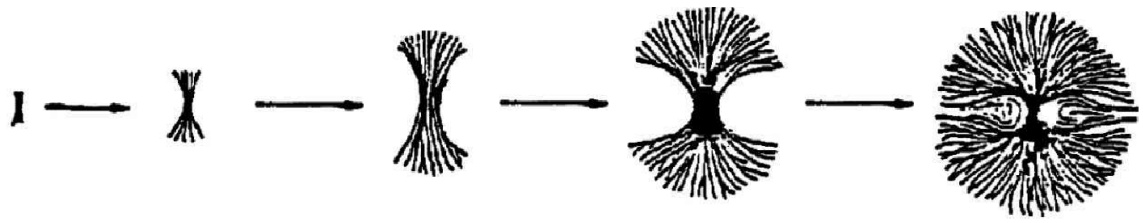

Figure 2. 6. Scheme of the formation of a spherulite from a single nucleus.

The current model of the spherulitic morphology consists in three main regions in the total spherulite. One of them corresponds to the crystalline region that is formed by the lamellae. The second region, between the crystalline regions, corresponds to the amorphous zone; this region consists in a disordered conformation of the chains with similar characteristics also observed in the melt. In some polymers

even exist a third region that consists in the interface between the crystalline region and the amorphous region due to the immobilization of the polymer chain caused by the crystals; this region is also known as rigid amorphous fraction (RAF).[25] All these regions are represented in Figure 2.7. The morphology and the size of the spherulites depend on some factors as the molecular weight, the crystallization conditions, the chemical nature of the polymer and the density of nuclei in the material.

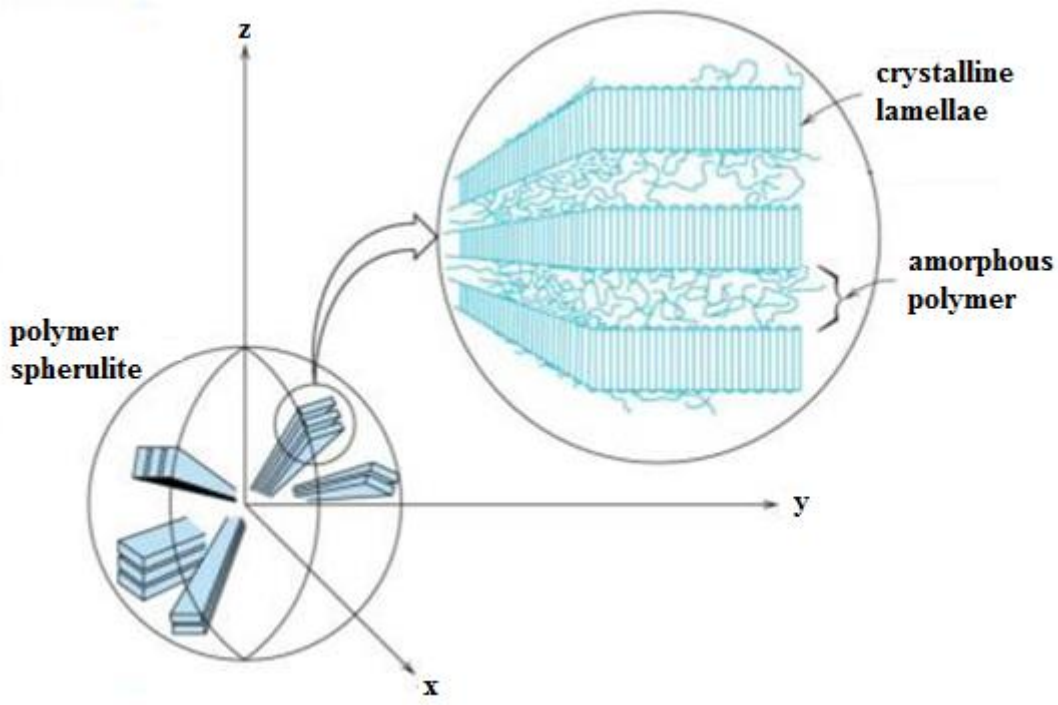

Figure 2. 7. Scheme of a spherulite and the different regions observed on it.

2.4 Crystallization Kinetics

The crystallization process in polymers is defined as a first order transition of a supercooled liquid. Whereas the low molecular weight materials can crystallize at the equilibrium melting point, polymers do it at high supercoolings. As it has been explained above, the crystallization process occurs between the melting process and the glass transition process. During the crystallization procedure from the molten state, when the temperature decreases the crystallization rate increases, due to the lower energy barrier needed at low temperatures for this phase transition process. At lower temperatures, the crystallization rate decreases due to the difficulty of the diffusion of the molecular segments. Therefore, in the crystallization process from the melt, at high temperatures, the crystallization rate is low and when the temperature decreases the crystallization rate increases until a limit of temperature, where from this temperature up to lower temperatures the crystallization rate decreases, forming a bell shape trend. In the case of the crystallization from the glassy state, the same behavior is observed, but now the process happens when the temperature increases. This means that at high temperatures the crystallization kinetics is controlled by thermodynamic factors, whereas at low temperatures the control is given by the diffusion of the molecular segments.[25]

Usually, polymer crystallization procedure is a combination of (i) primary crystallization process, (ii) secondary crystallization process and (iii) crystal reorganization process, that often happens after the secondary crystallization process. Within the primary crystallization process, the nucleation and the crystal growth are the important and relevant mechanism.

2.4.1 Nucleation

The crystallization process starts with the nucleation procedure in the molten state. The first step is the translational and rotational diffusion of crystallizable units with the proper position and orientation to be able to conform a stable nucleus. For that, it is necessary to surpass the enthalpy barrier required for the nucleus growth

and once this energy barrier is reached the addition of the chains and the correspondent growth process of the crystal can start.[26-30]

There are two types of nucleation procedures; the homogeneous process and the heterogeneous one. The homogeneous nucleation occurs in the bulk phase where the thermal fluctuations in the melt promotes the random aggregation of some polymer chains. If the size of the joined polymer chains has enough size they start growing, on the other hand if they do not reach the critical size value will disappear. The value of the critical size is related to the free energy barrier that is needed to exceed. During the nucleation step, the critical size value is able to separate the particles which energy of formation increases from that ones that their energy of formation decreases during the growth step. Once the particles exceed the value of the critical size, they turn into kinetically stable nuclei in a crystal.[29, 31] On the other case, the heterogeneous nucleation takes place in preexisting surfaces, which are non-soluble in the melt, as impurities, fillers or other components. The heterogeneous nucleation is a process thermodynamically favored due to the presence of these particles promotes the nucleation at low supercooling temperatures because the free energy barrier to be surpassed is smaller than the necessary to form a new nucleus.[19]

The critical radius of the sphere of the nuclei (r^*) is associated with the free energy barrier through the following equation:[21]

$$r^* = \frac{2\sigma T_m^0}{\Delta H_f \, \Delta T} \qquad \text{eq. 2.2}$$

where σ is the specific free surface energy of the nucleus at the surface, T_m^0 is the melting temperature in the equilibrium, ΔH_f is the enthalpy of fusion and ΔT is the supercooling ($T_m^0 - T_c$).

Moreover, the free energy barrier (ΔG^*) that must be exceed in order to form stable aggregates is expressed by the following equation:

$$\Delta G^* = \frac{16\pi\sigma^3 {T_m^0}^2}{3{\Delta H_f}^2 \Delta T^2} \qquad \text{eq. 2.3}$$

Equations 2.2 and 2.3 demonstrate that nucleation occurs easier at low crystallization temperatures because the free energy barrier associated with the process is smaller due to the nucleus critical size needed is also smaller.

The nucleation rate ($\dot{N}$) and the temperature are related in the formation rate of the nuclei that have exceed the critical size and are able to grow by the following equation proposed by Turnbull and Fisher (see eq. 2.4).[32]

$$\dot{N} = N_0 e^{(\frac{E_D}{kT} - \frac{\Delta G^*}{kT})} \qquad \text{eq. 2.4}$$

where N_0 is the number of chain segments, E_D is the activation energy for the diffusion process and ΔG^* is the free energy for the formation of an aggregate with critical dimensions.

Equations 2.3 and 2.4 show that during the cooling from the melt ΔG^* decreases progressively, therefore the nucleation rate increases. When the temperature has the lowest possible value and the crystallization process is still available, the nucleation rate reaches the maximum value, then, at lower temperatures the nucleation rate decreases again forming a bell shape curve. This reduction in the nucleation rate is explained with the increases in the viscosity at lower temperatures and the correspondent reduction of the chains diffusion process.

In the case of the previously mentioned heterogeneous nucleation, the process occurs on the surfaces, heterogeneities, particles or impurities that randomly exists in the molten state. The heterogeneous nucleation is the common process in polymers due to the difficulty in the synthesis of pristine polymers without any impurities or leftovers during the processes. In addition, the heterogeneous nucleation is a

thermodynamic favored process, where the particles or impurities help to this procedure to take place at smaller ΔT values, in consequence the free energy barrier observed to form a nucleus is smaller.

2.4.2 Crystal growth

The growth of the crystals occurs through the secondary and tertiary nucleation of the system. First, a secondary nucleus will be formed and then some tertiary nucleation events will take place.[21] The spherulitic growth is a process that is controlled by the diffusion and the secondary nucleation of the material. The tendency of the spherulitic growth rate (G) regarding the temperature is similar to the behavior of the primary nucleation explained before. The representative curve of the spherulitic growth rate against the isothermal crystallization temperature employed or the supercooling has a bell shape with a maximum, as it is displayed in Figure 2.8. In the left part of the curve, at low isothermal crystallization temperatures or high supercooling values, the dominant term is the diffusion of the molecules, at temperatures close to the T_g, where the viscosity is high and the movement of the molecules to the front becomes difficult and the growth decreases to zero values. In the right part of the curve, at high isothermal crystallization temperatures and low supercooling values, the thermodynamic forces of the secondary nucleation procedure control the overall growth rate of the process.[33]

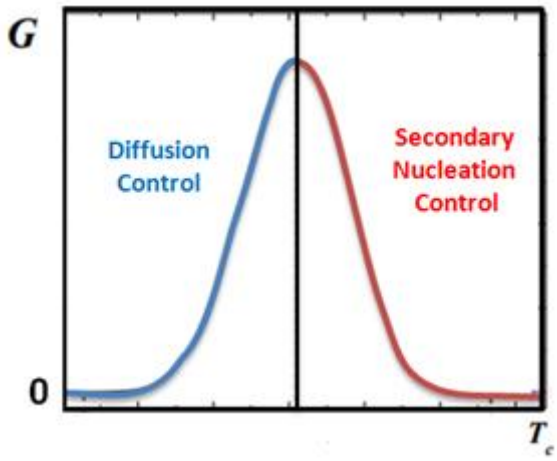

Figure 2. 8. Crystal growth rate (G) as a function of the isothermal crystallization temperature (T_c).

The initial crystallization step is dominated by the primary crystallization, i.e. once the crystal growth is completed and the spherulites are colliding between them the secondary crystallization process starts. This secondary crystallization consists in the crystallization of the amorphous parts between the spherulites, the crystallization of new secondary branches inside the spherulites, the thickening of the crystal lamellae and the growth of spherulites with some kind of defects. Moreover, during long times of crystallization processes (for instance isothermal crystallization) a reorganization of the crystalline state can also observe.[34]

2.4.3 Lauritzen and Hoffman theory

Since 1957, when Keller proposed the "folded chain model" for the polyethylene single crystals, it is assumed that a crystal is formed by a polymer chain that fold back and forth on itself reentering in the lamellae structure.[35] At the beginning, it was thought that the chain folding was energetically non-favored due to the torsion of the chains on the surface of the lamellae and they will require more energy than a linear chain. However, it has been demonstrated that the folding action of polymer

chains is a natural action during the crystallization process enhanced by kinetic effects.[36]

In 1960, Lauritzen and Hoffman proposed a theory in order to explain the experimental results obtained during the polymer chains crystallization process.[28, 37] Nowadays, the Lauritzen and Hoffman theory is one of the most employed analytical approach in polymer crystallization field due to its simplicity.

The Lauritzen and Hoffman theory is based on the secondary nucleation, i.e., the growth of the crystals takes place in a previous crystalline structure. Two factors define the three different regimes of behavior in dependence with the supercooling. These factors are the rate of deposition of secondary nuclei (*i*) and the rate of lateral surface spreading (*g*).[38]

In the regime I, when the *i* value is too much lower that the *g* value, a secondary new nucleous can grow before another one can be nucleated. This phenomenon happens at high crystallization temperatures or low supercooling values. In the regime II, when the value of *i* and *g* are in the same order of magnitude, more than one nuclei can grow at the same time, therefore the nucleation rate increases and different layers can be created. The regime II exits at moderate supercooling values. In the regime III, where the *i* value is higher than the *g* value, multiple nucleation processes can occur at the same time. This phenomenon happens at low crystallization temperatures or high supercooling values.

The Lauritzen and Hoffman theory can predict the temperature dependence of the spherulitic growth rate as:[28]

$$G(T) = G_0 exp\left(\frac{-U^*}{R(T_c - T_\infty)}\right) exp\left(\frac{-k_g}{T_c \Delta T f}\right) \qquad \text{eq. 2.5}$$

where *G* is the spherulitic growth rate, G_0 is the growth rate constant, U^* is the activation energy necessary for the transport of the molecular segment to the place where the crystallization happens (it is usually taken as a constant value of 6280

J/mol), R is the gas constant, T_c is the crystallization temperature, T_∞ is the hypothetical temperature where all the motion associated with the viscous flow ceases (usually taken as Tg -30 K), K_g is the nucleation parameter, ΔT is the supercooling and f is the correction factor that depends on the temperature.

The value of G_0 is defined as:

$$G_0 = \frac{C_i}{n_u} \qquad \text{eq. 2.6}$$

where C_i is a value that depends on the growth regime and n_u is the value of the repetitive units in the macromolecular chain. Therefore, inserting the equation 2.6 in equation 2.5 it is possible to assume that polymers with high molecular weights have low crystal growth rate.

The K_g parameter can be defined as:

$$k_g = \frac{jb\sigma\sigma_e T_m^0}{k\Delta H} \qquad \text{eq. 2.7}$$

where j is a value that depends on the regime (4 in the case of regimes I and II and 2 for regime III), b is the layer thickness, σ is the specific free energy of the lateral surface of the crystal, σ_e is the specific free energy of the folding surface, T_m^0 is the equilibrium melting temperature, k is the Boltzmann constant (1.38 x 10^{-23} J/k) and ΔH is the heat of fusion per unit volume.

The f correction factor is expressed as:

$$f = \frac{2T}{T_m^0 - T} \qquad \text{eq. 2.8}$$

where T is the temperature of the polymer in that instant and T_m^0 is the equilibrium melting temperature.

2.4.4 Avrami theory

One of the best techniques to follow the crystallization kinetics from isothermal experiments is the Differential Scanning Calorimetry (DSC) technique and the combination with methods developed by the Avrami theory. The Avrami model describes the conversion of the material from one state (normally the melt) to another one (the crystalline state) at a constant temperature.

During the decades of 1930 and 1940 Kolmogoroff, Johnson, Evans and Avrami developed a model that explain the crystallization phenomena of materials. This model did not include the molecular process of the nucleation and it assumed that the crystallization starts randomly.[39-41] The Avrami model and its limitations can be expressed by the following equation known as Avrami equation:[31, 33]

$$1 - V_c = \exp(-k\mathrm{t}^n) \qquad \text{eq. 2.9}$$

where V_c is the relative volumetric transformed fraction and k the overall crystallization rate constant which includes contributions from both nucleation and growth, t is the experimental time, and n is the Avrami index.

The Avrami index value (n) reflects the mechanism of nucleation and the morphology of the crystals, so can be divided in two terms:[42, 43]

$$n = n_d + n_n \qquad \text{eq. 2.10}$$

where n_d represents the growth dimensionality and n_n the nucleation time dependance of the growing crystals.

The values of the term n_n fluctuates in a range of 0-1, where the value 0 corresponds to the instantaneous nucleation and the value 1 to the sporadic nucleation. In the case of polymers the nucleation is not only spontaneous or sporadic, so the values of this term can be in the whole range between 0 and 1. The term n_d represents the dimension of the crystals and has a bigger range of values, between 1 and 3. In the case of polymers the value is between 2 and 3, where the value 1 corresponds to needle morphology (1 dimension). When the crystals grow in axialites aggregates

(2 dimensions) the value is 2, and if the crystals form spherulites (superstructure of 3 dimensions) the value is 3.[8, 31, 33] In Table 2.1 are shown all the possible combinations for the total Avrami index.

Table 2.1. Combinations of the terms related to the Avrami index and their respective explanations.

Nucleation dependence (n_n)	Crystal dimensionality (n_d)	Avrami index (n)	Description
0	1	1	Instantaneous needle
1	1	2	Sporadic needle
0	2	2	Instantaneous axialite
1	2	3	Sporadic axialite
0	3	3	Instantaneous spherulite
1	3	4	Sporadic spherulite

The overall crystallization rate provides a quantitative evaluation of the evolution of the crystallization including the contribution of the nucleation and the growth of the crystals. It is directly related to the half crystallization time ($\tau_{50\%}$):[31]

$$K = \left(\frac{1}{\tau_{50\%}}\right)^n ln2 \qquad \text{eq. 2.11}$$

where $1/\tau_{50\%}$ is the inverse of the half crystallization time, that can be considered an experimental measurement of the overall crystallization rate, $\tau_{50\%}$ that corresponds to the time needed to achieve the 50% of the overall crystallization and n is the Avrami index.

The Avrami equation describes the overall crystallization until the crystals start to hit between them, which occurs when the primary crystallization is finished. This is the reason of essential requirement to select a good conversion range for the fitting of the primary crystallization data. Lorenzo *et al.*[44] determined that a range between

the 3 and 20 % of conversion is enough to ensure that there is not any impingement between the spherulites during the crystallization, and the approximation of the Avrami theory always is during the free growth of the crystals. The initial data are not taking in account due to the experimental errors; moreover, at higher conversion of 50% the secondary crystallization produces some reorganization process so these data are also omitted.

In the isothermal crystallization process, once the isothermal crystallization temperature is reached, there is a period at the beginning where there is not any crystallization process observed. This time is defined as the induction time (t_0). Mathematically, the Avrami equation is only defined when crystallization starts. Therefore, the experimental induction time should be subtracted from the total experimental time. The modified Avrami equation is expressed as:

$$1 - V_c = \exp(-k(\mathrm{t} - t_0)^n) \qquad \text{eq. 2.12}$$

and the relative volume fraction can be calculated as:

$$V_\mathrm{c} = \frac{W_c}{W_c + \left(\frac{\rho_c}{\rho_a}\right)(1 - W_c)} \qquad \text{eq. 2.13}$$

where W_c is the mass fraction of the polymer, ρ_c is the total crystalline density of the polymer and ρ_a is the amorphous density of the polymer. W_c is calculated from the following equation (eq. 2.14), from the integration of the DSC experimental data measured during the isothermal crystallization:[45]

$$W_c = \frac{\Delta H\ (t)}{\Delta H_{total}} \qquad \text{eq. 2.14}$$

where $\Delta H(\mathrm{t})$ is the enthalpy variation as function of the time spent at a given crystallization temperature and ΔH_total is the maximum enthalpy value reached at the end of the isothermal crystallization process.

With the employment of the Avrami equation, used in the proper conversion range, it is possible to fit the predictions of the Avrami theory (morphology and kinetics). The value of the Avrami index can be obtained from the slope and the overall crystallization rate constant from the intercept. To ensure that the fitting of the Avrami equation is adequate a correlation data (R^2) of at least 0.999 is recommended. The predicted exothermic curve of crystallization and the theoretical relative amorphous fraction (1-V_c) are also given by the Avrami prediction in order to compare with the experimental data. In the Figure 2.9a is represented one example of the Avrami linear fit for a PVDF homopolymer sample. Figure 2.9 also shows the predicted crystallization curve (b) and the relative amorphous fraction (c) for the same sample. All these data are obtained using the Origin plug-in developed by Lorenzo *et al*.[44, 46]

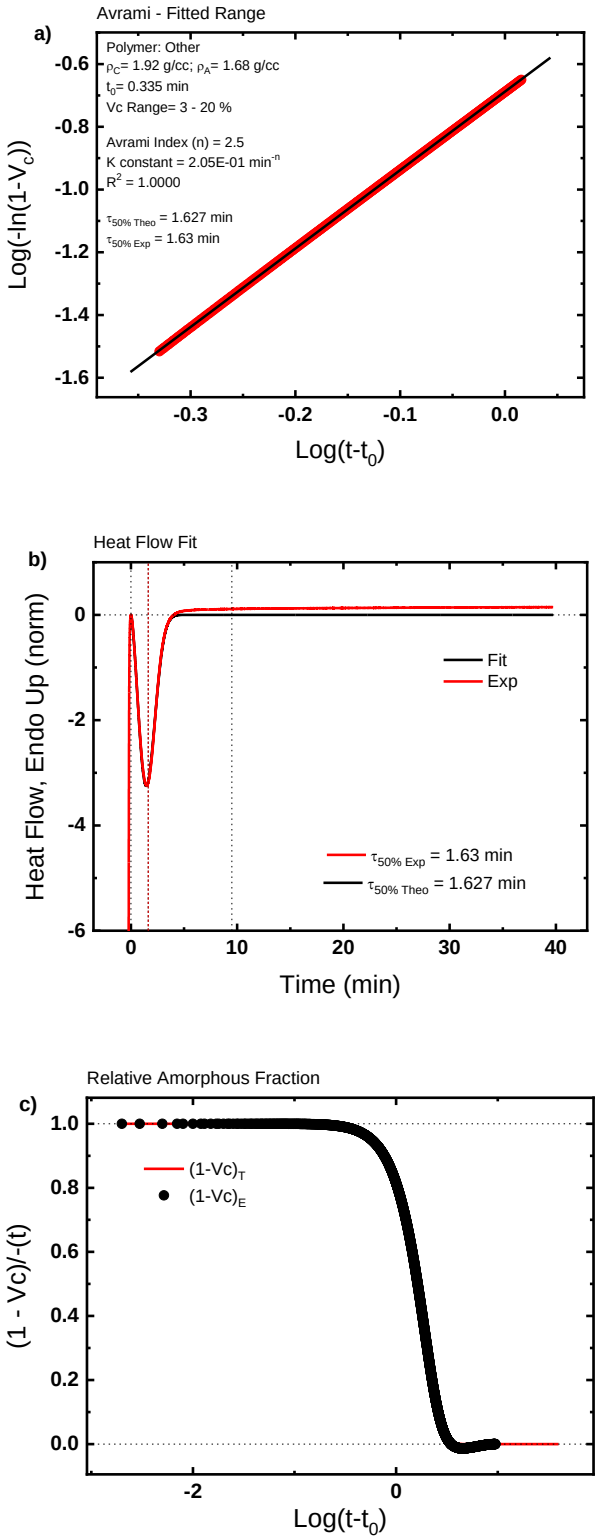

Figure 2. 9. a) Representation of the Avrami fit equation, b) isothermal crystallization curve prediction and c) relative amorphous fraction as a function of time for a PVDF homopolymer sample.

For the Avrami fit used in Figure 2.9a the logarithm terms are applied in both sides of the Avrami equationand the following equation is obtained:

$$\log(-\ln[1 - V_c(t - t_o)]) = \log k + n \log(t - t_0) \qquad \text{eq. 2.15}$$

Figure 2.9b shows the Avrami experimental data obtained during an isothermal crystallization process obtained by DSC and it is possible to observe how precise the prediction (fit vs exp) of the Avrami model is.

2.5 References

1. Hyvärinen, M.; Jabeen, R.; Kärki, T., The Modelling of Extrusion Processes for Polymers—A Review. *Polymers* **2020,** 12, (6).

2. Abeykoon, C.; Martin, P. J.; Kelly, A. L.; Brown, E. C., A review and evaluation of melt temperature sensors for polymer extrusion. *Sensors and Actuators A: Physical* **2012,** 182, 16-27.

3. Vlachopoulos, J.; Strutt, D., Polymer processing. *Materials Science and Technology* **2003,** 19, (9), 1161-1169.

4. Simões, M. F.; Pinto, R. M. A.; Simões, S., Hot-melt extrusion in the pharmaceutical industry: toward filing a new drug application. *Drug Discovery Today* **2019,** 24, (9), 1749-1768.

5. Boudenne, A.; Ibos, L.; Candau, Y.; Thomas, S., *Handbook of multiphase polymer systems*. John Wiley & Sons: 2011.

6. Jackson, A. G., *Handbook of Crystallography: for electron microscopists and others*. Springer Science & Business Media: 2012.

7. Hamley, I., The Physics of Block Copolymers Oxford Univ. In Press: 1998.

8. Hiemenz, P. C., T.P. Lodge, Polymer chemistry. *CRC Press* **2007,** 2nd edition.

9. Abetz, V.; Simon, P. F. W., Phase Behaviour and Morphologies of Block Copolymers. In *Block Copolymers I*, Abetz, V., Ed. Springer Berlin Heidelberg: Berlin, Heidelberg, 2005; pp 125-212.

10. Piorkowska, E.; Rutledge, G. C., *Handbook of polymer crystallization*. John Wiley & Sons: 2013.

11. Douzinas, K. C.; Cohen, R. E.; Halasa, A. F., Evaluation of domain spacing scaling laws for semicrystalline diblock copolymers. *Macromolecules* **1991,** 24, (15), 4457-4459.

12. Ryan, A. J.; Hamley, I. W.; Bras, W.; Bates, F. S., Structure Development in Semicrystalline Diblock Copolymers Crystallizing from the Ordered Melt. *Macromolecules* **1995,** 28, (11), 3860-3868.

13. Rangarajan, P.; Register, R. A.; Adamson, D. H.; Fetters, L. J.; Bras, W.; Naylor, S.; Ryan, A. J., Dynamics of Structure Formation in Crystallizable Block Copolymers. *Macromolecules* **1995,** 28, (5), 1422-1428.

14. Guerin, G.; Rupar, P.; Molev, G.; Manners, I.; Jinnai, H.; Winnik, M. A., Lateral Growth of 1D Core-Crystalline Micelles upon Annealing in Solution. *Macromolecules* **2016,** 49, (18), 7004-7014.

15. Zhang, B.; Chen, J.; Baier, M. C.; Mecking, S.; Reiter, R.; Mülhaupt, R.; Reiter, G., Molecular-Weight-Dependent Changes in Morphology of Solution-Grown Polyethylene Single Crystals. *Macromolecular Rapid Communications* **2015,** 36, (2), 181-189.

16. Park, C.; Yoon, J.; Thomas, E. L., Enabling nanotechnology with self assembled block copolymer patterns. *Polymer* **2003,** 44, (22), 6725-6760.

17. Ortmann, P.; Trzaskowski, J.; Krumova, M.; Mecking, S., Precise Microstructure Self-Stabilized Polymer Nanocrystals. *ACS Macro Letters* **2013,** 2, (2), 125-127.

18. Weeks, J. J., Melting Temperature and Change of Lamellar Thickness with Time for Bulk Polyethylene. *Journal of research of the National Bureau of Standards. Section A, Physics and chemistry* **1963,** 67A, (5), 441-451.

19. Gedde, U. W.; Hedenqvist, M. S., *Fundamental polymer science*. Springer: 2019; Vol. 2.

20. Crist, B., Thermodynamics of statistical copolymer melting. *Polymer* **2003,** 44, (16), 4563-4572.

21. Gedde, U., *Polymer physics*. Springer Science & Business Media: 1995.

22. Schultz, J. M., *Polymer crystallization: the development of crystalline order in thermoplastic polymers*. Amer Chemical Society: 2001.

23. Gedde, U. W.; Mattozzi, A., Polyethylene Morphology. In *Long Term Properties of Polyolefins*, Albertsson, A.-C., Ed. Springer Berlin Heidelberg: Berlin, Heidelberg, 2004; pp 29-74.

24. Sperling, L. H., *Introduction to physical polymer science*. John Wiley & Sons: 2005.

25. Mandelkern, L., *Crystallization of Polymers: Volume 2, Kinetics and Mechanisms*. Cambridge University Press: 2004.

26. Hoffman, J. D.; Davis, G. T.; Lauritzen, J. I., The Rate of Crystallization of Linear Polymers with Chain Folding. In *Treatise on Solid State Chemistry: Volume 3 Crystalline and Noncrystalline Solids*, Hannay, N. B., Ed. Springer US: Boston, MA, 1976; pp 497-614.

27. Flory, P. J., *Principles of polymer chemistry*. Cornell university press: 1953.

28. Lauritzen, J. I.; Hoffman, J. D., Formation of Polymer Crystals with Folded Chains from Dilute Solution. *The Journal of Chemical Physics* **1959,** 31, (6), 1680-1681.

29. Reiter, G.; Strobl, G. R., *Progress in understanding of polymer crystallization*. Springer: 2007; Vol. 714.

30. Sharples, A., Introduction to polymer crystallization. **1966**.

31. Van Krevelen, D. W.; Te Nijenhuis, K., *Properties of polymers: their correlation with chemical structure; their numerical estimation and prediction from additive group contributions*. Elsevier: 2009.

32. Turnbull, D.; Fisher, J. C., Rate of Nucleation in Condensed Systems. *The Journal of Chemical Physics* **1949,** 17, (1), 71-73.

33. Müller, A. J.; Michell, R. M.; Lorenzo, A. T., Isothermal Crystallization Kinetics of Polymers. *Polymer Morphology: Principles, Characterization, and Processing* **2016,** 714, 181-203.

34. Wang, Z. G.; Hsiao, B. S.; Sauer, B. B.; Kampert, W. G., The nature of secondary crystallization in poly(ethylene terephthalate). *Polymer* **1999,** 40, (16), 4615-4627.

35. Keller, A.; O'Connor, A., Large Periods in Polyethylene: the Origin of Low-Angle X-ray Scattering. *Nature* **1957,** 180, (4597), 1289-1290.

36. Peterlin, A., Folded chain model of highly drawn polyethylene. *Polymer Engineering & Science* **1969,** 9, (3), 172-181.

37. Lauritzen, J. I., Jr.; Hoffman, J. D., Theory of Formation of Polymer Crystals with Folded Chains in Dilute Solution. *Journal of research of the National Bureau of Standards. Section A, Physics and chemistry* **1960,** 64A, (1), 73-102.

38. Mark, J. E., *Physical properties of polymers handbook*. Springer: 2007; Vol. 1076.

39. Avrami, M., Kinetics of Phase Change. II Transformation-Time Relations for Random Distribution of Nuclei. *The Journal of Chemical Physics* **1940,** 8, (2), 212-224.

40. Avrami, M., Granulation, Phase Change, and Microstructure Kinetics of Phase Change. III. *The Journal of Chemical Physics* **1941,** 9, (2), 177-184.

41. Avrami, M., Kinetics of Phase Change. I General Theory. *The Journal of Chemical Physics* **1939,** 7, (12), 1103-1112.

42. Balsamo, V.; Urdaneta, N.; Pérez, L.; Carrizales, P.; Abetz, V.; Müller, A. J., Effect of the polyethylene confinement and topology on its crystallisation within semicrystalline ABC triblock copolymers. *European Polymer Journal* **2004,** 40, (6), 1033-1049.

43. Müller, A. J.; Balsamo, V.; Arnal, M. L., Nucleation and Crystallization in Diblock and Triblock Copolymers. In *Block Copolymers II*, Abetz, V., Ed. Springer Berlin Heidelberg: Berlin, Heidelberg, 2005; pp 1-63.

44. Lorenzo, A. T.; Arnal, M. L.; Albuerne, J.; Müller, A. J., DSC isothermal polymer crystallization kinetics measurements and the use of the Avrami equation to fit the data: Guidelines to avoid common problems. *Polymer Testing* **2007,** 26, (2), 222-231.

45. Castillo, R. V.; Müller, A. J., Crystallization and morphology of biodegradable or biostable single and double crystalline block copolymers. *Progress in Polymer Science* **2009,** 34, (6), 516-560.

46. Pérez-Camargo, R. A.; Liu, G.-M.; Wang, D.-J.; Müller, A. J., Experimental and Data Fitting Guidelines for the Determination of Polymer Crystallization Kinetics. *Chinese Journal of Polymer Science* **2022,** 40, (6), 658-691.

Chapter 3

Experimental Part

3.1 Materials

In this section, the different samples characterized during this PhD thesis will be discussed. The main information about the homopolymers, blends formed from these homopolymers, the random copolymers, the different block copolymers (di-block, triblock, or miktoarm stars), and the PVDF stars have been described during this chapter.

3.1.1 Homopolymers

In this thesis, different **poly (vinylidene fluoride) (PVDF)** homopolymers were characterized. Some PVDF were commercial, and others were synthesized as precursors to prepare the finally studied copolymer materials. In the following paragraphs, they will be explained.

PVDF is a common material employed in lithium batteries as electrodes, in electronic devices or in diffusion membranes, due to its good physical and chemical properties. (See Chapter 1) This fluoropolymer has a glass transition temperature of around -35 ºC, and the degree of crystallinity is between 50-60%, depending on the molecular weight, for example. The melting temperature is in a range between 160-180 ºC (also depending on the molecular weight, on the crystalline phase, etc.). The PVDF homopolymers employed in this work were a commercial PVDF supplied by Aldrich Ltd. and three synthetized PVDF, their molecular weight was different. These polymers were synthesized by the group of Professor Nikos Hadjichristidis in Kaust, Saudi Arabia.

Another homopolymer studied in this work was the **poly (ethylene oxide) (PEO).** This is a common polymer used as a polymer electrolyte in batteries. This polymer has a glass transition temperature of around -55 ºC, a degree of crystallinity of around 80% and a melting temperature close to 65 ºC.[1] In this thesis, the PEO

homopolymer employed, synthesized by the group of Professor Nikos Hadjichristidis in Kaust, is joint to an alkyne group.

The last homopolymer characterized in this thesis was **poly methylene (PM),** which is similar to polyethylene (PE), the only difference between them resides in the type of polymerization. This is the most common plastic employed, mainly, in packaging. The glass transition temperature of this thermoplastic polymer is around -100 ºC, and depends mainly on the degree of crystallinity and the molecular weight of the polymer. The melting temperature of the homopolymer used during this work is around 125 ºC. In addition, in this case, this homopolymer has been synthesized by the group of Professor Nikos Hadjichristidis in Kaust, and the PM chain is joined to a hydroxyl group, forming the final PM-OH homopolymer.

3.1.2 Functional macromolecular systems

One of the goals of this thesis is to study the crystallization procedure and the crystalline polymer phases (polymorphism) found in PVDF. In order to achieve these purposes, different functional macromolecular materials are prepared. The main line followed was to study these properties in different copolymer systems, either random copolymers and/or block copolymers. In addition, polymer blends are also studied in order to compare these systems with the copolymer ones and see how the topology affects the crystallization process.

a) Poly vinylidene fluoride (PVDF) based blends

First, PM-PVDF based blends were studied. Blends were prepared by mixing the individual precursor components used during the block copolymers synthesis, in this case, PM-OH from one side and PVDF homopolymer from the other one. The blends were prepared with the same compositions studied in the case of the block copoly-

mer samples. For the preparation, first, the PVDF and the PM mixtures were dissolved in cyclohexane. Then, each mixture was drop-casted. Afterward, a fume hood was used to slowly evaporate the solvent, and finally, under vacuum conditions, the samples were dried.

The detailed preparation and the analysis of these samples will be given in Chapter 5 with the respective analysis of the PM-*b*-PVDF block copolymer sample.

b) Poly (vinylidene fluoride) (PVDF) based random copolymers

Commercially available poly (vinylidene fluoride) (PVDF) polymers copolymerized with trifluoroethylene (TrFE), forming P(VDF-*co*-TrFE) random copolymers are studied. Different random copolymers of P(VDF-*co*-TrFE) with different molar ratios were supplied by Piezotech® FC (France). The chemical structure of this type of random copolymers is given in Figure 3.1. In this work, 80/20, 75/25 and 70/30 VDF/TrFE molar ratios were used. In Chapter 4, more details about these samples and their respective characterizations will be given.

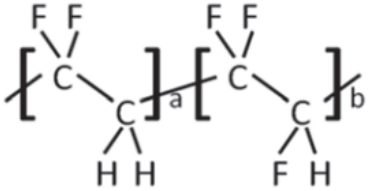

Figure 3. 1. Chemical structure of the P(VDF-*co*-TrFE) random copolymers.

c) Poly (vinylidene fluoride) (PVDF) based block copolymers

Three different types of PVDF block copolymers were studied in this thesis. All the PVDF block copolymer systems were synthesized by the group of Professor Nikos Hadjichristidis in KAUST (Saudi Arabia).

In Chapter 5 the characterization, synthesis, and comparison of two PM-*b*-PVDF linear diblock copolymers with different compositions (PM_{23}-*b*-$PVDF_{77}$ and PM_{38}-

b-$PVDF_{62}$), a synthesized PVDF homopolymer and one PM-OH homopolymer with similar molecular weights to their respective comonomers will be studied. The structure of the diblock copolymer and its scheme is shown in Figure 3.2.

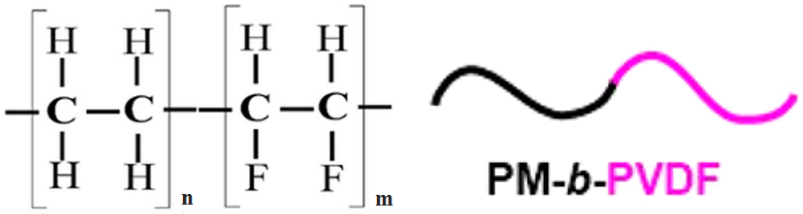

Figure 3. 2. Structure of the PM-*b*-PVDF block copolymer and its corresponding scheme.

The analysis of a PM-*b*-PS-*b*-PVDF (PS: polystyrene) linear triblock copolymer system will be described in Chapter 6. Two different triblock copolymers with different compositions between them (PM_{13}-*b*-PS_{27}-*b*-$PVDF_{60}$ and PM_{11}-*b*-PS_{22}-*b*-$PVDF_{67}$), one synthesized PVDF homopolymer and one PM-*b*-PS precursor sample (with the same molecular weights than in the triblock copolymers) were studied. In Figure 3.3, the triblock copolymer structure and its scheme is represented.

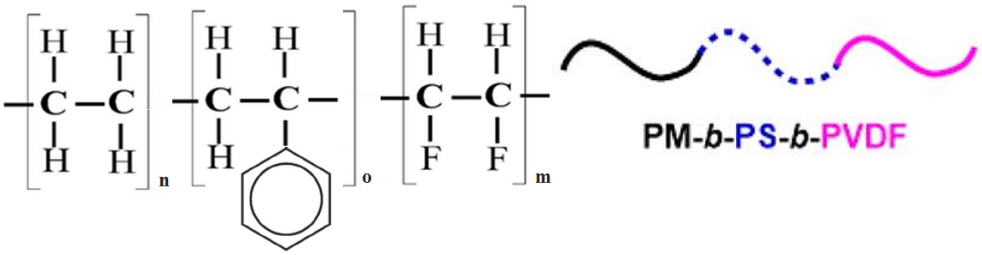

Figure 3. 3. The structure of PM-*b*-PS-*b*-PVDF sample and its scheme.

The third type of PVDF block copolymer analysed in the present work has a novel miktoarm star structure with the addition of two PEO (poly ethylene oxide) arms. These miktoarm star block copolymers have two PVDF arms in the same plane and two PEO arms in a perpendicular plane with a common centre, as it is shown in Figure 3.4. In Chapter 7, the synthesis and the characterization of three $(PVDF)_2$-*b*-

$(PEO)_2$ miktoarm star block copolymers with different compositions ($(PVDF_{29})_2$-*b*-$(PEO_{272})_2$, $(PVDF_{66})_2$-*b*-$(PEO_{227})_2$ and $(PVDF_{106})_2$-*b*-$(PEO_{159})_2$) and similar molecular weight between them, one 2-arm PVDF precursor ($(PVDF_{29}\text{-}N_3)_2$) and one PEO precursor (PEO_{227}-Alkyne) will be studied.

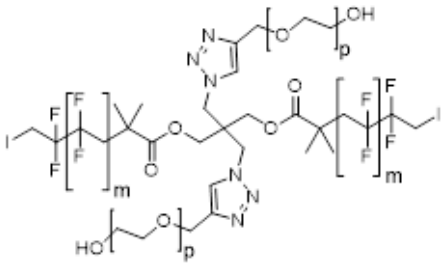

Figure 3. 4. Structure of $(PVDF)_2$-*b*-$(PEO)_2$ miktoarm star block copolymers.

d) Poly (vinylidene fluoride) (PVDF) based stars

A system of PVDF stars was studied to know how the number of PVDF arms affects the crystallization process and the polymorphism of PVDF. A linear PVDF (1-arm), and 3, 4, 6-arms PVDF were synthesized by the group of Professor Nikos Hadjichristidis in Kaust with similar molecular weights between them. A representative scheme of their structures is presented in Figure 3.5, where the red lines represent the PVDF chains. All the analyses of these samples will be explained in Chapter 8.

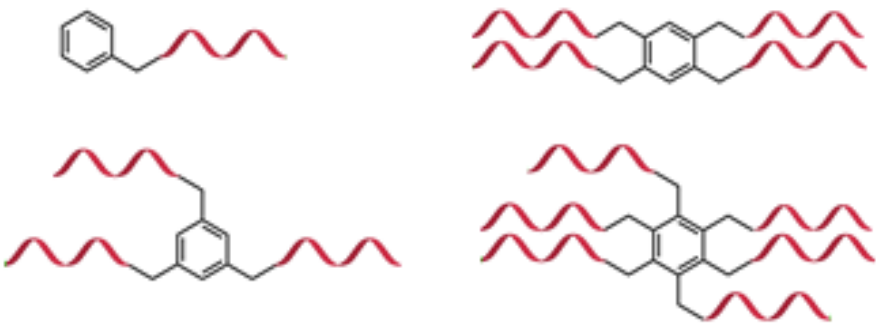

Figure 3. 5. Representation of the different structures of the PVDF stars, where the red lines represent the PVDF.

3.2 Experimental Techniques

In this section, the main characterization techniques employed in the samples presented before are described. For the analysis of the samples, different calorimetric protocols, X-ray analysis, infrared studies, dielectric experiments, and different microscope techniques were employed.

3.2.1 Differential Scanning Calorimetry (DSC)

Differential scanning calorimetry is a thermoanalytical technique in which the difference in the amount of heat required to increase the temperature of a sample and a reference is measured as a function of either time or temperature. With this technique, it is possible to detect the kinetic data of heat transitions, the purity of the materials, and measure the heat of first and second order transitions of the materials, such as the glass transition temperature (T_g) or the melting (T_m) and crystallization (T_c) processes.[2]

Experimentally, two pan holders are needed in the DSC equipment, one for the sample material and the other one for the empty reference. In this work, the reference consists of an empty aluminum pan, whereas the sample material is encapsulated in another pan with a recommended weight of between 3 and 10 mg. Briefly, the technique consists of two heating circuits that control the temperature average between the two ovens, which contain the sample and the reference. The first circuit modifies the temperature of both ovens, at a constant speed previously selected in the software. The second circuit tries to compensate the difference in the temperatures between the two ovens when any thermal process happens during the measurement of the sample, keeping the temperature of the sample and the reference always constant. The equipment measures the power necessary to maintain the sample oven at the same temperature that the reference oven is.

All the DSC experiments presented in this work were performed with a PerkinElmer DSC 8000 equipment with an Intracooler II as a cooling system. The calorimeter was calibrated with indium and tin before the measurements were carried out. All the experiments were performed employing ultra-high purity nitrogen as a purge gas.

Pyris manager software was employed in order to plot all the thermal curves and determine the thermal parameters of the processes that the samples experience during the experiments. For instance, some of the thermal parameters useful in the polymers field are the melting temperature (T_m), the crystallization temperature (T_c), the melting and crystallization enthalpy (ΔH_m and ΔH_c, respectively), the glass transition temperature (T_g), the Curie transition temperature (T_{Curie}) and/or the cold crystallization temperature (T_{cc}). In order to obtain these different thermal parameters different experimental protocols can be carried out and will be explained on the following.

For **non-isothermal** DSC scans, first, the samples were heated at 20 ºC/min to 20 ºC above the melting temperature of the sample. The samples were kept at this temperature for 3 minutes in order to erase the thermal history, and then they were cooled at different cooling rates to room temperature (RT) or -30 ºC (depending on the system studied). Finally, the samples were heated again at 20 ºC/min to the same temperature employed in the first step.

The experimental protocol suggested by Lorenzo *et al.*[3, 4] was used to determine the overall isothermal crystallization process of the material. First, the **minimum isothermal crystallization temperature** ($T_{c,min}$) to be used was found. This was done by heating the sample to 20 ºC above its melting temperature for 3 minutes to ensure that the sample was completely melted, then it was cooled down at 60 ºC/min to a chosen T_c and immediately heated up again to the molten state (at 20 ºC/min). The lowest T_c, which does not generate any latent heat of fusion during a subsequent DSC heating scan, was selected as the minimum T_c used.

Figure 3.6 shows schematically the steps carried out to perform **isothermal crystallization** protocols. Samples were melted (20 ºC above the melting temperature during 3 min) to remove any crystalline thermal history. From that temperature, they were cooled at 60 ºC/min (at this cooling rate, the calorimeter has excellent control of the temperature) to (as mentioned above) a previously chosen isothermal crystallization temperature, T_c. At this temperature, the samples were kept crystallizing until saturation, around 40 min in all the samples. After the completed crystallization, a heating scan was carried out at 20 ºC/min until melting. Normally a number of ten different isothermal crystallization temperatures per sample is enough to calculate the kinetic parameters. All the kinetic calculations were performed with the complimentary Origin® plugin developed by Lorenzo *et al*. [3, 4]

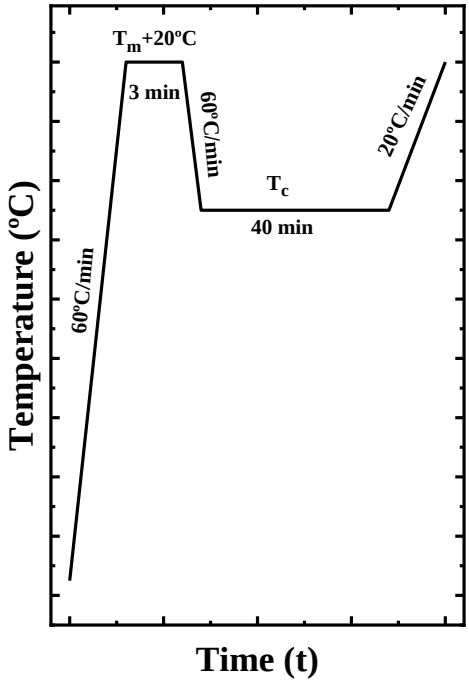

Figure 3. 6. Isothermal crystallization protocol followed during this thesis work.

The **self-nucleation** (SN) experiments were performed following the protocol recommended by Müller *et al.*[5, 6] All the scans carried out during the SN experiments were at 20 ºC/min. First, the thermal history of the material is erased at 20 ºC above the melting temperature during 3 minutes. For the next step, the sample is cooled from the molten state to a low temperature to ensure the crystallization of the material (this temperature depends on the polymer analysed) and is held 3 minutes at this temperature. Then the sample is heated to a previously selected SN temperature, T_s, and remained at this temperature during 5 minutes. The following step is cooling down the sample from the T_s to the crystallization temperature chosen and keep the sample 3 minutes at this temperature. In this step, depending on the *Domain* that the sample is, some changes in the value of the T_c can be observed towards higher values in comparison with the previous T_s employed. Finally, the sample is heated again to the molten state, also this step is important to monitor due to the possible annealing process that occurs in this step and can be appreciated in the subsequent melting peaks. After this step, the experiment can be repeated by changing the T_s value to another one. In Figure 3.7 are shown all the steps of this SN protocol graphically.

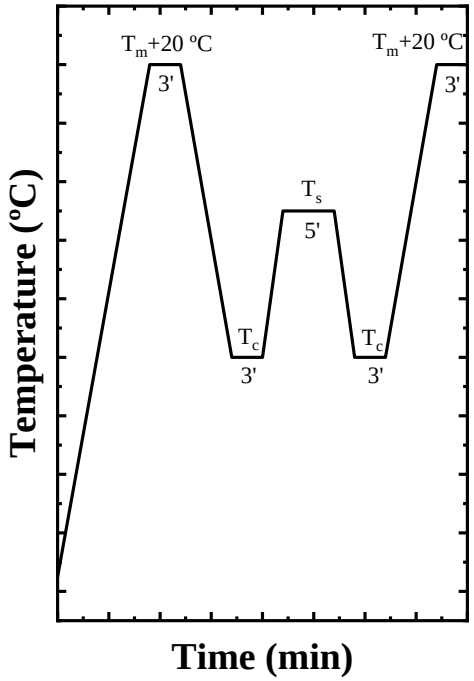

Figure 3. 7. Self-Nucleation protocol followed in the present thesis work.

Briefly, three *Domains* can be appreciated or distinguished during the SN process for the materials.[7, 8] A material is in *Domain* I when the melting process occurs completely, and the thermal history of the sample is erased, so that isotropic and relaxed random coils exist in the molten state. The *Domain* II encompasses a T_s range where self-nuclei remain in the polymer, but the temperature is not high enough to produce annealing of any unmolten crystal fragments that could act as self-seeds. *Domain II* is identified because upon cooling from T_s values located in this *Domain*, the crystallization peak temperature increases as the nucleation density is increased. The lowest T_s value in Domain II is known as the ideal self-nucleation temperature, $T_{s,ideal}$, as it produces the maximum self-nucleation effect without any annealing. The nucleation density is increased exponentially as T_s is decreased in *Domain II*. This nucleation density increased produces the shift of the crystallization temperature to

higher values. Finally, *Domain III* occurs when the applied T_s temperature can only partially melts the crystals in the sample and unmolten crystals anneal (thickening) during the 5 min holding time at T_s, therefore in the subsequent heating run, an additional melting peak is observed due to the melting of the annealed crystals.

The **Successive Self-nucleation and Annealing** (SSA) experiment was carried out following the protocol suggested by Müller *et al*.[9, 10] As in the SN procedure, all the scans were also performed at 20 ºC/min. The first step is to erase the thermal history of the sample by heating it 20 ºC above the melting temperature and keeping the sample at that temperature for 3 minutes. Then the sample is cooled down to the same crystallization temperature chosen before in the SN protocol. After 3 minutes at that temperature, the sample is heated to the ideal self-nucleation temperature ($T_{s,ideal}$) and maintained during 5 minutes at this temperature. The $T_{s,ideal}$ is the lowest temperature observed in *Domain II* during the SN experiment. In this thesis and in order to compare the samples between them, the $T_{s,ideal}$ chosen for all the samples corresponds to the $T_{s,ideal}$ obtained for the PVDF homopolymer. During the procedure, the sample is cooled again to the crystallization temperature and held at that temperature for 3 minutes. This protocol is repeated, decreasing the T_s value 5 ºC compared to the previous cycle in each process. Finally, the sample is heated to the molten state to observe the results of the thermal fractionation.

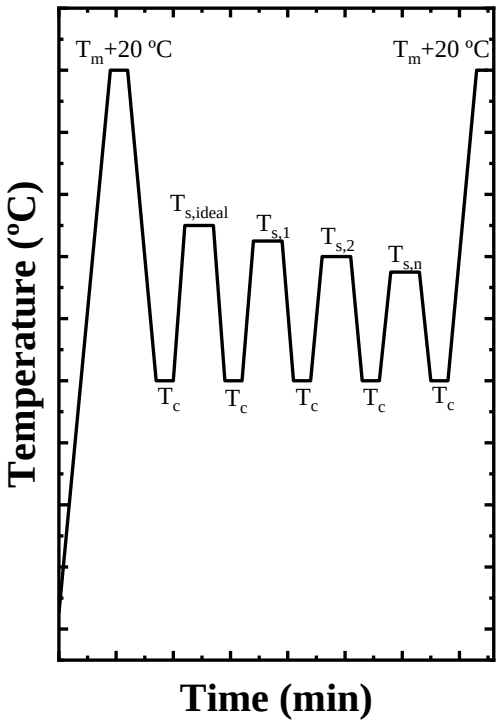

Figure 3. 8. Steps of the SSA protocol followed in this thesis work. All the scans were carried out at 20 ºC/min.

3.2.2 Small and Wide Angle X-ray Scattering (SAXS and WAXS)

X-Ray-Diffraction are non-destructive techniques that are usually employed to determine the crystalline structures of materials.

Wide Angle X-ray Scattering (WAXS) refers to the analysis of Bragg peaks scattered with wide angles to cover a wide range of scattering variables down to small *d*-spacing, which corresponds to the intermolecular distances. These peaks appear due to the nanocrystalline structures of the materials. WAXS is used to study the short-range order of the systems. The X-ray oriented to the solid materials will promote the scattering of a predictable pattern based on the internal structure of the

materials. With this diffraction pattern generated, it is possible to determine the composition of a synthesized material, the type of crystals formed in the solid-state, the crystal size, and the dimensions of the crystalline cells. The scattering intensity is plotted as a function of the 2θ (º) angle or the *q*-scattering vector (nm^{-1}). A semi-crystalline solid consists of a regular space of ordered atoms that can be described by planes. The distance between the planes is named as *d*-spacing. The intensity of this *d*-space pattern is proportional to the number of atoms that are found in the ordered planes.

Small Angle X-ray Scattering (SAXS) is a technique able to quantify differences at the level of nanoscale size distributions. To reach these results an analysis of the dispersion of the X-Ray beam after crossing the atoms of the materials is done, the range of angles in this, called as small angle is typically 0.1 - 5°. Depending on the angular range where the scattering signal is recorded, SAXS technique is able to provide structural information of dimensions between 1 and 100 nm. Moreover, SAXS can be a good technique used to know the behavior of the materials, with more than one component in the molten state, as for instance, it is possible to study the miscibility between different polymers in the melt. The scattering intensity also is plotted as a function of the 2θ (º) angle or the q scattering vector (nm^{-1}).

In this work, the SAXS and WAXS experiments were performed using synchrotron radiation at beamline BL11-NCD in the ALBA synchrotron facilities. By this technique, it is possible to observe the structural *in situ* evolution of the samples during cooling or heating scans at rates identical to those used in the DSC experiments, allowing a meaningful comparison between the data. Samples were measured in a Linkam hot-stage coupled to a liquid nitrogen cooling system. The samples were first cooled from the melt at different cooling rates until room temperature or -30 ºC, depending on the sample measured. Subsequently, the samples were heated again to the molten state at 20 ºC/min in all cases. The energy of the X-ray source was 12.4 keV (λ = 1.0 Å). In the WAXS configuration, a Rayonix LX255-HS sample

detector with an active area of 230.4 x 76.8 mm^2 was employed. A sample to detector distance of 15.5 mm with a tilt angle of 27.3º was employed; the resulting pixel size was 44 µm2. In the case of the SAXS configuration, the sample detector was a Pilatus 1M, which had an activated image area of 168.7 x 179.4 mm^2, a total number of pixels of 981 x 1043, a 172 x 172 μm^2 pixel size, and a 25 frames per s^{-1} rate and the distance employed was 6463 mm.

3.2.3 Fourier Transform Infrared Spectroscopy (FTIR)

FTIR is a technique employed in order to obtain the absorption or emission infrared spectrum at different wavelengths of the samples analysed. This technique irradiates a beam with many frequencies of light at the same time and the detector measures the beam absorbed by the sample. Then the beam is changed to different combination of frequencies obtaining a new data point. This process is repeated many times in a short period of time. The Fourier transform is used to convert the domain in cm into its inverse domain, wavenumbers in cm^{-1}.

In this work, a Nicolet 6700 Fourier transform infrared spectrometer equipped with an Attenuated Total Reflectance (ATR) Golden Gate MK II accessory with a diamond crystal was employed. Film samples were previously melted and then crystallized at different cooling rates in an external Linkam hot-stage, and after the thermal treatments, they were studied using the FTIR equipment. The measurements were carried out always at room temperature.

3.2.4 Polarized Light Optical Microscopy (PLOM)

PLOM technique is characterized by the employment of at least one polarizer in the microscope with the aim that the sample receives a beam of polarized light. Usually, the polarized optical microscope has two polarizers, with the sample placed between them, positioned in the light path. The second polarizer is the analyser and is positioned between the objective rear aperture and the observation device. This

design is made to observe samples with optical anisotropic properties. If the polarizers are crossed, the beam light only can go in the orthogonal direction and the light is not transmitted. This effect happens when there is not a sample in the holder, an amorphous material with an isotropic structure is observed or the polymer is in the molten state. In this case, the final image observed will be a homogeneous background. If the sample observed is a semicrystalline polymer with the crystals already formed, there is an interference phenomenon that allows to the beam light to pass through the microscope and reach the detector. The image observed in this case will be an area with bright yellow and blue colours that corresponds to the anisotropic crystals regions and a dark background that corresponds to the amorphous or molten region. Apart from the observation of the samples, PLOM also is a useful tool for the measurement of the spherulitic or axialitic growth rate with the employment of a special software and it is possible to calculate the nuclei density of the samples.

In this work all samples were analyzed by an Olympus BX51 polarized optical microscope coupled to a Linkam hot-stage, that uses nitrogen to control the temperature and manages the cooling rate. An Olympus SC50 camera linked to the microscope was employed to observe the samples and take micrographs. Samples were measured directly in bulk, covering by a glass cover when the sample is in the molten state, or were previously dissolved in a specific solvent, and drop casted on a glass substrate and dried at room temperature.

3.2.5 Transmission Electron Microscopy (TEM)

TEM technique employs an electrons beam that is directed through an ultrathin sample and the sample has to be prepared with a thickness of less than 100 nm. The image of the sample obtained is formed from the interaction of the electrons with the sample. The resolution of this technique (order of nm) is higher than light microscopes (order of μm), so using TEM microscopy in polymers permit even to observe the lamellae of the crystalline phase of the materials. Sometimes, when there is more than one compound in each material, it is necessary, depending on the type

of materials, a previous stained of the sample in order to observe the crystalline lamellae of one of the components.

In this work, all the samples were stained with RuO_4 before the measurements by immersing thin strips of material in this solution for 16 h. Then, the samples were cut in ultra-thin sections at room temperature with a diamond knife on a Leica EMFC6 ultra-microtome device. These 90 nm thick ultra-thin sections were mounted on a 200 mesh copper grid and then observed by a TECNAI G2 20 TWIN TEM equipped with a LaB6 filament operating at an accelerating voltage of 120 kV.

3.2.6 Broadband Dielectric Spectroscopy (BDS)

BDS technique study the relaxation processes that are caused by the rotational fluctuations of the molecular dipoles. This technique is based on the application of an external electrical field to a sample, creating spontaneous dipole moments in the material.[11] When the electrical field is removed, the dipoles can return to the same state of energy giving information about the spontaneous fluctuations in the material. Employing this technique is possible to obtain information about the dynamical processes of characteristic parts in the materials. BDS measures the dielectric properties of a medium as a function of the frequency, by an external oscillating electrical field, or of the time.

The complex dielectric permittivity, $\varepsilon^*(\omega) = \varepsilon'(\omega) - i\varepsilon''(\omega)$, where ε' is the real part and ε'' is the imaginary part, was obtained as a function of the frequency (ω) and temperature by using a Novocontrol high-resolution dielectric analyzer (Alpha analyzer) (Novocontrol, Montabaur, Germany). The sample cell was set in a cryostat, whose temperature was controlled via a nitrogen gas jet stream coupled with a Novocontrol Quatro controller. Samples were placed between two flat gold-plated electrodes (10 and 20 mm in diameter), forming a parallel plate capacitor with a 0.1 mm thick Teflon spacer. Frequency sweeps were performed at a constant temperature with a stability of ± 0.1 ºC.

In the analysis of the data, the ratio $\varepsilon^*/\varepsilon_\infty$ is used to minimize the effect of the uncertainties in the sample geometry when different samples are compared. ε_∞, determined through the behavior at very low temperatures and at high frequencies, is free of dipole reorientation contributions and only related to the induced polarization phenomena. Therefore, no significant differences in the actual ε_∞ values among the different samples should exist.

BDS measurements were carried out as follows. Samples were heated up to the molten state inside the cryostat. At that temperature was held for 5 min to ensure a homogeneous filling of the capacitor and to obtain a fully amorphous initial state. Then, measurements started at from the melt, cooling the samples in isothermal steps of 10 ºC down to -100 ºC, and subsequently heating them up to the melt, again in 10 ºC steps. Samples were tested at different temperatures over a frequency range of 10^{-1} to 10^{7} Hz.

3.3 References

1. Cimmino, S.; Martuscelli, E.; Silvestre, C.; Canetti, M.; De Lalla, C.; Seves, A., Poly(ethylene oxide)/poly(ethyl methacrylate) blends: Crystallization, melting behavior, and miscibility. *Journal of Polymer Science Part B: Polymer Physics* 1989, 27, (9), 1781-1794.

2. Höhne, G.; McNaughton, J.; Hemminger, W.; Flammersheim, H.-J., *Differential scanning calorimetry*. Springer Science & Business Media: 2003.

3. Lorenzo, A. T.; Arnal, M. L.; Albuerne, J.; Müller, A. J., DSC isothermal polymer crystallization kinetics measurements and the use of the Avrami equation to fit the data: Guidelines to avoid common problems. *Polymer Testing* 2007, 26, (2), 222-231.

4. Pérez-Camargo, R. A.; Liu, G.-M.; Wang, D.-J.; Müller, A. J., Experimental and Data Fitting Guidelines for the Determination of Polymer Crystallization Kinetics. *Chinese Journal of Polymer Science* 2022, 40, (6), 658-691.

5. Lorenzo, A. T.; Arnal, M. L.; Sánchez, J. J.; Müller, A. J., Effect of annealing time on the self-nucleation behavior of semicrystalline polymers. *Journal of Polymer Science Part B: Polymer Physics* 2006, 44, (12), 1738-1750.

6. Michell, R. M.; Mugica, A.; Zubitur, M.; Müller, A. J., Self-Nucleation of Crystalline Phases Within Homopolymers, Polymer Blends, Copolymers, and Nanocomposites. In *Polymer Crystallization I: From Chain Microstructure to Processing*, Auriemma, F.; Alfonso, G. C.; de Rosa, C., Eds. Springer International Publishing: Cham, 2017; pp 215-256.

7. Fillon, B.; Wittmann, J. C.; Lotz, B.; Thierry, A., Self-nucleation and recrystallization of isotactic polypropylene (α phase) investigated by differential scanning calorimetry. *Journal of Polymer Science Part B: Polymer Physics* 1993, 31, (10), 1383-1393.

8. Sangroniz, L.; Cavallo, D.; Müller, A. J., Self-Nucleation Effects on Polymer Crystallization. *Macromolecules* 2020, 53, (12), 4581-4604.

9. Müller, A. J.; Michell, R. M.; Pérez, R. A.; Lorenzo, A. T., Successive Self-nucleation and Annealing (SSA): Correct design of thermal protocol and applications. *European Polymer Journal* 2015, 65, 132-154.

10. Müller, A. J.; Arnal, M. L., Thermal fractionation of polymers. *Progress in Polymer Science* 2005, 30, (5), 559-603.

11. Kremer, F.; Schönhals, A., *Broadband dielectric spectroscopy*. Springer Science & Business Media: 2002.

Chapter 4

Effect of the TrFE Content on the Crystallization of P(VDF-co-TrFE) copolymers

4.1 Introduction

Up to now, in several works, crystal characteristics e.g., structure, and phase transitions of P(VDF-*co*-TrFE) copolymers have been widely studied by X-ray and Raman techniques.[1-3] Moreover, the polarization hysteresis loops of P(VDF-*co*-TrFE) thin films have also been widely analysed.[4-6] Linked with all these properties, the processing conditions are another important tool, and different works discussing this aspect are also found in the literature. For example, annealing processes have been applied at different temperatures as 120, 130 or 140 ºC during different times (from 1 hour to 24 hours) to observe how these conditions affect the final structure and their ferroelectric properties.[7-9] Spampinato *et al*. have revealed in their work that the annealing temperature affects the remnant polarization value, and they established that the best temperature range for processing was between 133 and 137 ºC. Regarding the annealing time, they concluded that only 15 minutes were enough to obtain a high ferroelectric performance and that this annealing time will affect mainly the coercive field value.[10]

In this chapter, we study the overall crystallization kinetics in P(VDF-*co*-TrFE) random copolymers with different compositions and compare them with a standard PVDF homopolymer to observe how the TrFE comonomer affects the crystallization process on PVDF. We have employed different experimental techniques such as Differential Scanning Calorimetry (DSC), Polarized Light Optical Microscopy (PLOM), and Wide Angle X-ray Scattering (WAXS). Isothermal and non-isothermal experiments have been performed, and the nucleation rate, the growth rate, and different kinetic parameters have been calculated to determine the nucleating effect of TrFE in PVDF and how this comonomer can affect the crystallization of the all-trans crystalline phase. Additionally, self-nucleation and Successive Self-Nucleation and Annealing (SSA) thermal fractionation studies have been performed to investigate the inclusion of TrFE in PVDF crystals. Finally, a fully ferroelectric study

has been performed by recording the polarization versus electric field hysteresis loops of different copolymers composition based capacitors. These results are analysed and correlated with the kinetics studied by DSC experiments.

4.2 Materials and methods.

4.2.1 Materials

A commercial PVDF is used in this work (Aldrich Ltd., M_w = 180000 g/mol, M_n = 71000 g/mol) as homopolymer sample. Different random copolymers of P(VDF-*co*-TrFE) with different molar ratios were supplied by Piezotech® FC (France). In this work, 80/20; 75/25, and 70/30 VDF/TrFE molar ratios were used.

4.2.2 Methods

a) Differential Scanning Calorimetry (DSC)

A Perkin Elmer DSC 8000 with an Intracooler II as a cooling system was employed to carry out the DSC experiments. The equipment was calibrated with indium and tin standards.

The non-isothermal procedure consists of a first heating scan of the material to 200 ºC and holding the sample at this temperature for 3 minutes to erase the thermal history. Then the sample is cooled down at 20 ºC/min from the molten state to 25 ºC and held for 1 minute at this temperature. After this step, a new heating scan at 20 ºC/min is performed up to the molten state.

For the isothermal crystallization experiments, the protocol employed was the same described by Müller *et al.*[11, 12] First, the minimum crystallization temperature ($T_{c,min}$) is estimated. To find this temperature, the sample is heated to the molten state (200 ºC) and held for 3 minutes at this temperature. The following step is cooling the sample at 60 ºC/min to a previously selected crystallization temperature (T_c). At the moment that this T_c is reached, the sample is immediately heated up at 20 ºC/min

to the melt. If no melting peak is appreciated during this second heating scan, this is a valid crystallization temperature. The experiments are repeated at lower T_c values until a melting peak is found during the subsequent heating scan, indicating that the sample was able to crystallize during cooling at 60 ºC/min. Hence this temperature is discarded, and the immediately higher T_c value is employed as $T_{c,min}$.

Once the value of the $T_{c,min}$ is obtained, the isothermal crystallization experiments are carried out in the widest possible experimental range. As in the previous experiments, the sample is heated up to 200 ºC and maintained during 3 minutes at this temperature. Then the sample is quickly cooled down (60 ºC/min) to a previously selected T_c and held at this T_c for 40 minutes to let the sample crystallize until saturation. When the crystallization process is finished, the sample is heated up at 20 ºC/min to the molten state. The process starts again with the next T_c selected.

The self-nucleation (SN) experiments were performed following the protocol proposed by Müller *et al.*[13, 14] All the scans carried out during the SN experiments were made at 20 ºC/min. First, the thermal history of the material is erased at 200 ºC for 3 minutes. For the next step, the sample is cooled from the molten state to 100 ºC to ensure the crystallization of the material and is held for 3 minutes at this temperature. Then the sample is heated to a previously selected SN temperature, T_s, and remained at this temperature for 5 minutes. The following step is cooling down the sample from the T_s to the crystallization temperature chosen and keeping the sample for 3 minutes at this temperature. In this step, depending on the *Domain* that the sample is, some changes in the value of the T_c can be observed towards higher values in comparison with the previous T_s employed. Finally, the sample is heated again to the molten state, also this step is important to monitor due to the possible annealing process that can be observed in this *Domain* and can be appreciated in the subsequent melting peaks. After this step, the experiment is repeated by changing the T_s value to another one. Briefly, three *Domains* can be appreciated or distinguished during the SN process for the materials. A material is in *Domain* I when the melting process of the material occurs completely, and the thermal history of the

sample is erased. In *Domain* II, the material can self-nucleate but the temperature is not high enough to provoke an annealing process. When an annealing peak is detected, the sample is within *Domain* III. In the results and discussion section, in the self-nucleation part, there is an extensive explanation for each *Domain,* and the behaviour of the sample in each *Domain* can be well appreciated.

The Successive Self-nucleation and Annealing (SSA) experiment was carried out following the protocol designed by Müller *et al*.[15, 16] As in the SN procedure, all the scans were also performed at 20 ºC/min. The first step is to erase the thermal history of the sample by heating it to 200 ºC and keeping the sample at that temperature for 3 minutes. Then the sample is cooled down to 100 ºC. After 3 minutes at that temperature, the sample is heated to the ideal self-nucleation temperature ($T_{s,ideal}$) and maintained during 5 minutes at this temperature. The $T_{s,ideal}$ is the lowest temperature observed in *Domain II* during the SN experiment. In this work and in order to compare the samples between them, the $T_{s,ideal}$ chosen for all the samples corresponds to the $T_{s,ideal}$ obtained for the commercial PVDF homopolymer. During the procedure, the sample is cooled again to the crystallization temperature and held at that temperature for 3 minutes. This protocol is repeated again decreasing the T_s value 5 ºC compared to the previous cycle measured in each process. Finally, the sample is heated to the molten state to observe the results obtained during the thermal fractionation process.

b) Wide Angle X-ray Scattering (WAXS)

The systems were studied by wide angle X-ray scattering (WAXS) on a Bruker D8 Advance diffractometer (Bruker, Bremen, Germany) working in parallel beam geometry with Cu K_α transition photons of wavelength λ= 1.54 Å. The measurements were performed at room temperature in reflection mode (θ-2θ configuration) after a heating-cooling process to erase the samples' thermal history, varying the scattering angle 2θ from 10º to 30º with steps of 0.05º. The scattered intensities are shown as a function of momentum transfer Q, $Q= 4\pi \lambda^{-1} \sin\theta$.

c) Polarized Light Optical Microscopy (PLOM)

The equipment employed to analyse the samples was an Olympus BX51 polarized optical microscope with a Linkam hot-stage coupled to control the temperature and the heating and cooling rates. To control the thermal process, liquid nitrogen was employed in the Linkam hot-stage. The micrographs were taken by an Olympus SC50 camera linked to the microscope. The samples were previously dissolved in DMF (dimethylformamide), and the solutions with a concentration of around 4% were drop-casted in a glass substrate and dried at room temperature before the measurements. The growth rate of the spherulites observed was calculated from the slope of the spherulite radius versus time plots, which were always found linear.

d) TF Analyzer

Ferroelectric measurements, basically polarization hysteresis loops, were performed on parallel capacitors and recorded at room temperature using the TF Analyzer 2000E of aixACCT Systems. A continuous sinusoidal wave with a 0.1 Hz frequency was used, and a 150 MV/m electric field was applied to ensure saturation. To prepare the capacitors, the aluminum (Al) electrodes were thermally evaporated onto clean glass substrates to form 100 nm thick bottom electrodes (ME400B PLASSYS evaporator) where the P(VDF-*co*-TrFE) films are later coated. 100 nm thick top Al electrodes were finally thermally evaporated. The temperature inside the evaporator was kept below 70 ºC. The sample preparation was performed by taking a solution containing 10 wt% of P(VDF-*co*-TrFE) (for three different compositions) in cyclopentanone and spin-coating it on previously prepared Al/glass substrates. Before the experiments, an annealing process was done in all three studied samples. The samples were heated from room temperature until 135 ºC, and they kept at this temperature for 15 min, following the procedure published by Spampinato *et al.*[10]

4.3 Results ands discussion

4.3.1 Non-isothermal crystallization

First, the P(VDF-*co*-TrFE) copolymers and the PVDF homopolymer were analysed by DSC under non-isothermal conditions.

Figure 4.1a shows the cooling process from the melt for copolymers and for the neat PVDF. In the homopolymer, only one crystallization peak is observed at 120 ºC, whereas in the random copolymers different exotherms can be appreciated. The peak observed at high temperatures (~ 120-125 ºC) for the copolymers corresponds to the crystallization peak of the PVDF phase. It can be observed how this crystallization temperature increases when the amount of TrFE also increases. Moreover, in the copolymers, other peaks are appreciated at lower temperatures. These peaks correspond to the PVDF Curie transition, associated with the Curie temperature (T_{Curie}). This temperature indicates the phase transition between the polar phase and non-polar phase of the different copolymers. At temperatures above this T_{Curie} the material is paraelectric, whereas if the system is below the T_{Curie}, the material is ferroelectric. It is well-known in the literature that for P(VDF-*co*-TrFE) copolymers, when the amount of PVDF increases, the T_{Curie} also increases.[2, 17]

In Figure 4.1b, the heating DSC curves of the same samples are shown. In this case, the melting peak that corresponds to the neat PVDF homopolymer is at higher temperatures than the melting peaks observed for the PVDF phase within the copolymers, which appears at temperatures below that of the neat PVDF and also for the neat poly(trifluoroethylene) (PTrFE) studied in the literature.[18, 19] As it happens for the crystallization temperature when the composition of TrFE increases, the melting temperature also increases in the copolymers.[20, 21] One hypothesis for this behaviour is the nucleation effect observed on the PVDF (discussed below), where the TrFE comonomer acts as a nucleating agent increasing both the crystallization and the melting temperatures (only one or two degrees for melting temperature).

For the copolymers, the Curie transition is observed at lower temperatures, below the crystallization exotherm of the PVDF component. This transition exhibits a reversible Curie point at which the ferroelectric polymers show a transformation from a polar ferroelectric state to a non-polar paraelectric state or vice versa. In the DSC heating scans (Figure 4.1b), a transition from a ferroelectric to a paraelectric phase appears.[22] Below this Curie point, the crystalline structure in the ferroelectric phase is composed of all-trans chains (*TTT*). On the other hand, above the Curie point, the paraelectric crystalline structure essentially consists of a statistical combination of *TT*, TG^{+}, and TG^{-} rotational isomers, composed of the α-phase ($TG^{+}TG^{-}$) and a phase that consists of α-phase with trans defects.[9, 23]

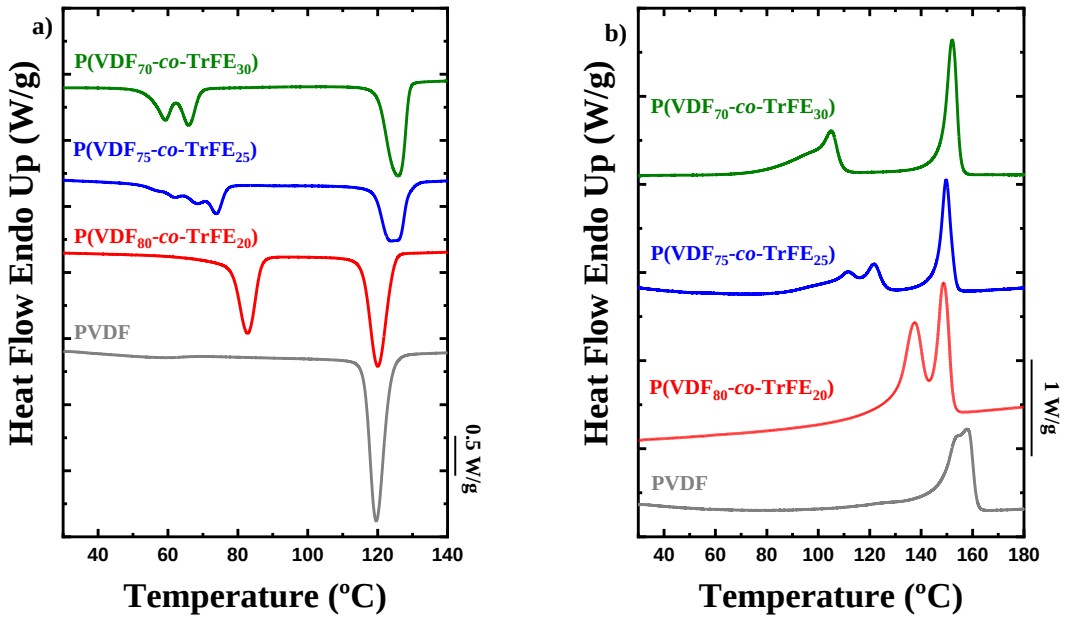

Figure 4. 1. DSC experiments for the PVDF homopolymer and P(VDF-*co*-TrFE) copolymers at different compositions. a) Cooling process from the molten state at 20 ºC/min and b) heating scan at 20 ºC/min after the previous cooling process.

The WAXS analysis performed at room temperature after a cooling process (Figure 4.2) reveals that copolymers crystallize in all-trans conformation (β-phase) and the neat PVDF in the α-phase. Figure 4.2 shows for the random copolymers, a shift

to lower q values in the reflection of the β-phase when the content of TrFE increase, this shift is generated by the inclusion of the TrFE in the PVDF crystals.[2, 21]

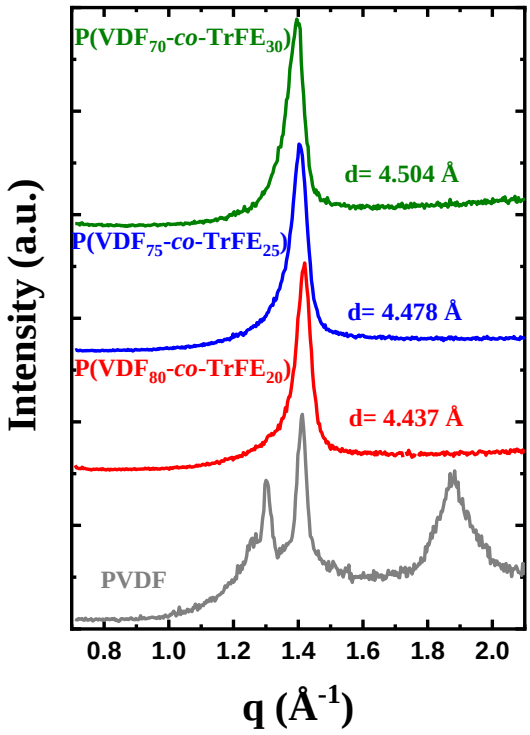

Figure 4. 2. WAXS analysis of the neat PVDF homopolymer and P(VDF-*co*-TrFE) copolymers after a cooling scan at 20 ºC/min. The d values were added in order to appreciate the TrFE inclusion in the PVDF crystals.

All the calorimetric data extracted from the non-isothermal crystallization experiments are listed in Table 4.1. The values of the melting and crystallization enthalpies are exposed in this Table, in the case of an exclusion of the TrFE in the PVDF crystals the values of the enthalpies should decrease dramatically when the content of TrFE increases. In our case this is not happening, therefore is possible to speculate with a scenario of inclusion of the TrFE in the PVDF crystals.

Table 4. 1. Calorimetric data of all the samples obtained after the DSC heating and cooling scans at 20 ºC/min.

Sample	T_c (ºC)	ΔH_c (J/g)	T_m (ºC)	ΔH_m (J/g)	$T_{curie,\ c}$ (ºC)	$T_{curie,\ h}$ (ºC)
PVDF	120	38.4	158	31.0	-	-
P(VDF$_{80}$-*co*-TrFE$_{20}$)	120	28.9	149	25.1	83	137
P(VDF$_{75}$-*co*-TrFE$_{25}$)	124	20.2	150	19.5	74 68 62	112 122
P(VDF$_{70}$-*co*-TrFE$_{30}$)	126	26.3	152	26.1	66 59	105

4.3.2 Isothermal crystallization

The isothermal crystallization of the PVDF homopolymer and the random copolymers was also studied to determine the kinetics of the crystallization process at different compositions of TrFE. First, all the samples were observed on the polarized light optical microscope (PLOM) and the growth rate of the crystals was measured.

Figure 4.3 shows the isothermal superstructural growth rates (either spherulites or axialites) from the melt of the samples obtained employing the PLOM technique, where the solid lines plotted are calculated using the Lauritzen and Hoffman theory.[24] In the case of the random copolymers, due to the high nucleation density observed, only the crystal growth at crystallization temperatures higher than 135 ºC were measured. Figure 4.3 shows the growth rates (G) as a function of the crystallization temperature (T_c). It is observed how the neat PVDF superstructures have a very different temperature dependence compared to the copolymer system. Hence, the G values are faster than the random copolymers at high crystallization temperatures, but the G versus T_c curves crossed at lower temperatures. Among the random copolymers, the general trend is that of a reduction in growth rate as TrFE is incorporated in the copolymers, a trend that can be rationalized by the inclusion of TrFE chains within the PVDF crystals, which apparently limit the secondary nucleation process of PVDF chains.

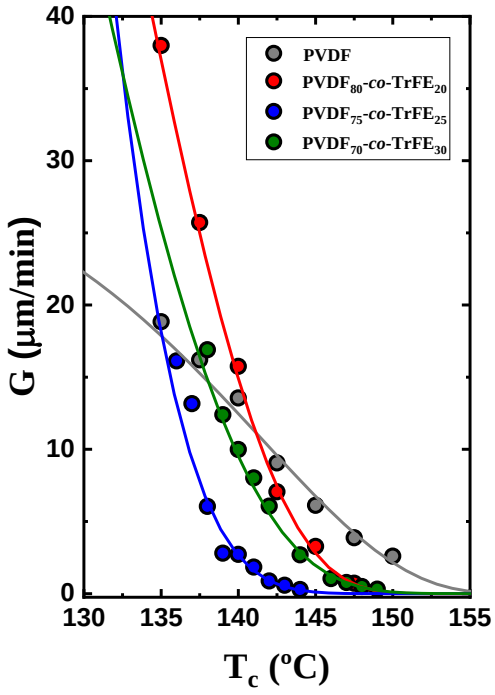

Figure 4. 3. Superstructural growth rates obtained by PLOM for the PVDF homopolymer and P(VDF-*co*-TrFE) random copolymers at different compositions against the crystallization temperature.

The parameters obtained using the Lauritzen and Hoffman theory are listed in Table 4.2. The values of K_g^G observed are the parameters obtained from Figure 4.3. These values are valid for the overall crystallization temperatures as the L-H solid lines exhibit in Figure 4.3. In the case of the neat PVDF, at high temperatures the *G* values are higher than the copolymer ones, however when the isothermal temperature decreases the *G* values of the neat PVDF decreases and tends to lower values. Therefore, the K_g^G values of the samples do not have any tendency with the proportion of TrFE or PVDF, because the overall values are compensated for the whole range of temperatures.

Table 4. 2. List of the parameters obtained through the Lauritzen and Hoffman theory applied in the PLOM experiments.

Sample	Kg^G **(K^2)**	R^2	σ_e **(erg/cm^2)**	Σ **(erg/cm^2)**	Q **(erg)**
PVDF homopolymer	$6.73x10^4$	0.970	60.4	7.86	$2.2x10^{-13}$
P(VDF_{80}-*co*-$TrFE_{20}$)	$3.86x10^4$	0.998	35.1	7.86	$1.29x10^{-13}$
P(VDF_{75}-*co*-$TrFE_{25}$)	$9.70x10^4$	0.970	87.5	7.86	$3.23x10^{-13}$
P(VDF_{70}-*co*-$TrFE_{30}$)	$5.84x10^4$	0.970	52.4	7.86	$1.93x10^{-13}$

Apart from the spherulite growth rate, the morphology of the superstructures formed was also studied. As observed in Figure 4.4a, the PVDF homopolymer exhibits clear negative spherulites with well-defined Maltese cross extinction patterns. As TrFE is incorporated into the copolymers, the morphology changes from spherulites to axialites. This is possible to see in Figure 4.4b, c and d. In Figure 4.4b, when the TrFE content is still low (80/20) some spherulites are still visible coexisting with axialites. If the TrFE content increases, the morphology changes to mostly axialites with a relatively similar size (i.e., instantaneously nucleated). In the case of the sample with the highest content on TrFE, P(VDF_{70}-*co*-$TrFE_{30}$) (Figure 4.4d), the morphology is formed by microaxialites where the nucleation density is very high. Figure 4.4 clearly shows that the inclusion of TrFE has a nucleating influence on PVDF at the examined isothermal crystallization temperatures (indicated in the Figure caption), as the number of primary nuclei and its density increases as the amount of TrFE also increases in the copolymer.

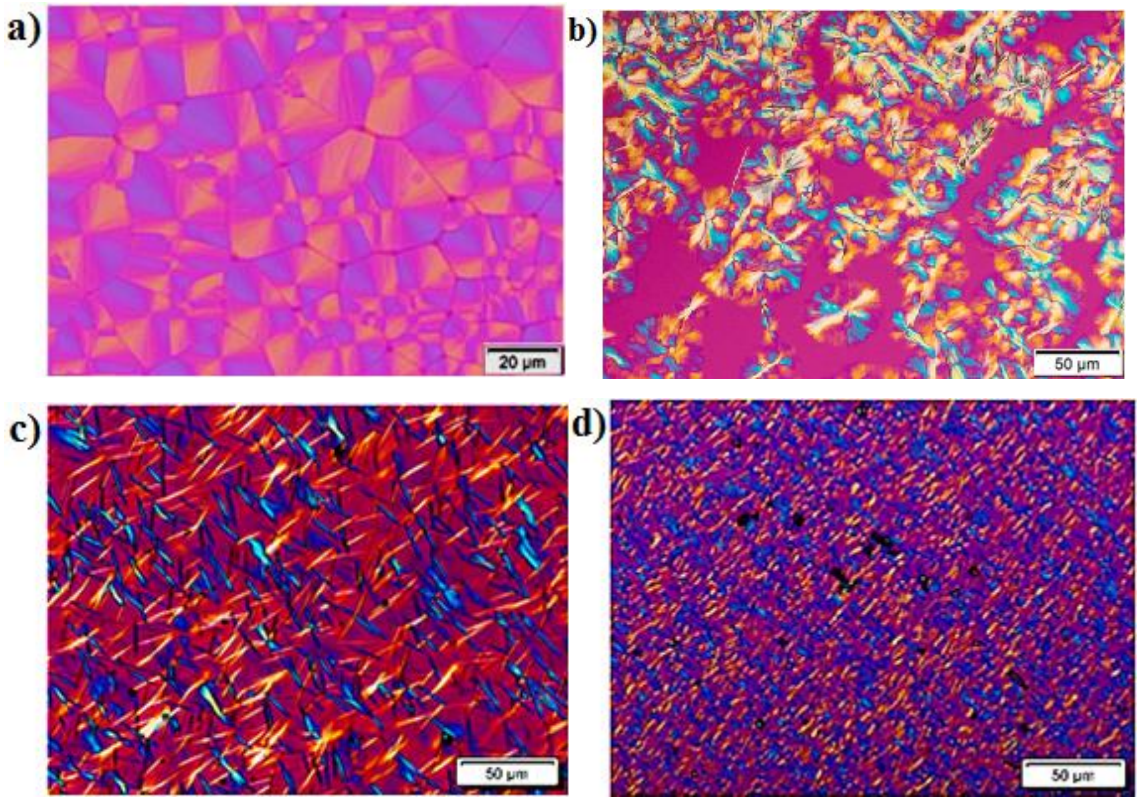

Figure 4. 4. Representative PLOM images taken during an isothermal crystallization process of: a) PVDF homopolymer at 140 ºC, b) P(VDF_{80}-*co*-$TrFE_{20}$) at 140 ºC, c) P(VDF_{75}-*co*-$TrFE_{25}$) at 139 ºC and d) P(VDF_{70}-*co*-$TrFE_{30}$) at 140 ºC.

The crystallization process was also studied by Differential Scanning Calorimetry (DSC) to estimate the primary nucleation rate before crystallization starts (from incubation time data), the overall crystallization kinetics (including both primary and secondary nucleation data), and the melting point of the isothermally crystallized polymorphs.

The primary nucleation rate was obtained through the inverse of the induction or incubation time (t_0). This represents the primary nucleation rate before any exothermic crystallization heat can be detected in the DSC. Figure 4.5 shows the inverse of the induction time against the crystallization temperature. At high crystallization temperatures the samples have similar nucleation rate values. When the crystallization temperature decreases, the PVDF homopolymer has the lowest nucleation rate

values. For most cases, the incorporation of TrFE tends to increase the primary nucleation density and the primary nucleation rate before crystallization starts, according to DSC.

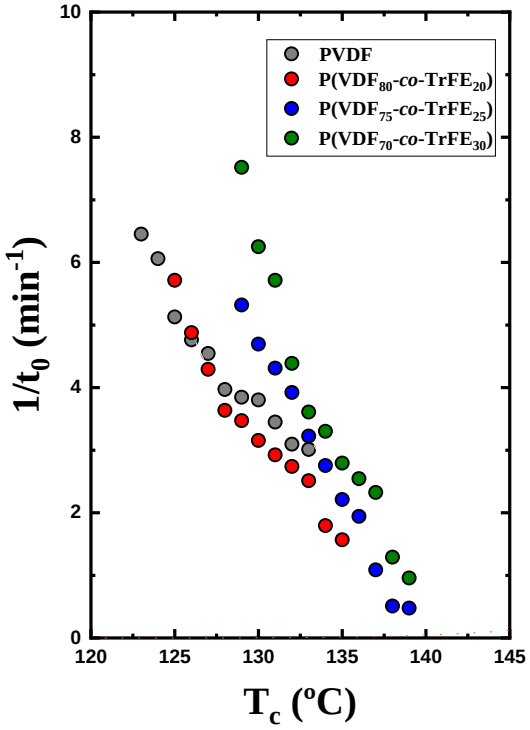

Figure 4. 5. Inverse of the induction time for neat PVDF and copolymers at different compositions against the isothermal crystallization temperature.

The inverse of the half crystallization time ($\tau_{50\%}$) was experimentally determined as it represents a quantitative measure of the overall crystallization rate that includes both nucleation and growth during the solidification from the melt to the semicrystalline state. During the isothermal crystallization experiments, the half crystallization time is the time needed by the material to attain 50% relative conversion to the semicrystalline state.

Figure 4.6 shows the inverse of the half crystallization time as a function of the isothermal crystallization temperature. The solid lines plotted were calculated by the

Lauritzen and Hoffman theory. The P(VDF_{75}-*co*-$TrFE_{25}$) and P(VDF_{70}-*co*-$TrFE_{30}$) samples crystallize faster at similar T_c values in comparison to the P(VDF_{80}-*co*-$TrFE_{20}$) and neat PVDF, whose overall crystallization rates are similar. A comparison between Figure 4.6 (where both nucleation and growth influence the results) and Figure 4.3, where only growth is taken into account, indicates that there is a competition between the increase in primary nucleation and the decrease in secondary nucleation (growth) when the TrFE content increases in the copolymers. As a result, the increase in primary nucleation seems to be the determining factor in the overall increase in crystallization kinetics for the copolymers with 25 and 30% of TrFE in comparison with the neat PVDF or the copolymer with the lowest amount of TrFE.

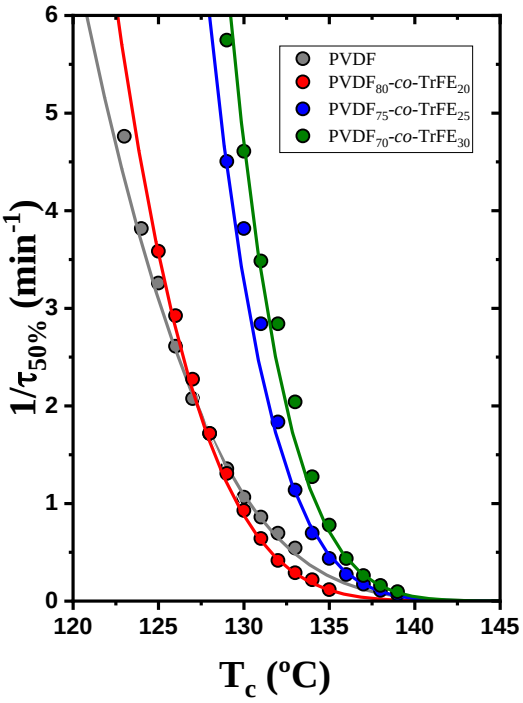

Figure 4. 6. Inverse of the half crystallization time for neat PVDF and copolymers at different compositions as a function of the isothermal crystallization temperature.

All the parameters extracted from the fitting of the Lauritzen and Hoffman theory by DSC experiments are listed in Table 4.3. In this case, the K_g^{τ} values have a logical

tendency with the TrFE content on the copolymer samples. The neat PVDF and P(VDF$_{80}$-*co*-TrFE$_{20}$) samples have similar values as can be observed in Figure 4.6a. When the content of TrFE increases the values of K_g^{τ} also increases. In addition, the values of K_g^{τ} are higher than the values of K_g^{G} (see Table 4.2), these results are consistent because the values of K_g^{G} only includes the growth of the crystals whereas the K_g^{τ} includes growth and nucleation processes.

Table 4. 3. All the parameters calculated through the Lauritzen and Hoffman theory applied for every sample by DSC experiments.

Sample	K_g^{τ} (K^2)	R^2	σ_e (erg/cm^2)	σ (erg/cm^2)	Q (erg)
PVDF homopolymer	$1.29x10^5$	0.996	116.2	7.86	$4.29x10^{-13}$
P(VDF$_{80}$-*co*-TrFE$_{20}$)	$1.26x10^5$	0.998	113.9	7.86	$4.20x10^{-13}$
P(VDF$_{75}$-*co*-TrFE$_{25}$)	$1.46x10^5$	0.994	131.8	7.86	$4.86x10^{-13}$
P(VDF$_{70}$-*co*-TrFE$_{30}$)	$1.63x10^5$	0.995	146.7	7.86	$5.42x10^{-13}$

The equilibrium melting temperature (T_m^0) values employed in each sample and used in the Lauritzen and Hoffman theory are estimated by the Hoffman-Weeks method (Figure 4.7 and Table 4.4).[25, 26]

Table 4. 4. Equilibrium melting temperature values for each sample obtained by Hoffman-Weeks theory.

Sample	PVDF homopolymer	P(VDF$_{80}$-*co*-TrFE$_{20}$)	P(VDF$_{75}$-*co*-TrFE$_{25}$)	P(VDF$_{70}$-*co*-TrFE$_{30}$)
T_m^0 (ºC)	163.3	158.4	161.1	163.0

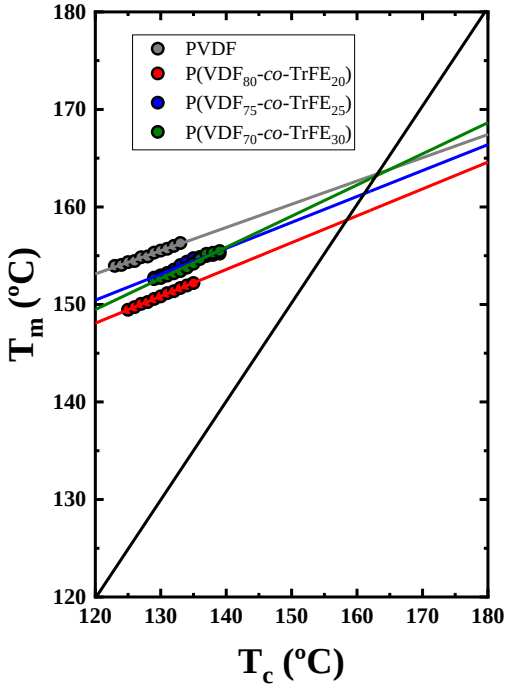

Figure 4. 7. Isothermal crystallization temperature against the melting temperature in order to achieve the equilibrium melting temperature (T_m^0) by Hoffman-Weeks method for neat PVDF and the copolymers.

To predict the overall crystallization kinetics during the primary crystallization regime, the Avrami theory was employed. The form of the Avrami equation employed is the following:[12]

$$1 - V_c(t - t_0) = exp(-k(t - t_0)^n) \qquad \text{eq. 4.1}$$

where V_c is the fraction of the relative volume fraction transformed to the semi-crystalline state, t is the time employed in the experiment, t_0 is the induction time before the crystallization start, k is the constant of the overall crystallization rate and n is the Avrami index (related with the time dependence of the nucleation and the crystal geometry).

The Avrami index is composed by two terms:[27, 28]

$$n = n_d + n_n \qquad \text{eq. 4.2}$$

where n_d is the dimensionality of the crystals growing and n_n represents the nucleation kinetics contribution. For polymers, the dimensionality expected is 2D or 3D that corresponds to a value of n_d of 2 or 3, for axialitic or spherulitic morphology, respectively. The value of n_n fluctuate between 0 and 1, where 0 is for a pure instantaneous nucleation and 1 corresponds to purely sporadic nucleation.

The application of the Avrami equation in every isothermal temperature carried out allows to obtain the Avrami index (n). To apply this equation it is necessary that the crystallization process starts when the sample reaches the isothermal crystallization temperature previously selected and not during the cooling step. The n value can predict the morphology of the crystals in the isothermal crystallization procedures. If the value is lower than 1.5 the crystals formed are needles (1D), when the value is between 1.5 and 2.4 the crystals should be instantaneously nucleated axialites (2D) and if n values are between 2.5 and 3.4 the crystals could be sporadically nucleated axialites or instantaneously nucleated spherulites (i.e., n = 3). When the Avrami index is between 3.5 and 4 it is possible to ensure that the crystal morphology is 100% spherulitic (i.e., n = 4 for sporadically nucleated spherulites).[11, 12, 29]

All the Avrami indexes obtained are presented in Figure 4.8a. The PVDF homopolymer has all the n values higher than 2.5, which is consistent with the spherulitic morphology observed previously by PLOM (Figure 4.4a). The random copolymers have values between spherulites and axialites and it is possible to observe how the n value decreases when the TrFE content increases. In some cases, Figure 4.8a reports values of the Avrami index close to 2 for the two copolymers with the highest TrFE contents, which correspond to instantaneously axialites, which is consistent with the morphologies observed in Figures 4.4c and 4.4d.

Figure 4.8b plots the $k^{(1/n)}$ values for each isothermal crystallization temperature. This value is an indicative of the overall crystallization rate predicted by the Avrami theory.[11, 12] The comparison of these values with those obtained experimentally by DSC (Figure 4.6) demonstrates the accuracy of the Avrami theory due to the high similarity in all the results gathered.

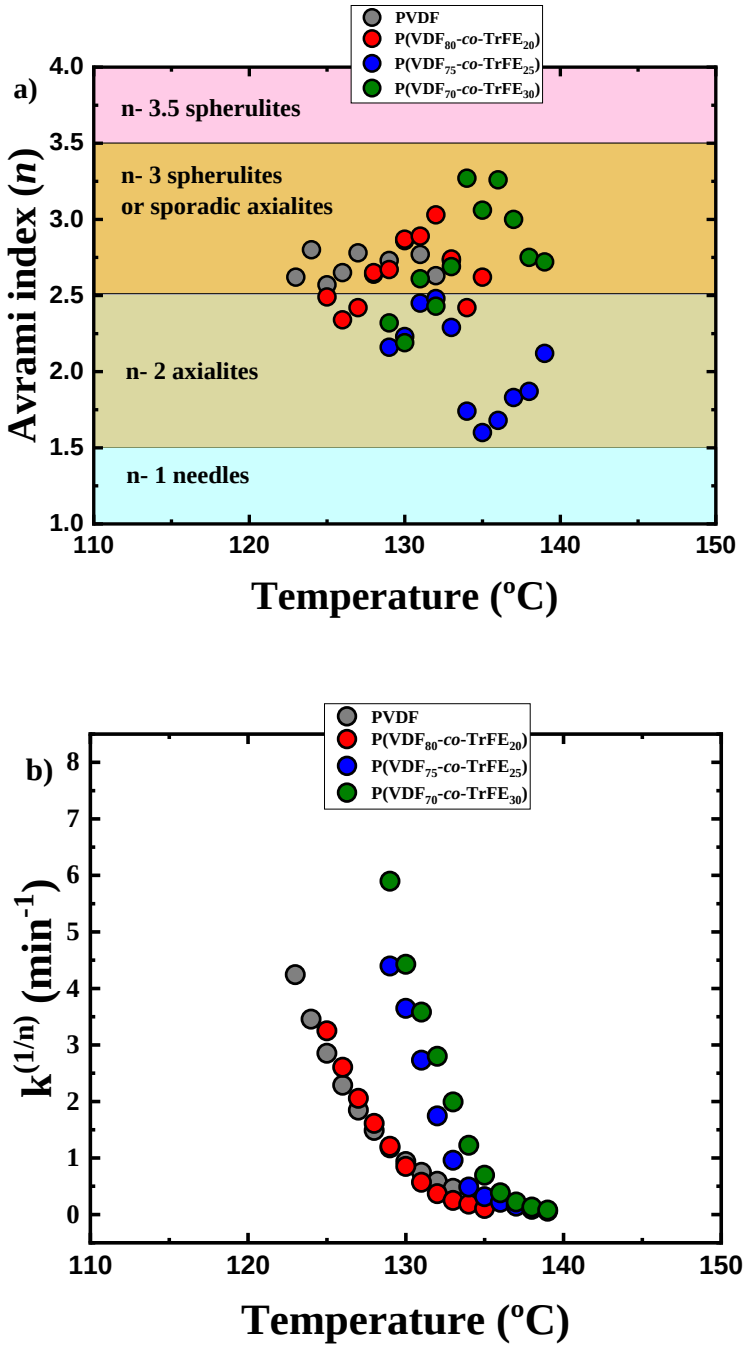

Figure 4. 8. a) Avrami index values for neat PVDF and copolymers at different compositions against their respective isothermal crystallization temperatures and b) crystallization rate obtained by the Avrami model in each isothermal temperature measured.

After the isothermal crystallization procedure, the analysis of the subsequent DSC heating scans was carried out. Figure 4.9 presents DSC heating curves measured immediately after the isothermal crystallization of the PVDF homopolymer

sample. In neat PVDF, at low isothermal crystallization temperatures, two melting peaks are observed. The first melting peak, located around 155 ºC corresponds to the α-phase that it is the most common and stable crystalline phase in PVDF when the polymer is crystallized from the molten state.[30, 31] The second melting peak (also corresponding to the melting of α-phase crystals) or shoulder observed is the reorganization of the α-crystals during the heating process. This second peak tends to disappear when the isothermal crystallization temperatures increases.

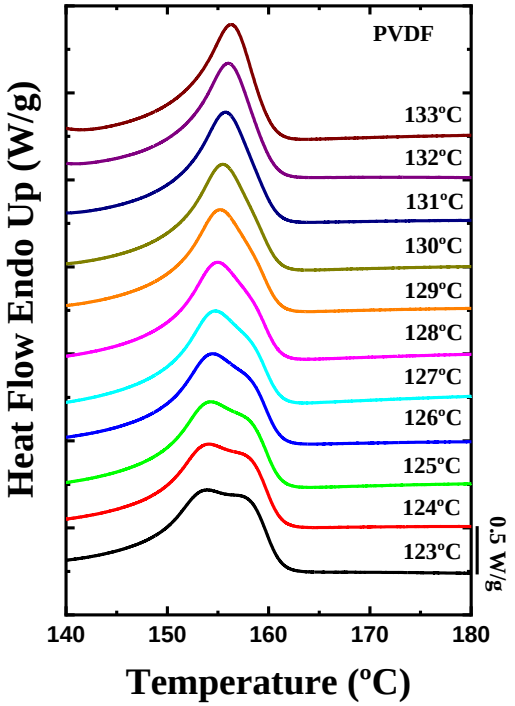

Figure 4. 9. DSC heating scans after the isothermal crystallization process of PVDF homopolymer.

The DSC heating scans for random copolymers at different compositions after the isothermal crystallization processes are presented in Figure 4.10. All the samples presented have the same behaviour, where only one melting peak is observed and located at around 150 ºC. This melting peak corresponds to a crystalline structure

composed essentially of TG^+TG^- chains (i.e., the α-phase) because the melting temperature observed occurs at higher temperatures than the Curie transition detected for all the copolymer samples.

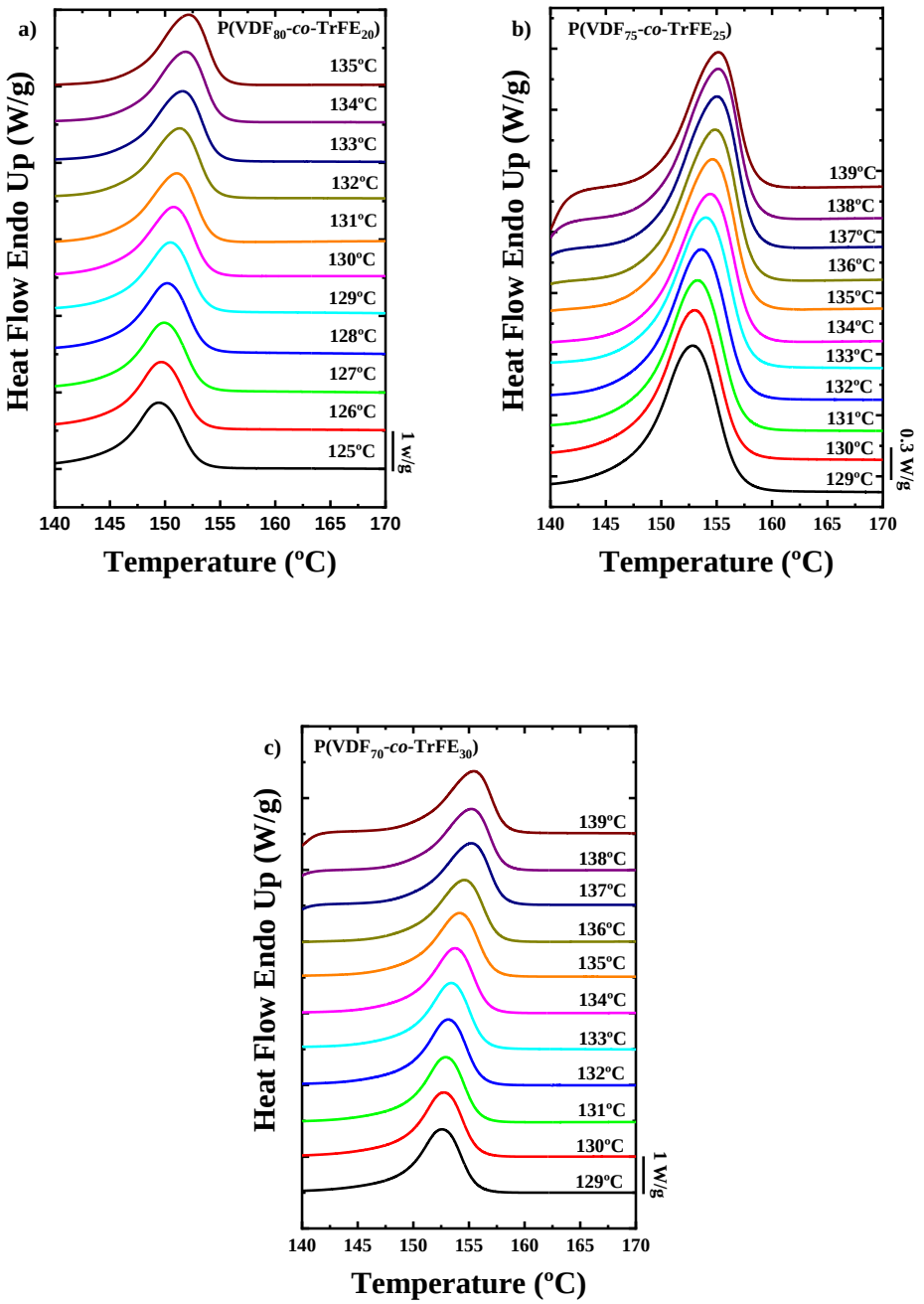

Figure 4. 10. DSC heating curves after the isothermal crystallization process of a) P(VDF$_{80}$-co-TrFE$_{20}$), b) P(VDF$_{75}$-co-TrFE$_{25}$) and c) P(VDF$_{70}$-co-TrFE$_{30}$) samples.

4.3.3 Self-Nucleation (SN) and Successive Self-Nucleation and Annealing (SSA)

In theory, the best nucleating agent for a polymer is made up by its own crystal fragments.[14, 32, 33] To check the nucleating effect of the TrFE in the PVDF, self-nucleation experiments were carried out in the homopolymer and in the three copolymers studied. Figure 4.11 shows the results obtained after the SN protocol in the PVDF homopolymer. The cooling scans after the holding time (5 minutes) at the indicated T_s temperatures are plotted in Figure 4.11a, and the subsequent heating scans are presented in Figure 4.11b. The colours of the lines is an indicative to know in which *Domain* the polymer is, at the temperature indicated. Red denotes *Domain I* (melting *Domain*), blue *Domain II* (self-nucleation *Domain*) and green *Domain III* (self-nucleation and annealing *Domain*). Figure 4.11c shows the different *Domains* observed superimposed on the standard melting curve of the PVDF homopolymer sample.

In *Domain I* the melting process of the polymer occurs completely and the thermal history of the material is erased, so that isotropic and relaxed random coils exist in the molten state. For neat PVDF *Domain I* occurs at temperatures higher or equal to 167 ºC (Figure 4.11), and there are no changes in the crystallization temperature of the material upon cooling from *Domain I*.

Domain II encompasses a T_s range where self-nuclei remain in the polymer but the temperature is not high enough to produce annealing of any unmolten crystal fragments that could act as self-seeds. For more information on self-nucleation *Domains*, the reader is referred to two recent reviews.[14, 33] *Domain II* is identified because upon cooling from T_s values located in this *Domain*, the crystallization peak temperature increases, as the nucleation density is increased. Finally, *Domain III* occurs when the applied T_s temperature can only partially melt the crystals in the sample and unmolten crystals anneal (thicken) during the 5 min holding time at T_s, therefore in the subsequent heating run, an additional melting peak is observed due to the melting of the annealed crystals (Figure 4.11b).

The PVDF is located in *Domain II* after self-nucleation with T_s temperatures in the range between 162 ºC and 166 ºC (see Figure 4.11a). The lowest T_s value in *Domain II* is known as the ideal self-nucleation temperature, $T_{s\ ideal}$, as it produces the maximum self-nucleation effect (i.e., maximum increase in T_c values) without any annealing. The nucleation density is increased exponentially as T_s is decreased in *Domain II*. This nucleation density increase produces the shift of the crystallization temperature to higher values. This behaviour is observed in Figure 4.11c when the material is in the range of temperatures within *Domain II*. The increase in the crystallization temperature in *Domain II* can cause small changes in the melting point, as observed in Figure 4.11b. At 166 ºC the PVDF exhibits a bimodal melting peak as a result of reorganization during the scan. As the T_s temperature is lower to 163 ºC the melting turns monomodal, as crystallization took place at much higher temperatures during cooling, already producing more stable crystals that do not need to reorganize during melting process.

The PVDF homopolymer shows a small annealing peak at T_s = 161 ºC signaling the onset of *Domain III* (Figure 10b). From this temperature to lower values of T_s the material is located in *Domain III*. The self-nucleation behaviour of PVDF is typical of most semicrystalline polymers in the bulk displaying the three SN Domains and very clear transitions between them.[14, 33]

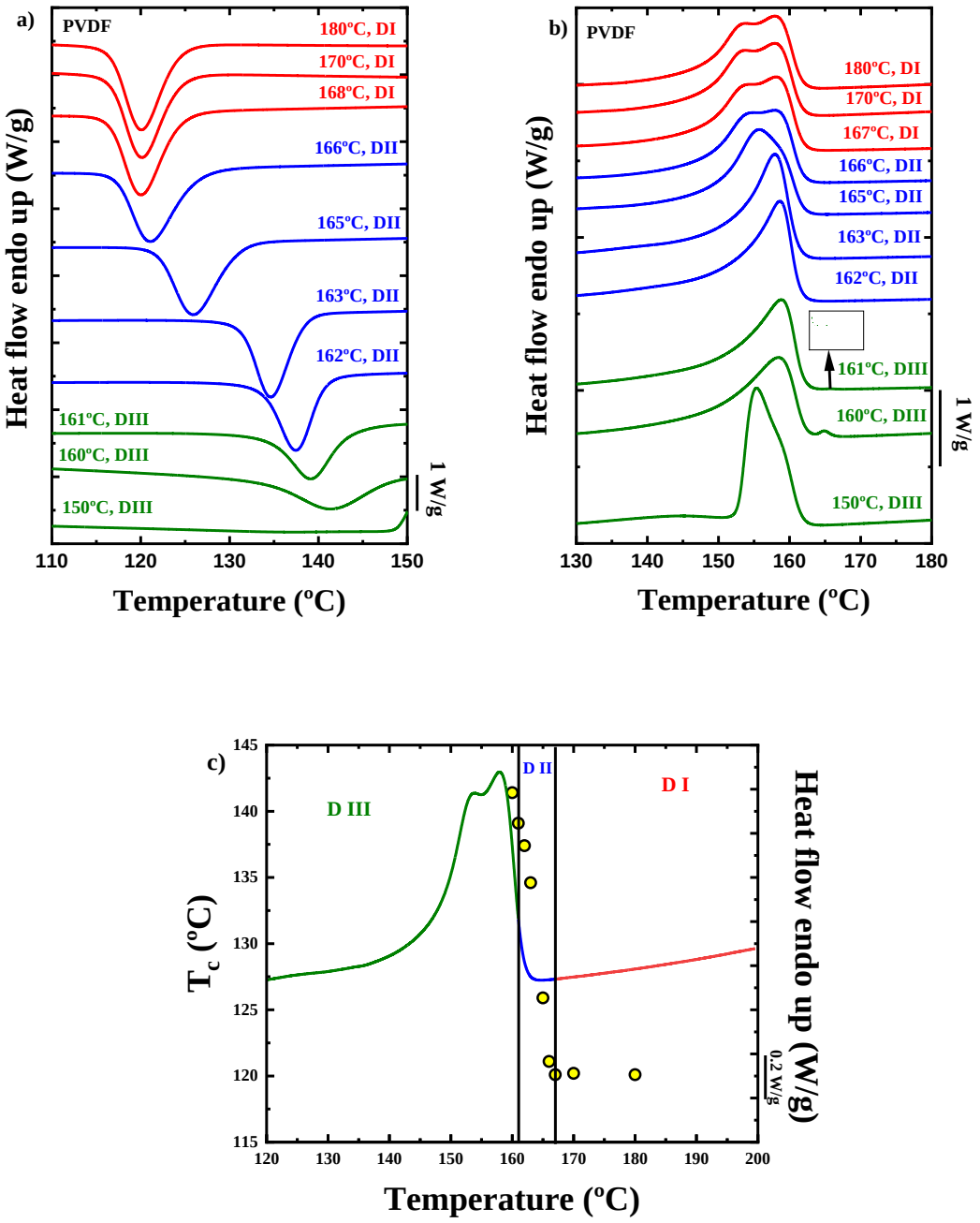

Figure 4. 11. a) DSC cooling scans after 5 minutes at the indicated T_s values, b) subsequent DSC heating scans for the PVDF homopolymer and c) representation of each Domain in the self-nucleation process superimposed on a standard melting curve of the PVDF homopolymer sample. The circles represent the crystallization temperature (left Y axis) at corresponding T_s value (X axis).

The results obtained by the self-nucleation protocol in the random copolymers are displayed in Figure 4.12. There is a large difference between the PVDF and the random copolymers. In the three random P(VDF-*co*-TrFE) copolymers *Domain II* is absent. The TrFE content in the copolymers affects the self-nucleation process and it can be observed how the T_s value range in each *Domain* is altered with the composition. The P(VDF_{80}-*co*-$TrFE_{20}$) sample is in *Domain I* at T_s values of 147ºC and higher, upon decreasing the self-nucleation temperature to 146 ºC the material directly change to *Domain III*. The P(VDF_{75}-*co*-$TrFE_{25}$) sample jumps directly from *Domain I* to *Domain III* at a T_s value of 150 ºC. Finally, in sample P(VDF_{70}-*co*-$TrFE_{30}$) there is a jump from *Domain I* to *Domain III* at 151 ºC and again there is no any presence of *Domain II* in the sample.

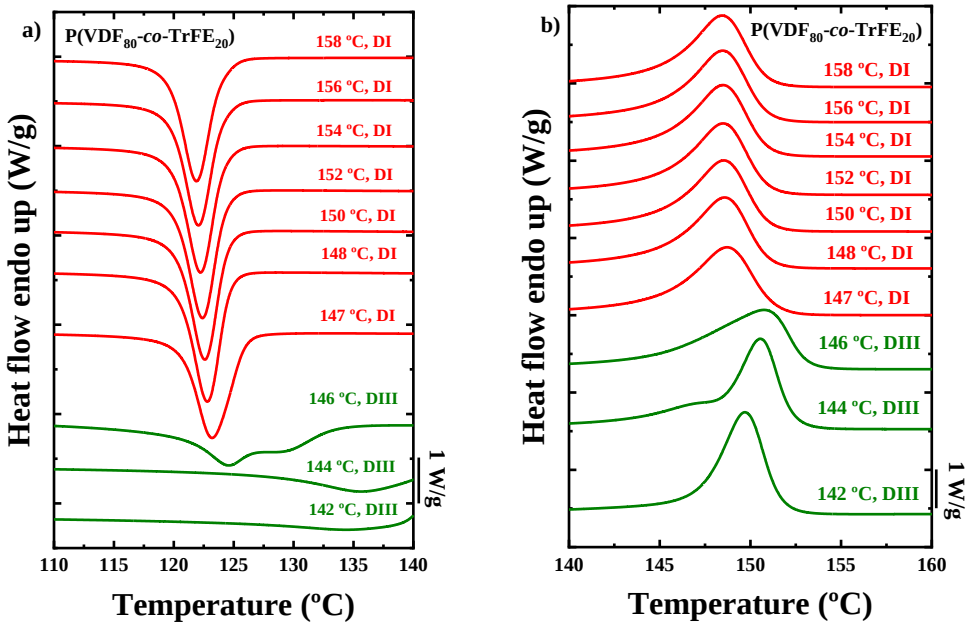
a)
P(VDF80-co-TrFE20)
158 °C, DI
156 °C, DI
154 °C, DI
152 °C, DI
150 °C, DI
148 °C, DI
147 °C, DI
146 °C, DIII
144 °C, DIII
142 °C, DIII
1 W/g
Heat flow endo up (W/g)
Temperature (°C)
b)
P(VDF80-co-TrFE20)
158 °C, DI
156 °C, DI
154 °C, DI
152 °C, DI
150 °C, DI
148 °C, DI
147 °C, DI
146 °C, DIII
144 °C, DIII
142 °C, DIII
1 W/g
Heat flow endo up (W/g)
Temperature (°C)

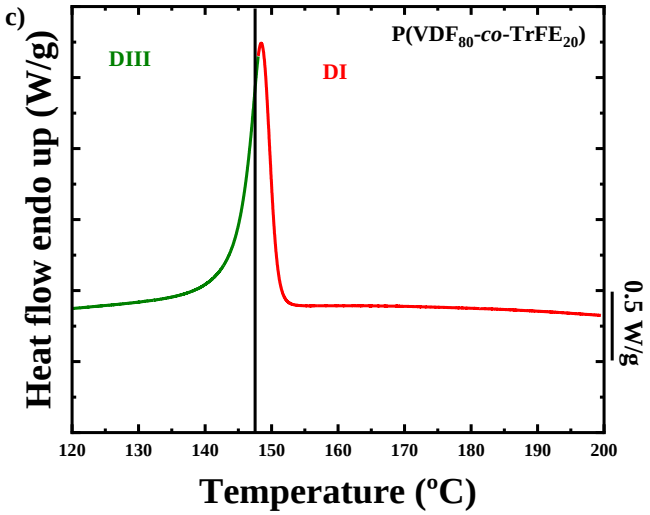
c)
P(VDF80-co-TrFE20)
DIII
DI
0.5 W/g
Heat flow endo up (W/g)
Temperature (°C)

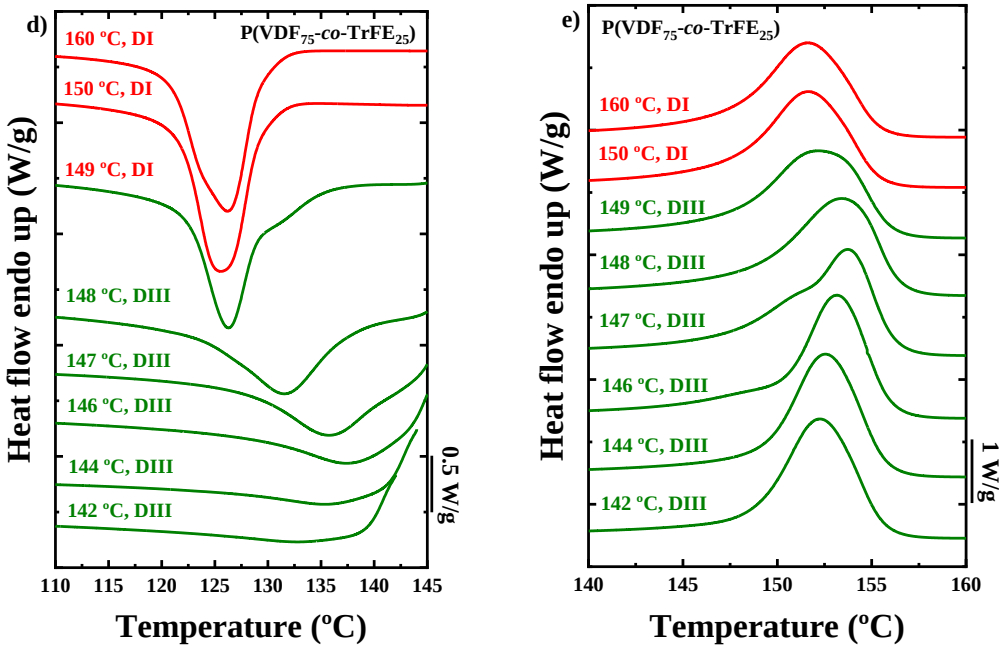
d)
P(VDF75-co-TrFE25)
160 °C, DI
150 °C, DI
149 °C, DI
148 °C, DIII
147 °C, DIII
146 °C, DIII
144 °C, DIII
142 °C, DIII
0.5 W/g
Heat flow endo up (W/g)
110 115 120 125 130 135 140 145
Temperature (°C)
e)
P(VDF75-co-TrFE25)
160 °C, DI
150 °C, DI
149 °C, DIII
148 °C, DIII
147 °C, DIII
146 °C, DIII
144 °C, DIII
142 °C, DIII
1 W/g
Heat flow endo up (W/g)
140 145 150 155 160
Temperature (°C)

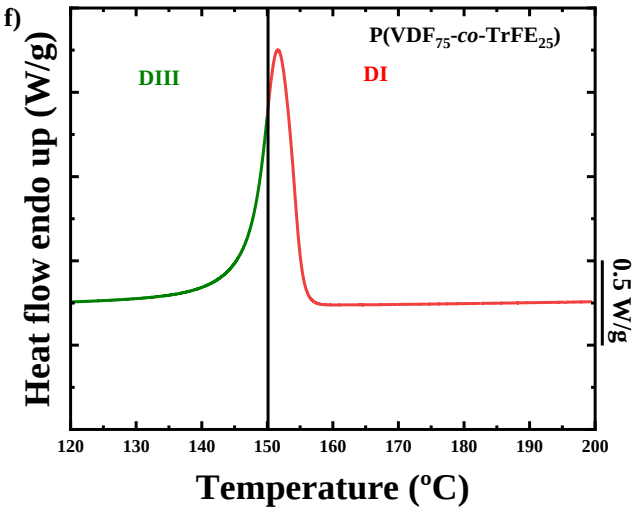
f)
P(VDF75-co-TrFE25)
DIII
DI
0.5 W/g
Heat flow endo up (W/g)
120 130 140 150 160 170 180 190 200
Temperature (°C)

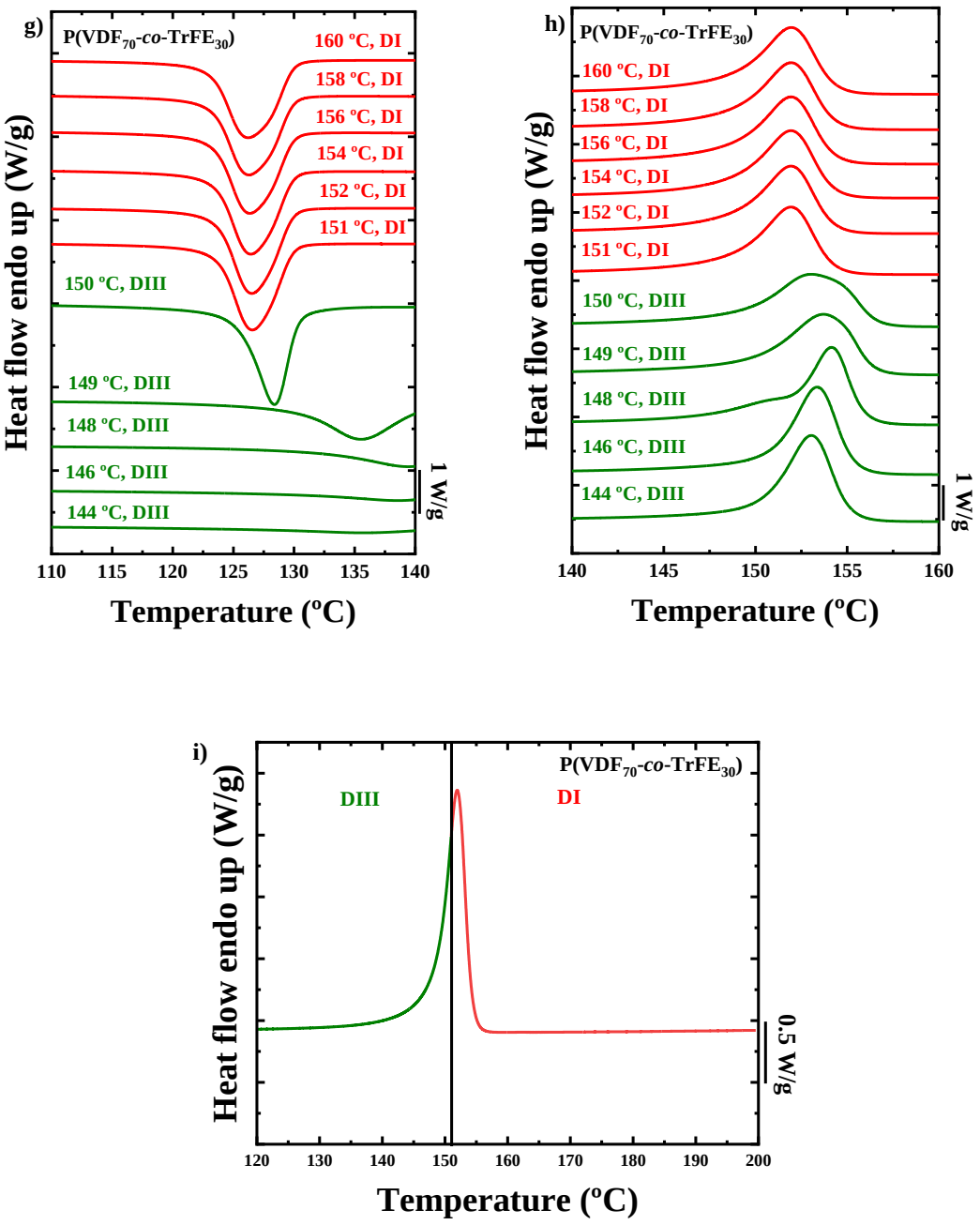

Figure 4. 12. DSC cooling sweeps after 5 minutes at the indicated T_s values for a) PVDF$_{80}$-*co*-TrFE$_{20}$, d) P(VDF$_{75}$-*co*-TrFE$_{25}$) and g) P(VDF$_{70}$-*co*-TrFE$_{30}$) samples. DSC heating scans after the cooling process for b) P(VDF$_{80}$-*co*-TrFE$_{20}$), e) P(VDF$_{75}$-*co*-TrFE$_{25}$) and h) P(VDF$_{70}$-*co*-TrFE$_{30}$) samples and representation of each Domain in the self-nucleation process in a standard melting curve of c) P(VDF$_{80}$-*co*-TrFE$_{20}$), f) P(VDF$_{75}$-*co*-TrFE$_{25}$) and i) P(VDF$_{70}$-*co*-TrFE$_{30}$) samples.

To appreciate better these jumps between *Domains*, the crystallization and melting enthalpies against the T_s values have been presented in Figure 4.13, where it is possible to observe how the crystallization enthalpy decreases when the material is in *Domain III*.

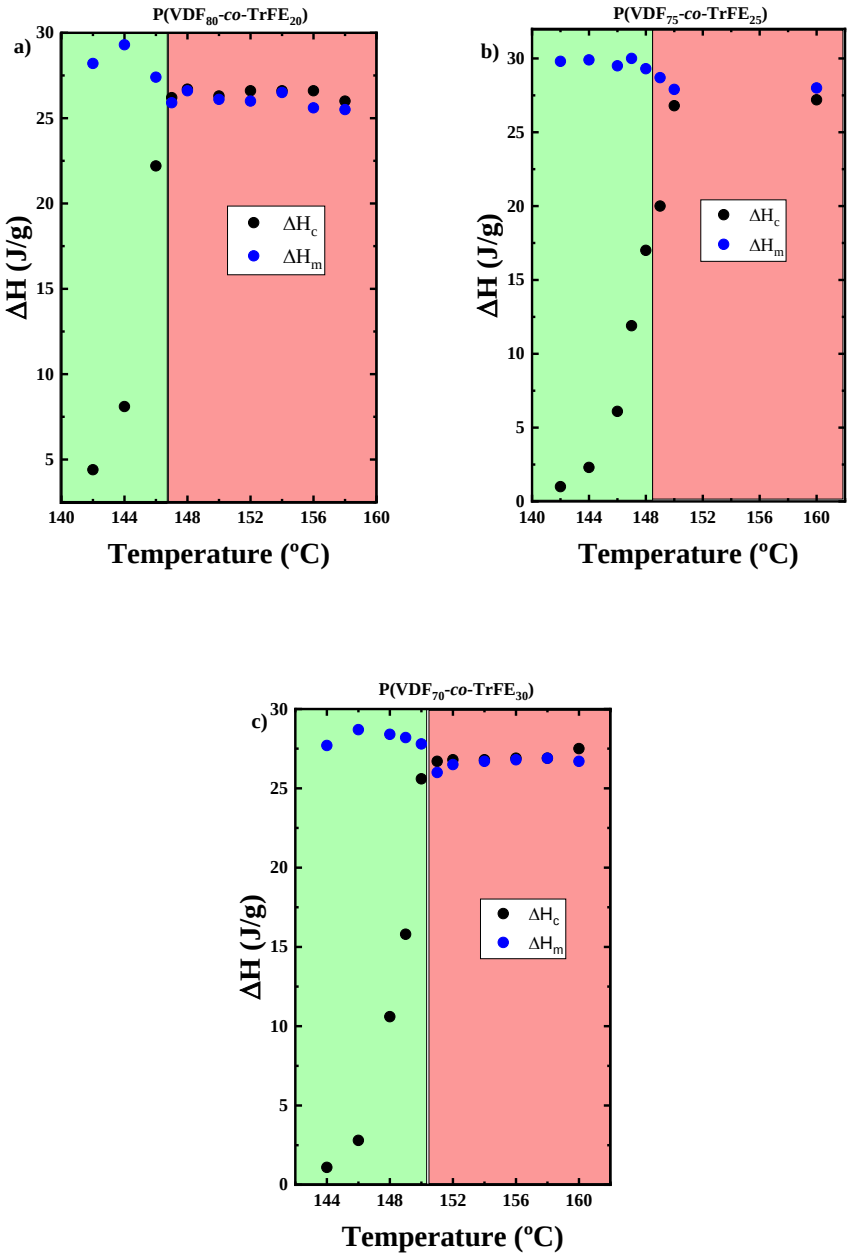

Figure 4. 13. Crystallization and melting enthalpies in each T_s value for the a) P(VDF$_{80}$-*co*-TrFE$_{20}$), b) P(VDF$_{75}$-*co*-TrFE$_{25}$) and c) P(VDF$_{70}$-*co*-TrFE$_{30}$). The green part indicates the temperatures that belong to the *Domain* III and the red part corresponds to the *Domain* I.

In addition, the melting temperature and the crystallization temperature of the curves after the self-nucleation protocol at the corresponding T_s values are plotted in Figure 4.14 in order to observe better the change of the different *Domains* during the experiments.

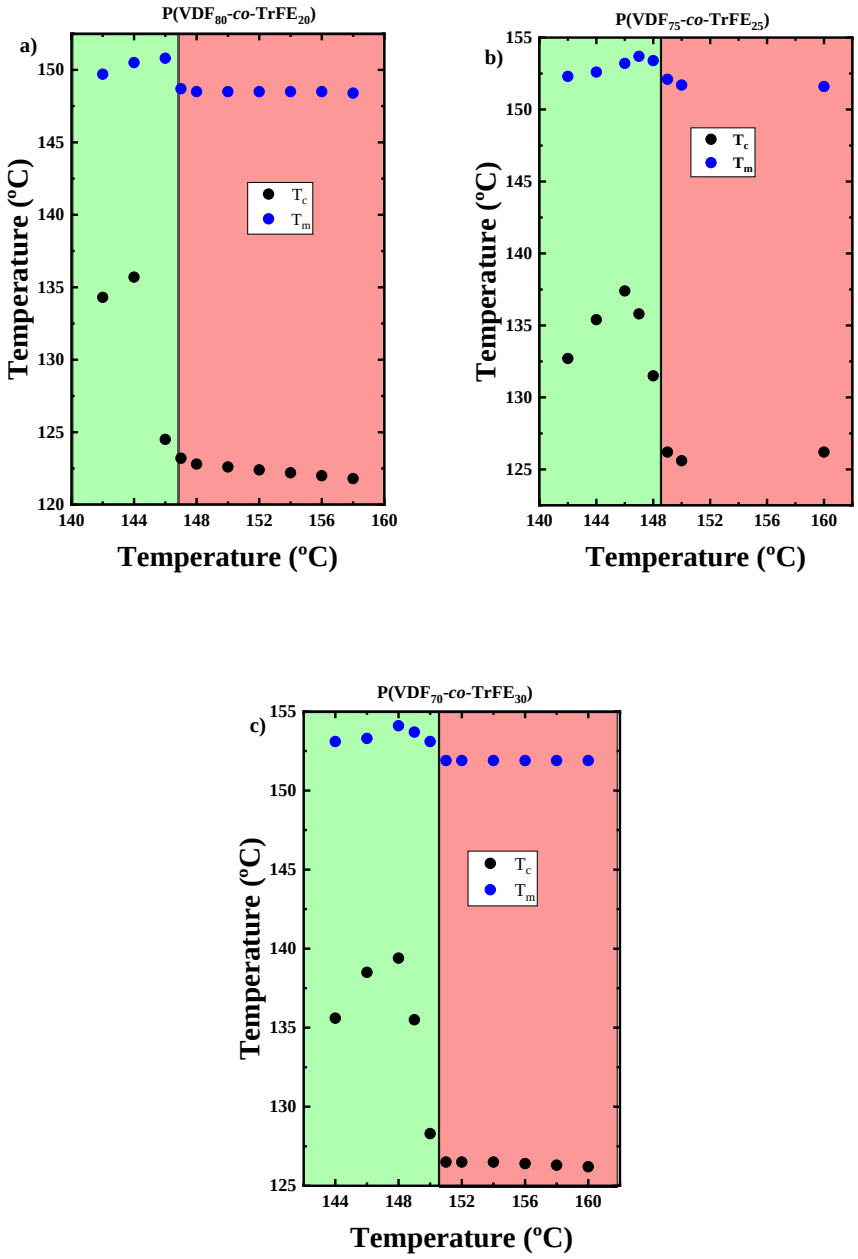

Figure 4. 14. Melting and crystallization temperatures at respective T_s values for a) P(VDF$_{80}$-*co*-TrFE$_{20}$), b) P(VDF$_{75}$-*co*-TrFE$_{25}$) and c) P(VDF$_{70}$-*co*-TrFE$_{30}$). The green part indicates the temperatures that belong to the *Domain* III and the red part corresponds to the *Domain* I.

In general, as the intrinsic nucleation density in polymeric materials increases, *Domain II* tends to reduce its width and eventually disappears. This behaviour is typical of many high-density polyethylenes (HDPE).[13] In the case of PVDF, the material clearly exhibits the three self-nucleation *Domains*, but when the TrFE counits are incorporated randomly into the copolymers, the nucleation density increases so much that the material is incapable of being self-nucleated without undergoing annealing. As in the case of HDPE, there seems to be a saturation value of the nucleation density above which self-nucleation without annealing is not possible anymore, and *Domain II* disappears. These results are consistent with the morphology change and the reduction of Avrami indexes observed in the copolymers.

The SSA treatment was carried out for all the samples, and the heating curves after the fractionation processes are collected in Figure 4.15. The vertical lines in the Figure indicate the T_s employed for the fractionation of the materials. The heating curve after SSA for the PVDF homopolymer sample reveals that it can be thermally fractionated. The DSC trace shows a series of endothermic peaks representing thermal fractions with different lamellar thicknesses (the higher the T_m value, the thicker the average lamellae). PVDF exhibits a monomodal fractionation profile after SSA that is probably proportional to its molecular weight distribution and/or intermolecular interactions. Linear PVDF should not contain defects that interrupt its crystallisable sequences. However, a small number of head-to-tail addition during polymerization could be present and may also contribute to facilitate molecular segregation during crystallization and hence thermal fractionation. In perfectly linear polymers without any defects that can interrupt the crystallizable sequences, the two possible sources for fractionation are the distribution of molecular weights[14, 15] and the existence of intermolecular interactions capable of acting like sticky “defects” in the chains.[34] This last effect is present in most polar molecules, so its presence in PVDF is also possible.

Unexpectedly, the random copolymers exhibit a very different SSA thermal fractionation profile. For the copolymer with the lowest TrFE incorporation, there is

only one melting endotherm after SSA process and a small shoulder at lower temperatures, which seems to be an ill-defined second thermal fraction. In any case, the thermal fractionation capacity has dramatically decreased in this P(VDF_{80}-*co*-$TrFE_{20}$) sample. The other two copolymer samples with a higher amount of TrFE are incapable of undergoing thermal fractionation during the SSA process. It is well known that incorporating comonomers in random copolymers where counit exclusion predominates during crystallization significantly increases the SSA thermal fractionation capacity.[14, 15] In the present case, the inclusion of TrFE does not lead to an increase in fractionation capacity. Therefore, the results presented in Figure 4.15 evidence that TrFE chains are included within the PVDF crystals. However, the total lack of fractionation in random copolymers is unexpected and represents a unique result in the field of SSA thermal fractionation processes. Materials like HDPE homopolymers that are 100% linear and non-polar do not experience fractionation (or the fractionation is very limited), a fact that has been attributed to the low sensitivity of HDPE chains to become fractionated based only on molecular weight distribution.[14, 15, 35, 36] What is remarkable about the results presented here is how the fractionation not only does not increase with comonomer incorporation, as one would have expected when exclusion dominates the behaviour, but that it is strongly inhibited. The SSA protocol in the random P(VDF-*co*-TrFE) copolymers only produces annealing of the samples, thereby increasing their melting points in comparison to the samples crystallized from the melt at 20 ºC/min, as show the thin red lines extracted from Figure 4.1b. The total lack of fractionation in the copolymers is difficult to explain, as it will depend on the exact nature of the SSA fractionation ability of PVDF.[35, 36]

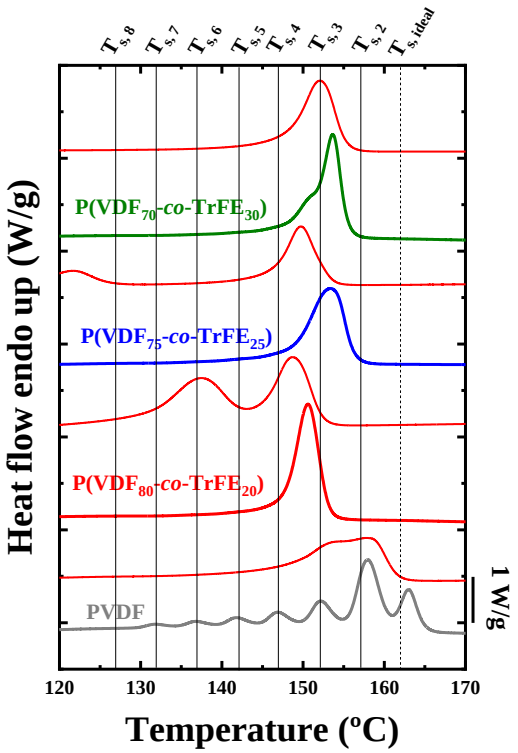

Figure 4. 15. Heating curves after the SSA protocol for neat PVDF and for the indicated copolymers. The thin red lines represent the heating curves at 20 ºC/min extracted from DSC scans after a cooling at 20 ºC/min.

4.3.4 Polarization vs Electric fiel measurements

Figure 4.16a presents the polarization as a function of electric field (*P* vs. *E*) hysteresis loops obtained by applying an external electric field of 150 MV/m at a frequency of 0.1 Hz for the three different copolymer compositions studied (80/20, 75/25 and 70/30 ones). Considering that the processing conditions were the same for the three of them, the ferroeletric response for the P(VDF$_{75}$-co-TrFE$_{25}$) is the best. The remnant polarization, P_r, value is 89 mC/m^2 for the processing conditions explained before. The other two compositions exhibit lower values of P_r, being 82 mC/m^2 for P(VDF$_{80}$-*co*-TrFE$_{20}$) sample and 80 mC/m^2 for P(VDF$_{70}$-*co*-TrFE$_{30}$) sample. The coercive field, E_c, value is higher for P(VDF$_{80}$-*co*-TrFE$_{20}$) sample, 78 MV/m, and is reduced for the other two samples, being 65 MV/m for the P(VDF$_{70}$-*co*-TrFE$_{30}$) composition and even lower for the P(VDF$_{75}$-*co*-TrFE$_{25}$) sample, 50

MV/m. Figure 4.16b presents the corresponding electric current as a function of the electric field (*I* vs. *E*) curves. Sharper switching peaks are observed for 75/25 and 70/30 compositions, which suggest a faster ferroelectric switching. With these results, it is possible to establish that the P(VDF$_{75}$-*co*-TrFE$_{25}$) sample manifests the best ferroelectric response in terms of higher P_r, lower E_c, and faster switching rate.

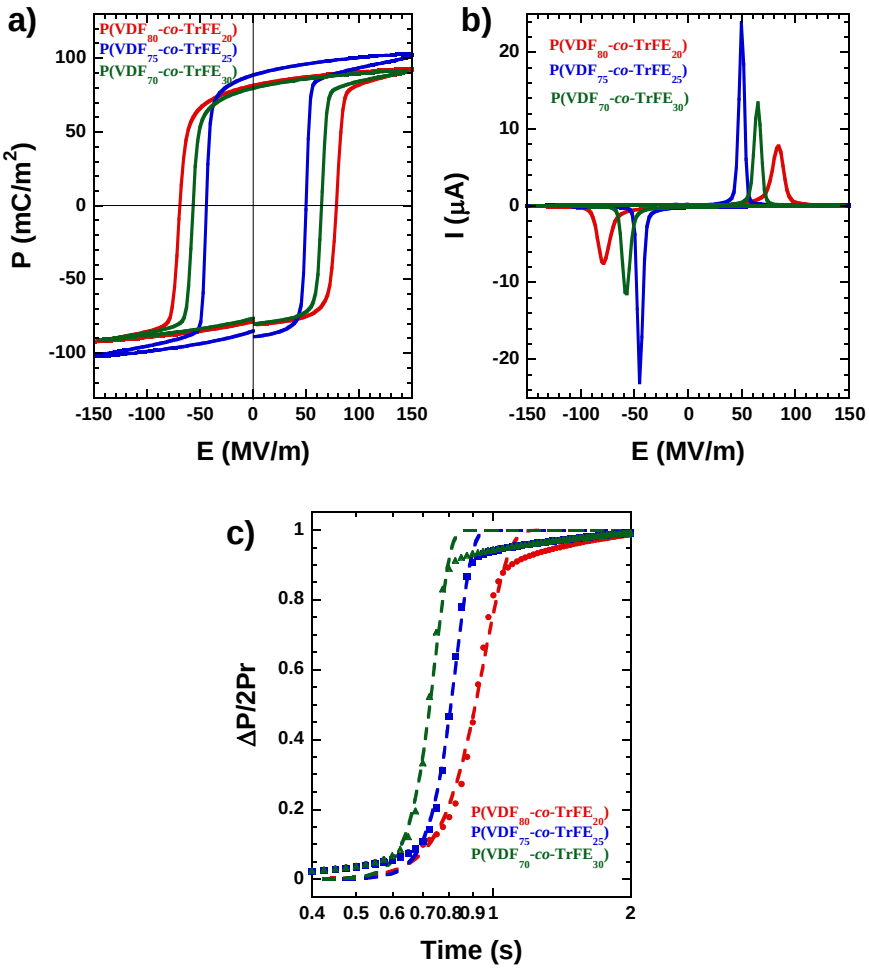

Figure 4. 16. a) Polarization vs. electric field hysteresis loop for the three P(VDF-*co*-TrFE) based compositions studied, b) the corresponding current vs. electric field data, c) switching transients of copolymers as a function of time at room temperature at a constant electric field of 150 MV/m, and Dashed lines are the fits according to the KAI models.

To understand the mechanism of polarization switching, the results are considered with the nucleation and growth theory described by a model developed by Ishibashi and Tagaki,[37] the so-called Kolmogorov-Avrami-Ishibashi (KAI) model and

based on the classical Kolmogorov[38] and Avrami theory.[39] This model considers that the switching transient as a function of time can be described by the following equation:

$$\Delta P(t)/2P_r = 1 - \exp\left[-\left(\frac{t}{t_0}\right)^{n'}\right] \qquad \text{eq. 4.3}$$

where t_0 is the characteristic switching time and n' is a parameter proportional to the dimensionality of the polarization switching, respectively.

Figure 4.16c shows a typical polarization transient at room temperature for the different compositions studied. The dashed lines in Figure 4.16c are the fitting curves in order to indicate that the KAI model can fit the experimental data. The dimensionality of the switching mechanism in ferroelectric polymers is still unclear, and several works have been published during the last years trying to solve or explain this issue.[40-43] The study of the dimensionality of the switching mechanism is outside the scope of this work.

The results obtained here indicate that the switching time and coercive field decrease with increasing TrFE content. However, when the TrFE content is increased above a certain point (above 25% in the case of the samples examined here), the maximum and remanent polarization start to decrease due to the lower dipole moment of the TrFE defects, 1.4D compared with 2.1D for VDF, in the crystalline lamellae.[44]

4.4 Conclussions

The results obtained in this chapter are consistent with literature reports that indicate that TrFE units can be included in the PVDF crystal lattice. Such inclusion can decrease the isothermal growth rate of crystals at high crystallization temperatures but, on the other hand, increases the nucleation rate and nucleation density in the copolymers substantially. The increase in nucleation rate dominates the overall

crystallization kinetics of the copolymers, provoking an increase in the resulting crystallization rate with respect to neat PVDF.

The remarkable increase in nucleation density provoked by TrFE inclusion in the copolymers causes the disappearance of *Domain II*, as the nucleation density is so high that self-nucleation cannot induce further nucleation. SSA results indicate that the copolymers cannot be fractionated in contrast with neat PVDF. This is consistent with the inclusion of TrFE chains within the PVDF crystal lattice.

Finally, polarization studies have indicated that the P(VDF_{75}-*co*-$TrFE_{25}$) sample manifests the best ferroelectric response in terms of higher P_r, lower E_c, and faster switching rate. Above 25% TrFE inclusion in the PVDF crystals, the maximum and remanent polarization start to decrease due to the lower dipole moment of the TrFE defects.

4.5 References

1. Legrand, J. F., Structure and ferroelectric properties of P(VDF-TrFE) copolymers. *Ferroelectrics* 1989, 91, (1), 303-317.

2. Lovinger, A. J.; Furukawa, T.; Davis, G. T.; Broadhurst, M. G., Crystallographic changes characterizing the Curie transition in three ferroelectric copolymers of vinylidene fluoride and trifluoroethylene: 1. As-crystallized samples. *Polymer* 1983, 24, (10), 1225-1232.

3. Tashiro, K.; Kobayashi, M., Structural phase transition in ferroelectric fluorine polymers: X-ray diffraction and infrared/Raman spectroscopic study. *Phase Transitions* 1989, 18, (3-4), 213-246.

4. Ohigashi, H.; Koga, K.; Suzuki, M.; Nakanishi, T.; Kimura, K.; Hashimoto, N., Piezoelectric and ferroelectric properties of P (VDF-TrFE) copolymers and their application to ultrasonic transducers. *Ferroelectrics* 1984, 60, (1), 263-276.

5. Kimura, K.; Ohigashi, H., Polarization Behavior in Vinylidene Fluoride-Trifluoroethylene Copolymer Thin Films. *Japanese Journal of Applied Physics* 1986, 25, (Part 1, No. 3), 383-387.

6. Koga, K.; Nakano, N.; Hattori, T.; Ohigashi, H., Crystallization, field - induced phase transformation, thermally induced phase transition, and piezoelectric activity in P(vinylidene fluoride - TrFE) copolymers with high molar content of vinylidene fluoride. *Journal of Applied Physics* 1990, 67, (2), 965-974.

7. Aliane, A.; Benwadih, M.; Bouthinon, B.; Coppard, R.; Domingues-Dos Santos, F.; Daami, A., Impact of crystallization on ferro-, piezo- and pyro-electric characteristics in thin film P(VDF–TrFE). *Organic Electronics* 2015, 25, 92-98.

8. Lovinger, A. J.; Johnson, G. E.; Bair, H. E.; Anderson, E. W., Structural, dielectric, and thermal investigation of the Curie transition in a tetrafluoroethylene copolymer of vinylidene fluoride. *Journal of Applied Physics* 1984, 56, (9), 2412-2418.

9. Barique, M. A.; Ohigashi, H., Annealing effects on the Curie transition temperature and melting temperature of poly(vinylidene fluoride/trifluoroethylene) single crystalline films. *Polymer* 2001, 42, (11), 4981-4987.

10. Spampinato, N.; Maiz, J.; Portale, G.; Maglione, M.; Hadziioannou, G.; Pavlopoulou, E., Enhancing the ferroelectric performance of P(VDF-co-TrFE) through modulation of crystallinity and polymorphism. *Polymer* 2018, 149, 66-72.

11. Pérez-Camargo, R. A.; Liu, G.-M.; Wang, D.-J.; Müller, A. J., Experimental and Data Fitting Guidelines for the Determination of Polymer Crystallization Kinetics. *Chinese Journal of Polymer Science* 2022, 40, (6), 658-691.

12. Lorenzo, A. T.; Arnal, M. L.; Albuerne, J.; Müller, A. J., DSC isothermal polymer crystallization kinetics measurements and the use of the Avrami equation to fit the data: Guidelines to avoid common problems. *Polymer Testing* 2007, 26, (2), 222-231.

13. Lorenzo, A. T.; Arnal, M. L.; Sánchez, J. J.; Müller, A. J., Effect of annealing time on the self-nucleation behavior of semicrystalline polymers. *Journal of Polymer Science Part B: Polymer Physics* 2006, 44, (12), 1738-1750.

14. Michell, R. M.; Mugica, A.; Zubitur, M.; Müller, A. J., Self-Nucleation of Crystalline Phases Within Homopolymers, Polymer Blends, Copolymers, and Nanocomposites. In *Polymer Crystallization I: From Chain Microstructure to Processing*, Auriemma, F.; Alfonso, G. C.; de Rosa, C., Eds. Springer International Publishing: Cham, 2017; pp 215-256.

15. Müller, A. J.; Michell, R. M.; Pérez, R. A.; Lorenzo, A. T., Successive Self-nucleation and Annealing (SSA): Correct design of thermal protocol and applications. *European Polymer Journal* 2015, 65, 132-154.

16. Müller, A. J.; Arnal, M. L., Thermal fractionation of polymers. *Progress in Polymer Science* 2005, 30, (5), 559-603.

17. Lovinger, A. J.; Furukawa, T.; Davis, G. T.; Broadhurst, M. G., Curie transitions in copolymers of vinylidene fluoride. *Ferroelectrics* 1983, 50, (1), 227-236.

18. Lovinger, A. J.; Cais, R. E., Structure and morphology of poly (trifluoroethylene). *Macromolecules* 1984, 17, (10), 1939-1945.

19. Yagi, T., Heat of Fusion and Crystallization Kinetics of Poly(trifluoroethylene). *Polymer Journal* 1980, 12, (1), 9-15.

20. Higashihata, Y.; Sako, J.; Yagi, T., Piezoelectricity of vinylidene fluoride-trifluoroethylene copolymers. *Ferroelectrics* 1981, 32, (1), 85-92.

21. Lovinger, A. J.; Furukawa, T.; Davis, G. T.; Broadhurst, M. G., Crystallographic changes characterizing the Curie transition in three ferroelectric copolymers of vinylidene fluoride and trifluoroethylene: 2. Oriented or poled samples. *Polymer* 1983, 24, (10), 1233-1239.

22. Teyssedre, G.; Bernes, A.; Lacabanne, C., Cooperative movements associated with the Curie transition in P(VDF-TrFE) copolymers. *Journal of Polymer Science Part B: Polymer Physics* 1995, 33, (6), 879-890.

23. Gregorio Jr, R.; Botta, M. M., Effect of crystallization temperature on the phase transitions of P(VDF/TrFE) copolymers. *Journal of Polymer Science Part B: Polymer Physics* 1998, 36, (3), 403-414.

24. Hoffman, J. D.; Lauritzen, J. I., Jr., Crystallization of Bulk Polymers With Chain Folding: Theory of Growth of Lamellar Spherulites. *Journal of research of the National Bureau of Standards. Section A, Physics and chemistry* 1961, 65A, (4), 297-336.

25. Hoffman, J. D.; Weeks, J. J., Melting process and the equilibrium melting temperature of polychlorotrifluoroethylene. *J. Res. Natl. Bur. Stand., Sect. A* 1962, 66, (1), 13-28.

26. Marand, H.; Xu, J.; Srinivas, S., Determination of the Equilibrium Melting Temperature of Polymer Crystals: Linear and Nonlinear Hoffman−Weeks Extrapolations. *Macromolecules* 1998, 31, (23), 8219-8229.

27. Balsamo, V.; Urdaneta, N.; Pérez, L.; Carrizales, P.; Abetz, V.; Müller, A. J., Effect of the polyethylene confinement and topology on its crystallisation within semicrystalline ABC triblock copolymers. *European Polymer Journal* 2004, 40, (6), 1033-1049.

28. Müller, A. J.; Balsamo, V.; Arnal, M. L., Nucleation and Crystallization in Diblock and Triblock Copolymers. In *Block Copolymers II*, Abetz, V., Ed. Springer Berlin Heidelberg: Berlin, Heidelberg, 2005; pp 1-63.

29. Müller, A. J.; Michell, R. M.; Lorenzo, A. T., Isothermal Crystallization Kinetics of Polymers. *Polymer Morphology: Principles, Characterization, and Processing* 2016, 714, 181-203.

30. Miyazaki, T.; Takeda, Y.; Akasaka, M.; Sakai, M.; Hoshiko, A., Preparation of Isothermally Crystallized γ-Form Poly(vinylidene fluoride) Films by Adding a KBr Powder as a Nucleating Agent. *Macromolecules* 2008, 41, (7), 2749-2753.

31. Sencadas, V.; Costa, C. M.; Gómez Ribelles, J. L.; Lanceros-Mendez, S., Isothermal crystallization kinetics of poly(vinylidene fluoride) in the α-phase in the scope of the Avrami equation. *Journal of Materials Science* 2010, 45, (5), 1328-1335.

32. Fillon, B.; Thierry, A.; Wittmann, J. C.; Lotz, B., Self-nucleation and recrystallization of polymers. Isotactic polypropylene, β phase: β-α conversion and β-α growth transitions. *Journal of Polymer Science Part B: Polymer Physics* 1993, 31, (10), 1407-1424.

33. Sangroniz, L.; Cavallo, D.; Müller, A. J., Self-Nucleation Effects on Polymer Crystallization. *Macromolecules* 2020, 53, (12), 4581-4604.

34. Jang, Y.-J.; Sangroniz, L.; Hillmyer, M. A., Ductile gas barrier poly(ester–amide)s derived from glycolide. *Polymer Chemistry* 2022, 13, (26), 3882-3891.

35. Arnal, M. L.; Sánchez, J. J.; Müller, A. J., Miscibility of linear and branched polyethylene blends by thermal fractionation: use of the successive self-nucleation and annealing (SSA) technique. *Polymer* 2001, 42, (16), 6877-6890.

36. Arnal, M. L.; Cañizales, E.; Müller, A. J., Thermal and morphological evaluation of very low density polyethylene/high density polyethylene blends. *Polymer Engineering & Science* 2002, 42, (10), 2048-2063.

37. Ishibashi, Y.; Takagi, Y., Note on Ferroelectric Domain Switching. *Journal of the Physical Society of Japan* 1971, 31, (2), 506-510.

38. Kolmogorov, A. N., Étude de l'équation de la diffusion avec croissance de la quantité de matière et son application à un problème biologique. *Bull. Univ. Moskow, Ser. Internat., Sec. A* 1937, 1, 1-25.

39. Avrami, M., Kinetics of Phase Change. I General Theory. *The Journal of Chemical Physics* 1939, 7, (12), 1103-1112.

40. Anwar, S.; Asadi, K., One-Dimensional Polarization Dynamics in Ferroelectric Polymers. *ACS Macro Letters* 2019, 8, (5), 525-529.

41. Zhao, D.; Katsouras, I.; Asadi, K.; Blom, P. W. M.; de Leeuw, D. M., Switching dynamics in ferroelectric P(VDF-TrFE) thin films. *Physical Review B* 2015, 92, (21), 214115.

42. Hu, W. J.; Juo, D.-M.; You, L.; Wang, J.; Chen, Y.-C.; Chu, Y.-H.; Wu, T., Universal Ferroelectric Switching Dynamics of Vinylidene Fluoride-trifluoroethylene Copolymer Films. *Scientific Reports* 2014, 4, (1), 4772.

43. Genenko, Y. A.; Zhukov, S.; Yampolskii, S. V.; Schütrumpf, J.; Dittmer, R.; Jo, W.; Kungl, H.; Hoffmann, M. J.; von Seggern, H., Universal Polarization Switching Behavior of Disordered Ferroelectrics. *Advanced Functional Materials* 2012, 22, (10), 2058-2066.

44. Yang, L.; Tyburski, B. A.; Dos Santos, F. D.; Endoh, M. K.; Koga, T.; Huang, D.; Wang, Y.; Zhu, L., Relaxor Ferroelectric Behavior from Strong Physical Pinning in a Poly(vinylidene fluoride-co-trifluoroethylene-co-chlorotrifluoroethylene) Random Terpolymer. *Macromolecules* 2014, 47, (22), 8119-8125.

Chapter 5

Phase Transitions in Poly(vinylidene fluoride)/Polymethylene-Based Diblock Copolymers and Blends

---

5.1 Introduction

In general, the properties of the blends and/or copolymers are different depending on the synthesis and on the processing conditions presented in the sample.[1-3] If the polymers are not compatible, the segregation observed in the material is different for blends and for copolymers. Segregation in blends happens on a larger scale due to the macro-phase segregation behaviour.[4] Immiscible block copolymers cannot segregate into macro-phases due to their covalent bonds, but micro-phase segregation into regular domain patterns can occur.[5] Daoulas *et al.* have demonstrated by mesoscopic simulations that the differences between the block copolymers and blends in poly (*p*-phenylene vinylene) (PPV) and polyacrylate systems are due to this segregation phenomenon that makes the materials different for light-emitting diodes, so the final applications of both materials are not the same.[6]

In this chapter, we study the crystallization of a polymethylene (PM) and PVDF system, polymers that are not miscible. We compare the PVDF homopolymer with two different PM/PVDF blends and two different PM-*b*-PVDF block copolymers in the same proportion in order to see the relevance of the segregation in the final properties of both materials. Using Differential Scanning Calorimetry (DSC), we study the behaviour of these samples during the non-isothermal crystallization and during an isothermal process. Microscopy techniques and Small-Angle X-Ray Scattering (SAXS) are employed to study the miscibility between both polymers. Finally, the samples are fully characterized by Broadband Dielectric Spectroscopy (BDS), Fourier Transform Infrared Spectroscopy (FTIR), and Wide-Angle X-Ray Scattering (WAXS).

5.2 Material and methods

5.2.1 Materials

The diblock copolymers of polymethylene (PM) and poly(vinylidene fluoride) (PVDF) have been synthesized by Hadjichristidis et al. and published in a previous work.[7] In brief, the synthesis involves the following steps. First, a polyhomologation of dimethylsulfoxonium methylide using triethylborane as initiator followed by oxidation/hydrolysis to afford PM-OH. Then the esterification of the OH group with 2,2-bromoisobutyrylbromide to introduce bromide at the chain end. After it, halide exchange (Br→I) using sodium iodine to produce the macro-chain transfer agent (macro-CTA) and at the end Iodine transfer polymerization (ITP) of VDF with the macro-CTA and 1,1-bis(tert-butylperoxy)cyclohexane as the initiator (see Scheme 5.1 below).

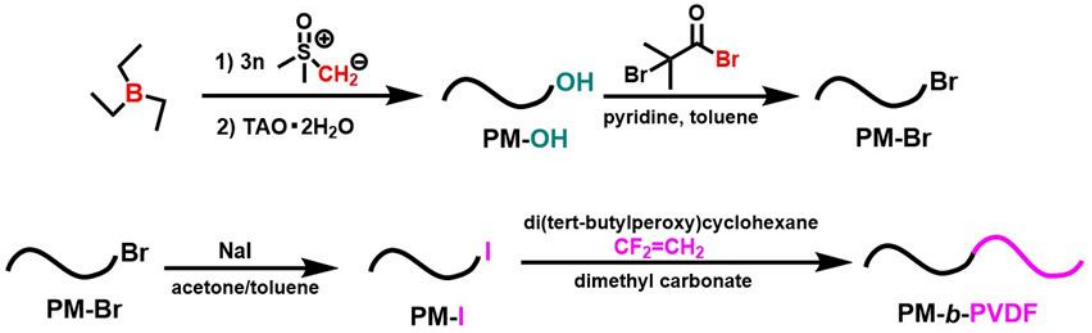

Scheme 5. 1. Synthesis of PM-*b*-PVDF diblock copolymer by polyhomologation and ITP.

The synthesis of linear polyvinylidene fluoride (PVDF) homopolymer has been accomplished via reversible addition−fragmentation chain-transfer (RAFT) polymerization of vinylidene fluoride (VDF) using (S-benzyl O-ethylxathate) as chain transfer agent (CTA) and 1,1-bis(tert-butylperoxy)cyclohexane (Luperox 331P80, Sigma-Aldrich, Munich, Germany) as initiator in dimethyl carbonate at 80 ^{o}C .

Synthesis of RAFT Chain Transfer Agents (CTA)

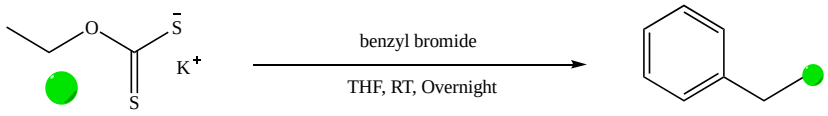

Scheme 5. 2. Synthesis of the CTA.

S-benzyl O-ethylxanthate (CTA). In a 100 ml round bottom flask, benzyl bromide (1 g, 5.84 mmol) and potassium ethyl xanthate (1.12 g, 7 mmol) were dissolved in anhydrous THF (50 mL) as is showed in the Scheme 5.2. After degassing, the reaction mixture was stirred overnight at room temperature under argon. The reaction mixture was quenched with brine (100 mL) and extracted 3 times with dichloromethane (3x150 mL). The combined organic extracts were dried over $MgSO_4$, filtered, and concentrated by rotary evaporation. The (CTA) was obtained as a yellowish oil in >99% yield (1.2 g, 5.74 mmol). ^{1}H NMR (500 MHz, $(CD_3)_2CO$, δ (ppm), Figure 5.1): 7.26-7.42 (m, 5H, $C_6\mathbf{H_5}$-), 4.64-4.68 (q, 2H, O-$\mathbf{CH_2}$-CH_3), 4.42 (s, 2H, C_6H_5-$\mathbf{CH_2}$-S), 1.39-1.42 (t, 3H, O-CH_2-$\mathbf{CH_3}$). ^{13}C NMR (500 MHz, $(CD_3)_2CO$, δ (ppm): 213.66, 137.25, 130.10, 129.58, 128.49, 71.13, 40.17, 14.24.

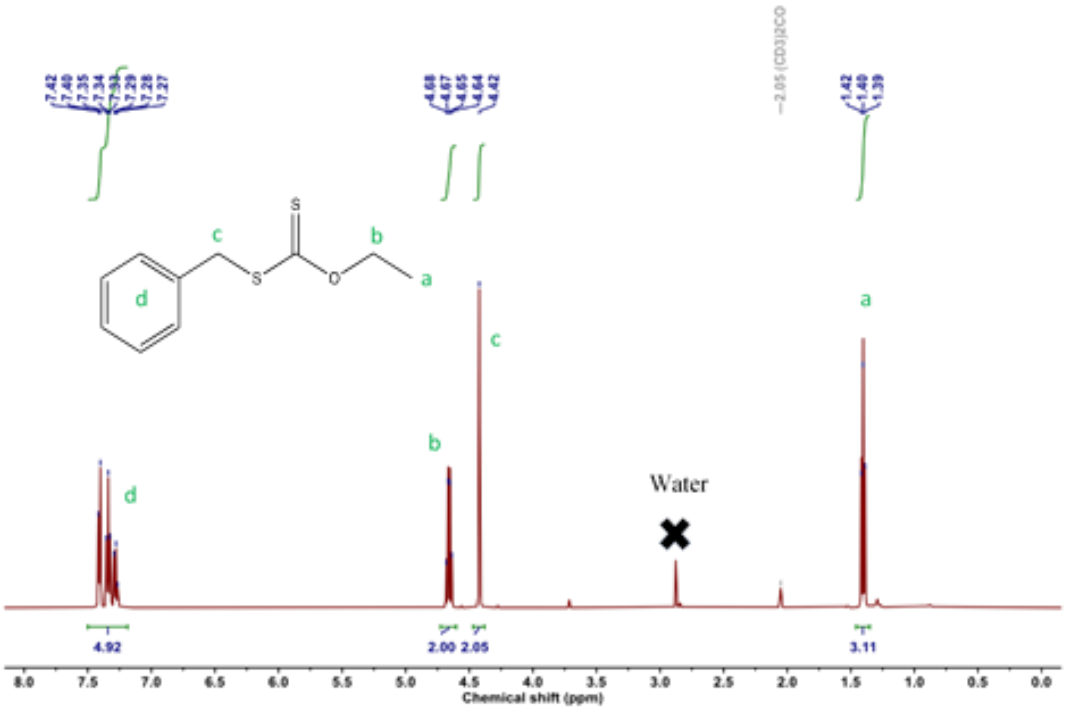

Figure 5. 1. ^{1}H NMR (500 MHz) spectrum of **CTA** in $(CD_3)_2CO$ at 40 ^{0}C.

Synthesis of Linear PVDF

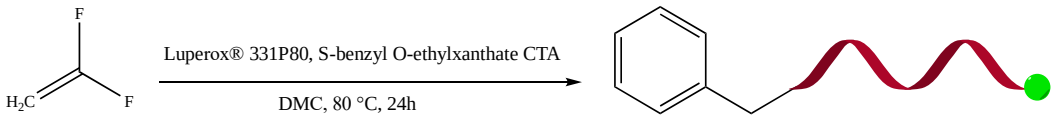

Scheme 5. 3. Synthesis of the linear PVDF.

A Parr autoclave was filled with S-benzyl O-ethylxanthate, CTA (71.9 mg, 0.339 mmol) and 1,1-bis(tert-butylperoxy)cyclohexane (Luperox® 331P80), initiator (88.14 mg, 0.339 mmol) dissolved in dimethyl carbonate (75 mL) as is showed in the Scheme 5.3. The reactor was cooled in a liquid nitrogen bath to condense VDF gas (21.7 g, 339 mmol) into an autoclave under weight control. It was then heated gradually up to 80 °C, and the evolutions of pressure and temperature were recorded. The reaction was stopped after 24 h, and the autoclave was cooled to room temperature and then placed in an ice bath. After the non-reacted monomer was purged, the

reactor was opened and a colorless liquid was obtained. The solution was concentrated by rotary evaporation, precipitated in methanol, dried under vacuum for 24 h at 40 °C (7.4 g as a white powder). ^{1}H NMR (500 MHz, DMF-d_7, δ (ppm), Figure 5.2): 1.43-1.48 (t, CTA, –CF_2–CH_2–S(C=S)OCH_2–**CH_3**; –CH_2–CF_2–S(C=S)OCH_2–**CH_3**), 2.37 (t, PVDF, –CF_2–**CH_2–CH_2**– CF_2–,HH addition), 2.50 (t, CTA,C_6H_5-**CH_2**-), 3.03 (t, PVDF, –CF_2–**CH_2**– CF_2–,HT addition), 4.2 (t, PVDF– CF_2–**CH_2**–S–), 4.73-4.79 (q, CTA, –CF_2–CH_2–S(C=S)O**CH_2**–CH_3; –CH_2–CF_2–S(C=S)O**CH_2**–CH_3), 6.43 (tt, PVDF, –CH_2–CF_2–**H**), 7.23-7.39 (m, CTA, –**C_6H_5**).

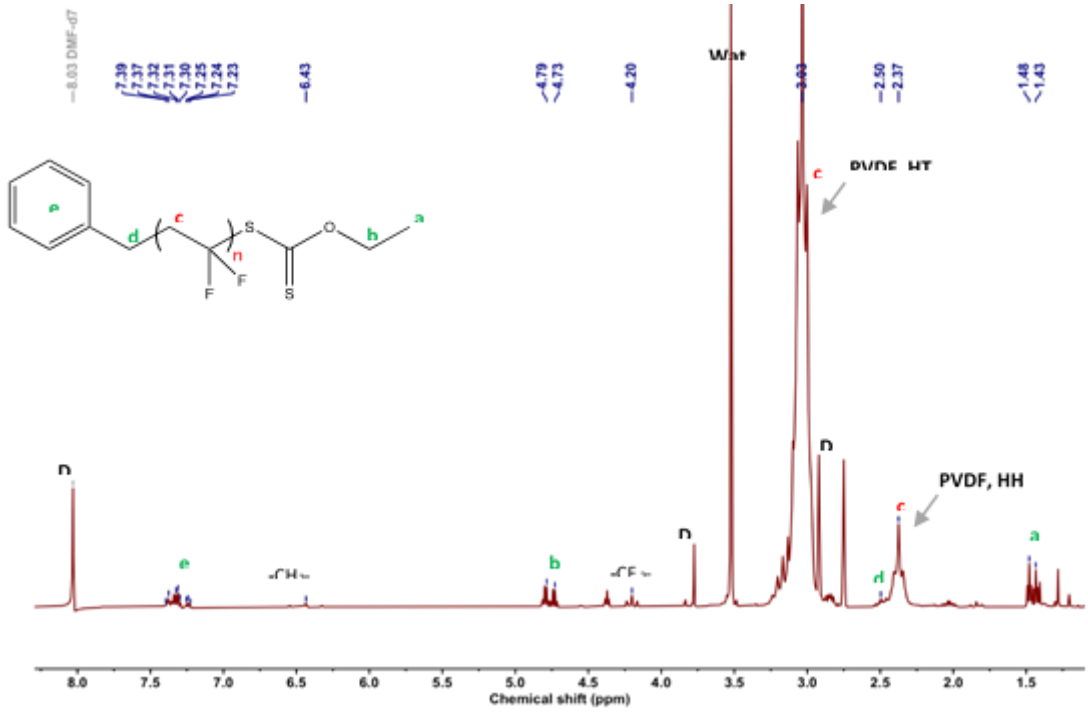

Figure 5. 2. ^{1}H NMR (500 MHz) spectrum of Linear PVDF in DMF-d_7 at 25 °C.

^{19}F NMR (500 MHz, DMF-d_7, δ (ppm), Figure 5.3): −116.97 (–CH_2–**CF_2–CF_2**–CH_2–, HH reverse addition), −115.72 (–CH_2–**CF_2**–H), −114.68 (–CH_2–**CF_2–CF_2**–CH_2–,HH reverse addition), −114.43 ((–CH_2–**CF_2–CF_2**–CH_2–S–), −114.04 (–CH_2–**CF_2–CF_2**–CH_2–S–), −108.74 (–**CF_2**–CH_3), −96.15 (–CH_2–CH_2–**CF_2**–CH_2–, TT reverse addition), −94.29 (CH_3–O–(C=O)–O–CH_2–CH_2–**CF_2**–), -93.46 (–CH_2–**CF_2**–CH_2–CF_2H), −92.79 (–CH_2–CH_2–CF_2–CH_2–**CF_2**–CH_2–CF_2–, regular HT addition), −92.35 (–CH_2–**CF_2**–CH_2–, regular HT addition).

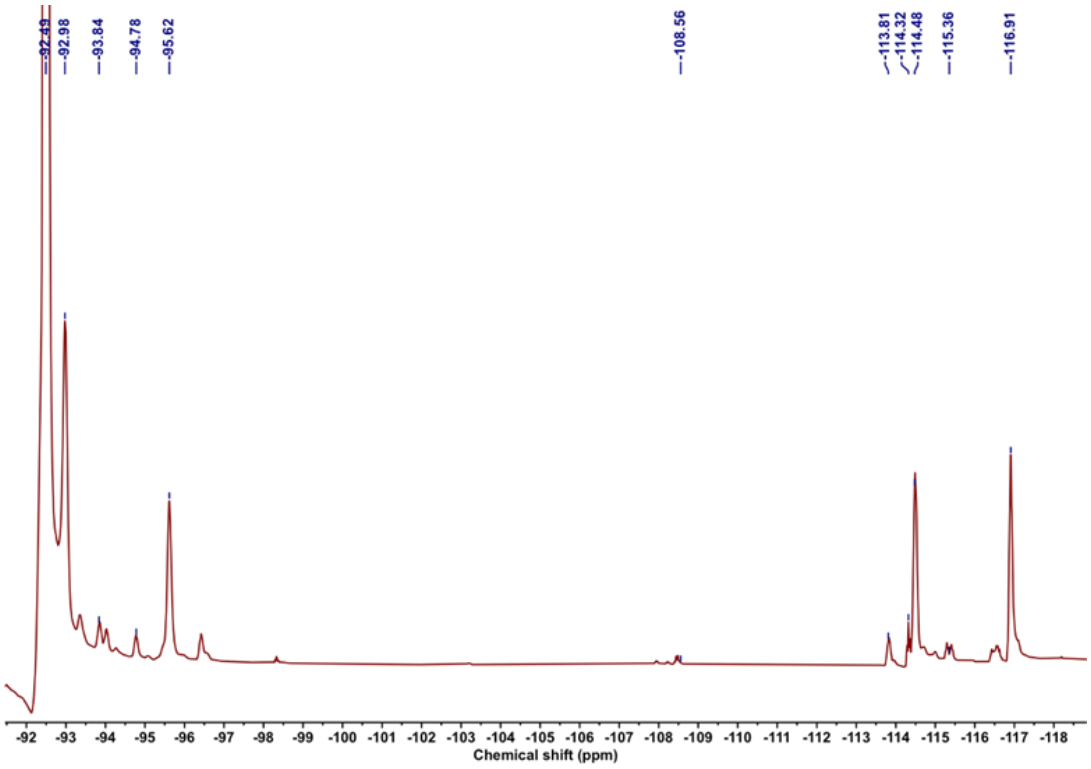

Figure 5. 3. ^{19}F NMR (500 MHz) spectrum of Linear PVDF in DMF-d_7 at 25 ºC.

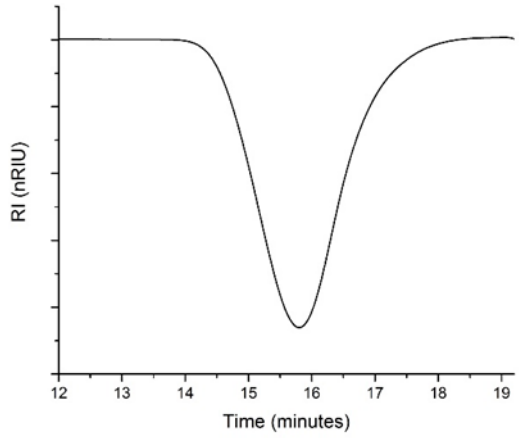

Figure 5. 4. GPC trace (DMF, 40 ^{0}C, PS standard) of linear PVDF (negative refractive index increment).

The polymerization conditions and molecular characteristics of the synthesized PVDF are given in Table 5.1.

Table 5. 1. Polymerization conditions and molecular characteristics of the linear PVDF synthesized by RAFT polymerization.

Polymer	Initiator	CTA	M	$[I]_0$:$[CTA]_0$:$[M]_0$	DP^a	Mn^a (g mol^{-1})	$Đ^b$
Linear PVDF-	Luperox® 331P80	S-benzylO-ethylxanthate	VDF	1: 1: 1000	120	7600	1.5

[a]Degree of polymerization and *Mn* were determined by ^{1}H NMR. [b]Determined by GPC in DMF, calibrated with linear PS standards.

Blends

Blends were prepared by mixing the homopolymers that are the precursors of the block copolymers, PM-OH and PVDF. The blends were prepared in the same compositions used for the block copolymers so that they could be compared. First, the PVDF and the PM mixtures were stirred until the total dissolution in cyclohexane for 24 h at 50 °C. Then, each mixture was drop-casted onto Teflon holders. Afterward, a fume hood was used to slowly evaporate the solvent, and finally, under vacuum conditions, the samples were well-dried in an oven at 40 °C for 72 h. All the polymers used in this chapter and their molecular characteristics are listed in Table 5.2.

Table 5. 2. Principal characteristics of all samples employed during this chapter. The subscripts indicate the wt % of each block.

Sample	Topology	M_n (g/mol) [a]	M_n PM (g/mol) [a]	M_n PVDF (g/mol) [a]	Đ [b]
PM_{23}-*b*-$PVDF_{77}$	Linear diblock copolymer	28.6 K	6.6 K	22.0 K	PM: 1.12 PVDF: 1.29
PM_{38}-*b*-$PVDF_{62}$	Linear diblock copolymer	17.6 K	6.6 K	11.0 K	PM: 1.12 PVDF: 1.25
$PM_{23}PVDF_{77}$	Blend	-	5.6 K	7.6 K	
$PM_{38}PVDF_{62}$	Blend	-	5.6 K	7.6 K	
PVDF	Linear homopolymer	7.6 K	-	7.6 K	1.50 [c]
PM-OH	Linear homopolymer	5.6 K	5.6 K	-	1.12 [d]

[a] All M_n were determined by ^{1}H NMR, toluene-d_8, and DMF-d_7 mixture; [b] Direct GPC characterization of PM-*b*-PVDF copolymers was impossible due to the difficulty in finding a common solvent for both blocks. The results given in the Table correspond to each block after hydrolysis of the junction point; [c] HT-GPC (trichlorobenzene as eluent, 145 °C, PS standards) for PM-OH and [d] GPC (dimethylformamide as eluent, 35 °C, PS standards).

5.2.2 Methods

a) Differential Scanning Calorimetry (DSC)

A Perkin Elmer DSC 8000 equipment was used to carry out the DSC experiments. This equipment uses an Intracooler II as a cooling system. Before the measurements were performed, the equipment was calibrated using indium and tin standards.

For the non-isothermal procedure, first, the samples were heated up to 200 ºC and held there for 3 min to ensure that the thermal history of the materials was completely erased. Then, samples were cooled at different cooling rates (60, 20, 5, and 1 °C/min) from the melt to 25 °C and then heated again to the molten state at a constant rate of 20 °C/min.

The protocol used to carry out the isothermal crystallization procedure was the same followed by Lorenzo et al.[8] First, the minimum crystallization temperature ($T_{c,\min}$) was found. For that, samples were heated up to 200 °C and held there for 3 min. Then, samples were cooled fast (at 60 °C/min) to a previously selected T_c. When this T_c was reached, samples were heated at 20 °C/min to the same melting temperature. When no peaks were observed in the subsequent heating scan, the T_c mentioned in the second step was considered as the minimum isothermal crystallization temperature.[8]

The isothermal crystallization procedure consisted in a series of different steps. First, samples were melted at 200 °C and held there for 3 min to erase the thermal history of the material. Then, samples were cooled down at 60 °C/min to the selected isothermal crystallization temperature and held at this T_c for 40 min to achieve crystallization saturation. Once this crystallization process was finished, samples were heated at 20 °C/min to the previous melting temperature, and the process was restarted to the next programmed T_c.[8]

b) Small and Wide Angle X-Ray Scattering (SAXS/WAXS)

Block copolymer samples were analyzed using Wide-Angle X-Ray Scattering (WAXS) and Small-Angle X-Ray Scattering (SAXS). These experiments were carried out in the ALBA Synchrotron facility using synchrotron radiation at the BL11-NCD beamline. Samples were measured in capillaries using a Linkam hot-stage system equipped with liquid nitrogen to control the temperature. The samples were melted at 200 °C for 3 min and then cooled down at the chosen cooling rate. The energy of the X-ray source was 12.4 keV (λ = 1.0 Å). The WAXS system configuration employed was a Rayonix LX255-HS sample detector with an active area of 230.4 × 76.8 mm. A sample to detector distance of 15.5 mm with a tilt angle of 27.3° was employed. The resulting pixel size was 44 μm^2. For the SAXS experiments, the configuration was a Pilatus 1M sample detector, which had the following characteristics: active image area = 168.7 × 179.4 mm^2, the total number of pixels = 981 ×

1043, pixel size = 172 × 172 μm^2, rate = 25 frames/sec and the distance used was 6463 mm.

c) Polarized Light Optical Microscopy (PLOM)

All samples were analyzed by an Olympus BX51 polarized optical microscope coupled to a Linkam hot-stage that uses nitrogen (N_2) to control the temperature and manages the cooling rate. An Olympus SC50 camera linked to the microscope was employed to observe the samples and take micrographs. Samples were dissolved in acetone or cyclohexane, and drops of the solutions were placed on a glass substrate and dried at room temperature.

d) Fourier Transform Infrared Spectroscopy (FTIR)

A Nicolet 6700 Fourier Transform Infrared Spectrometer equipped with an Attenuated Total Reflectance (ATR) Golden Gate MK II with a diamond crystal was employed to analyse the samples. Samples were melted directly from the bulk at 200 °C in a Linkam hot-stage and then cooled down at 1 °C/min employing N_2 in the cooling process. FTIR measurements were carried out after the cooling process at room temperature.

e) Transmission Electron Microscopy (TEM)

All samples were stained with RuO_4 before the measurements by immersing thin strips of material in this solution for 16 h. Then, the samples were cut in ultra-thin sections at room temperature with a diamond knife on a Leica EMFC6 ultra-microtome device. These 90 nm thick ultra-thin sections were mounted on a 200 mesh copper grid and then observed by a TECNAI G2 20 TWIN TEM equipped with a LaB6 filament operating at an accelerating voltage of 120 kV.

f) Broadband Dielectric Spectroscopy (BDS)

The complex dielectric permittivity, $\varepsilon^*(\omega) = \varepsilon'(\omega) - i\varepsilon''(\omega)$, where ε' is the real part and ε'' is the imaginary part, was obtained as a function of the frequency (ω)

and temperature (*T*) by using a Novocontrol high-resolution dielectric analyser (Alpha analyser) (Novocontrol, Montabaur, Germany). The sample cell was set in a cryostat, whose temperature was controlled via a nitrogen gas jet stream coupled with a Novocontrol Quatro controller. Samples were placed between two flat gold-plated electrodes (10 and 20 mm in diameter) forming a parallel plate capacitor with a 0.1 mm thick Teflon spacer. Frequency sweeps were performed at a constant temperature with a stability of ±0.1 °C. BDS measurements were carried out as follows. Samples were heated up to 200 °C inside the cryostat. This temperature was held for 5 min to ensure a homogeneous filling of the capacitor and to obtain a *fully* amorphous initial state. Then, measurements started at 200 °C, cooling the samples in isothermal steps of 10 °C down to −100 °C, and subsequently heating them up to 200 °C, again in 10 °C steps. Samples were tested at different temperatures over a frequency range of 10^{-1} to 10^{7} Hz.

5.3 Results and discussion

5.3.1 Miscibility between polymethylene (PM) and poly vinylidene fluoride (PVDF)

The final properties of materials that are made up of more than one component can be affected by their miscibility. The Flory interaction parameter χ_{12} can be estimated by the following semi-empirical equation (Equation (5.1)):[9]

$$\chi_{12} = 0.34 + \frac{V_1}{RT}(\delta_1 - \delta_2)^2 \qquad \text{eq. 5.1}$$

where χ_{12} is the interaction parameter, V_1 is the molar volume of the matrix component (PVDF in our case) calculated through the molar mass of the repeating unit (M = 64.03 g/mol), and the amorphous density (ρ = 1.68 g/cm^3), in this case, V_1 = 38.1 cm^3/mol, R is a constant the value of which is 1.987 cal/mol K, T is the temperature chosen to calculate the miscibility (473 K in order to know the miscibility in the molten state), and δ_1 (8.57 (cal/cm^3)$^{1/2}$) and δ_2 (7.9 (cal/cm^3)$^{1/2}$) are the solubility parameters. In our case, the calculated χ_{12} is 0.36 at 200 °C.

To calculate the segregation strength in the case of block copolymers, the χ_{12} value is multiplied by N, the degree of polymerization. When the value obtained is below 10, the polymers are miscible with each other; if the estimated value is between 10 and 30, there is a weak segregation; and if it is between 30 and 50, there is a medium segregation. Only when the calculated value is above of 50, it is possible to predict that there will be a strong segregation. For our samples, we have calculated that the segregation strength is 117 for the PM$_{23}$-*b*-PVDF$_{77}$ and 72 in the case of PM$_{38}$-*b*-PVDF$_{62}$. Therefore, we can expect a strong segregation in the melt for both samples.

Nevertheless, SAXS results do not show any evidence of phase segregation in the melt. Figure 5.5 shows the SAXS curves for both block copolymers at different temperatures during a heating sweep at 20 °C/min. When the copolymers are in the molten state (above 165 °C), there is not any segregation peak observed, indicating

that either the electron density contrast in the melt is not enough to produce a signal or that the copolymers are either very weakly segregated or melt-mixed. The prominent SAXS peaks observed at temperatures below the melting point of PVDF are due to the average long period values of the constituent crystalline lamellae. As expected, they shift to lower q values (i.e., larger long periods) as temperature increases.

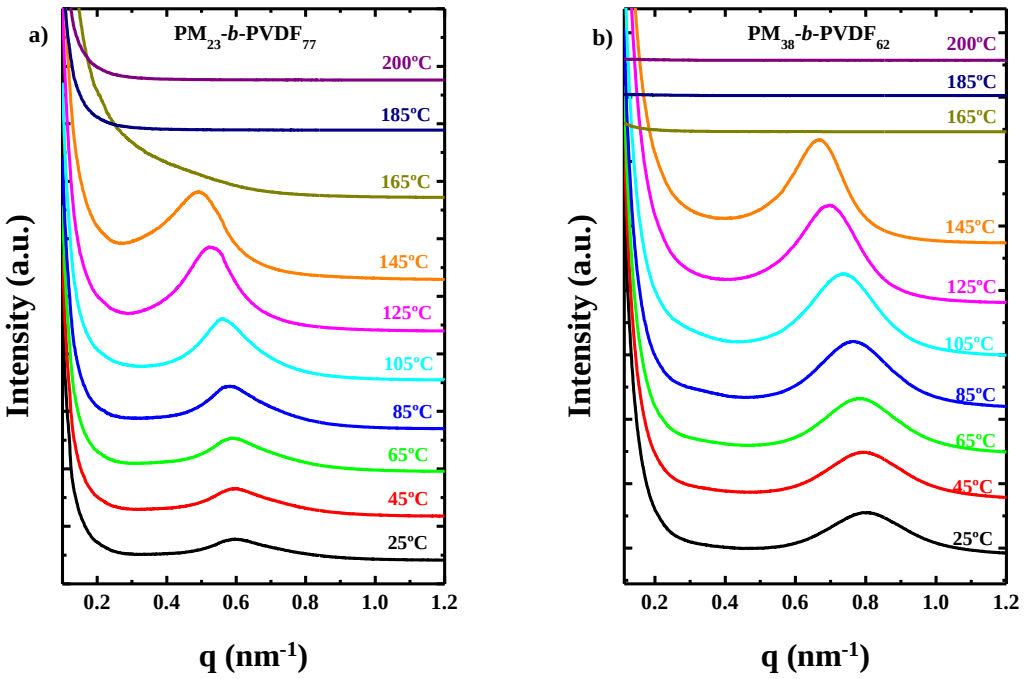

Figure 5. 5. SAXS analysis at different temperatures during heating scans at 20 °C/min after a cooling process also at 20 °C/min of a) PM_{23}-*b*-$PVDF_{77}$ sample and b) PM_{38}-*b*-$PVDF_{68}$ sample.

PLOM was used to observe the crystallization process in the different samples and to check if the segregation behaviour is different between block copolymers and blends. Figure 5.6a shows the crystallization of PM_{38}-*b*-$PVDF_{62}$ during a cooling sweep from the melt at 20 °C/min. In a strongly segregated diblock copolymer with this composition, the expected microphase separated morphology in the melt would

be that of a lamellar assembly. Additionally, if the segregation is strong, each block has to crystallize within the confined microdomain morphology produced during the phase segregation in the melt. As a result, it would be impossible to observe spherulites.

The micrograph shown in Figure 5.6a was taken at a temperature higher than the melting point of the PM block in the copolymer (i.e., T = 130 °C). The PVDF block crystallizes as spherulites in this case. This observation indicates that the diblock copolymer crystallizes either from a weakly segregated melt, from which break out leads to spherulites formation, or from a melt mixed state, which can also explain the observation of spherulites. As shown in Figure 5.6b, when the temperature is lower than the PM block crystallization temperature (micrograph taken at 25 °C), a subtle change in the birefringence is observed. This change in birefringence has been highlighted by surrounding the most noticeable areas with a white circle. In order to quantify this, change in the transmitted light intensity during the cooling process was measured using the ImageJ software.[10] The PLOM results obtained in Figures 5.6a and 5.6b indicate that these copolymers are either miscible or weakly segregated. These results are consistent with the lack of phase segregation observed by SAXS. On the other hand, Figure 5.6c shows the complete crystallization of both phases (PM and PVDF) in the blends after a cooling scan at 20 °C/min at T = 25 °C from the molten state. The phase segregation between the phases is evident. PVDF crystallizes as spherulites, and PM crystallizes in microaxialites (difficult to see in the micrograph due to their small size). This result suggests that there is evident macrophase segregation in the blends.

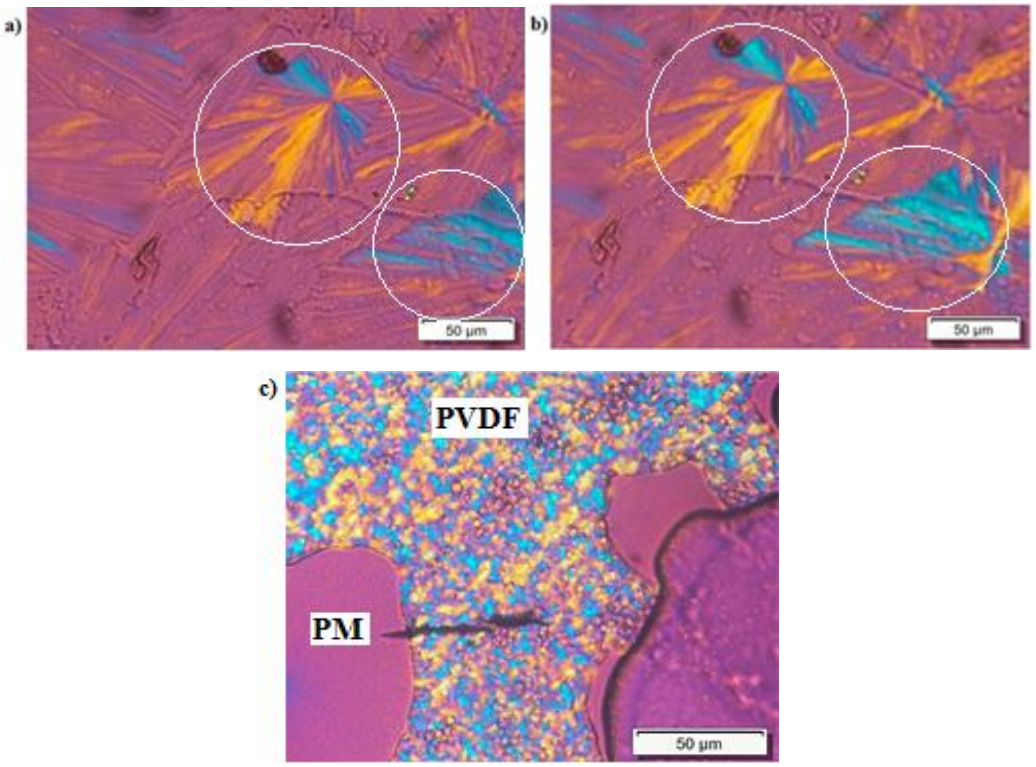

Figure 5. 6. PLOM images of a) PVDF block spherulites in the PM_{38}-*b*-$PVDF_{62}$ diblock copolymer sample after having been cooled at 20 °C/min to a T = 130 °C and b) crystallization of the PM block in the PM_{38}-*b*-$PVDF_{62}$ sample after having been cooled at 20 °C/min to T = 25 °C. c) Evident phase segregation of the PVDF and PM phases in a $PM_{23}PVDF_{77}$ blend sample after a cooling process at 20 °C/min down to T = 25 °C.

The software ImageJ was used in order to quantify the change in the birefringence during the cooling at 20 ºC/min for both copolymers. The intensity was measured by taking one picture at each 10 ºC during the whole cooling process, always measuring the same zone in all the pictures. Moreover, the intensity was normalized to obtain a range of values between 0 and 1. Figure 5.7 shows the intensity of the chosen zone against the temperature for both block copolymers. In both samples in the molten state, the intensity is the lowest. When the temperature reaches 130-140 ºC, the crystallization of the PVDF block starts, and the intensity increases its value. When the cooling process continues and the value of the temperature is around 100 ºC, there is a new change in the value of intensity that corresponds to the crystallization of the PM block. Therefore, the crystallization of the PM block inside the

PVDF block spherulites is demonstrated. This change happens as the PM block crystallizes within the already formed PVDF spherulites, just within the intraspherulitic amorphous regions, as has been observed before for other block copolymer systems, such as PCL-*b*-PLLA or PEO-*b*-PCL.[11, 12]

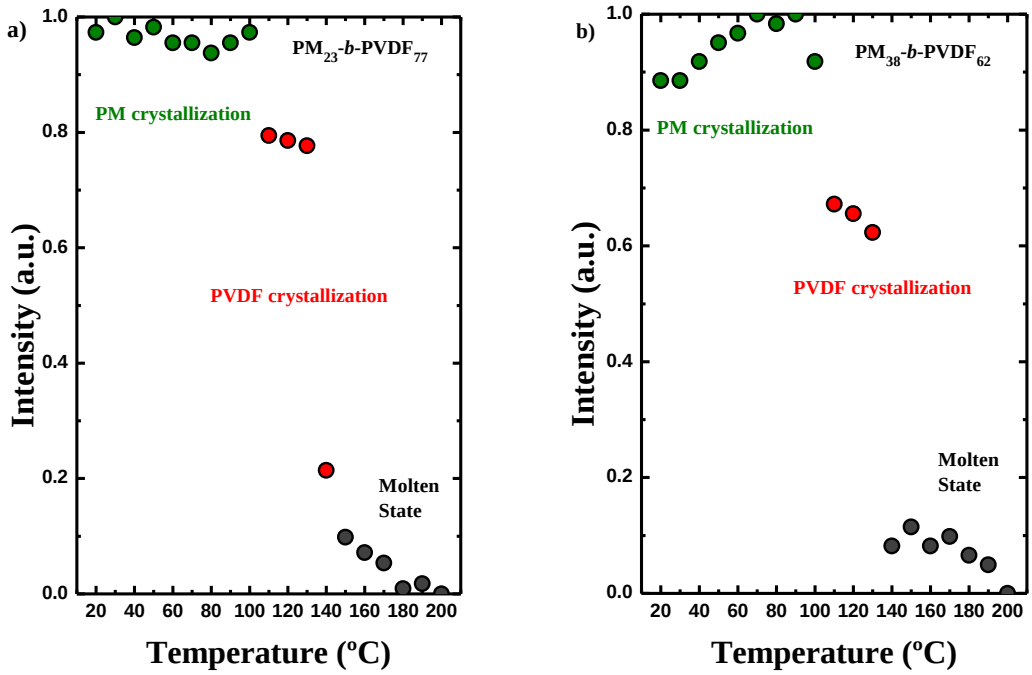

Figure 5. 7. Values of the intensity of the colours against the temperature during the cooling process at 20 ºC/min using the ImageJ software of a) PM_{23}-b-$PVDF_{77}$ and b) PM_{38}-b-$PVDF_{62}$.

TEM was used to see the differences in the miscibility and the lamellar structure between the block copolymers and the blends. Figure 5.8 shows the TEM images for the PM_{23}-*b*-$PVDF_{77}$ diblock copolymer sample (Figure 5.8a) and the $PM_{23}PVDF_{77}$ blend sample (Figure 5.8b), respectively. Figure 5.8a shows a close-up region of a spherulite whose centre is located to the right of the micrograph. A large number of lamellae that have grown from the right to the left of the micrograph can be observed. We were not able to distinguish the lamellae belonging to the

PVDF block or to the PM block, as they seem to have similar sizes. Their co-existence without any discontinuity suggests that both blocks crystallize from a miscible melt. No signs of phase separation were observed for the block copolymer samples.

On the other hand, in Figure 5.8b, it is possible to observe the evident phase segregation between PVDF and PM phases in the $PM_{23}PVDF_{77}$ blend. In summary, taking into account the collected evidence by PLOM and TEM, we can conclude that the PM and PVDF samples employed here are miscible when they form diblock copolymers, but they are immiscible when they are physically blended. This aspect is important to take into account in the following sections.

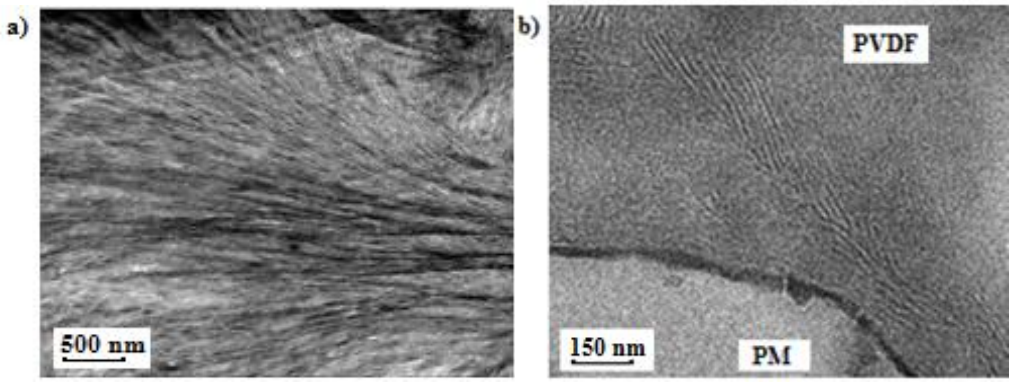

Figure 5. 8. TEM images for a) PM_{23}-*b*-$PVDF_{77}$ linear diblock copolymer and b) $PM_{23}PVDF_{77}$ blend after cooling the samples at 20 °C/min to 25 °C.

5.3.2 How the Cooling Rate Affects the Crystallization of the PVDF Phase in Block Copolymers and Blends

Blends and block copolymers were studied at different cooling rates in order to observe how this parameter affects the crystallization of PVDF in both systems. The cooling rates employed were 1, 5, 20, and 60 °C/min, and the heating rate used after the cooling process was always 20 °C/min. A PVDF homopolymer was also studied for comparative purposes.

Figure 5.9a shows the DSC cooling scans at 20 °C/min of the PVDF homopolymer, the PM homopolymer (PM-OH), the two different diblock copolymers, and

their respective blends at the same compositions. The crystallization (Figure 5.9a) peaks located at higher temperatures correspond to the PVDF component. In the blends, the PVDF component crystallizes at higher temperatures than the PVDF homopolymer (which is one of the components used to formulate the blend). This corresponds to a nucleating effect of the molten PM-OH phase, which can be explained by a transference of impurities from the PM phase to the PVDF phase during blending, as is already described for other systems in the literature.[13-15] On the other hand, the PVDF blocks in the diblock copolymers have lower T_c values than the PVDF homopolymer sample, a possible sign of miscibility between the blocks. The other crystallization peak, at lower temperatures, corresponds to the PM blocks. In this case, the crystallization of the PM in the diblock copolymers is bimodal and occurs at higher temperatures than those observed for the blends and for the PM homopolymer. This higher crystallization temperature could be related to a nucleating effect of the PVDF block crystals.

The subsequent DSC heating curves performed at 20 °C/min are plotted in Figure 5.9b and show that the melting peak that corresponds to the PM crystalline phase shows up at lower temperatures than that one observed for the PVDF. It is clear that the blends are totally immiscible, and the melting points of the PM phase (which shows a bimodal character) in the blends are very similar and located at the same temperatures as in the PM homopolymer. On the other hand, in the block copolymers, the PM block melting peak is a monomodal sharp endotherm that peaks at significantly higher values than that of the PM homopolymer or the PM phase in the blends. Regarding the melting peaks associated with the PVDF phases in the blends, these are located in the same temperature range as those of the PVDF homopolymer, once again suggesting that PM and PVDF are immiscible. In summary, due to the phase segregation encountered in the blends, the melting peaks of the blends correspond to those observed for each homopolymer in the same temperature range.

For the PVDF phase, melting is characterized by two main peaks. Due to the polymorphism observed in PVDF, different phases can be formed in the same sample.[16] In the case of the diblock copolymers, even a third minor peak appears at higher temperatures. This peak could be either a third crystalline phase or the result of a crystal reorganization that has been occurred during the heating process. The first melting peak in PVDF usually corresponds to the less stable, ferroelectric β-phase, and the second melting peak, to the paraelectric α-phase.[17]

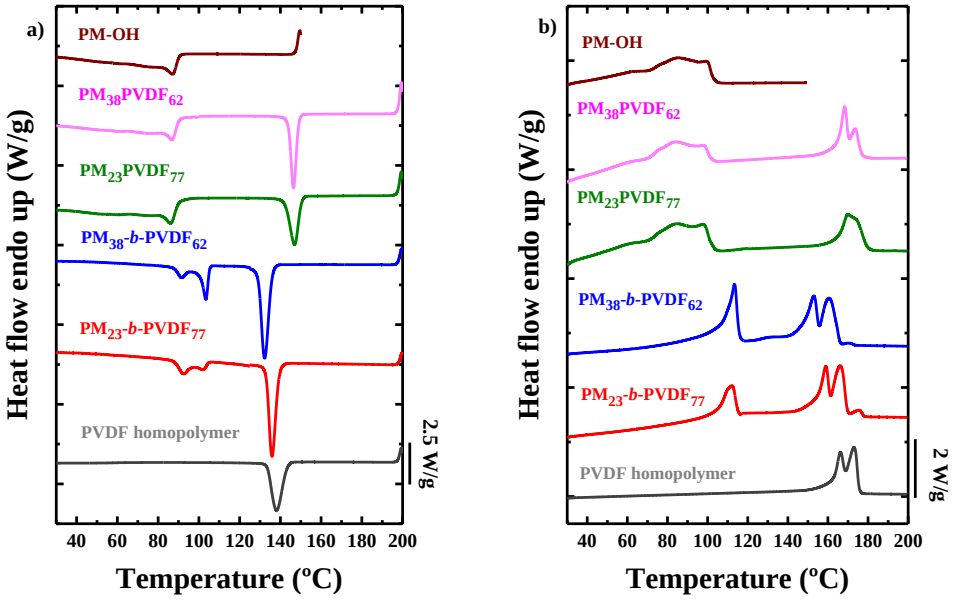

Figure 5. 9. DSC scans of the blends, the diblock copolymer, and homopolymer samples. a) Cooling curves at 20 °C/min and b) heating curves at 20 °C/min after the previous cooling process.

Figure 5.10 shows the comparison of the DSC heating scans of the samples (all performed at 20 °C/min) in the PVDF melting range obtained after using different cooling rates. The PM_{23}-*b*-$PVDF_{77}$ diblock copolymer (Figure 5.10a) shows three melting peaks at the different cooling rates studied, except at 1 °C/min, where only one main peak with a lower temperature shoulder is observed. The third peak observed at around 175 °C seems to be related to a crystal reorganization process, and

Figure 5.10a shows that it does not depend on the cooling rate used (except for the experiment performed at 1 °C/min). The height and the area of the other two peaks seem to remain constant at all the cooling rates except at 1 °C/min, where the behaviour of the subsequent melting curve is completely different. First, there is not a third peak, and second, the first peak, probably the β-phase peak, has almost disappeared, so at 1 °C/min, the α-phase peak is promoted. This is a common behaviour reported in the literature for the PVDF: at low cooling rates, the formation of the most stable phase is promoted.[18, 19]

The second diblock copolymer (Figure 5.10b), PM_{38}-*b*-$PVDF_{62}$, shows different behaviour. At high cooling rates, the α-phase peak is larger than the β-phase peak, but when the cooling rate decreases, the α-phase peak also decreases, and the β-phase peak is the majority phase in the copolymer. For instance, at 1 °C/min, the promotion of the β-phase is evident. The crystallization behaviour of the PVDF at 1 °C/min is completely different from the behaviour shown by the PM_{23}-*b*-$PVDF_{77}$ copolymer: the formation of the less stable phase is promoted in this case.

On the other hand, both PM/PVDF blends exhibit similar behaviour (Figure 5.10c and 5.10d). In this case, it seems that the amount of PM in the blend has no effect on the crystallization of the PVDF phase. The formation of the β-phase is always promoted in the blends, even at high cooling rates, where it coexists with the α-phase. When the cooling rate is decreased (5 °C/min), the α-phase almost disappears, and a new high-temperature peak appears, which is associated to a different crystalline phase that is more stable than the last two ones explained. It has been reported in the literature that at these high temperatures (higher than 175 °C) the γ-phase, which is also polar, crystallizes.[20, 21] When samples are cooled at 1 °C/min, the α-phase peak completely disappears, and the β-phase and the γ-phase coexist. For comparative purposes, a PVDF homopolymer was also studied at different cooling rates (Figure 5.10e). As can be seen at high cooling rates, the α-phase and the β-phase coexist; however, when the cooling rate is decreased, the PVDF tends to crys-

tallize preferentially in the β-phase. At 1 °C/min, the three crystalline phases mentioned above coexist, and the β-phase is the main crystalline phase. A small shoulder at high temperatures corresponds to the α-phase, and finally, the new stable melting peak appears, which probably corresponds to the previously mentioned γ-phase. All the calorimetric parameters obtained by DSC are listed in Table 5.3.

Table 5. 3. Melting and crystallization temperatures and enthalpies for each block copolymer, blend, and homopolymer sample studied.

Sample	Polymer	Rate (°C/min)	$T_{m,PM}$ (°C)	$T_{m,\alpha}$ (°C)	$T_{m,\beta}$ (°C)	$T_{m,\gamma}$ (°C)	T_c (°C)	ΔH_m (J/g)	ΔH_c (J/g)
Homopolymer	PVDF	1	-	-	170.9	178.1	150.6	52.6	69.8
		5	-	173.5	168.2	-	144.0	53.8	60.4
		20	-	173.0	166.3	-	138.2	54.3	57.0
		60	-	172.5	165.0	-	129.3	53.8	58.5
PM_{23}-*b*-$PVDF_{77}$	PM	1	113.0	-	-	-	107.9	19.9	4.6
		5	112.2	-	-	-	105.6	25.1	3.4
		20	112.1	-	-	-	102.3	23.7	3.0
		60	111.9	-	-	-	98.3	24.3	1.6
	PVDF	1	-	170.9	-	-	147.8	67.1	67.0
		5	-	167.6	161.1	-	141.7	66.6	69.5
		20	-	166.1	158.9	-	135.9	70.6	71.6
		60	-	165.4	157.3	-	128.9	71.0	60.8
PM_{38}-*b*-$PVDF_{62}$	PM	1	114.4	-	-	-	108.4	38.4	25.6
		5	113.7	-	-	-	106.3	40.6	19.6
		20	113.4	-	-	-	103.4	43.2	18.8
		60	112.7	-	-	-	98.9	43.6	12.6
	PVDF	1	-	164.3	158.7	-	141.9	60.7	66.9
		5	-	162.1	155.2	-	137.6	57.4	72.3
		20	-	160.4	153.0	-	132.3	64.8	76.1
		60	-	159.1	150.6	-	124.2	70.4	65.7
$PM_{23}PVDF_{77}$	PM	1	100.5	-	-	-	92.7	24.6	37.5
		5	98.5	-	-	-	90.1	23.9	12.2
		20	97.8	-	-	-	86.1	13.1	10.9
		60	97.1	-	-	-	80.8	13.8	12.9
	PVDF	1	-	-	172.7	179.3	157.4	30.5	33.6
		5	-	174.4	170.7	176.9	152.5	37.3	38.9
		20	-	174.2	170.1	-	147.0	33.5	37.4
		60	-	173.4	167.8	-	141.0	35.0	37.7
$PM_{38}PVDF_{62}$	PM	1	100.9	-	-	-	94.3	17.2	17.9
		5	99.6	-	-	-	91.5	12.5	13.2
		20	98.1	-	-	-	86.8	20.5	14.1
		60	97.4	-	-	-	80.8	21.9	14.4
	PVDF	1	-	-	172.2	179.1	157.5	25.8	26.8
		5	-	174.5	170.2	176.7	151.5	25.8	29.5
		20	-	173.6	168.4	-	146.4	26.8	28.9
		60	-	173.1	167.3	-	139.8	27.1	29.7

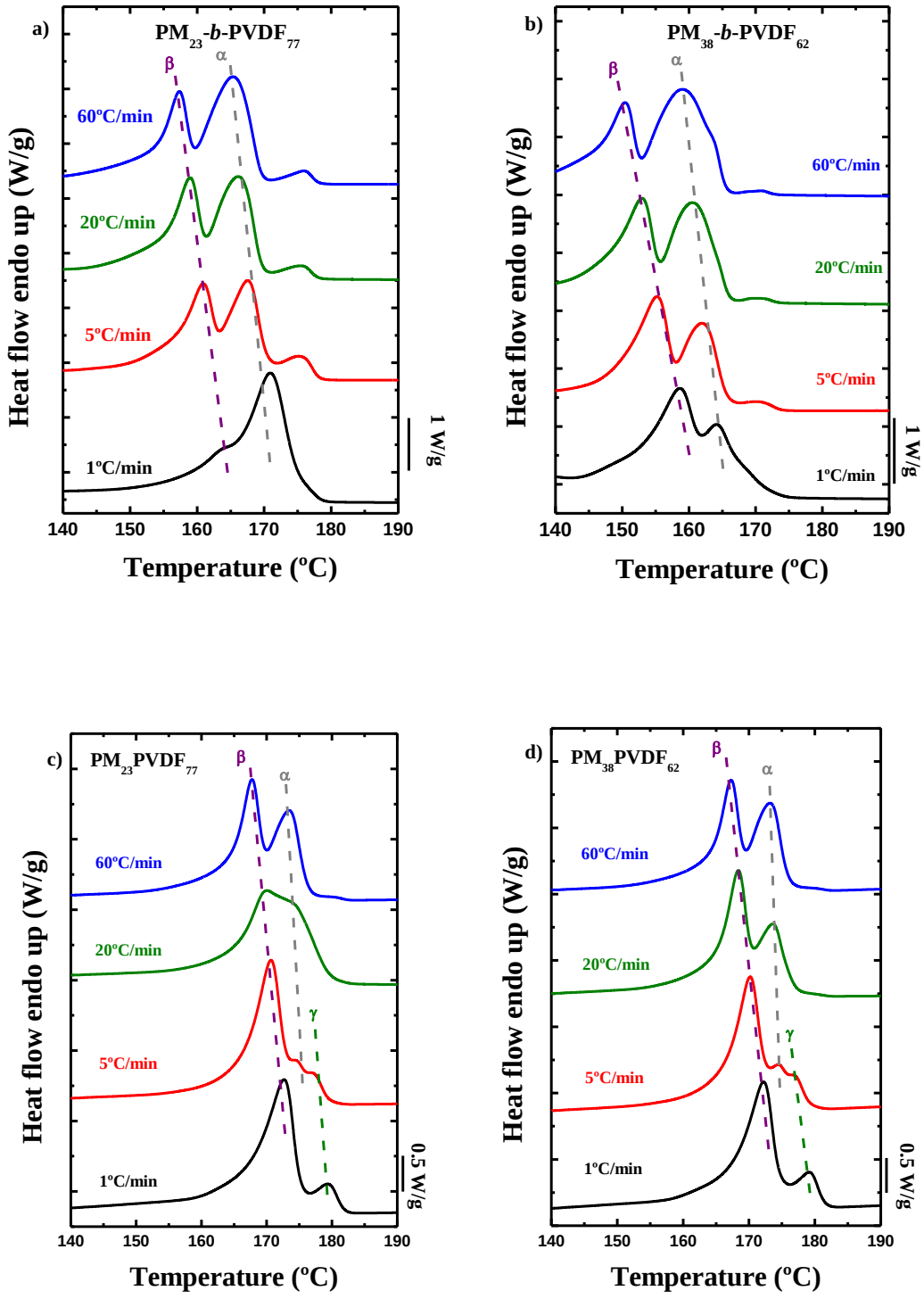
a)
PM23-b-PVDF77
β
α
60°C/min
20°C/min
5°C/min
1°C/min
1 W/g
Heat flow endo up (W/g)
140 150 160 170 180 190
Temperature (°C)
b)
PM38-b-PVDF62
β
α
60°C/min
20°C/min
5°C/min
1°C/min
1 W/g
Heat flow endo up (W/g)
140 150 160 170 180 190
Temperature (°C)
c)
PM23PVDF77
β
α
γ
60°C/min
20°C/min
5°C/min
1°C/min
0.5 W/g
Heat flow endo up (W/g)
140 150 160 170 180 190
Temperature (°C)
d)
PM38PVDF62
β
α
γ
60°C/min
20°C/min
5°C/min
1°C/min
0.5 W/g
Heat flow endo up (W/g)
140 150 160 170 180 190
Temperature (°C)

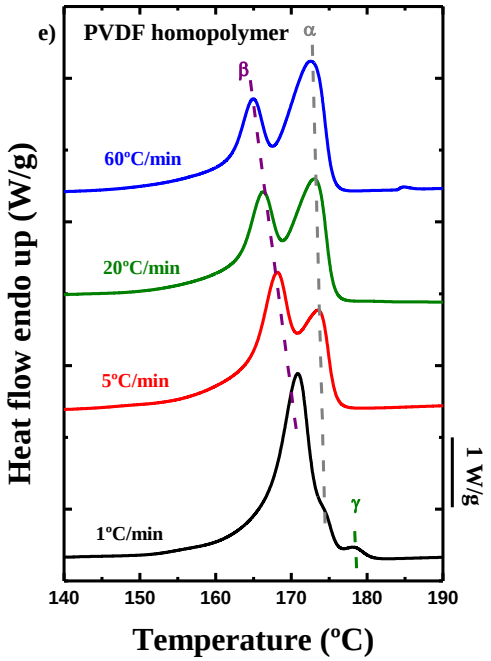

Figure 5. 10. DSC heating scans for PVDF component after different cooling rates were used for: a) PM_{23}-*b*-$PVDF_{77}$ and b) PM_{38}-*b*-$PVDF_{62}$ block copolymers, c) $PM_{23}PVDF_{77}$, d) $PM_{38}PVDF_{62}$, and e) PVDF homopolymer samples.

DSC heating scans performed after cooling the samples at 1 °C/min show that the crystalline phase obtained depends on the sample and the origin of the sample. Samples cooled at 1 °C/min were analyzed by FTIR to verify in which phases the PVDF component crystallizes. Figure 5.11 shows the FTIR results for the PM homopolymer, the PVDF homopolymer, both diblock copolymers, and both blends, at room temperature after the samples were cooled from the melt at 1 °C/min. The wavenumber range studied was 1400–600 cm^{-1}, which is where the most useful information for PVDF can be observed. There is a large band located at 720 cm^{-1} and a smaller one at 1377 cm^{-1}, where the main characteristic bands for the PM polymer are detected.[22] There is also a weak band located at 801 cm^{-1}. Moreover, we can observe that the main peaks perceived for PM do not overlap with the main bands associated with PVDF.

When the crystallization of the PVDF homopolymer happens at a low cooling rate, three very weak bands can be seen at 1214, 976, and 796 cm^{-1}, which correspond to the α-phase. This means that the formation of the α-phase is not really promoted in the homopolymer. Moreover, there are two additional more intense main bands, at 1275 and 840 cm^{-1}, which are related to the crystalline β-phase. This means that, surprisingly, the PVDF homopolymer is able to crystalize in the ferroelectric β-phase when the polymer is crystallized slowly from the melt.

The spectra for both diblock copolymers show bands for the crystalline α-phase and β-phase. The PM_{23}-*b*-$PVDF_{77}$ shows only one small band located at 1278 cm^{-1}, corresponding to the β-phase, but there is not any band at 840 cm^{-1}. This indicates the presence of a small amount of β-phase in the copolymer. In addition, the FTIR spectrum of this sample clearly shows the bands corresponding to the α-phase, which indicates that the crystallization observed at 1 °C/min corresponds mainly to the paraelectric α-phase, which confirms the DSC results.

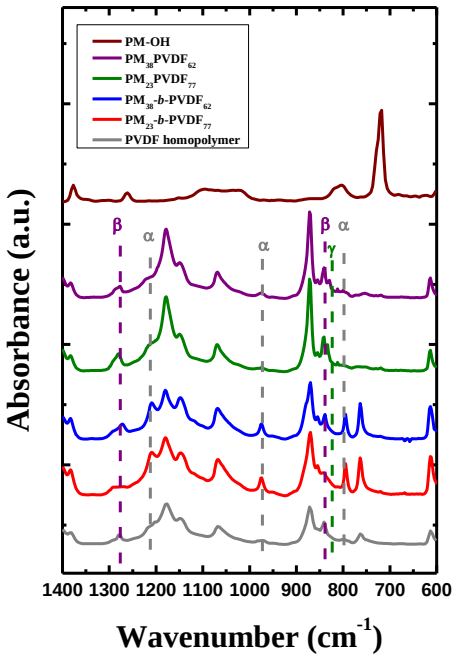

Figure 5. 11. FTIR spectra of PM-OH, PVDF homopolymer, PM_{23}-*b*-$PVDF_{77}$, PM_{38}-*b*-$PVDF_{62}$, $PM_{23}PVDF_{77}$, and $PM_{38}PVDF_{62}$ samples after a cooling sweep at 1 °C/min. The grey dashed line shows the bands for the α-phase; the purple dashed line is for the β-phase, and the green dashed line corresponds to the γ-phase.

On the other hand, the spectrum of the PM_{38}-*b*-$PVDF_{62}$ sample shows the α-crystals bands mentioned before and the band located at 1278 cm^{-1} that corresponds to the β-phase. The FTIR analysis of this diblock copolymer demonstrates that the α-phase and the β-phase coexist simultaneously after samples have been cooled at 1 °C/min. Again, this behaviour confirms the DSC results: at low cooling rates, the formation of the β-phase is promoted, but the α-phase remains present.

The FTIR spectra for the two blends (Figure 5.11) shows the two main bands corresponding to the β-phase and a new band located at 811 cm^{-1}, which corresponds to the γ-phase crystals.[23] The entire characteristic bands for PM and PVDF are shown in Table 5.4.

Table 5. 4. Values and description of the main FTIR bands for α, β, γ-phases for PVDF and PM.

Wavenumber (cm^{-1})	**Phase**	**Description[24, 25]**
720	PM	C-C rocking deformation
796	α-PVDF	CH_2 rocking
811	γ-PVDF	-
840	β-PVDF	CH_2,CF_2 asymmetric stretching vibration
976	α-PVDF	CH out of plane deformation
1214	α-PVDF	CF stretching
1232	γ-PVDF	CF out of plane deformation
1275	β-PVDF	CF out of plane deformation
1377	PM	CH_3 symmetric deformation

WAXS experiments were performed to investigate what phases crystallized during the cooling process at 1 °C/min from the molten state (Figure 5.12). The main reflections for the PM are located at 15.2 and 16.7 nm^{-1} as can be seen in the pattern of the PM-OH sample. PM crystallizes in an orthorhombic unit cell with parameters

a = 0.742 nm, b = 0.495 nm, c = 0.255 nm, and β = 90°, with a *P*-D_{2h} space group.[26, 27] The crystallographic planes for these peaks are (110) and (200), respectively.[28, 29]

PVDF has different crystalline phases, which appear as WAXS reflections at different *q*-values (see Figure 5.12). The peaks that are located at *q*-values of 12.6, 13.1, 14.2, and 18.9 nm^{-1} correspond to the crystalline α-phase, and the reflections of this paraelectric phase have the following crystallographic planes: (100), (020), (110), and (120/021).[30-32] The α-phase of PVDF is characterized by a pseudo-orthorhombic unit cell with a = 0.496 nm, b = 0.964 nm, c = 0.462 nm, and β = 90° and has a *P2/C* space group.[33, 34] In our case, these reflections appear for the diblock copolymers, the blends, and the homopolymer samples. These reflexions are more intense in the homopolymer and in the PM_{23}-*b*-$PVDF_{77}$ sample than in the other ones. Based on this result and the FTIR spectra, we can conclude that during the crystallization of the PM_{23}-*b*-$PVDF_{77}$ sample the formation of the α-phase is always promoted at low cooling rates.

However, apart from the characteristic peaks of the α-phase, the other samples containing PVDF display one extra peak or shoulder in their patterns at 13.5 nm^{-1} (Figure 5.12). This new reflection corresponds to the crystallization of the β-phase, which has the (200/110) crystal plane.[35] The β-phase of PVDF is characterized by an orthorhombic unit cell, which has a *Cm2m* space group and the following dimensions: a = 0.847 nm, b = 0.490 nm, and c = 0.256 nm.[36] The presence of this peak is in agreement with the results obtained before by DSC analysis, which suggests that the formation of the β-phase is promoted in samples that were previously cooled at 1 °C/min and coexists with a small amount of crystalline α-phase. It seems that the amount of PM in the diblock copolymer can affect the PVDF crystallization in order to promote the desired β-phase.

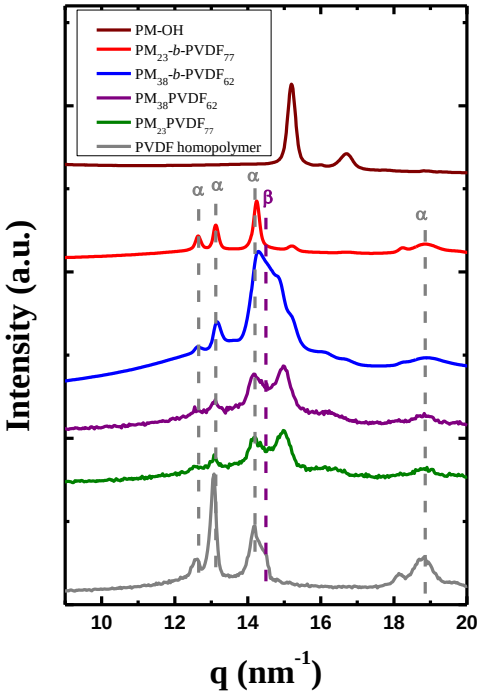

Figure 5. 12. WAXS diffraction patterns of PM-OH and PVDF homopolymers, both blends, and both block copolymers at room temperature after a crystallization process at 1 °C/min. The grey dashed lines indicate the peaks associated to the α-phase, and the purple dashed line indicates the peak of the β-phase.

5.3.3 Dynammic studies in PVDF and its copolymers

Figure 5.13 shows the BDS results for PVDF and its copolymers with PM. In particular, Figures 5.13a–c display dielectric spectra: the imaginary part of the complex dielectric permittivity as a function of the frequency. The data presented correspond to the one collected by isotherms from −100 to 0 °C in steps of 10 °C (measured on heating). The corresponding experiments on cooling are nearly indistinguishable. In general, the relaxation processes are characterized by a single maximum, which shift towards higher frequencies and increase in intensity as the temperature is increased.

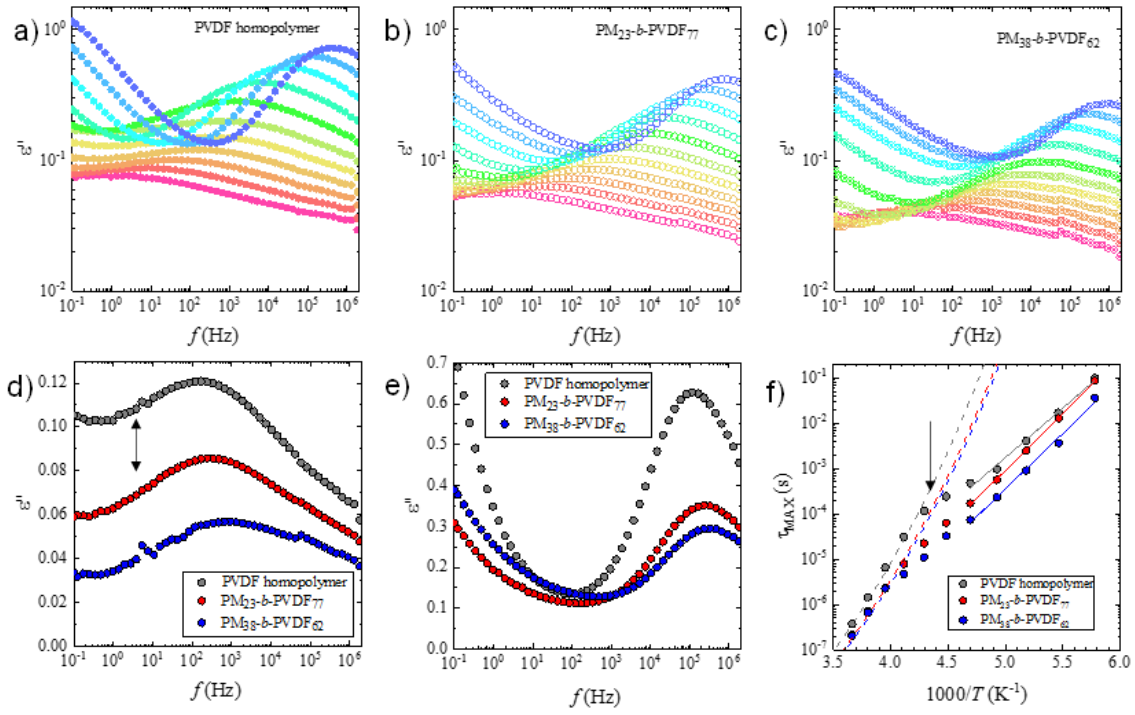

Figure 5. 13. Dielectric spectra (imaginary part of the complex dielectric permittivity as a function of the frequency) for a) PVDF homopolymer, b) PM_{23}-*b*-$PVDF_{77}$, c) PM_{38}-*b*-$PVDF_{62}$, as well as dielectric relaxations of the studied samples at d) −70 °C and e) −10 °C and f) relaxation map of the studied samples.

At low temperatures (−100 °C to −60 °C), a weak and broad peak is observed for all samples, although with different characteristics. PVDF displays the highest intensity peaks, reaching ε'' values of around 0.1. In the case of the diblock copolymers, the intensity of the relaxations decreases with PM content. We also observe that, as PM content increases, the relaxation peaks maxima shift towards higher frequencies. As an example, Figure 5.13d shows the dielectric relaxations of the samples at −70 °C. In addition to the differences already discussed, PVDF displays a pronounced asymmetry towards low frequencies (black arrow in Figure 5.13d). However, the relative intensity of this low-frequency signal decreases for the samples containing PM blocks.

Comparing with previous literature reports, and taking into consideration the intensity and position of the peaks, we are able to assign the low-temperature process

to the local β-relaxation of PVDF related to local motions of polar groups in the polymer.[37-40] As the temperature is further increased (T > −60 °C), the relaxation peaks suffer important changes. In all cases, as the maxima moves towards higher frequencies, the peaks are narrower and show a dramatic intensity increase. These changes in the dielectric relaxation occur at temperatures close to the glass transition of PVDF (−43 to −23 °C).[41] Thus, we can relate the changes to the α-relaxation of the PVDF. This relaxation process is related to the segmental motion of the PVDF polymer chain taking place at temperatures above the glass transition (T_g), as widely reported.[37, 38, 41-43] Please, notice that our experimental results show a continuous change in the dielectric spectra, going from the β- to α-relaxation, instead of separated peaks observed in previous works.[37-39, 42, 43] Nonetheless, although in this chapter the α-relaxation peak cannot be well resolved at low frequencies, the data show an increased broadness at T = −50 to −40 °C. The peak is better resolved in the PVDF sample than in PM-*b*-PVDF copolymers, which indicates that the PVDF segmental relaxation is affected by the presence of PM units. In fact, in the −50–0 °C temperature range, PM-*b*-PVDF copolymers show lower segmental relaxation intensities and slightly faster dynamics compared to the PVDF. Figure 5.13e presents a comparison of the datasets at −10 °C where this evidence can be observed.

Figure 5.13f shows the relaxation map of the samples. The relaxation time (τ_{MAX}) is calculated from the maxima of the dielectric relaxation peaks. In all cases, we observe two trends in the temperature dependence of relaxation times. At low temperatures (−100 ≤ T (°C) ≤ −60), the relaxation times followed an Arrhenius behaviour, as described by:

$$\tau_{\mathrm{MAX}} = \tau_0 \exp\left[\frac{E_A}{kT}\right] \qquad \text{eq. 5.2}$$

where E_A is the activation energy, k is Boltzmann's constant, and τ_0 a pre-exponential factor. The obtained results are shown in Figure 5.13f as continuous lines and are summarized in Table 5.5. For PVDF, we find E_A = 42 kJ/mol, which increases slightly for the PM-*b*-PVDF systems (~48 kJ/mol). These values are quite similar to

the one reported before by Sy and Mijovic (~43 kJ/mol)[37] for the local relaxation of PVDF, while slightly lower than that observed by Linares and collaborators (~60 kJ/mol).[38]

At temperatures above −60 °C, the relaxation times of the samples show a deviation from the low-temperature Arrhenius trend. In all the studied samples, a sort of "kink" appears at temperatures around −50 to −60 °C (see arrow in Figure 5.13f). We relate these changes to the effect of the segmental relaxation of PVDF on the relaxation times. We also observe that the kink's intensity is reduced in the block copolymer as the PM content increase. These sorts of trends, or anomalies, have been reported before for PVDF-based systems. For example, Sy and Mijovic observed a similar behaviour in local motions of semi-crystalline PVDF/PMMA blends.[37] In that work, the temperature dependence of the relaxation times of PVDF/PMMA blends is described as a gradual crossover from local to segmental motions, which is clearly different from an α-β merging. The 90/10 PVDF/PMMA showe the most pronounced kink, which decrease as the PMMA content increase. However, the neat PVDF do not show this signature. Martínez-Tong *et al.*[44] also observe a continuous transition in the dielectric relaxation map of a PVDF copolymer with trifluoroethylene P(VDF-*co*-TrFE), with a VDF mol content of 76%. In that work, the authors observe a crossover from the segmental relaxation to the ferroelectric-paraelectric relaxation of the polymer. Just at the transition temperatures (~47–57 °C), a small kink can be detected in the relaxation plot. Finally, very recently, Napolitano and collaborators observed an anomalous behaviour in the local relaxation of PVDF copolymers with hexafluoropropylene (HFP).[40] In their work, the dielectric relaxation experiments show that, close to the T_g, the PVDF-HFP copolymers display a so-called "anomalous minimum" in the local relaxation. The authors relate their findings to the bonds formed by fluorine entities, similar to those observed in propylene glycol systems. Moreover, the authors also observe that the anomalous process weakened when the PVDF-HFP samples are prepared as ultrathin polymer films. This nano-confinement induce reduction in the anomaly is

explained by means of the minimal model and related to an asymmetry in the well potential describing the molecular motion. In this chapter, we observe that PM-*b*-PVDF samples show a reduction of the observed kink, whose intensity decrease as PM content was increase. This could indicate that the PM block is inducing local confinement effects on the samples.

Finally, we attempted to model the data points in the −50–0 °C temperature range using the Vogel–Fulcher–Tamman (VFT) equation, described by:[45]

$$\tau_{\mathrm{MAX}} = \tau_{\infty} \exp\left[\frac{D T_{\mathrm{VFT}}}{T - T_{\mathrm{VFT}}}\right] \qquad \text{eq.5.3}$$

where τ_{∞} is a pre-exponential factor, D is a dimensionless parameter related to the dynamic fragility[46] and T_{VFT} the Vogel temperature. The results obtained are summarized in Table 5.5 and the fits are shown in Figure 5.13f by dashed lines. We highlight that the value of τ_{∞} was set at 10^{-14} s, based on the discussion of Angell.[46, 47] For all samples, we obtain a D = 21, indicating a small deviation from an Arrhenius process. This value is slightly larger than the ones reported before (D = 12–15) for PVDF.[37, 43] However, it is fairly comparable to the one obtained by Martínez-Tong and collaborators for the P(VDF-*co*-TrFE) copolymer (D = 21.6). Finally, we are able to predict the dynamic glass transition temperature ($T_{\mathrm{g-BDS}}$) of the samples in our study from the VFT fit. This parameter is defined as the temperature where the segmental relaxation time reach 100 s. The results obtained, shown in Table 5.5, allowed to determine a $T_{\mathrm{g-BDS}}$ = −80 °C for PVDF. This value decrease for the PM-*b*-PVDF samples with increasing PM content, which is in line with the faster dynamics observed. The $T_{\mathrm{g-BDS}}$ obtained are lower than the usual ones reported for PVDF by different methods (T_{g} = −63 to 23 °C).[48, 49] However, we emphasize that both the PVDF and PM-*b*-PVDF copolymers have low molecular weights (6–8 kDa), which would explain the obtained results. In addition, we should take into account that, in semicrystalline polymers, the dynamics in the more amorphous environments dominate the dielectric relaxation peak frequency position.[50]

Table 5. 5. Arrhenius fit results for PVDF and its copolymers with PM.

Sample	τ_0 (s)	E_A (kJ/mol)	τ_0 (s)	D	T_{VFT} (°C)	T_{g-BDS} (°C)
PVDF	$2{\cdot}10^{-14\pm1}$	42 ± 1			-151 ± 1	-80 ± 1
PM_{23}-*b*-$PVDF_{77}$	$3{\cdot}10^{-16\pm1}$	48 ± 1	10^{-14}	21 ± 1	-154 ± 1	-85 ± 1
PM_{38}-*b*-$PVDF_{62}$	$2{\cdot}10^{-16\pm1}$	47 ± 1			-155 ± 1	-86 ± 1

5.3.4 How the isothermal crystallization affects PVDF based blends and block copolymer samples

Figure 5.14 shows the spherulitic growth rate of PVDF, its copolymers and the prepared blends as a function of the isothermal crystallization temperature. The high nucleation density observed in the blends only allow us to measure spherulites at relatively high crystallization temperatures. Experiments were performed by cooling the samples from the melt to a chosen crystallization temperature in the range from 131 to 164 °C. Spherulitic growth rates for each sample, *G* (μm/min), were determined at different crystallization temperatures from the slope of radius versus time plots (which were always linear).

Figure 5.14a shows the spherulitic growth rate *G* (μm/min) as a function of T_c. As can be seen, the growth rate is faster in the copolymers than in the blends and the homopolymer sample in the low temperature range. However, the comparison is difficult, as the crystallization ranges of the sample do not overlap. *G* dramatically decreases when the PVDF is blended with PM. The supercooling required for crystallization increases when the PVDF is blended with PM, as a result of the change in the equilibrium melting temperature. When *G* is plotted as a function of supercooling ($\Delta T = T_m^0 - T_c$), using the equilibrium melting temperatures (T_m^0) determined by the Hoffman–Weeks method, in Figure 5.14b the curves are now shifted along the x-axis reducing the differences between the overall crystallization curves versus T_c. In this representation as a function of supercooling, it is easier to observe the above mentioned trends.

It is unexpected that the growth rate (Figure 5.14b) of the PVDF component decreases in the blends as compared to the neat PVDF. One possible explanation could be that even though the blends are immiscible (as indicated by the DSC results), the molten PM-OH is capable of interacting with the PVDF (though the OH group) reducing the PVDF diffusion to the growth front.

In the diblock copolymers case, the growth rate of the PVDF block decreases as the PM content in the copolymer decreases. It can also be noted that the temperature dependence of the growth rate between the neat PVDF homopolymer and the PVDF blocks in the diblock copolymers is very different. This is easily captured by the Lauritzen and Hoffman fits, which are represented as solid lines in Figure 5.14.

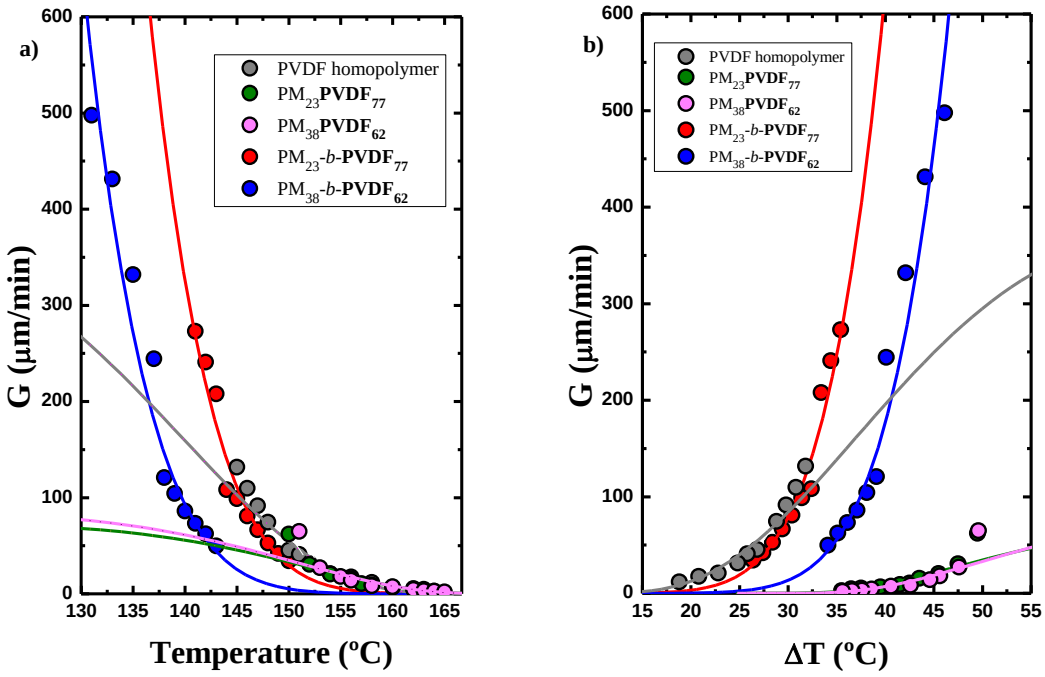

Figure 5. 14. a) Spherulitic growth rates determined by PLOM for homopolymer PVDF, the PVDF block of the diblock copolymers, and the PVDF phase within the blends studied and b) spherulitic growth rates as a function of supercooling. The solid lines are the fits to the Lauritzen–Hoffman (LH) theory.

Isothermal crystallization experiments were performed by DSC to determine the overall crystallization rate of the samples (which include both nucleation and growth contributions). Differences in the PVDF polymorphism and its crystallization kinetics were observed depending on the structural forms of the respective samples. The Avrami theory and the Lauritzen and Hoffman theory were employed to describe the primary crystallization process in polymers and to plot several kinetic crystallization parameters as a function of the crystallization temperature.[51, 52]

Figure 5.15a shows the inverse of the induction time (t_0) versus the isothermal crystallization temperature (T_c) for the different PVDF samples. The induction time is equivalent to the primary nucleation time before any crystallization is detected by the DSC. The inverse of the induction time is proportional to the primary nucleation rate of the PVDF components in the different samples. The nucleation rate depends on the composition and the nature of the samples. The nucleation rate of the PVDF block within the PM_{38}-*b*-$PVDF_{62}$ sample is faster than in the homopolymer sample, while in the blend, the PVDF phase has a slower nucleation rate.

Figure 5.15b shows the inverse of the half crystallization time ($\tau_{50\%}$) versus the isothermal crystallization temperature (T_c). The $1/\tau_{50\%}$ value is the inverse of the time needed to achieve the 50% of the total transformation to the semicrystalline state during the isothermal crystallization process and represents an experimental measure of the overall crystallization rate, which includes both growth and nucleation contributions.

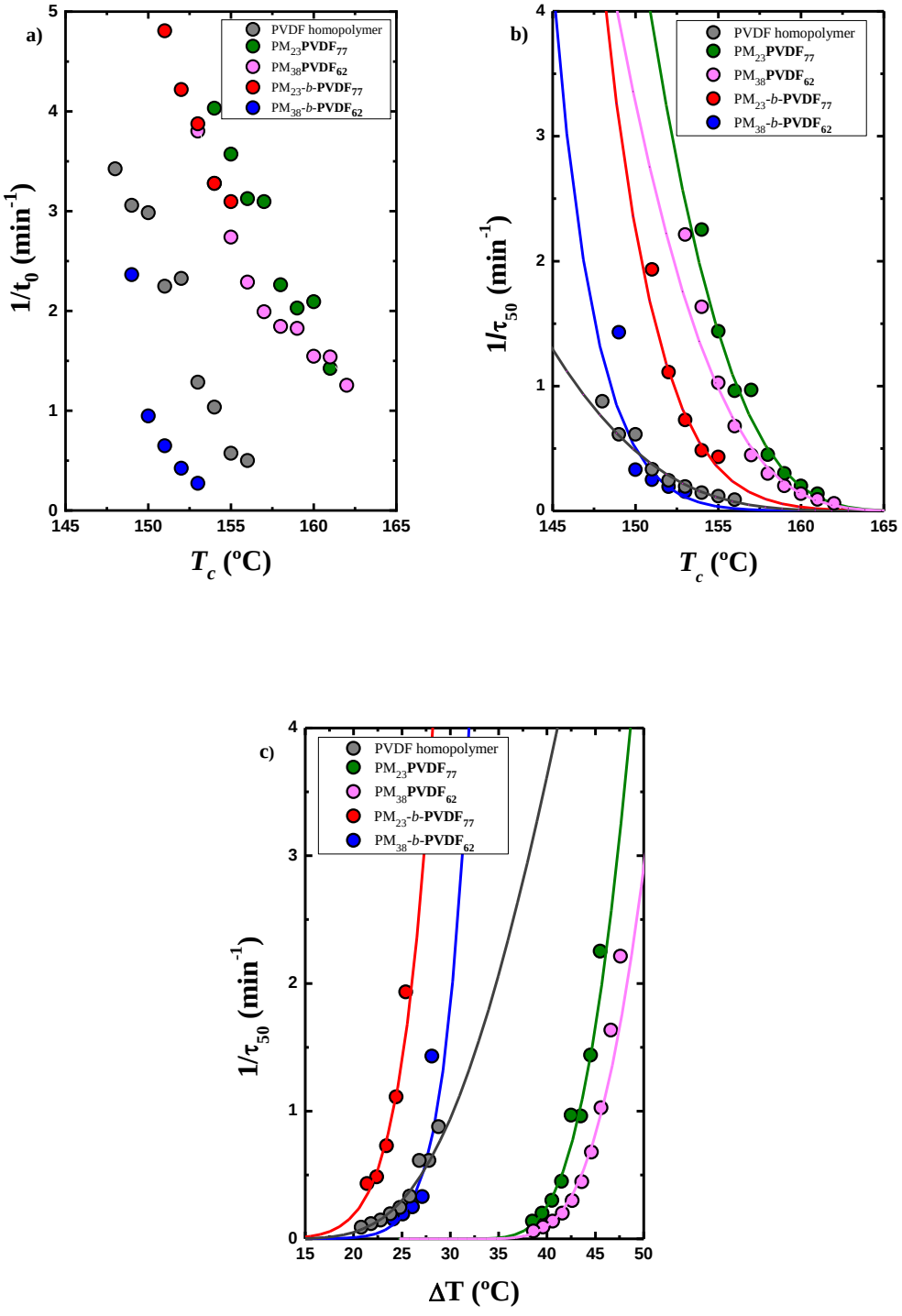

Figure 5. 15. a) $1/t_0$ as a function of crystallization temperature and inverse of half-crystallization time for the PVDF component of all samples shown as a function of b) T_c and c) ΔT for all the PVDF samples measured by DSC. The solid lines are the fits to the Lauritzen–Hoffman (LH) theory.

Figure 5.15b reflects a combined trend of the observed nucleation behaviour (Figure 5.15a) and the spherulitic growth behaviour (Figure 5.14a). Both the PVDF homopolymer and the $PM_{23}PVDF_{77}$ blend exhibit the lowest overall crystallization rates. However, as in the overall crystallization, both nucleation and spherulitic growth rate contribute; in this case, $1/\tau_{50\%}$ does not decrease as dramatically as *G* for the rest of the materials. Therefore, the changes in nucleation density strongly affect the overall crystallization rates determined by DSC in these PVDF-based blend samples. Figure 5.15c shows these results when they are plotted against the supercooling (ΔT) and the curves are shifted in the x-axis standardizing the differences in crystallization temperature exhibited by the different samples.

The Avrami theory is a useful tool to fit the overall crystallization kinetics of polymers during the primary crystallization regime.[53-55] The Avrami theory is given by the following equation:

$$1 - V_c(t - t_0) = \exp(-k(t - t_0)^n) \qquad \text{eq. 5.4}$$

where V_c is the relative volumetric transformed fraction, *t* is the time of the experiment, t_0 is the induction time before the crystals start to grow, *k* is the overall crystallization rate constant, and *n* is the Avrami index, which is related to the time dependence of the nucleation and the crystal growth geometry.

By applying the Avrami equation to the isothermal crystallization curves at each chosen crystallization temperature, it is possible to calculate the Avrami index (*n*), but it is only possible when the crystallization starts at the isothermal temperature selected and not during the cooling, as happened in the case of the PM. Figure 5.16a shows all the *n* values for the crystallization of the PVDF component in all the samples studied during this chapter. Usually, for polymers, *n* is between 1.5 and 4. When this value is higher than 2.4, the crystals of the polymer grow as spherulites. In our case, all the samples have an *n* value higher than 2.5 with the exception of the PM_{38}-*b*-$PVDF_{62}$ sample. For the samples with an *n* value below 2.5, crystals grow in 2D,

forming axialites. Figure 5.16b shows the evolution of the $k^{1/n}$ value at different crystallization temperatures, and these values are proportional to the overall crystallization rate. The comparison between Figures 5.14b and 5.16b demonstrates that the theoretical results obtained through the Avrami theory are really close to the experimental results obtained using the Lauritzen and Hoffman method as the trends in the data are similar($1/\tau_{50\%}$).

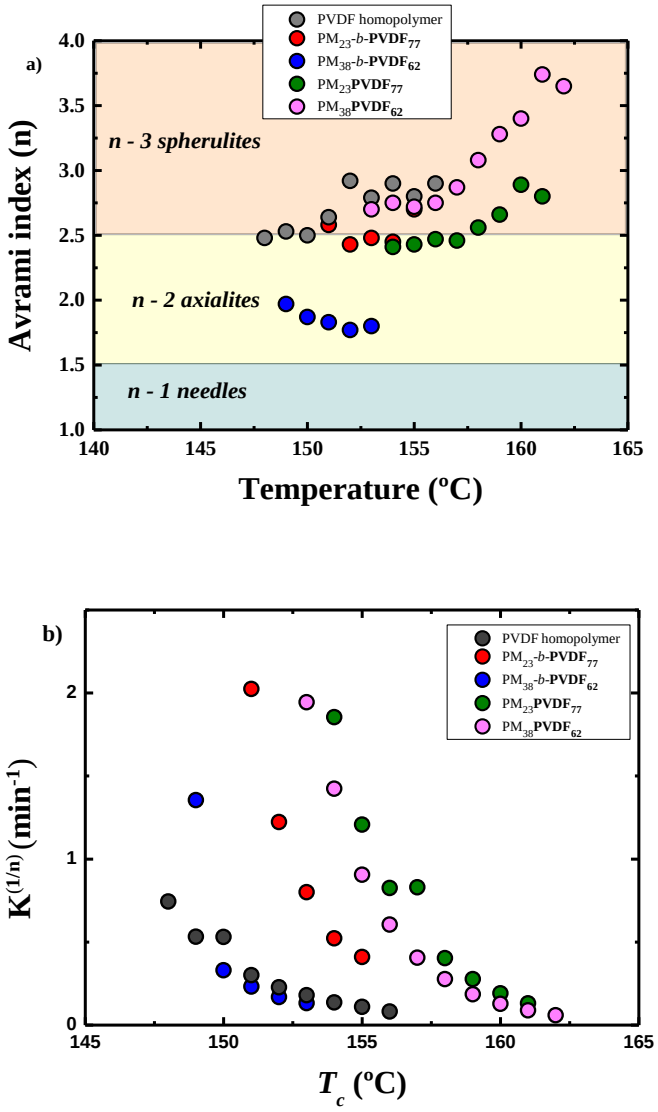

Figure 5. 16. a) PVDF Avrami index values for all the temperatures used in the isothermal crystallization and b) isothermal crystallization rate obtained by the Avrami model.

Using the isothermal crystallization temperature and the melting temperature obtained after the isothermal process, as Hoffman-Weeks theory predicted, it is possible to obtain the PVDF equilibrium melting temperature (T_m^0) for each sample. This method consists in using the melting temperatures obtained in the heating process after the isothermal crystallization procedure and plotting them against their respective crystallization temperatures obtaining a linear plot. When extrapolating this linear fit, the intersection with the $T_m = T_c$ line is the equilibrium melting temperature.[56, 57] The values for the T_m^0 of all samples containing PVDF are shown in Table 5.6. In the case of the diblock, the melting peaks used to obtain the T_m^0 are from the melting of the α-phase, because is the only one stable during all the temperatures. However, for the homopolymer and the blends the α-phase does not exist so the melting peaks used to obtain the T_m^0 are from the β-phase. These values were used to plot Figures 5.14b and 5.15c in the main article. In this chapter the T_m^0 values are in a big range of 176-201 ºC according to the PVDF T_m^0 values reported in other works that are in an interval between 172-201 ºC.[58, 59] In the Figure 5.17 are plotted the melting temperatures against their isothermal crystallization temperatures to calculate the equilibrium melting temperature with the cross with the diagonal line fitted.

Table 5. 6. Equilibrium melting temperature *(T_m^0)* for the PVDF homopolymer, PVDF blends and PVDF block copolymers.

Sample	PVDF homopolymer	PM_{23}-*b*-$PVDF_{77}$	PM_{38}-*b*-$PVDF_{62}$	$PM_{23}PVDF_{77}$	$PM_{38}PVDF_{62}$
T_m^0 **(°C)**	176.8	176.4	177.1	199.5	200.6

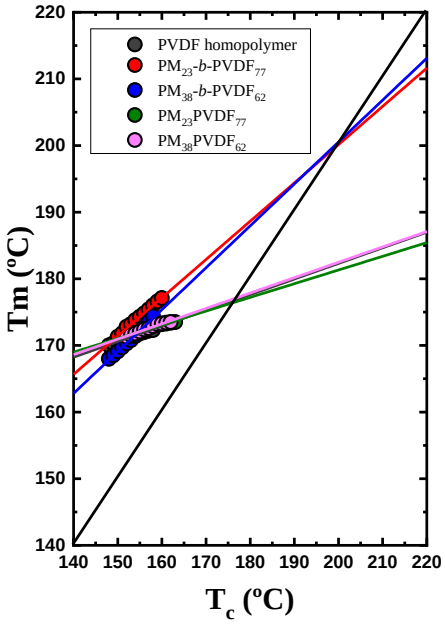

Figure 5. 17. Melting temperatures against crystallization temperatures with their respective linear fit to calculate the equilibrium melting temperature using the Hoffman-Weeks method.

The analysis of the heating curves after the isothermal crystallization processes may allow us to know how the PVDF crystallizes and which crystalline phase is obtained after these procedures. Figure 5.18 shows all the melting curves for the PVDF component in each sample at all the isothermal crystallization temperatures studied. The T_c selected through the $T_{c,\min}$ method are similar for the block copolymers and the homopolymer sample, while the blends have higher T_c values.

The PVDF homopolymer (Figure 5.18a) has two melting peaks when the isothermal crystallization temperature used was low: one main peak at low temperatures and another small peak at higher temperatures. The main peak corresponds to the β-phase, and the second peak to the α-phase. When the crystallization temperature increases, the peak from the α-phase starts decreasing until it disappears and a new peak appears at even higher temperatures. This new peak corresponds to the

crystalline γ-phase. This means that the PVDF low molecular weight homopolymer sample can crystallize in all ferroelectric phases when is crystallized at low cooling rates and also during an isothermal process at high crystallization temperatures.

The behaviour of the PVDF block in the diblock copolymers (Figure 5.18b and 5.18c) is completely different from the homopolymer sample. In this case, only two melting peaks are observed when the isothermal crystallization temperature used was low. In the case of the PM_{23}-*b*-$PVDF_{77}$ sample, the main peak is observed at higher temperatures. When the crystallization temperature increases, the first peak tends to disappear and only the main peak, which belongs to the α-phase, remains.

For the PM_{38}-*b*-$PVDF_{62}$ sample, at low crystallization temperatures, the first melting peak is promoted (β phase), but as the isothermal crystallization temperature is increased, the size of this peak starts to decrease, and at high crystallization temperatures, only one peak is observed, which also corresponds to the α-phase.

Both PM/PVDF blends (Figure 5.18d and 5.18e) have similar melting curves regardless of the PM content. Both blends show three peaks at low isothermal crystallization temperatures: the largest one is located at low temperatures and corresponds to the β-phase; then, there is a shoulder at about 175 °C, which is the melting peak of the α-phase, and finally, the last one at higher temperatures is the melting peak of the γ-phase. When the crystallization temperature is increased, only the shoulder of the α-phase disappears, while both ferroelectric phases remain.

As during isothermal crystallization, the PVDF component develops a complex polymorphic structure that changes with crystallization temperature; this helps to explain the complex trends observed in the growth kinetics (Figure 5.14), nucleation rate (Figure 5.15a), and overall crystallization rate (Figure 5.15c).

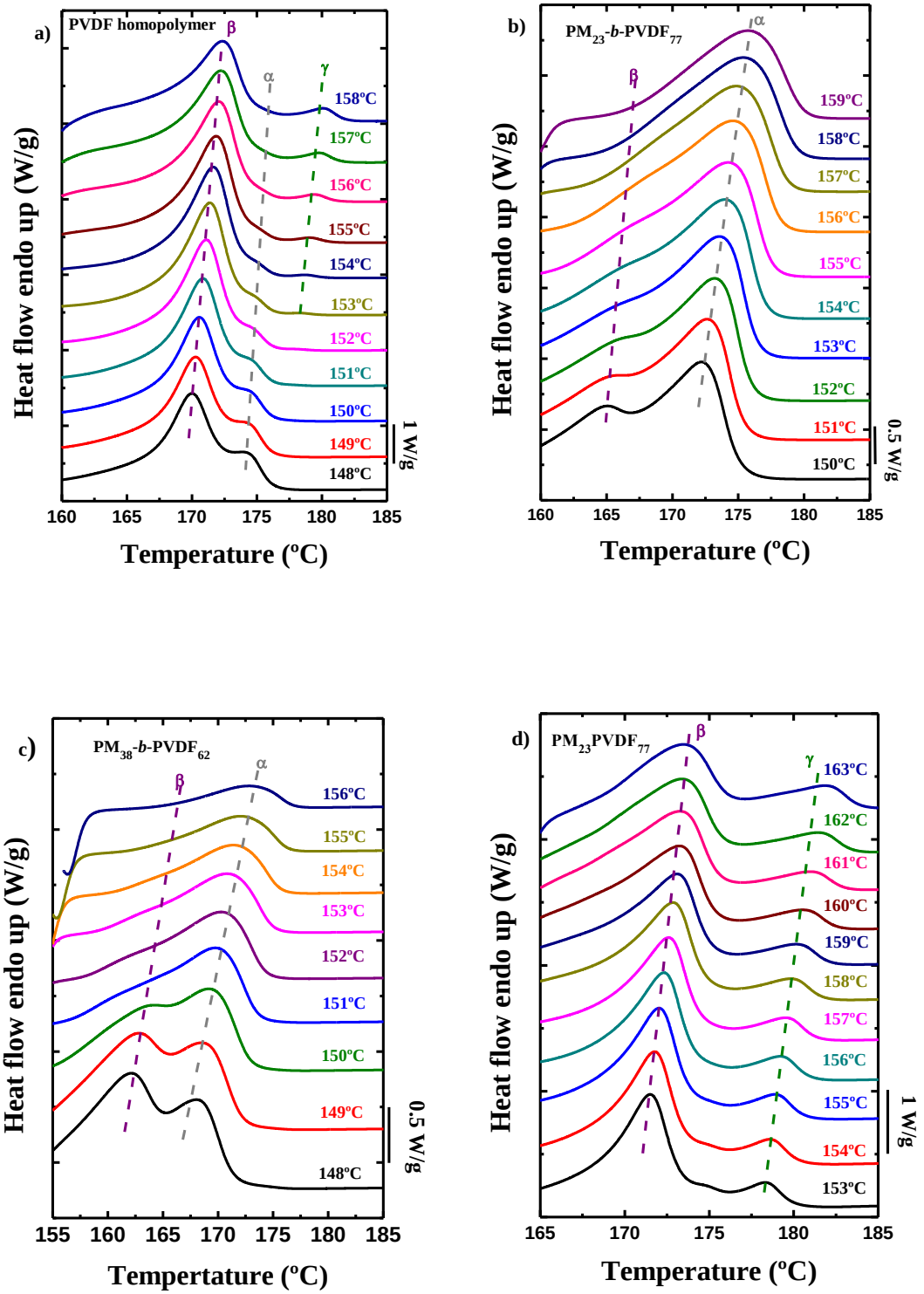
a)
PVDF homopolymer
β
α
γ
158°C
157°C
156°C
155°C
154°C
153°C
152°C
151°C
150°C
149°C
148°C
1 W/g
Heat flow endo up (W/g)
160 165 170 175 180 185
Temperature (°C)
b)
PM23-b-PVDF77
α
β
159°C
158°C
157°C
156°C
155°C
154°C
153°C
152°C
151°C
150°C
0.5 W/g
Heat flow endo up (W/g)
160 165 170 175 180 185
Temperature (°C)
c)
PM38-b-PVDF62
α
β
156°C
155°C
154°C
153°C
152°C
151°C
150°C
149°C
148°C
0.5 W/g
Heat flow endo up (W/g)
155 160 165 170 175 180 185
Tempertature (°C)
d)
PM23PVDF77
β
γ
163°C
162°C
161°C
160°C
159°C
158°C
157°C
156°C
155°C
154°C
153°C
1 W/g
Heat flow endo up (W/g)
165 170 175 180 185
Temperature (°C)

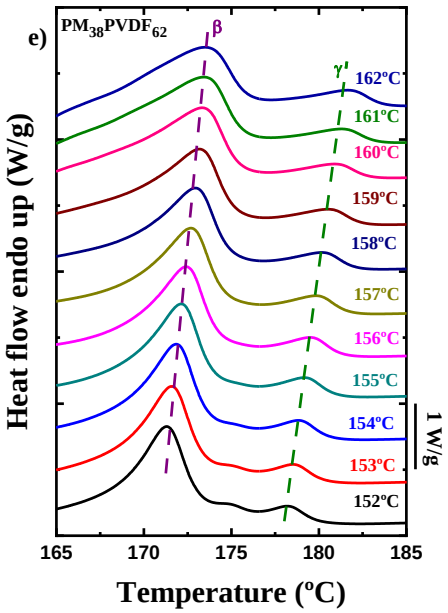

Figure 5. 18. DSC PVDF melting curves after the isothermal crystallization at different temperatures of a) PVDF homopolymer, b) PM_{23}-*b*-$PVDF_{77}$, c) PM_{38}-*b*-$PVDF_{62}$, d) $PM_{23}PVDF_{77}$, and e) $PM_{38}PVDF_{62}$ samples.

5.4 Conclusions

The complex crystallization of PVDF was found to depend on the nature of its chemical environment. We found significant differences in crystallization and polymorphic structure depending on whether the PVDF was a homopolymer (the homopolymer of the diblock copolymers), present as a block in the studied diblock copolymers, and present as a phase in the blends. The crystallization conditions were also found to dramatically affect the number and amount of the polymorphic crystalline phases produced.

DSC, PLOM, and TEM results clearly indicated that the blends prepared here are immiscible and phase segregate. On the other hand, the linear diblock copolymers crystallize from a mixed melt or very weakly segregated melt according to SAXS, TEM, and PLOM.

We were able to clearly identify the different crystalline phases formed by the PVDF component in the different samples examined (i.e., α, β, and γ phases) by DSC, FTIR, and WAXS. Their number and content varied depending on sample composition, cooling rate employed, or isothermal crystallization temperature used during isothermal crystallization tests.

The BDS results indicated that the PVDF block in the copolymers has lower T_g values than the homopolymer, which was in line with the faster chain dynamics observed in them. The spherulitic growth, nucleation, and overall crystallization rates were determined, and different values were obtained depending on the sample. This is not surprising considering that the melting after isothermal crystallization revealed that the polymorphic structure of each sample varied during isothermal crystallization.

5.5 References

1. Imai, S.; Hirai, Y.; Nagao, C.; Sawamoto, M.; Terashima, T., Programmed Self-Assembly Systems of Amphiphilic Random Copolymers into Size-Controlled and Thermoresponsive Micelles in Water. *Macromolecules* **2018,** 51, (2), 398-409.

2. Imai, S.; Takenaka, M.; Sawamoto, M.; Terashima, T., Self-Sorting of Amphiphilic Copolymers for Self-Assembled Materials in Water: Polymers Can Recognize Themselves. *Journal of the American Chemical Society* **2019,** 141, (1), 511-519.

3. Jiang, Z.; Liu, H.; He, H.; Ribbe, A. E.; Thayumanavan, S., Blended Assemblies of Amphiphilic Random and Block Copolymers for Tunable Encapsulation and Release of Hydrophobic Guest Molecules. *Macromolecules* **2020,** 53, (7), 2713-2723.

4. Cho, J., Analysis of Phase Separation in Compressible Polymer Blends and Block Copolymers. *Macromolecules* **2000,** 33, (6), 2228-2241.

5. Leibler, L., Theory of microphase separation in block copolymers. *Macromolecules* **1980,** 13, (6), 1602-1617.

6. Zhang, J.; Kremer, K.; Michels, J. J.; Daoulas, K. C., Exploring Disordered Morphologies of Blends and Block Copolymers for Light-Emitting Diodes with Mesoscopic Simulations. *Macromolecules* **2020,** 53, (2), 523-538.

7. Zapsas, G.; Patil, Y.; Bilalis, P.; Gnanou, Y.; Hadjichristidis, N., Poly(vinylidene fluoride)/Polymethylene-Based Block Copolymers and Terpolymers. *Macromolecules* **2019,** 52, (5), 1976-1984.

8. Lorenzo, A. T.; Arnal, M. L.; Albuerne, J.; Müller, A. J., DSC isothermal polymer crystallization kinetics measurements and the use of the Avrami equation to fit the data: Guidelines to avoid common problems. *Polymer Testing* **2007,** 26, (2), 222-231.

9. Hiemenz, P. C. L., T.P., Polymer chemistry. *CRC Press* **2007,** 2nd edition.

10. Schneider, C. A.; Rasband, W. S.; Eliceiri, K. W., NIH Image to ImageJ: 25 years of image analysis. *Nature Methods* **2012,** 9, (7), 671-675.

11. Hamley, I. W.; Castelletto, V.; Castillo, R. V.; Müller, A. J.; Martin, C. M.; Pollet, E.; Dubois, P., Crystallization in Poly(l-lactide)-b-poly(ε-caprolactone) Double Crystalline Diblock Copolymers: A Study Using X-ray Scattering, Differential Scanning Calorimetry, and Polarized Optical Microscopy. *Macromolecules* **2005,** 38, (2), 463-472.

12. Castillo, R. V.; Müller, A. J., Crystallization and morphology of biodegradable or biostable single and double crystalline block copolymers. *Progress in Polymer Science* **2009,** 34, (6), 516-560.

13. Bartczak, Z.; Galeski, A.; Krasnikova, N. P., Primary nucleation and spherulite growth rate in isotactic polypropylene-polystyrene blends. *Polymer* **1987,** 28, (10), 1627-1634.

14. Su, Z.; Dong, M.; Guo, Z.; Yu, J., Study of Polystyrene and Acrylonitrile−Styrene Copolymer as Special β-Nucleating Agents To Induce the Crystallization of Isotactic Polypropylene. *Macromolecules* **2007,** 40, (12), 4217-4224.

15. Yang, B.; Ni, H.; Huang, J.; Luo, Y., Effects of Poly(vinyl butyral) as a Macromolecular Nucleating Agent on the Nonisothermal Crystallization and Mechanical Properties of Biodegradable Poly(butylene succinate). *Macromolecules* **2014,** 47, (1), 284-296.

16. Roerdink, E.; Challa, G., Influence of tacticity of poly(methyl methacrylate) on the compatibility with poly(vinylidene fluoride). *Polymer* **1978,** 19, (2), 173-178.

17. Li, M.; Stingelin, N.; Michels, J. J.; Spijkman, M.-J.; Asadi, K.; Feldman, K.; Blom, P. W. M.; de Leeuw, D. M., Ferroelectric Phase Diagram of PVDF:PMMA. *Macromolecules* **2012,** 45, (18), 7477-7485.

18. Bormashenko, Y.; Pogreb, R.; Stanevsky, O.; Bormashenko, E., Vibrational spectrum of PVDF and its interpretation. *Polymer Testing* **2004,** 23, (7), 791-796.

19. Gradys, A.; Sajkiewicz, P.; Adamovsky, S.; Minakov, A.; Schick, C., Crystallization of poly(vinylidene fluoride) during ultra-fast cooling. *Thermochimica Acta* **2007,** 461, (1), 153-157.

20. Soin, N.; Boyer, D.; Prashanthi, K.; Sharma, S.; Narasimulu, A. A.; Luo, J.; Shah, T. H.; Siores, E.; Thundat, T., Exclusive self-aligned β-phase PVDF films with abnormal piezoelectric coefficient prepared via phase inversion. *Chemical Communications* **2015,** 51, (39), 8257-8260.

21. Gregorio, R.; CapitãO, R. C., Morphology and phase transition of high melt temperature crystallized poly(vinylidene fluoride). *Journal of Materials Science* **2000,** 35, (2), 299-306.

22. Gulmine, J. V.; Janissek, P. R.; Heise, H. M.; Akcelrud, L., Polyethylene characterization by FTIR. *Polymer Testing* **2002,** 21, (5), 557-563.

23. Ince-Gunduz, B. S.; Alpern, R.; Amare, D.; Crawford, J.; Dolan, B.; Jones, S.; Kobylarz, R.; Reveley, M.; Cebe, P., Impact of nanosilicates on poly(vinylidene fluoride)

crystal polymorphism: Part 1. Melt-crystallization at high supercooling. *Polymer* **2010,** 51, (6), 1485-1493.

24. Lanceros-Méndez, S.; Mano, J. F.; Costa, A. M.; Schmidt, V. H., FTIR AND DSC STUDIES OF MECHANICALLY DEFORMED β-PVDF FILMS. *Journal of Macromolecular Science, Part B* **2001,** 40, (3-4), 517-527.

25. Boccaccio, T.; Bottino, A.; Capannelli, G.; Piaggio, P., Characterization of PVDF membranes by vibrational spectroscopy. *Journal of Membrane Science* **2002,** 210, (2), 315-329.

26. Tasumi, M.; Shimanouchi, T., Crystal Vibrations and Intermolecular Forces of Polymethylene Crystals. *The Journal of Chemical Physics* **1965,** 43, (4), 1245-1258.

27. Hughes, D. J.; Mahendrasingam, A.; Oatway, W. B.; Heeley, E. L.; Martin, C.; Fuller, W., A simultaneous SAXS/WAXS and stress-strain study of polyethylene deformation at high strain rates. *Polymer* **1997,** 38, (26), 6427-6430.

28. Lv, F.; Wan, C.; Chen, X.; Meng, L.; Chen, X.; Wang, D.; Li, L., Morphology diagram of PE gel films in wide range temperature-strain space: An in situ SAXS and WAXS study. *Journal of Polymer Science Part B: Polymer Physics* **2019,** 57, (12), 748-757.

29. Bartczak, Z.; Argon, A. S.; Cohen, R. E.; Kowalewski, T., The morphology and orientation of polyethylene in films of sub-micron thickness crystallized in contact with calcite and rubber substrates. *Polymer* **1999,** 40, (9), 2367-2380.

30. Bachmann, M. A.; Lando, J. B., A reexamination of the crystal structure of phase II of poly(vinylidene fluoride). *Macromolecules* **1981,** 14, (1), 40-46.

31. Newman, B. A.; Yoon, C. H.; Pae, K. D.; Scheinbeim, J. I., Piezoelectric activity and field-induced crystal structure transitions in poled poly(vinylidene fluoride) films. *Journal of Applied Physics* **1979,** 50, (10), 6095-6100.

32. Doll, W. W.; Lando, J. B., The polymorphism of poly(vinylidene fluoride) V. The effect of hydrostatic pressure on the melting behavior of copolymers of vinylidene fluoride. *Journal of Macromolecular Science, Part B* **1970,** 4, (4), 897-913.

33. Geiss, D.; Hofmann, D., Investigation of structural changes in PVDF by modified X-ray texture methods. *IEEE Transactions on Electrical Insulation* **1989,** 24, (6), 1177-1182.

34. Hasegawa, R.; Takahashi, Y.; Chatani, Y.; Tadokoro, H., Crystal Structures of Three Crystalline Forms of Poly(vinylidene fluoride). *Polymer Journal* **1972,** 3, (5), 600-610.

35. Lando, J. B.; Olf, H. G.; Peterlin, A., Nuclear magnetic resonance and x-ray determination of the structure of poly(vinylidene fluoride). *Journal of Polymer Science Part A-1: Polymer Chemistry* **1966,** 4, (4), 941-951.

36. Davis, G. T.; McKinney, J. E.; Broadhurst, M. G.; Roth, S. C., Electric-field-induced phase changes in poly(vinylidene fluoride). *Journal of Applied Physics* **1978,** 49, (10), 4998-5002.

37. Sy, J. W.; Mijovic, J., Reorientational Dynamics of Poly(vinylidene fluoride)/Poly(methyl methacrylate) Blends by Broad-Band Dielectric Relaxation Spectroscopy. *Macromolecules* **2000,** 33, (3), 933-946.

38. Linares, A.; Nogales, A.; Rueda, D. R.; Ezquerra, T. A., Molecular dynamics in PVDF/PVA blends as revealed by dielectric loss spectroscopy. *Journal of Polymer Science Part B: Polymer Physics* **2007,** 45, (13), 1653-1661.

39. Zhao, X.; Jiang, X.; Peng, G.; Liu, W.; Liu, K.; Zhan, Z., Investigation of the dielectric relaxation, conductivity and energy storage properties for biaxially oriented poly(vinylidene fluoride-hexafluoropropylene)/poly(methyl methacrylate) composite films by dielectric relaxation spectroscopy. *Journal of Materials Science: Materials in Electronics* **2016,** 27, (10), 10993-11002.

40. Nieto Simavilla, D.; Abate, A. A.; Liu, J.; Geerts, Y. H.; Losada-Peréz, P.; Napolitano, S., 1D-Confinement Inhibits the Anomaly in Secondary Relaxation of a Fluorinated Polymer. *ACS Macro Letters* **2021,** 10, (5), 649-653.

41. Hilczer, B.; Kułek, J.; Markiewicz, E.; Kosec, M.; Malič, B., Dielectric relaxation in ferroelectric PZT–PVDF nanocomposites. *Journal of Non-Crystalline Solids* **2002,** 305, (1), 167-173.

42. Martín, J.; Iturrospe, A.; Cavallaro, A.; Arbe, A.; Stingelin, N.; Ezquerra, T. A.; Mijangos, C.; Nogales, A., Relaxations and Relaxor-Ferroelectric-Like Response of Nanotubularly Confined Poly(vinylidene fluoride). *Chemistry of Materials* **2017,** 29, (8), 3515-3525.

43. Linares, A.; Nogales, A.; Sanz, A.; Ezquerra, T. A.; Pieruccini, M., Restricted dynamics in oriented semicrystalline polymers: Poly(vinilydene fluoride). *Physical Review E* **2010,** 82, (3), 031802.

44. Martínez-Tong, D. E.; Soccio, M.; Sanz, A.; García, C.; Ezquerra, T. A.; Nogales, A., Ferroelectricity and molecular dynamics of poly(vinylidenefluoride-trifluoroethylene) nanoparticles. *Polymer* **2015,** 56, 428-434.

45. Schönhals, A.; Kremer, F., Analysis of Dielectric Spectra. In *Broadband Dielectric Spectroscopy*, Kremer, F.; Schönhals, A., Eds. Springer Berlin Heidelberg: Berlin, Heidelberg, 2003; pp 59-98.

46. Angell, C. A., Formation of Glasses from Liquids and Biopolymers. *Science* **1995,** 267, (5206), 1924-1935.

47. Angell, C. A., Why C1 = 16–17 in the WLF equation is physical—and the fragility of polymers. *Polymer* **1997,** 38, (26), 6261-6266.

48. Nakagawa, K.; Ishida, Y., Annealing effects in poly(vinylidene fluoride) as revealed by specific volume measurements, differential scanning calorimetry, and electron microscopy. *Journal of Polymer Science: Polymer Physics Edition* **1973,** 11, (11), 2153-2171.

49. Grieveson, B. M., The glass transition temperature in homologous series of linear polymers. *Polymer* **1960,** 1, 499-512.

50. Arandia, I.; Mugica, A.; Zubitur, M.; Mincheva, R.; Dubois, P.; Müller, A. J.; Alegría, A., The Complex Amorphous Phase in Poly(butylene succinate-ran-butylene azelate) Isodimorphic Copolyesters. *Macromolecules* **2017,** 50, (4), 1569-1578.

51. Lorenzo, A. T.; Müller, A. J., Estimation of the nucleation and crystal growth contributions to the overall crystallization energy barrier. *Journal of Polymer Science Part B: Polymer Physics* **2008,** 46, (14), 1478-1487.

52. Hoffman, J. D.; Lauritzen, J. I., Jr., Crystallization of Bulk Polymers With Chain Folding: Theory of Growth of Lamellar Spherulites. *Journal of research of the National Bureau of Standards. Section A, Physics and chemistry* **1961,** 65A, (4), 297-336.

53. Reiter, G.; Strobl, G. R., *Progress in understanding of polymer crystallization*. Springer: 2007; Vol. 714.

54. Avrami, M., Granulation, Phase Change, and Microstructure Kinetics of Phase Change. III. *The Journal of Chemical Physics* **1941,** 9, (2), 177-184.

55. Avrami, M., Kinetics of Phase Change. II Transformation-Time Relations for Random Distribution of Nuclei. *The Journal of Chemical Physics* **1940,** 8, (2), 212-224.

56. Hoffman, J. D.; Weeks, J. J., Melting process and the equilibrium melting temperature of polychlorotrifluoroethylene. *J. Res. Natl. Bur. Stand., Sect. A* **1962,** 66, (1), 13-28.

57. Marand, H.; Xu, J.; Srinivas, S., Determination of the Equilibrium Melting Temperature of Polymer Crystals: Linear and Nonlinear Hoffman−Weeks Extrapolations. *Macromolecules* **1998,** 31, (23), 8219-8229.

58. Kalivianakis, P.; Jungnickel, B. J., Crystallization-induced composition inhomogeneities in PVDF/PMMA blends. *Journal of Polymer Science Part B: Polymer Physics* **1998,** 36, (16), 2923-2930.

59. Xiao, Q.; Wang, X.; Li, W.; Li, Z.; Zhang, T.; Zhang, H., Macroporous polymer electrolytes based on PVDF/PEO-b-PMMA block copolymer blends for rechargeable lithium ion battery. *Journal of Membrane Science* **2009,** 334, (1), 117-122.

Chapter 6

Morphology and crystallization of PVDF-based PM-b-PS-b-PVDF triblock terpolymers and their precursors

---

6.1 Introduction

In the present work, we have studied the crystallization of the PVDF block in a linear PM-*b*-PS-*b*-PVDF triblock terpolymer (where PM is polymethylene and PS is polystyrene). In a previous chapter, the PM-*b*-PVDF block copolymers were studied. In that case, the PVDF crystallizes in two different phases during non-isothermal experiments, and depending on the composition, the β-phase was promoted. Moreover, the cooling rate also played an important role during the experiments. In that case, when the PVDF was crystallized isothermally, the paraelectric α-phase was the main phase at high isothermal crystallization temperatures. In this chapter, an amorphous block, PS, is added and it is important to study how the presence of this block affects the crystallization of the previously studied PM-*b*-PVDF copolymers. The samples have been studied under isothermal and non-isothermal conditions changing the cooling rates to observe how the crystalline phases are affected.

With the aim to determine which phases are crystallizing in the PVDF block, different techniques are employed, such as Fourier Transform Infrared Spectroscopy (FTIR) and Wide Angle X-ray Scattering (WAXS). Differential Scanning Calorimetry (DSC) is used to measure the overall crystallization process in both non-isothermal and isothermal conditions. Polarized Light Optical Microscopy (PLOM) is employed to observe the morphology of the terpolymers during an isothermal crystallization process. Small Angle X-ray Scattering (SAXS) technique is applied to study the miscibility of the system.

6.2 Materials and methods

6.2.1 Materials

Two linear PM-*b*-PS-*b*-PVDF triblock terpolymers with different PVDF M_n values, a PM-*b*-PS-Br precursor sample, and a neat PVDF sample with a M_n value similar to the triblock terpolymer samples are studied. The synthesis of all the samples has already been published in previous work by Hadjichristidis *et al*.[1] Briefly, the synthesis of the PM-*b*-PS-Br precursor was made by employing an atom transfer radical polymerization (ATRP), dissolving a PM-Br macroinitiator in toluene and then the styrene was added, the mixture was heated and left during 18 hours and then purified. The triblock samples were synthesized in an autoclave, employing the precursor, one initiator previously dissolved, and VDF gas, a yellow liquid was obtained and concentrated by rotary evaporation. Finally, the material was precipitated in hexane. The M_n values of the samples and the M_n value of the respective blocks are listed in Table 6.1. The subscripts indicate the composition in wt% determined by ^{1}HNMR.

Table 6. 1. Number average molecular weights for the indicated samples.

Samples	M_n (PM block) (g/mol)	M_n (PS block) (g/mol)	M_n (PVDF block) (g/mol)	M_n total (g/mol)
PM_{34}-*b*-PS_{66}-Br	6.6K	13.0K	-	19.6K
PVDF homopolymer	-	-	35.0K	35.0K
PM_{13}-*b*-PS_{27}-*b*-$PVDF_{60}$	6.6K	13.0K	29.0K	48.6K
PM_{11}-*b*-PS_{22}-*b*-$PVDF_{67}$	6.6K	13.0K	40.0K	59.6K

6.2.2 Methods

a) Differential Scanning Calorimetry (DSC)

All the DSC experiments were performed with a Perkin Elmer DSC 8000 equipment and an Intracooler II cooling device. The calibration of the equipment was carried out using indium and tin standards.

For the non-isothermal experiments, the samples were heated up to 200 ºC, and held 3 minutes at this temperature to erase the thermal history. After this step, the samples were cooled at different cooling rates (60, 20, 5, and 1 ºC/min) from the melt to room temperature. Finally, the samples were heated to the molten state at a heating rate of 20 ºC/min.

The isothermal crystallization protocol employed was the same recommended by Müller *et al*.[2, 3] It is important first, to investigate the minimum crystallization temperature ($T_{c,min}$). First, the samples were heated to 200 ºC and held 3 min at that temperature. Then, the samples were cooled at 60 ºC/min to a selected crystallization temperature (T_c). Once this temperature is reached, the sample is immediately heated at 20 ºC/min to the molten state. No melting peak should be observed in this heating run, if the sample did not crystallize during cooling. The process is repeated for different T_c values. The T_{cmin} is the minimum crystallization temperature at which the sample does not crystallize during cooling.

During the isothermal crystallization process at a previously selected T_c the sample is held at that temperature for 40 minutes, as during this time the sample crystallizes until saturation. After the isothermal crystallization process, the sample is heated at 20 ºC/min to the molten state.

The self-nucleation (SN) protocol was carried out according to Müller *et al*.[4, 5] During the SN experiments, all the scans were at the same rate, 20 ºC/min. First, the samples were heated up to 200 ºC and held for 3 minutes at that temperature, after it, the samples were cooled to a temperature below the T_c, to ensure the crystallization of the polymer (100 ºC in the case of the PVDF), and held 3 minutes at this T_c.

Then the samples were heated to a selected self-nucleation temperature (T_s) and maintained 5 minutes at this T_s. After this time, the samples were cooled again to 100 ºC (in the case of PVDF components) and held for 3 minutes at that temperature. During this cooling process, changes in the T_c of the polymer can be detected depending on the *Domain* where the polymer is crystallizing in. If the polymer is in *Domain I* (at high T_s values), no changes in T_c are detected as the polymer is in the melting *Domain*, where its thermal history is erased. On the other hand, if lower T_s values are used, the sample can be in *Domain II* or self-nucleation *Domain.* In this case, increases in T_c will be observed as self-nucleation significantly increases the nucleation density of the material. The last step was the heating scan to the molten state. This step is also important, as there is the possibility (at the lowest T_s values employed) of the appearance of the annealing peak in the polymer, which is indicative of a change to the self-nucleation and annealing *Domain* or *Domain III*.

The successive self-nucleation and annealing (SSA) experiment was performed following the recommendations of Müller *et al*.[6, 7] As it is explained in the SN protocol, in this case, also the rates employed for the scans are always 20 ºC/min, in both cooling and heating sweeps. As in the previous protocols, the first step was heating the samples to 200 ºC and holding them for 3 minutes at that temperature. The next step was cooling the samples to the same T_c chosen in the SN protocol (100 ºC in this work), and the samples were maintained 3 minutes at that temperature. Then the samples were heated to the ideal self-nucleation temperature (T_{si}) (previously determined by self-nucleation studies), where the samples were held for 5 minutes. This T_{si} is the lowest temperature within *Domain II*. After this step, the samples were cooled to 100 ºC and held for 3 minutes at that temperature. These steps were repeated employing increasingly lower T_s values (5 ºC at a time) less in each cycle than the previous one. After the last $T_{s,}$ the samples were heated to the molten state, in this process it is possible to observe all the fractions created during the SSA protocol. In this chapter, the T_{si} chosen for the SSA experiments was the T_{si} of the neat PVDF in order to compare all the samples between them.

b) Fourier Transform Infrared Spectroscopy (FTIR)

The samples were analysed with a Nicolet 6700 Fourier Transform Infrared Spectrometer equipped with an Attenuated Total Reflectance (ATR) Golden Gate MK II with a diamond crystal. Before the FTIR measurements, the samples were prepared in a Linkam hot-stage, they were first melted at 200 ºC for 3 minutes directly from the bulk and then cooled down at different cooling rates to room temperature (RT). In this case, the cooling rates chosen were 60, 5, and 1 ºC/min using liquid N_2 in the cooling process, and all the samples were analysed at RT after the cooling scan. For the isothermal measurements, the samples were heated to 200 ºC and maintained 3 minutes at this temperature, then the samples were cooled at 60 ºC/min to the chosen isothermal temperature and maintained 2 hours at that temperature. Finally, the samples were cooled to RT at 20 ºC/min and analysed with the FTIR equipment.

c) Polarized Light Optical Microscopy (PLOM)

An Olympus BX51 polarized light optical microscopy was employed in order to observe the crystallization of the samples. The microscope is linked to a Linkam hot-stage to control the temperature and the heating and cooling rate during the experiments, using liquid N_2 in the cooling process. The experiments were followed by an Olympus SC50 camera linked to the microscope that permits recording videos and taking micrographs. PVDF homopolymer samples were prepared by drop casting in a glass substrate; previously, the samples were dissolved in dimethylformamide (DMF) with a 4% of concentration and dried at RT. The triblock copolymers were observed by the microscope directly from the bulk sample.

d) Small and Wide Angle X-ray Scattering (SAXS/WAXS)

Block copolymer samples, and the PM_{34}-*b*-PS_{66}-Br precursor sample were characterized by employing Wide Angle X-ray Scattering (WAXS) and Small Angle X-

ray Scattering (SAXS). Both characterizations were performed at the ALBA Synchrotron in the beamline BL11-NCD. The samples were made of powder and introduced into glass capillaries for the measurements. To control the temperature and the rate of the thermal processes, a Linkam hot-stage was used, employing liquid nitrogen for cooling. The X-ray source had an energy of 12.4 keV (λ= 1.0 Å). The WAXS detector employed was a Rayonix LX255-HS with an active area of 230.4 x 76.8 mm. The distance between sample and detector was 15.5 mm, and the angle employed was 27.3º, with these characteristics, the pixel size was 44 μm^2. The detector for the SAXS experiments was a Pilatus 1M with an active area of 168.7 x 179.4 mm, a total number of pixels of 981 x 1043, the distance employed was 6463 mm, and the consequent pixel size was 172 μm^2. Non-isothermal experiments were carried out. First, the samples were heated at 200 ºC for 3 minutes, and then a cooling process at 20 ºC/min was applied to the samples to RT. After it, the samples were heated at 20 ºC/min.

6.3 Results and discussion

6.3.1 Study of the miscibility

The knowledge about the miscibility of the compounds when a system is composed of more than one component is crucial to understanding the material's final properties. One theoretical parameter that can estimate the miscibility between two compounds is the Flory interaction parameter (χ_{12}), and the following equation can estimate this parameter:

$$\chi_{12} = 0.34 + \frac{V_1}{RT}(\delta_1 - \delta_2)^2 \qquad \text{eq. 6.1}$$

where V_1 is the molar volume of the matrix component calculated through the molar mass of the repeating unit and the amorphous density, R is a constant whose value is 1.987 cal/mol K, T is the temperature selected to calculate the interaction parameter (in our case is 473 K, temperature that corresponds to the molten state) and δ_1 and δ_2 are the solubility parameters of each component.

In this chapter, we have applied this equation to predict the miscibility between the PS and the PM in the precursor sample described above. In a previous chapter, it was demonstrated that the PM and the PVDF were miscible between them in the block copolymer samples presented. Once the χ_{12} is obtained, the segregation strength can be calculated by multiplying the χ_{12} parameter by the degree of polymerization, N. If the value obtained is below 10, it means that the polymers are miscible, when the calculated value is between 10 and 30, there is a weak segregation. There is a medium segregation if the value is between 30 and 50, and there is strong segregation in the case of values higher than 50. In our case, the estimated value for the segregation strength in the PM-*b*-PS system at 200 ºC is 343, which means that there is strong segregation between these two polymers in the molten state.

Apart from the Flory interaction parameter estimation, SAXS experiments were carried out for the triblock terpolymers and the PM_{34}-*b*-PS_{66}-Br precursor sample to

study their phase behavior during a heating scan at 20 ºC/min. Figure 6.1 shows the SAXS results at different temperatures for the three samples studied. All the samples show a sharp peak at around a *q*-value of 0.3 nm^{-1} at 200 ºC, where the samples are completely melted. This means microphase segregation is present in the melt. In this case, in the PM_{34}-*b*-PS_{66}-Br precursor, this peak also appears, so the micorphase segregation in the samples corresponds to PM and PS phases, as we have estimated previously by the Flory interaction parameter. In the case of the triblock terpolymer samples, the phase segregation between PM and PS, also triggers phase segregation in the melt.

It is interesting to note that in the case of the diblock precursor, the SAXS reflection does not shift significantly between the molten state and the semi-crystalline state, probably indicating that the copolymer is strongly segregated and that the crystallization must occur within the phase segregated microdomains. In this case there are no higher order reflexions but the composition would be consistent with lamellar microdomains.

In the case of the triblock terpolymers, there is a large change in the SAXS pattern upon melting the PM and then the PVDF block, that probably indicates that the phase structure in the melt is different from that of the semi-crystalline state. It is rather peculiar that the peak corresponding to the phase segregation state in the melt appears exactly at the same value of that of the diblock precursor. In fact, even at room temperature, we have remnants of the same SAXS reflection coexisting with a higher *q*-value peak that obviously corresponds to the PVDF lamellar long period. These results are compatible with a blend of PM_{34}-*b*-PS_{66}-Br precursor and PVDF instead of a triblock terpolymer. It is possible that the sample has experienced degradation and a cleavage of the PVDF block. Evidences to be presented below by PLOM, also indicate that macro-phase segregation is observed in the triblock terpolymer sample. In a triblock terpolymer, macro-phase segregation at the scale of a

micron is impossible. Hence, the only explanation is that the original triblock terpolymer samples have been degraded and that we are dealing instead with a PM_{34}-*b*-PS_{66}-Br/PVDF blend.

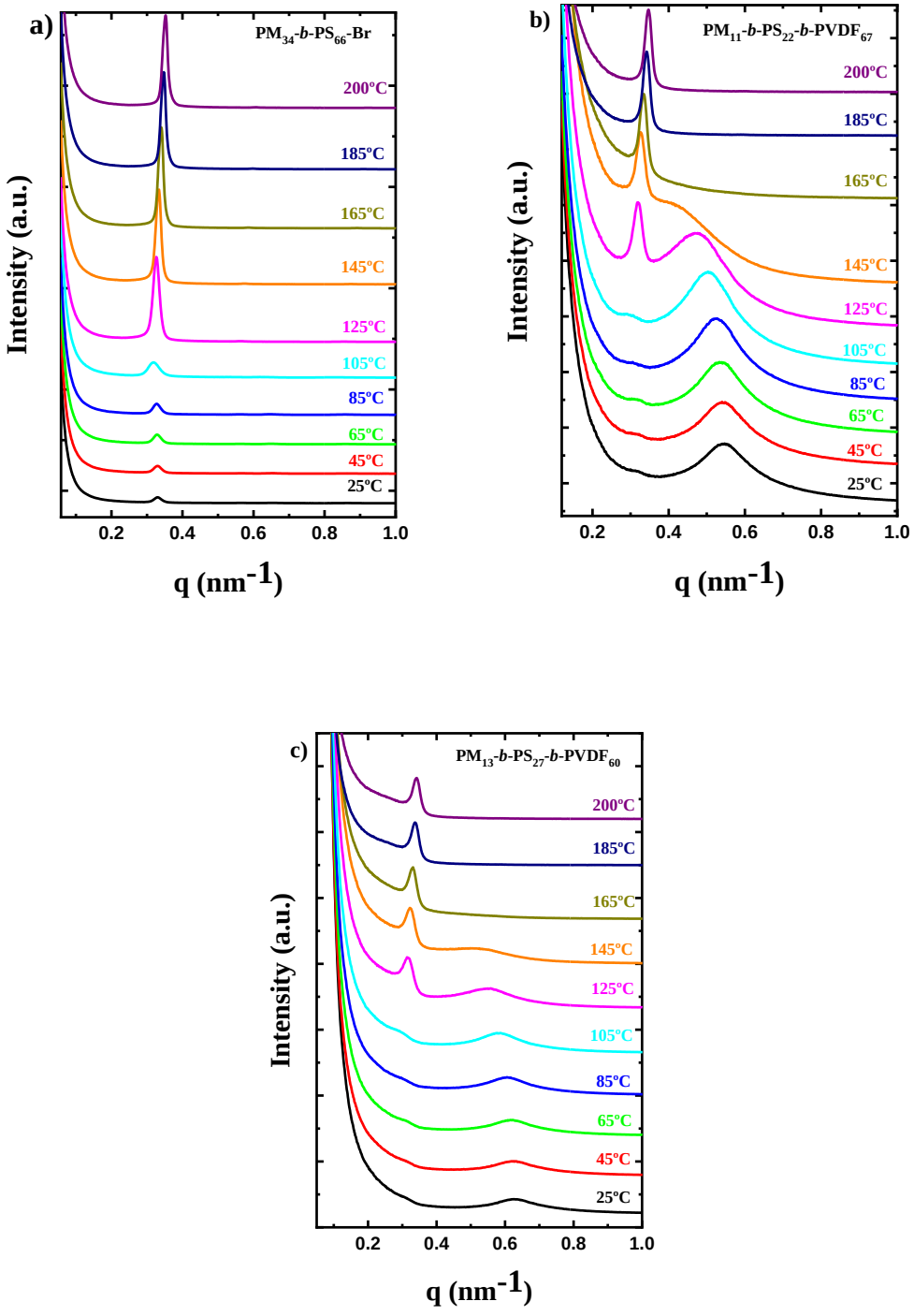

Figure 6. 1. SAXS diffractograms at different temperatures during a heating scan at 20 ºC/min for a) PM_{34}-*b*-PS_{66}-Br precursor, b) PM_{11}-*b*-PS_{22}-*b*-$PVDF_{67}$ and c) PM_{13}-*b*-PS_{27}-*b*-$PVDF_{60}$.

6.3.2 Non-isothermal crystallization

For the study of the crystallization of the triblock copolymers and the precursors under non-isothermal conditions, a cooling from the melt and a posterior heating scans, both at 20 ºC/min, were performed by DSC. Figure 6.2 shows both processes, heating and cooling scans. The block of PS remains always in the amorphous state, therefore any crystallization or melting peak observed in this figure does not correspond to this block. In the cooling sweep (Figure 6.2a), the triblock copolymers show two crystallization peaks, the peak at low temperatures that corresponds to the crystallization of the PM block and the peak at high temperatures that corresponds to the PVDF block. The crystallization peak of the PM block appears at lower temperatures compared to the PM block observed in the diblock precursor (PM_{34}-*b*-PS_{66}-Br). The crystallization peak of the PVDF appears at higher temperatures when it crystallizes in the triblock sample compared to when it crystallizes as a homopolymer, a fact that may be related to a change in nucleation.

The DSC heating curves are plotted in Figure 6.2b. At low temperatures the melting process of the PM block crystals appears and that of the PVDF block crystals at high temperatures. In the melting process of the PVDF block crystals, at least two melting peaks are observed in all cases, suggesting some polymorphism in the samples. These melting peaks correspond to two different crystalline phases. The only difference between the samples is that depending on the M_n value used, the peak size changes, and in consequence, the proportion of one crystalline phase or the other also changes.

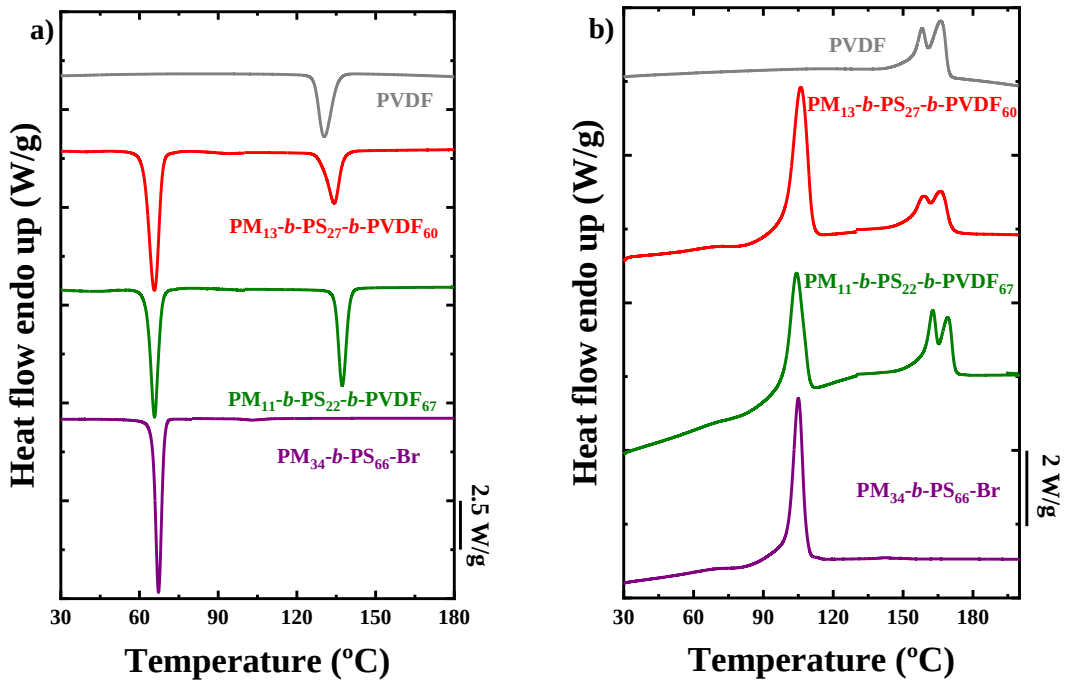

Figure 6. 2. DSC scans of the triblock copolymer samples, the PM_{34}-*b*-PS_{66}-Br precursor and the neat PVDF. a) Cooling process from the melt at 20 ºC/min and b) subsequent heating at 20 ºC/min.

The cooling process from the melt at 20 ºC/min was also studied by employing the PLOM technique. PLOM images are shown in Figure 6.3, Figure 6.3e shows how neat PVDF crystallizes in spherulites, as it was expected.[8-10] In the case of the triblock terpolymer samples, it should be noted that two phases are present. One of the phases in PVDF, as indicated by the spherulites observed and the second phase is made up of fine droplets. These droplets are most likely composed of PM_{34}-*b*-PS_{66}-Br that has been cleaved from the original triblock terpolymer. This confirms our hypothesis that the triblock terpolymers have degraded and are now PM_{34}-*b*-PS_{66}-Br/PVDF blends.

In the case of the PM_{34}-*b*-PS_{66}-Br precursor, Figure 6.3c shows the molten state of the sample, with the whole background in a purple colour. When this sample

reaches the temperature of 60 ºC (Figure 6.3d) a change in the colour of the background happens, corresponding to the PM block crystallization. The crystallization of the polymethylene microdomains within a phase segregated copolymer cannot be observed with PLOM because of their size is well below 0.5 microns. However, a change in the average birefringence value could be expected.

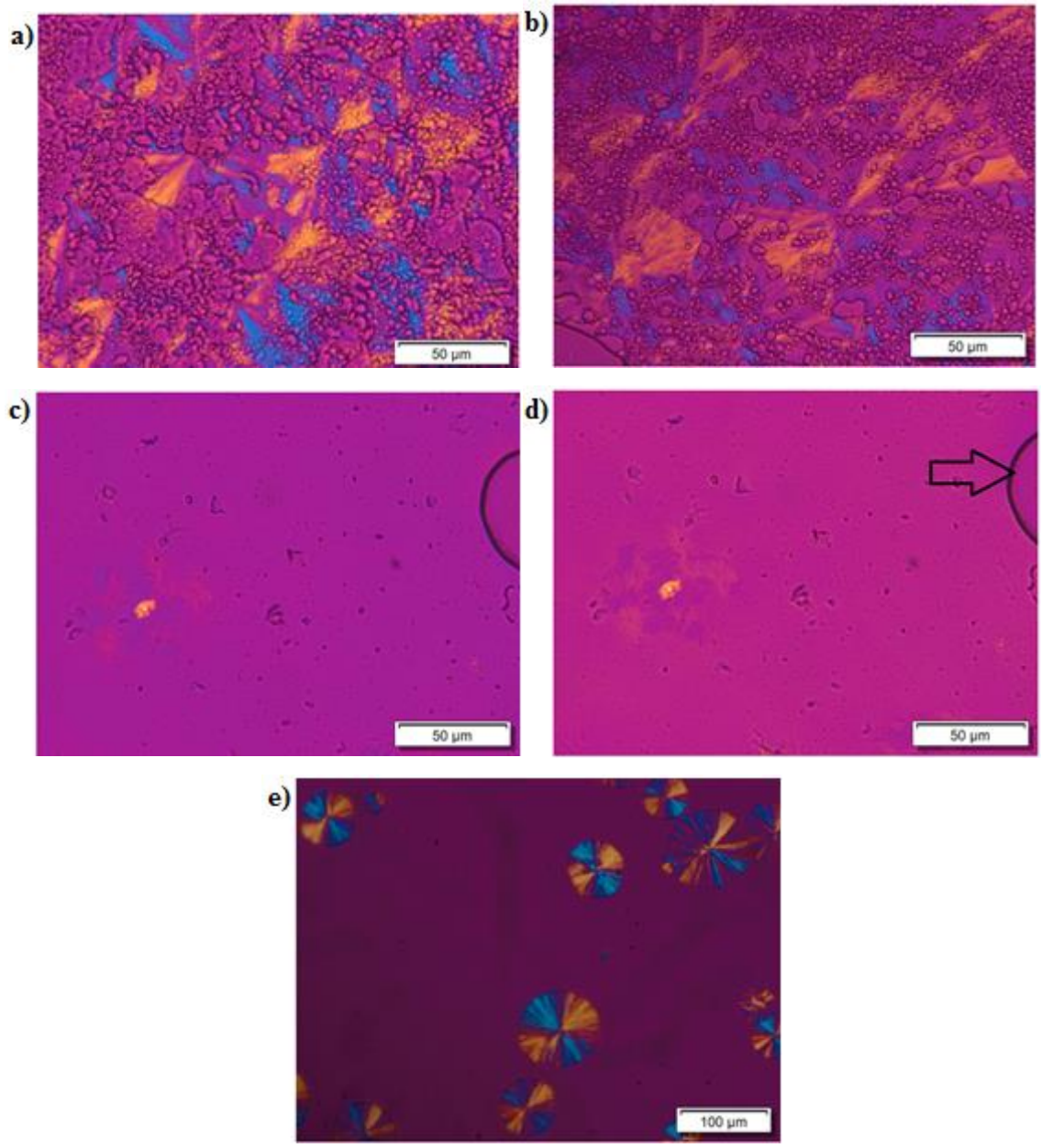

Figure 6. 3. PLOM images taken during a cooling at 20 ºC/min of a) PM_{13}-*b*-PS_{27}-*b*-$PVDF_{60}$ at 120 ºC, b) PM_{11}-*b*-PS_{22}-*b*-$PVDF_{67}$ at 120 ºC, c) PM_{34}-*b*-PS_{66}-Br at 200 ºC, d) PM_{34}-*b*-PS_{66}-Br at 60 ºC and e) neat PVDF at 120 ºC.

In the case of the crystallization of the PVDF from the molten state, the polymorphism of the PVDF can be related to the cooling rate employed.[11, 12] In this chapter, to see the differences with the cooling rate employed before (20 ºC/min) the samples

have been studied at cooling rates of 60, 5 and 1 ºC/min. Figure 6.4 shows the heating curves for the neat PVDF and two copolymer samples in the range of temperatures that correspond to the melting peak of the PVDF, after a cooling process at different rates, as explained above. For all the samples, the behaviour observed is quite similar, independently of the sample studied. When the cooling rate is high (60 ºC/min), the melting peak observed at high temperatures is larger than the melting peak observed at low temperatures. However, when the cooling rate decreases, the size of the high-temperature peak decreases and there is a promotion of the peak at low temperatures. When the cooling rate employed is at 1 ºC/min, the peak at high temperatures almost disappears, and only the peak at low temperatures remains. If this peak corresponds to the melting peak of the β-phase and the other peak belongs to the α-phase, the results show that if we use the lowest cooling rate studied (1 ºC/min), this rate promotes the β-phase in this PVDF based systems. This behaviour observed here is not usual because it is completely opposite to that one observed before for commercial PVDF, which always crystallizes in the α-phase independently of the cooling rate employed when the crystallization occurs from the melt.[13, 14] Moreover, some works report that high cooling rates promote the β-phase.[15] However, in a following chapter, we also report this behaviour in PVDF based miktoarm star block copolymers. In addition, we can observe a third peak at higher temperatures in the PM_{11}-*b*-PS_{22}-*b*-$PVDF_{67}$ sample (Figure 6.4c) when the cooling rate applied was 1 ºC/min. This third peak could be either a third crystalline phase, which it could correspond to the γ-phase, or a reordering of the crystals during the heating process. This third peak is not observable in the rest of the samples, so the M_n of the PVDF block can play an important role during the crystallization process of the samples. All the thermodynamic data extracted from the DSC experiments are listed in Table 6.2, and the values of the melting and cooling enthalpies have been normalized by the weight fraction of the PVDF component.

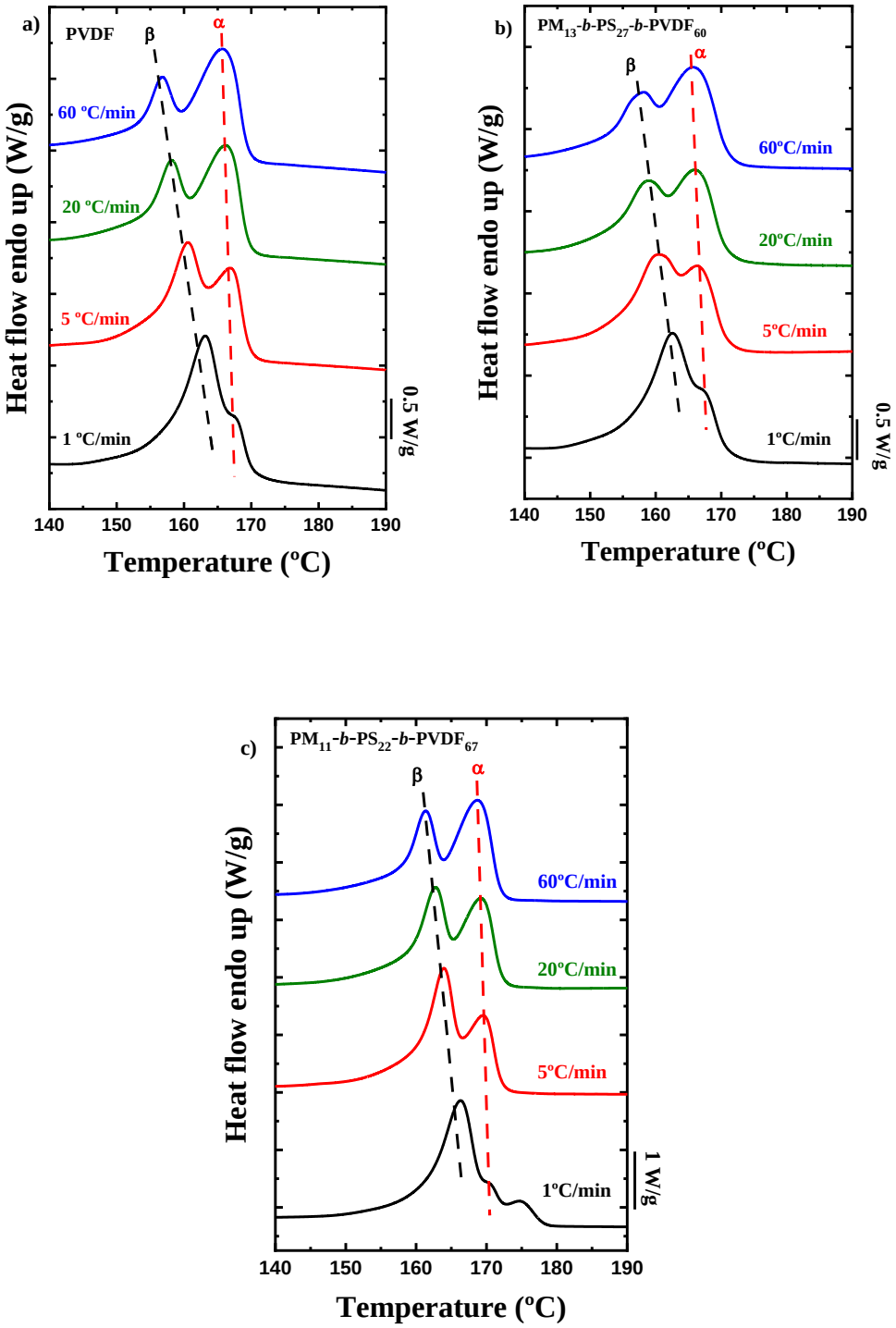

Figure 6. 4. Comparison of the DSC heating curve in the range of the melting point of the PVDF after a cooling scan at 60, 20, 5 and 1 °C/min for a) neat PVDF, b) PM_{13}-*b*-PS_{27}-*b*-$PVDF_{60}$ and c) PM_{11}-*b*-PS_{22}-*b*-$PVDF_{67}$.

Table 6. 2. Thermodynamic data for the PVDF block obtained by DSC at different cooling rates.

Sample	Cooling rate (ºC/min)	$T_{m,\beta}$ (ºC)	$T_{m,\alpha}$ (ºC)	$T_{m,\gamma}$ (ºC)	T_c (ºC)	ΔH_m (J/g)	ΔH_c (J/g)
PVDF homopolymer	1	163.1	167.5	-	143.3	52.8	50.1
	5	160.6	166.8	-	138.3	52.0	53.4
	20	158.2	166.1	-	130.4	55.4	55.7
	60	156.7	165.6	-	121.9	56.1	57.6
PM_{13}-*b*-PS_{27}-*b*-$PVDF_{60}$	1	162.7	166.9	-	143.8	45.2	43.0
	5	160.5	166.2	-	139.6	45.9	45.4
	20	159.0	166.0	-	134.3	46.6	47.9
	60	158.1	165.6	-	124.7	48.9	40.4
PM_{11}-*b*-PS_{22}-*b*-$PVDF_{67}$	1	166.2	170.4	174.6	148.1	55.0	56.6
	5	164.0	169.4	-	141.9	56.3	54.6
	20	162.6	169.2	-	137.3	55.9	58.15
	60	161.5	168.6	-	129.5	56.6	48.8

FTIR analysis was performed to identify the crystalline phases in the PVDF block. The FTIR analysis was carried out at RT after a cooling process at 60, 5, and 1 ºC/min from the melt. The results for the neat PVDF and the PM_{34}-*b*-PS_{66}-Br precursor are displayed in Figure 6.5. The wavenumber range shown in these samples is from 600 to 1300 cm^{-1}, where the main characteristic bands for the PVDF are present. The PM_{34}-*b*-PS_{66}-Br precursor also was analysed with the aim to know if the bands of the PM block or PS block can overlap with the bands of the PVDF block. This precursor sample was analysed at RT after a cooling process at 5 ºC/min. The result for this precursor (Figure 6.5a) shows that there is not any band that can interfere with the PVDF ones in the range studied. The main bands observed in this range for the PM_{34}-*b*-PS_{66}-Br precursor are at 753 and 695 cm^{-1}, which correspond to the PS block.[16, 17] The PM content in the precursor sample was not enough to see its bands by FTIR and are not appreciable in Figure 6.5a. The FTIR spectrum for the neat PVDF shown in Figure 6.5b presents in all the cooling rates studied, the

main infrared bands that correspond to the α- and β-phases. There are two main bands that correspond to β-phase, one at 1275 cm^{-1} and another one at 840 cm^{-1}.[18, 19] These bands are marked with black vertical dashed lines in Figure 6.5b. The PVDF α-phase has four characteristic bands, the values of these bands are 1214, 976, 796, and 764 $cm^{-1,}$ and these bands are represented with vertical red dashed lines in all Figures.[11, 20, 21] The result for neat PVDF is consistent with the results obtained by DSC scans, where the band of the β-phase at 840 cm^{-1} is clearly visible at the cooling rates of 5 and 1 ºC/min, whereas it is almost not appreciable at 60 ºC/min. Therefore, we can suggest that this neat PVDF crystallizes in α- and β-phases when the crystallization is from the molten state and the β-phase is promoted at low cooling rates. This peculiar behaviour is atributted to the lower M_n value of this PVDF in comparison with commercial PVDF samples.

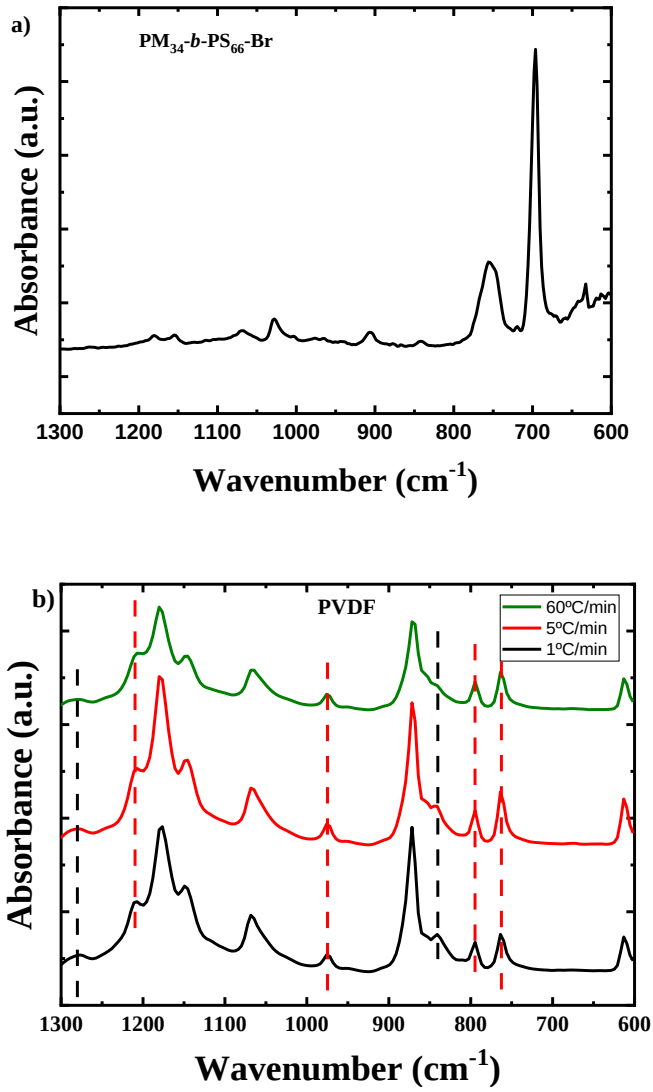

Figure 6.5. FTIR results for a) PM_{34}-*b*-PS_{66}-Br after a cooling from the melt at 5 ºC/min and b) PVDF homopolymer after a cooling at 60, 5 and 1 ºC/min.

The FTIR results for the triblock copolymers are presented in Figure 6.6. Both copolymers show the bands previously mentioned for the α- and β-phases, therefore, this analysis has corroborated that both phases co-exist in these triblock systems, as observed before by DSC. Regarding the DSC results for the sample PM_{11}-*b*-PS_{22}-*b*-$PVDF_{67}$, it showed a third peak when the crystallization rate was 1 ºC/min. As explained before, this peak could be associated to the appearance of the γ-phase or the

reorganisation of the crystals during the heating process. In the FTIR analysis of this sample after a cooling process at 1 ºC/min, there is not any band at 1232 or 833 cm^{-1}, that correspond to the γ-phase.[22] Therefore, this peak observed in the DSC is probably associated to the reorganisation of the crystals during the heating scan. The possibility that the amount of γ-phase is not high enough for detection cannot be completely rule out. All the possible bands for these systems and their descriptions are listed in Table 6.3.

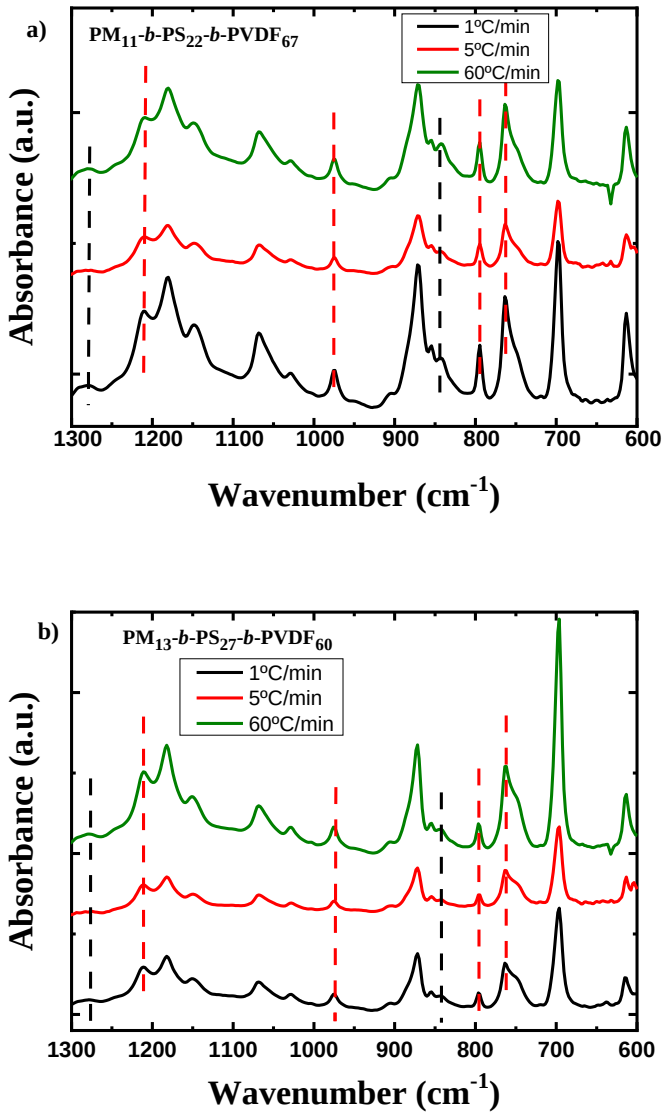

Figure 6. 6. FTIR analysis after a cooling at 60, 5 and 1 ºC/min of a) PM_{11}-*b*-PS_{22}-*b*-$PVDF_{67}$ and b) PM_{13}-*b*-PS_{27}-*b*-$PVDF_{60}$.

Table 6. 3. Main FTIR bands for the PVDF and the PS and their respective descriptions.

Wavenumber (cm^{-1})	Polymer	Description
695	PS	Benzene ring vibration
753	PS	Benzene ring vibration
764	α-PVDF	C-C in plane rocking vibration
796	α-PVDF	CH_2 rocking
833	γ-PVDF	-
840	β-PVDF	CH_2,CF_2 asymmetric stretching vibration
976	α-PVDF	CH out of plane deformation
1232	γ-PVDF	CF out of plane deformation
1275	β-PVDF	CF out of plane deformation

In order to verify the results obtained by DSC and FTIR, the block copolymers were analysed by the WAXS technique during the heating process at 20 ºC/min after a cooling process at 20 ºC/min. Figure 6.7 shows the WAXS diffractogram obtained during the mentioned heating scan for the PM_{34}-*b*-PS_{66}-Br precursor sample and the triblock copolymers. Figure 6.7a presents the WAXS results for the PM_{34}-*b*-PS_{66}-Br precursor, and the result indicates that at temperatures below 120 ºC, where the sample is in the crystalline state, two main peaks that belong to the crystals from the PM block are present. The size of these peaks decreases at 100 ºC, that means that the sample starts melting at 100 ºC, being the WAXS and DSC results in accordance. These peaks are at the values of 15.2 and 16.7 nm^{-1}, the PM crystallizes in an orthorhombic unit cell, and its parameters are a = 0.742 nm, b = 0.495 nm, c = 0.255 nm and β = 90º, the space group is a *P*-D_{2h}.[23, 24] Moreover, the crystallographic planes of these peaks are (110) for the peak at 15.2 nm^{-1} and (200) for the peak at 16.7 nm^{-1}.[25, 26]

Figure 6.7b and 6.7c show WAXS data during the heating scans for the triblock copolymer samples. For both copolymers, peaks corresponding to the PM block and

PVDF block are observed. The peaks that correspond to the PVDF can be classified depending on the crystalline phase obtained. The characteristic peaks for the paraelectric α-phase are at 12.6, 13.1, 14.2, and 18.8 nm^{-1}, and their corresponding crystallographic planes are (100), (020), (110) and (120/021), respectively.[27-29] The unit cell of the α-phase is a pseudo-orthorhombic unit with the parameter a = 0.496 nm, b = 0.964 nm, c = 0.462 nm, and β = 90º, and the space group corresponds to a *P2/C*.[30, 31] In both copolymers the reflections for the α-phase appear, in agreement with the FTIR results observed before. These peaks almost disappear at 160 ºC. The presence of the crystalline β-phase in both triblock copolymers is corroborated with the "shoulder" or "belly" that appears at 14.5 nm^{-1}. This peak corresponds to the (200/110) crystalline plane[32], and the β-phase is characterized by an orthorhombic unit cell with dimensions equal to a = 0.847 nm, b = 0.490 nm, c = 0.256 nm and with the *Cm2m* space group.[33] This shoulder disappears before the sample reaches 160 ºC, corroborating the previous results presented by DSC. Table 6.4 reports all the WAXS reflections obtained in our experiments and also the values reported in the literature.

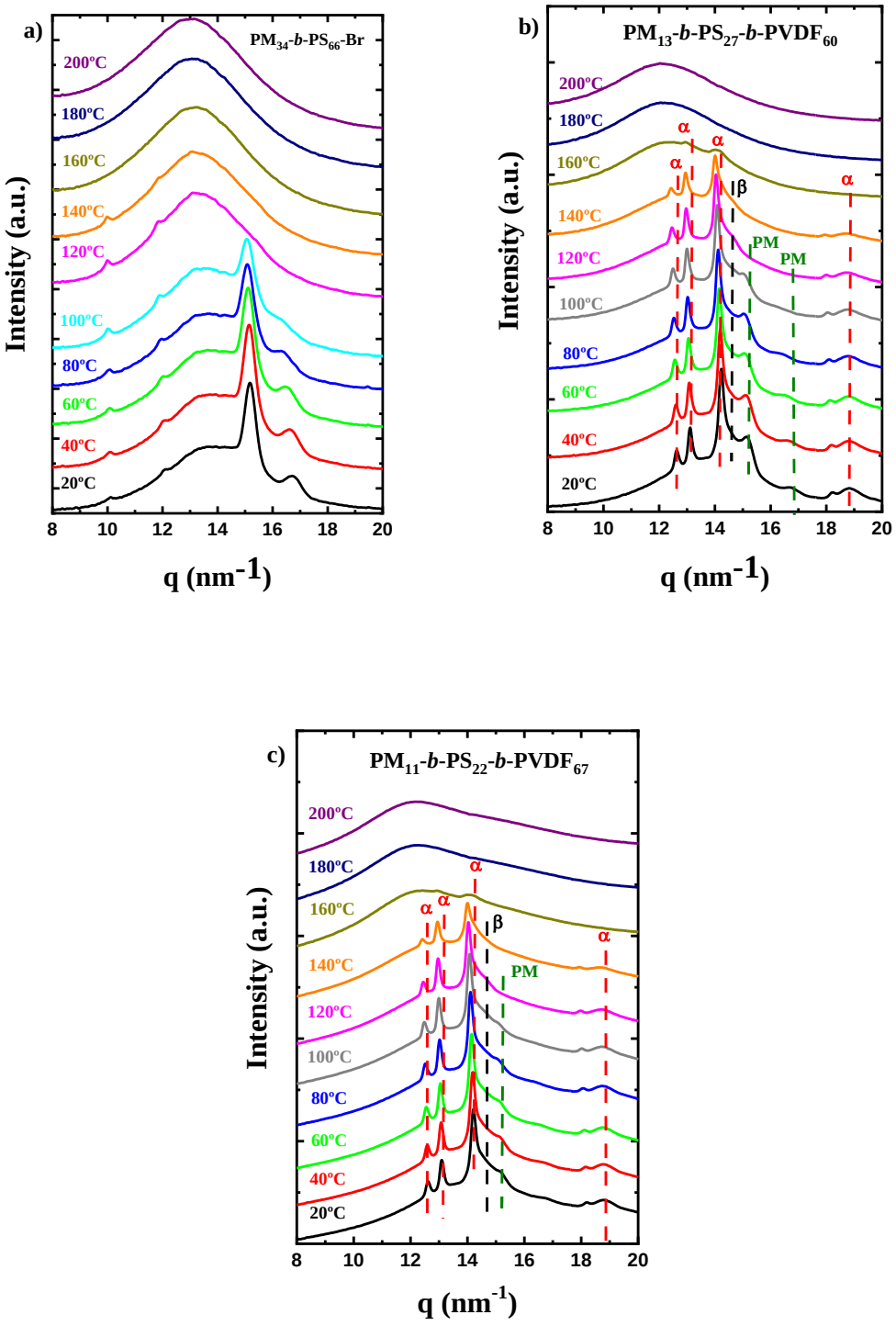

Figure 6. 7. WAXS scans during a heating sweep at 20 ºC/min after a previous cooling at 20 ºC/min of a) PM_{34}-*b*-PS_{66}-Br, b) PM_{13}-*b*-PS_{27}-*b*-$PVDF_{60}$ and c) PM_{11}-*b*-PS_{22}-*b*-$PVDF_{67}$.

After the analysis of the non-isothermal crystallization with DSC, FTIR and WAXS techniques, we can conclude that α- and β-phases are co-crystallizing in the PVDF for the triblock copolymer system when the crystallization is from the melt and at low cooling rates values the β-phase is always promoted.

Table 6. 4. *q*-, d_{hkl}, the d_{hkl} values reported and the crystalline planes obtained in the WAXS experiments for the PM_{34}-*b*-PS_{66}-Br precursor and both triblock copolymers.

Samples	*q* (nm^{-1})	*d* (nm)	*d* reported (nm)[32, 34, 35]	Crystalline planes
PM_{34}-*b*-PS_{66}-Br	15.2	0.41	0.41	(110)
	16.7	0.38	0.37	(200)
PM_{13}-*b*-PS_{27}-*b*-$PVDF_{60}$	12.6	0.5	0.49	(100)
	13.1	0.48	0.48	(020)
	14.2	0.44	0.44	(110)
	14.5	0.43	0.44	(200/110)
	15.2	0.42	0.41	(110)
	16.7	0.38	0.37	(200)
	18.8	0.33	0.33	(120/021)
PM_{11}-*b*-PS_{22}-*b*-$PVDF_{67}$	12.6	0.5	0.49	(100)
	13.1	0.48	0.48	(020)
	14.2	0.44	0.44	(110)
	14.5	0.43	0.44	(200/110)
	15.2	0.42	0.41	(110)
	18.8	0.33	0.33	(120/021)

6.3.3 Isothermal Crystallization

The isothermal crystallization of the PVDF samples was controlled and studied with the aim to know the kinetics of the crystallization process of each sample at different isothermal temperatures. Firstly, the samples were studied with PLOM where the samples were crystallized at different temperatures and the radii of the

PVDF spherulites were measured during the growth of the crystals. Again, the PVDF block is the main study of this manuscript. As it has been shown during the non-isothermal experiments, the PM block crystallizes in microdomains that are too small to be detected by PLOM, therefore it is not possible to measure the growth of the PM crystals. Figure 6.8 shows the results of the PVDF spherulites growth rates (G) of each sample against the T_c. The range of temperatures employed for the isothermal crystallization is between 140-156 ºC for all the samples. The results show that in the neat PVDF the spherulites grow slower than for the block copolymer samples. The comparison between the two triblock copolymers reveal that the sample with a higher proportion of PVDF crystallizes a bit faster than the other one, and both of them have the same tendency as shown in the solid lines calculated by the Lauritzen and Hoffman theory.[36]

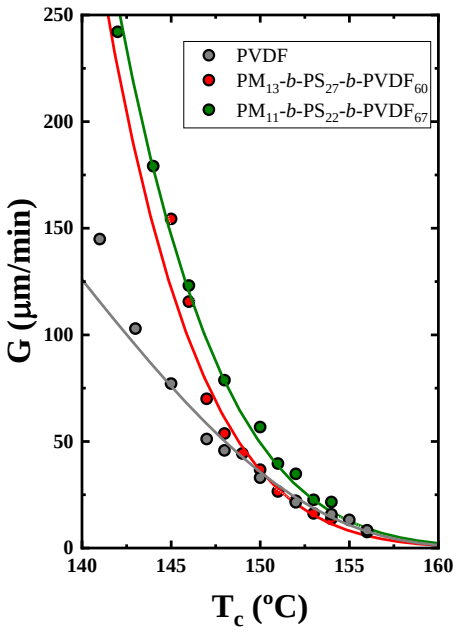

Figure 6. 8. Spherulitic growth of all the samples that contains PVDF against crystallization temperature.

The isothermal protocol was also performed by DSC to determine all the kinetic parameters during the crystallization process. In this case, only the crystallization of the PVDF block was possible. The drawback in the isothermal crystallization process of the PM is that it probably crystallizes during the cooling process (as in the case of the previous chapter). In the case of the PVDF, there are some isothermal crystallization temperatures where it was possible to apply the Avrami theory.[37, 38] The Lauritzen and Hoffman theory and the Avrami theory are employed with the aim to describe the primary crystallization process and the crystallization parameters as a function of the crystallization temperature used.

The isothermal crystallization are also analysed by the DSC technique. The inverse of the induction time (t_0) against the isothermal crystallization temperature is plotted in Figure 6.9. The induction time is correlated with the primary nucleation of the material before any crystallization has started. The inverse of the induction time ($1/t_0$) is equivalent to the primary nucleation rate of the polymer and can be affected by the the composition of the material. The results in Figure 6.9 reveal that the nucleation rate for the PVDF is higher when the polymer is within a triblock structure (or a blend) than in the homopolymer sample at the crystallization temperatures measured for this system. Moreover, the triblock copolymer PM_{13}-*b*-PS_{27}-*b*-$PVDF_{60}$ shows a higher nucleation rate than the PM_{11}-*b*-PS_{22}-*b*-$PVDF_{67}$ sample.

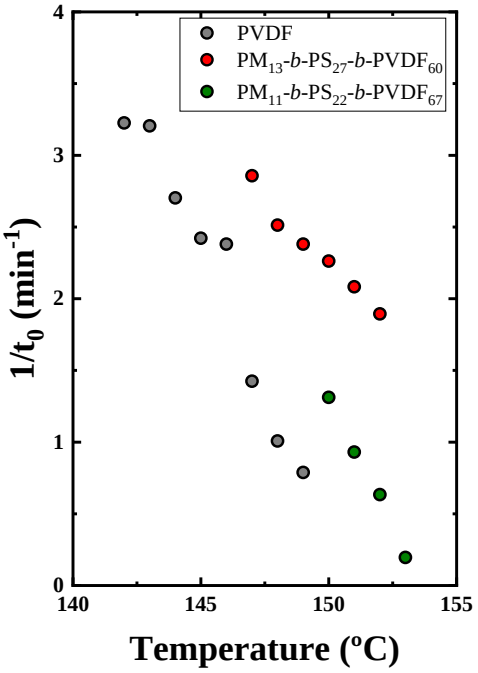

Figure 6. 9. Inverse of the induction time (t_0) for all the samples that contains PVDF against crystallization temperature.

Another kinetic parameter measured is the overall crystallization rate of the samples. The inverse of the half crystallization time ($\tau_{50\%}$) is calculated to know the overall crystallization rate, including the nucleation and growth processes. The $1/\tau_{50\%}$ value is the inverse of the time required to convert 50% of the sample to the semi-crystalline state during the isothermal experiment. Figure 6.10 exhibits the inverse of the half crystallization time at the corresponding crystallization temperatures for the PVDF in the samples studied. At the temperatures measured, the crystallization rate of the PVDF in the block copolymers is always higher than the crystallization rate observed for the neat PVDF. The sample PM_{11}-*b*-PS_{22}-*b*-$PVDF_{67}$ is the fastest one and this result is similar to the results obtained in the spherulitic grow behaviour by PLOM technique (Figure 6.8).

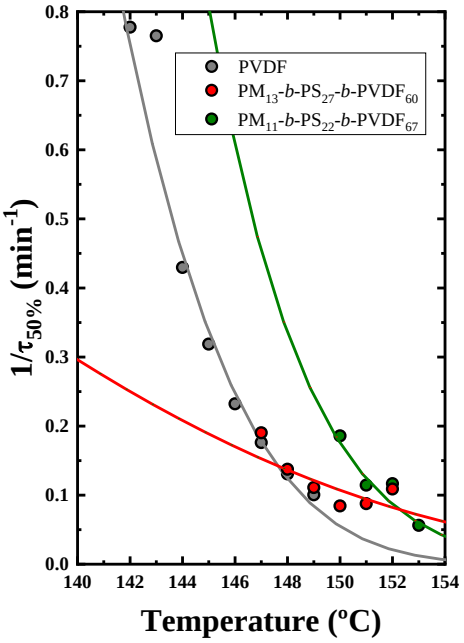

Figure 6. 10. Inverse of the half crystallization time ($\tau_{50\%}$) for all the samples that contain PVDF versus the crystallization temperature.

The Avrami theory is employed to know the primary crystallization in polymers. The following equation describes the mentioned theory:

$$1 - V_c(t - t_0) = exp(-k(t - t_0)^n) \qquad \text{eq. 6.2}$$

where V_c is the relative volume of transformed fraction, t_0 is the induction time before the crystallization process has started, t is the time required for the experiment, k is the constant for the overall crystallization rate, and n is the Avrami index.

Thanks to the application of the Avrami equation in each sample, it is possible to calculate the Avrami index (n) at every isothermal crystallization temperature measured in the DSC. Figure 6.11a exhibits the n values for the PVDF component for all samples at all isothermal crystallization temperatures studied. Normally the values of n fluctuate between 1 and 4. Depending on the value of n it is possible to predict the morphology during the isothermal crystallization process of the polymer.

If the value is lower than 1.5, the crystals formed are needles (1D). When the value is between 1.5 and 2.4, the crystals should be instantaneously nucleated axialites (2D), and if *n* values are between 2.5 and 3.4, the crystals could be sporadically nucleated axialites or instantaneously nucleated spherulites (i.e., *n*=3). When the Avrami index is between 3.5 and 4, it is possible to ensure that the crystal morphology is 100% spherulitic (i.e., *n*=4 for sporadically nucleated spherulites).[3, 39] For our samples, the neat PVDF and the PM_{11}-*b*-PS_{22}-*b*-$PVDF_{67}$ samples have values above 2.5, so the crystals expected during the isothermal crystallization experimenst should be spherulites or sporadic axialites in both cases. However, the PM_{13}-*b*-PS_{27}-*b*-$PVDF_{60}$ sample has values in the axialite regime when the isothermal crystallization temperature increases, but at low isothermal crystallization temperatures, i.e. 147 ºC, the *n* value is also in the spherulitic regime.

Figure 6.11b shows the evolution of $k^{1/n}$ values versus the respective isothermal crystallization temperature. This value is proportional to the overall crystallization rate; therefore, these values are comparable with those obtained using the $1/\tau_{50\%}$ values. The comparison of the results show that the Avrami theory is really close to the experimental data.

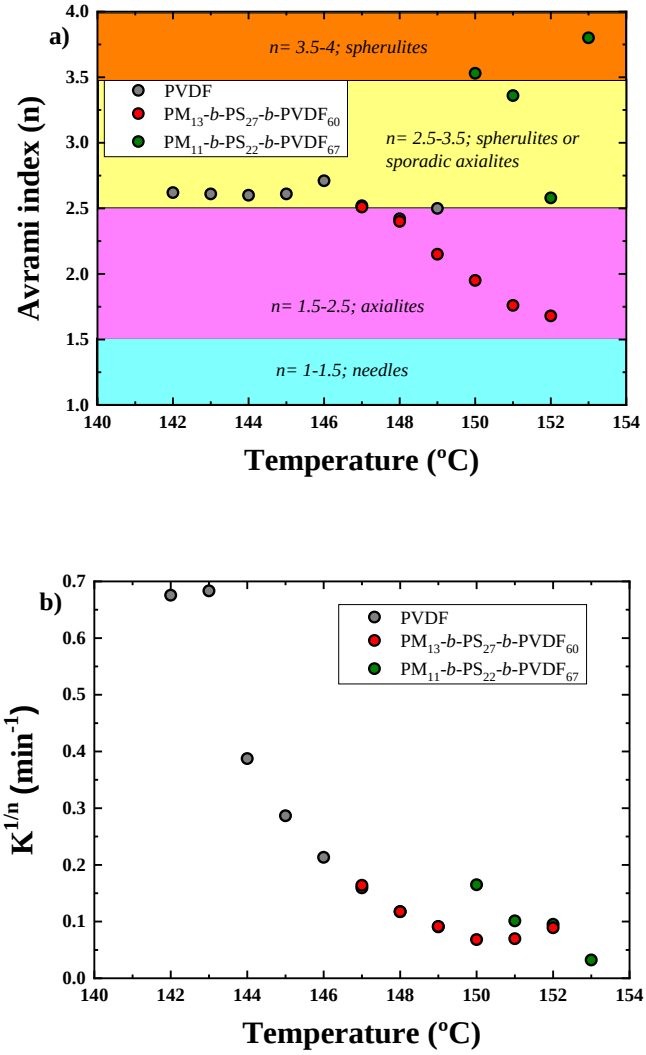

Figure 6. 11. a) Avrami index (*n*) for the PVDF in all the samples against the crystallization temperature. b) The normalized constant of the isothermal crystallization rate of the Avrami equation ($k^{1/n}$) as a function of the crystallization temperature.

After the study of the isothermal crystallization process in the PVDF, the analysis of the subsequent heating was carried out. This study can help us to understand better the overall crystallization of the PVDF and the polymorphism that can present during the isothermal protocol. The melting curves for the PVDF after the isothermal crystallization are plotted in Figure 6.12. All the samples show at least two melting

peaks at a certain crystallization temperature, so polymorphism is also presented in these systems when the crystallization is isothermally treated.

Neat PVDF (Figure 6.12a) has two melting peaks at low isothermal crystallization temperatures, the first one (probably the β-phase) is larger than the second one (probably the α-phase). When the crystallization temperature increases, the second melting peak decreases in size, until 149 ºC, where this peak almost disappears and only the first melting peak remains. At high isothermal crystallization temperatures, this first melting peak is promoted.

In the case of the PM_{13}-*b*-PS_{27}-*b*-$PVDF_{60}$ sample (Figure 6.12b), at low isothermal crystallization temperatures, the sample also presents two melting peaks, and, once again, that one at low temperatures is enhanced. At the crystallization temperature of 149 ºC, the first peak decreases in size, and a shoulder in the second peak appears. If the crystallization temperature continues increasing, the first peak tends to completely disappear, and the second peak seems to start undergoing a phase transition to higher temperatures. It can be a phase transition from α- to γ-phase. For the PM_{11}-*b*-PS_{22}-*b*-$PVDF_{67}$ sample (Figure 6.12c), the behaviour is quite similar, but in this case, the melting peaks of the phases are not overlapped. At low isothermal crystallization temperatures, there are only two peaks, then, when the isothermal temperature increases to 152 ºC, the second peak is reduced in size and a new peak emerges. If the isothermal temperature continues increasing, the first and the second peaks tend to disappear, and only the third peak remains at high isothermal temperatures.

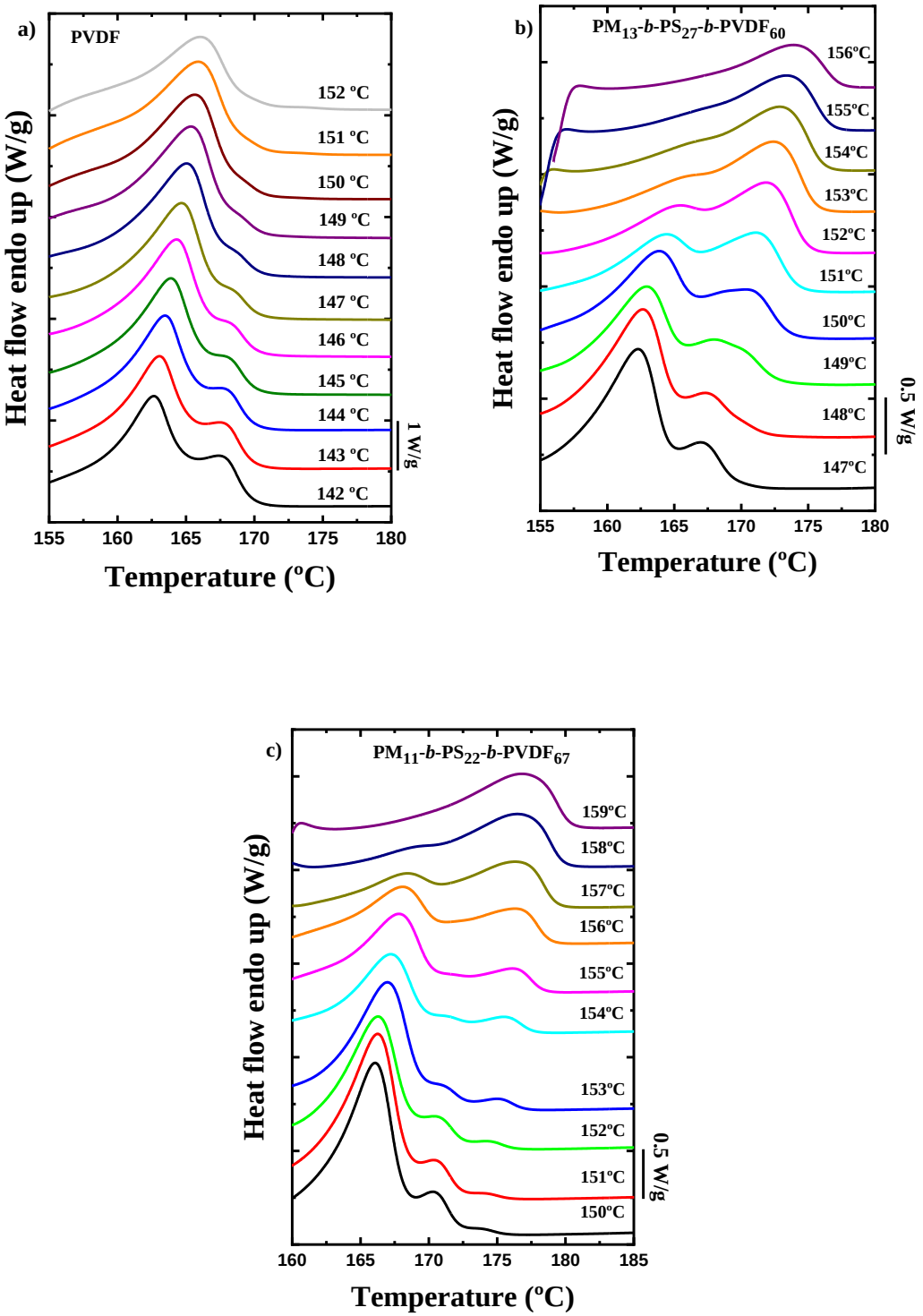

Figure 6. 12. DSC heating curves in the PVDF melting temperature range after an isothermal crystallization of a) neat PVDF, b) PM_{13}-*b*-PS_{27}-*b*-$PVDF_{60}$ and c) PM_{11}-*b*-PS_{22}-*b*-$PVDF_{67}$.

All the crystallization curves are shown in the Figure 6.13.

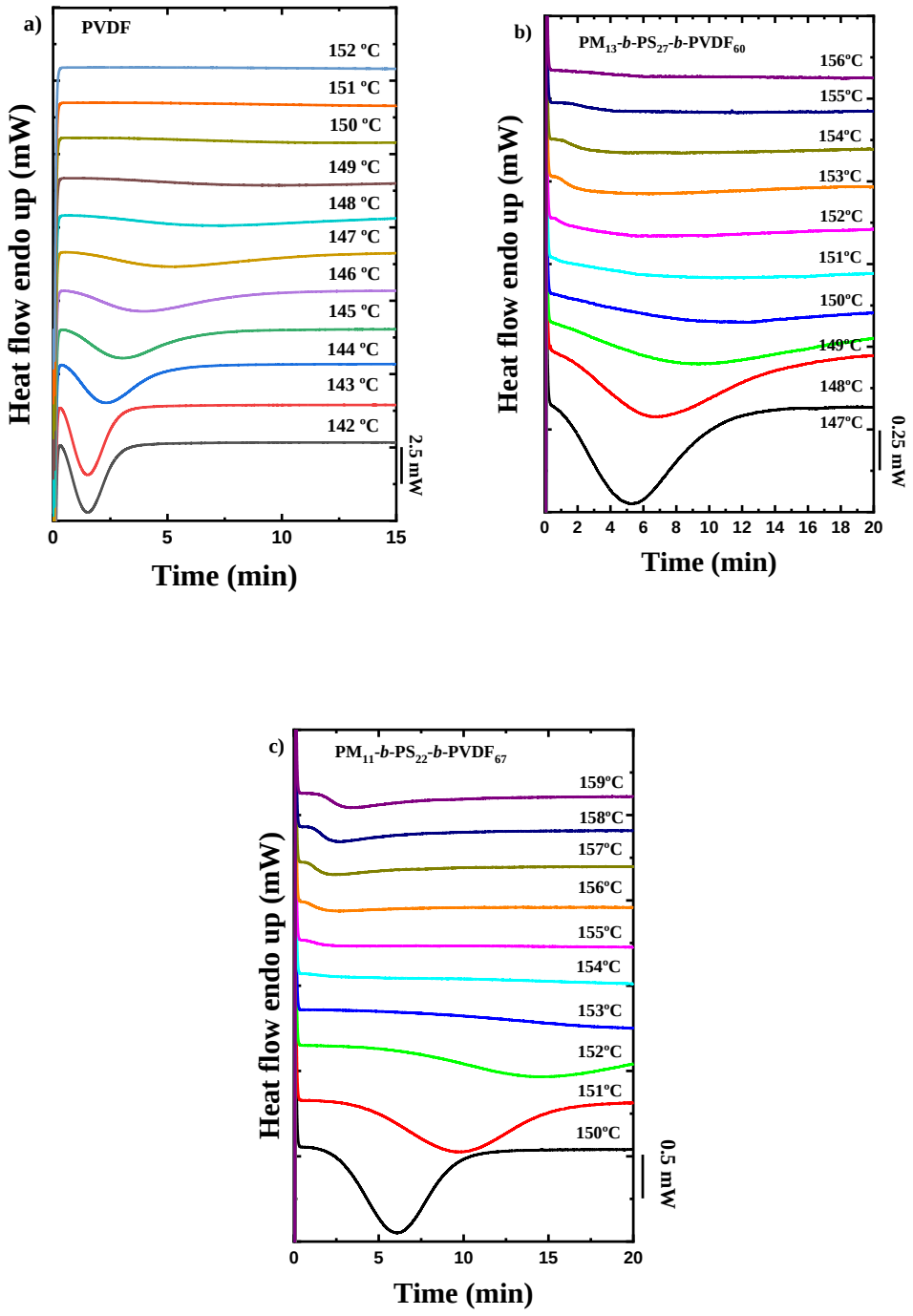

Figure 6. 13. DSC isothermal crystallization of the PVDF block for a) neat PVDF, b) PM_{13}-*b*-PS_{27}-*b*-$PVDF_{60}$ and c) PM_{11}-*b*-PS_{22}-*b*-$PVDF_{67}$.

In order to know which phases are crystallizing during the isothermal experiments, FTIR analysis has been performed after an isothermal treatment at high isothermal temperatures. The analysis of the PVDF phases by FTIR technique after the isothermal crystallization was carried out at RT. The samples were crystallized for two hours at one of the highest isothermal temperatures previously selected in the DSC and then cooled down at 20 ºC/min until RT before the measurement. The temperatures selected for each sample were 151 ºC for the neat PVDF, 156 ºC for the PM_{13}-*b*-PS_{27}-*b*-$PVDF_{60,}$ and 158 ºC for the PM_{11}-*b*-PS_{22}-*b*-$PVDF_{67}$. The results obtained are displayed in Figure 6.14.

Neat PVDF shows the two typical bands for the β-phase (at 1278 and 840 cm^{-1}) and also the bands for the α-phase (at 1214, 976, 796 and 764 cm^{-1}). The results in the DSC show only one peak with a small shoulder on it when the sample was isothermally crystallized at 151 ºC. The two crystalline phases can coexist at this temperature, as FTIR and DSC results suggested. The triblock terpolymer samples also show the main bands for the α- and β-phases, but in both cases the bands of the γ-phase are also presented, at 1232 and 833 cm^{-1}. After these evidences of the presence of the γ-phase in the triblock samples and the rest of the crystalline phases in all samples, it is possible to assign each melting peak in the isothermal DSC experiments to each crystalline phase. The melting peak at the lowest temperature value is from the melting of the β-phase, then the following small peak that only appears at low isothermal crystallization temperatures belongs to the α-phase, and finally the new crystalline phase that rises at high melting temperatures is the γ-phase.

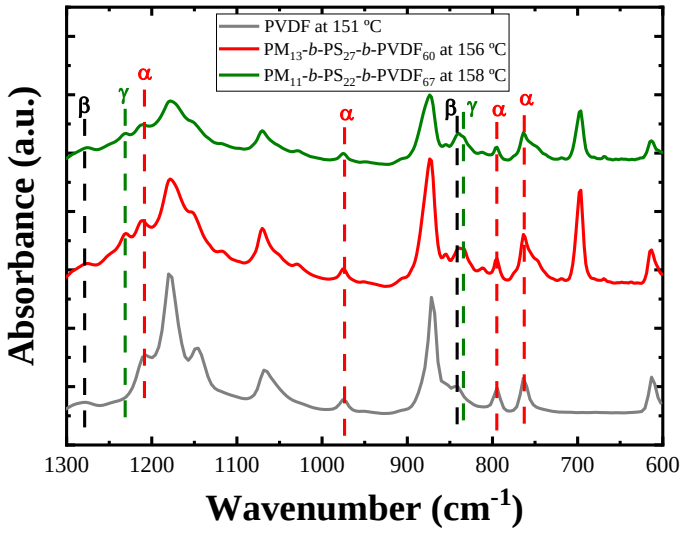

Figure 6. 14. FTIR analysis performed after an isothermal crystallization at the temperature remarked for all the samples that contain PVDF.

6.3.4 Self-nucleation (SN) and Successive Self-nucleation and Annealing (SSA)

Self-nucleation experiments were performed for the samples containing PVDF (triblock terpolymers and neat PVDF) to check if the self-nucleation *Domains* of the PVDF are changed. The best nucleating agent of a material is its own crystals because they have perfect epitaxy.[4, 7, 40] The results obtained through the SN protocol in neat PVDF are represented in the Figure 6.15. Figure 6.15a shows the cooling curves after the 5 minutes isothermal process at the selected T_s value, whereas in Figure 6.15b, the subsequent heating curves are displayed. Figure 6.15c shows the standard melting curve of the neat PVDF with all the *Domains*. The different *Domains* are represented in the Figures with different colours: all the lines in red colour belong to the *Domain I*, the *Domain II* is marked with blue lines, and the lines of the *Domain III* appear in green colour.

When the polymer is within *Domain I* the melting of the material occurs completely, and the thermal story is also completely erased. In the case of the neat PVDF

the *Domain I* is from 177 ºC to higher temperatures, and inside this *Domain* the melting curves of the material are not changing for all the T_s chosen.

Domain II is the range of temperatures where the material is able to produce its self-nuclei, but the temperature is still not enough to anneal the sample. The neat PVDF is in *Domain II* between 172-176 ºC. The ideal self-nucleation temperature (T_{si}), that is highly encouraged to employ in the SSA protocol, is the temperature with the lowest value within *Domain II*. Due to the importance of this T_s it is recommended to be accurate in the process of the separation among the *Domains*. This T_{si} is the temperature where the polymer produces the maximum self-nucleation avoiding the annealing process. In *Domain II* it is possible to observe an increment in the value of the crystallization temperature (see Figure 6.15a), this behaviour can be explained because the nucleation density increases exponentially in this *Domain* when the value of the T_s decreases. In this case, the T_{si} of the neat PVDF is 172 ºC, and this temperature will be employed in the SSA protocol for all the samples in order to compare the fractionation process between them.

In *Domain III*, a partial melting occurs, and the unmelted crystals anneal. It is possible to know when the material enters in *Domain III* when in the heating curves, a small annealing peak appears at higher temperatures. In the case of the neat PVDF, *Domain III* starts at 171 ºC, where there is a small shoulder, and it is highlighted to appreciate it better (Fig. 6.15b)

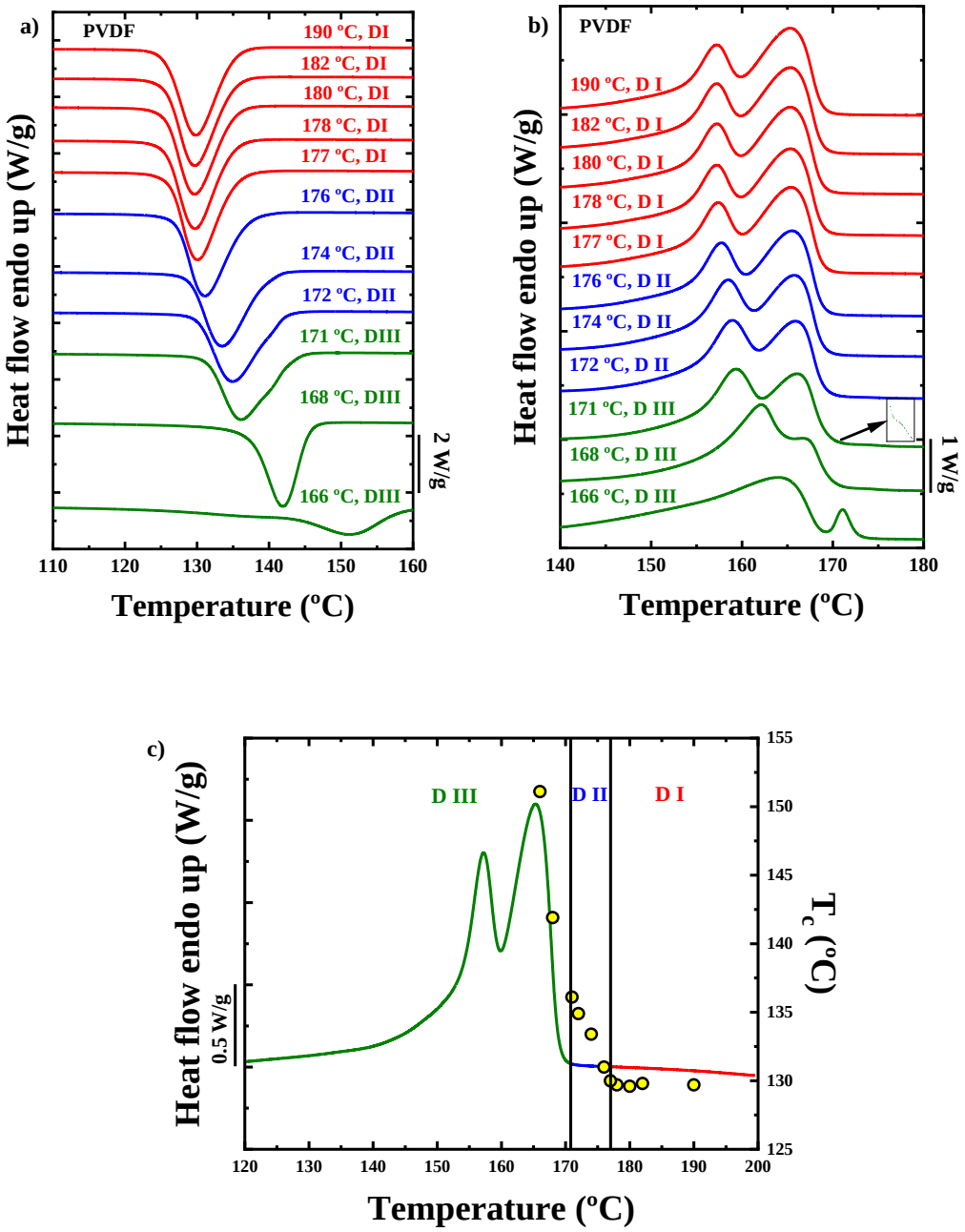

Figure 6. 15. DSC curves during the self-nucleation protocol for the neat PVDF. a) Cooling curves after the short isothermal step at the T_s, b) heating curves after the cooling process and c) representation of all the Domains in the self-nucleation process presented in a standard melting curve. The data point shows the crystallization temperature (right Y axis) at the subsequent T_s value.

The SN protocol was also applied to the triblock terpolymer samples for the PVDF component, and the results obtained are presented in Figure 6.16. The range of each *Domain* changes depending on the sample. In both block terpolymers, the three *Domains* are perfectly delimited. The triblock copolymer PM_{11}-*b*-PS_{22}-*b*-$PVDF_{67}$ has the same *Domain I* range as neat PVDF, whereas for the PM_{13}-*b*-PS_{27}-*b*-$PVDF_{60}$ sample, the *Domain I* starts at 175 ºC, two degrees lower compared to the neat PVDF. The vertical dashed line in Figure 6.16a has been added in order to appreciate better the change in the T_c between *Domain I* and *Domain II*. In the case of the triblock terpolymers the increment in the T_c during *Domain II* is only two degrees. *Domain III* starts at two degrees higher in the case of the block copolymer PM_{11}-*b*-PS_{22}-*b*-$PVDF_{67}$. Both triblock copolymers have annealing peaks at lower temperatures than the neat PVDF.

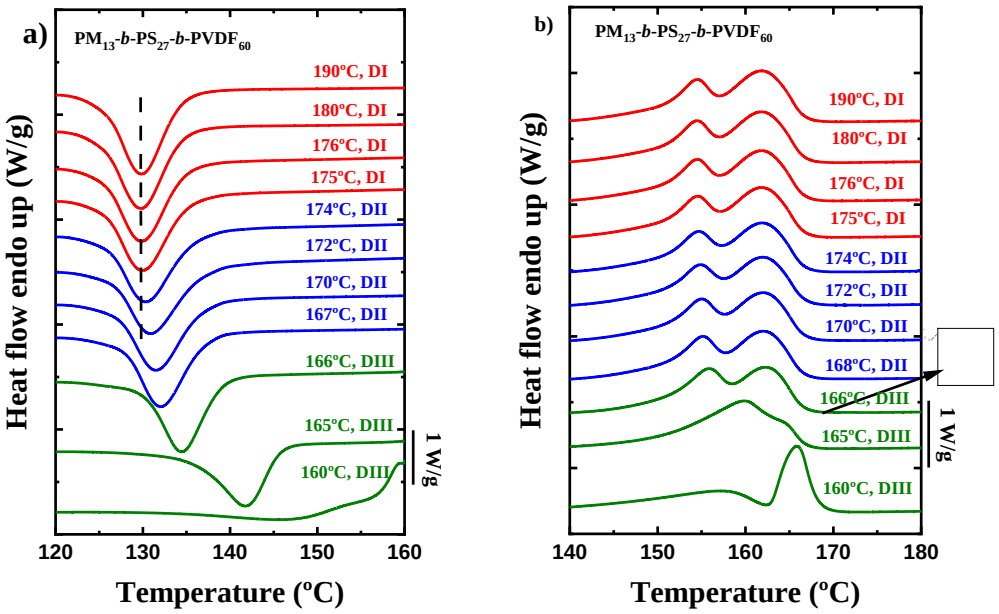
a)
PM13-b-PS27-b-PVDF60
190°C, DI
180°C, DI
176°C, DI
175°C, DI
174°C, DII
172°C, DII
170°C, DII
167°C, DII
166°C, DIII
165°C, DIII
160°C, DIII
1 W/g
Heat flow endo up (W/g)
120 130 140 150 160
Temperature (°C)
b)
PM13-b-PS27-b-PVDF60
190°C, DI
180°C, DI
176°C, DI
175°C, DI
174°C, DII
172°C, DII
170°C, DII
168°C, DII
166°C, DIII
165°C, DIII
160°C, DIII
1 W/g
Heat flow endo up (W/g)
140 150 160 170 180
Temperature (°C)

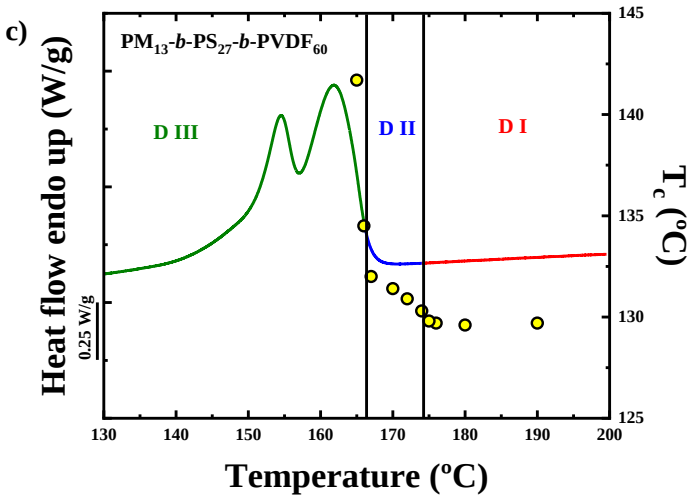
c)
PM13-b-PS27-b-PVDF60
D III
D II
D I
0.25 W/g
Heat flow endo up (W/g)
Tc (°C)
130 140 150 160 170 180 190 200
125 130 135 140 145
Temperature (°C)

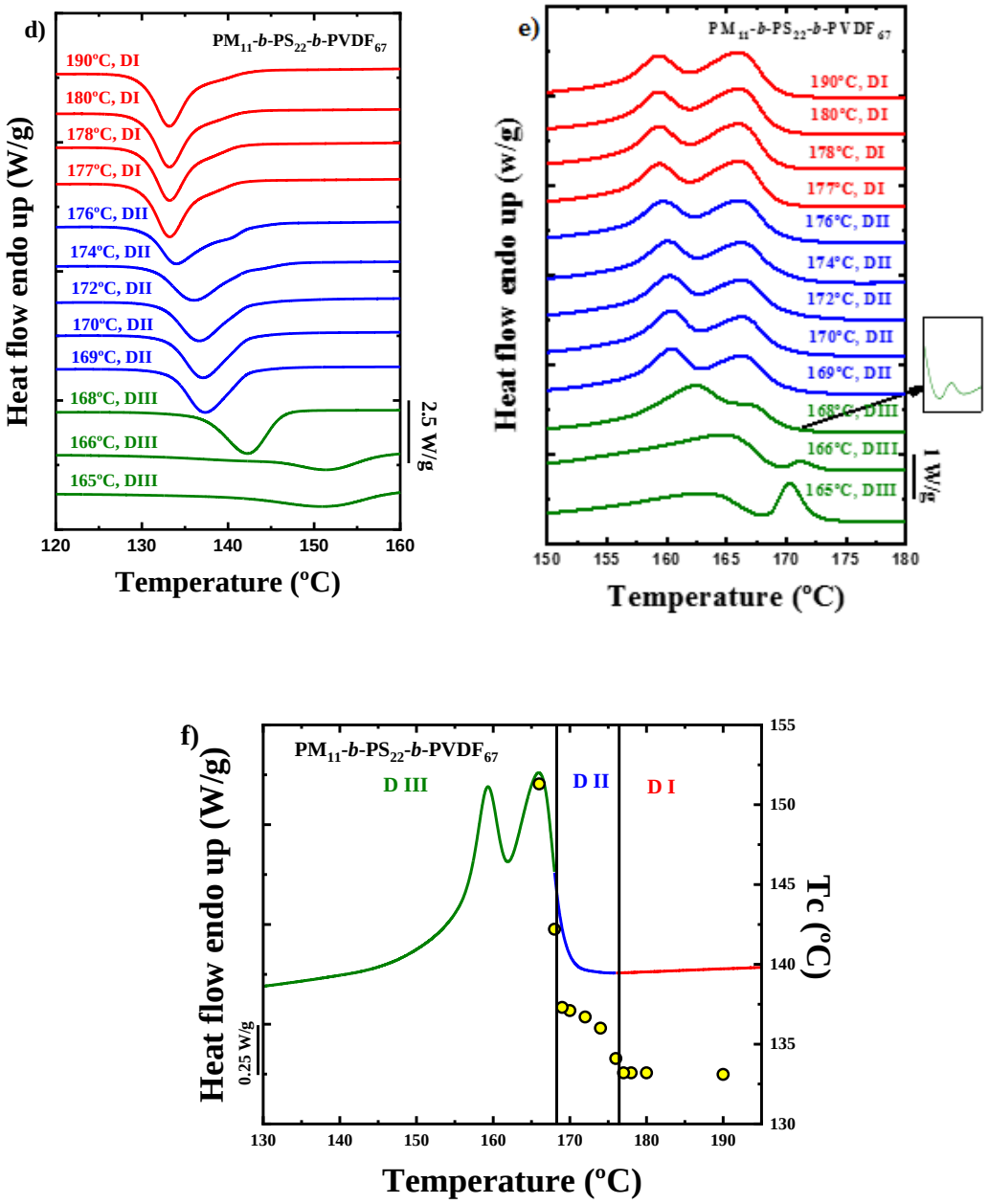

Figure 6. 16. a) Cooling curves after the short isothermal step at the T_s indicated for the PM_{13}-*b*-PS_{27}-*b*-$PVDF_{60}$, b) heating curves after the cooling process for the PM_{13}-*b*-PS_{27}-*b*-$PVDF_{60}$, d) cooling curves after the short isothermal step at the T_s indicated for the PM_{11}-*b*-PS_{22}-*b*-$PVDF_{67}$, and e) heating curves after the cooling process for the PM_{11}-*b*-PS_{22}-*b*-$PVDF_{67}$. The representation of all the *Domains* in the self-nucleation process presented in a standard melting curve for the c) PM_{13}-*b*-PS_{27}-*b*-$PVDF_{60}$ and f) PM_{11}-*b*-PS_{22}-*b*-$PVDF_{67}$ samples. The data point shows the crystallization temperature (right Y axis) at the subsequent T_s.

Finally, the SSA protocol was applied to thermally fractionate the samples that contain PVDF. The final heating scans at the end of the SSA protocol are plotted in Figure 6.17 for each sample. The heating curve of the samples represents the effect of the eight self-nucleation processes, and the corresponding annealing steps at the T_s indicated in a range of temperatures from 137 ºC to 172 ºC. In all the samples it is possible to observe the fractionation. The melting peak at different temperatures represents the melting of different lamellar size crystals formed during the SSA experiment. The melting peak at the highest temperature represents the melting of the crystals with the thickest lamellae, as the melting temperature decreases also, the lamellar size of the crystals decreases. The T_s at the highest temperature, the ideal self-nucleation temperature, does not produce any kind of thermal fraction because at this temperature there is not any annealing procedure as was observed in the SN protocol. The neat PVDF presents six main well-defined melting peaks and one small peak at temperatures close to 180 ºC. The PM_{13}-*b*-PS_{27}-*b*-$PVDF_{60}$ presents the same number of melting peaks as neat PVDF and at the same temperature, so their fractionation behaviour looks similar.

In general terms, the SSA fractionation behaviour is very similar between neat PVDF and the PVDF component in the triblock terpolymer samples. In fact, the main difference is the magnitude of the enthalpic change, reduced in the terpolymers because the DSC scans are reported in Joules per gram of sample, and only 60 and 67% of the sample is composed of PVDF.

Although there are small differences between the neat PVDF sample and the two multiphasic samples, the general behaviour of the PVDF phase is quite similar for all samples. This also support the hypothesis that the triblock terpolymer samples were degraded, and are now composed of a blend of cleaved PVDF molecules and PS-*b*-PM diblocks, as the evidence from PLOM and SAXS strongly suggest.

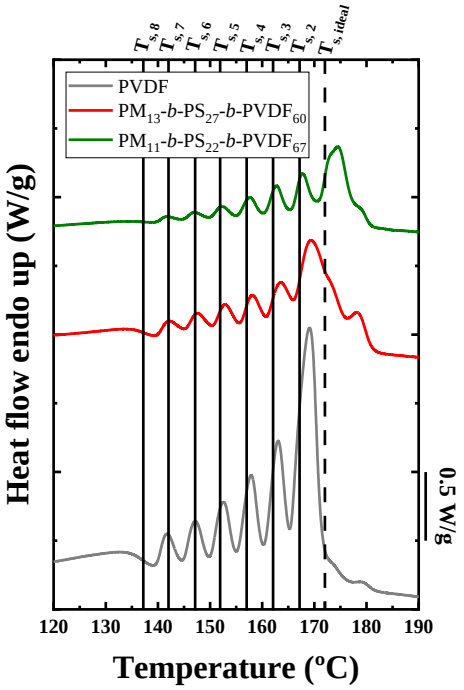

Figure 6. 17. Heating scan after the fractionation protocol in the samples that contain PVDF.

6.4 Conclusions

After studying in detail the two triblock terpolymer samples, it can be concluded that the samples behaved like immiscible blends of PVDF and PS-*b*-PM diblock copolymers. Strong evidences were obtained by both PLOM and SAXS that indicate that macro-phase segregation is present in the samples. This could come from a degradation of the samples, where the PVDF chains could have become cleaved away from the rest of the PS-*b*-PM molecules, either completely or partially. In general terms, the behaviour of the PVDF phase from a calorimetric point of view was not radically different from a neat PVDF sample. Some differences were found that could be due to the complex composition of the blends.

6.5 References

1. Zapsas, G.; Patil, Y.; Bilalis, P.; Gnanou, Y.; Hadjichristidis, N., Poly(vinylidene fluoride)/Polymethylene-Based Block Copolymers and Terpolymers. *Macromolecules* **2019,** 52, (5), 1976-1984.

2. Lorenzo, A. T.; Arnal, M. L.; Albuerne, J.; Müller, A. J., DSC isothermal polymer crystallization kinetics measurements and the use of the Avrami equation to fit the data: Guidelines to avoid common problems. *Polymer Testing* **2007,** 26, (2), 222-231.

3. Pérez-Camargo, R. A.; Liu, G.-M.; Wang, D.-J.; Müller, A. J., Experimental and Data Fitting Guidelines for the Determination of Polymer Crystallization Kinetics. *Chinese Journal of Polymer Science* **2022,** 40, (6), 658-691.

4. Lorenzo, A. T.; Arnal, M. L.; Sánchez, J. J.; Müller, A. J., Effect of annealing time on the self-nucleation behavior of semicrystalline polymers. *Journal of Polymer Science Part B: Polymer Physics* **2006,** 44, (12), 1738-1750.

5. Michell, R. M.; Mugica, A.; Zubitur, M.; Müller, A. J., Self-Nucleation of Crystalline Phases Within Homopolymers, Polymer Blends, Copolymers, and Nanocomposites. In *Polymer Crystallization I: From Chain Microstructure to Processing*, Auriemma, F.; Alfonso, G. C.; de Rosa, C., Eds. Springer International Publishing: Cham, 2017; pp 215-256.

6. Müller, A. J.; Michell, R. M.; Pérez, R. A.; Lorenzo, A. T., Successive Self-nucleation and Annealing (SSA): Correct design of thermal protocol and applications. *European Polymer Journal* **2015,** 65, 132-154.

7. Müller, A. J.; Arnal, M. L., Thermal fractionation of polymers. *Progress in Polymer Science* **2005,** 30, (5), 559-603.

8. Lovinger, A. J., Crystalline transformations in spherulites of poly(vinylidene fluoride). *Polymer* **1980,** 21, (11), 1317-1322.

9. Silva, M. P.; Sencadas, V.; Botelho, G.; Machado, A. V.; Rolo, A. G.; Rocha, J. G.; Lanceros-Mendez, S., α- and γ-PVDF: Crystallization kinetics, microstructural variations and thermal behaviour. *Materials Chemistry and Physics* **2010,** 122, (1), 87-92.

10.Gregorio, R.; CapitãO, R. C., Morphology and phase transition of high melt temperature crystallized poly(vinylidene fluoride). *Journal of Materials Science* **2000,** 35, (2), 299-306.

11.Bormashenko, Y.; Pogreb, R.; Stanevsky, O.; Bormashenko, E., Vibrational spectrum of PVDF and its interpretation. *Polymer Testing* **2004,** 23, (7), 791-796.

12.De Neef, A.; Samuel, C.; Stoclet, G.; Rguiti, M.; Courtois, C.; Dubois, P.; Soulestin, J.; Raquez, J.-M., Processing of PVDF-based electroactive/ferroelectric films: importance of PMMA and cooling rate from the melt state on the crystallization of PVDF beta-crystals. *Soft Matter* **2018,** 14, (22), 4591-4602.

13.Lovinger, A. J., Crystallization and morphology of melt-solidified poly(vinylidene fluoride). *Journal of Polymer Science: Polymer Physics Edition* **1980,** 18, (4), 793-809.

14.Arranz-Andrés, J.; Pérez, E.; Cerrada, M. L., Hybrids based on poly(vinylidene fluoride) and Cu nanoparticles: Characterization and EMI shielding. *European Polymer Journal* **2012,** 48, (7), 1160-1168.

15.Gradys, A.; Sajkiewicz, P.; Adamovsky, S.; Minakov, A.; Schick, C., Crystallization of poly(vinylidene fluoride) during ultra-fast cooling. *Thermochimica Acta* **2007,** 461, (1), 153-157.

16.Pushpadass, H. A.; Weber, R. W.; Dumais, J. J.; Hanna, M. A., Biodegradation characteristics of starch–polystyrene loose-fill foams in a composting medium. *Bioresource Technology* **2010,** 101, (19), 7258-7264.

17.Chen, G.; Liu, S.; Chen, S.; Qi, Z., FTIR Spectra, Thermal Properties, and Dispersibility of a Polystyrene/Montmorillonite Nanocomposite. *Macromolecular Chemistry and Physics* **2001,** 202, (7), 1189-1193.

18.Lanceros-Méndez, S.; Mano, J. F.; Costa, A. M.; Schmidt, V. H., FTIR AND DSC STUDIES OF MECHANICALLY DEFORMED β-PVDF FILMS. *Journal of Macromolecular Science, Part B* **2001,** 40, (3-4), 517-527.

19.Salimi, A.; Yousefi, A. A., Analysis Method: FTIR studies of β-phase crystal formation in stretched PVDF films. *Polymer Testing* **2003,** 22, (6), 699-704.

20.Cai, X.; Lei, T.; Sun, D.; Lin, L., A critical analysis of the α, β and γ phases in poly(vinylidene fluoride) using FTIR. *RSC Advances* **2017,** 7, (25), 15382-15389.

21.Salimi, A.; Yousefi, A. A., Conformational changes and phase transformation mechanisms in PVDF solution-cast films. *Journal of Polymer Science Part B: Polymer Physics* **2004,** 42, (18), 3487-3495.

22.Boccaccio, T.; Bottino, A.; Capannelli, G.; Piaggio, P., Characterization of PVDF membranes by vibrational spectroscopy. *Journal of Membrane Science* **2002,** 210, (2), 315-329.

23.Tasumi, M.; Shimanouchi, T., Crystal Vibrations and Intermolecular Forces of Polymethylene Crystals. *The Journal of Chemical Physics* **1965,** 43, (4), 1245-1258.

24.Hughes, D. J.; Mahendrasingam, A.; Oatway, W. B.; Heeley, E. L.; Martin, C.; Fuller, W., A simultaneous SAXS/WAXS and stress-strain study of polyethylene deformation at high strain rates. *Polymer* **1997,** 38, (26), 6427-6430.

25.Lv, F.; Wan, C.; Chen, X.; Meng, L.; Chen, X.; Wang, D.; Li, L., Morphology diagram of PE gel films in wide range temperature-strain space: An in situ SAXS and WAXS study. *Journal of Polymer Science Part B: Polymer Physics* **2019,** 57, (12), 748-757.

26.Bartczak, Z.; Argon, A. S.; Cohen, R. E.; Kowalewski, T., The morphology and orientation of polyethylene in films of sub-micron thickness crystallized in contact with calcite and rubber substrates. *Polymer* **1999,** 40, (9), 2367-2380.

27.Bachmann, M. A.; Lando, J. B., A reexamination of the crystal structure of phase II of poly(vinylidene fluoride). *Macromolecules* **1981,** 14, (1), 40-46.

28.Newman, B. A.; Yoon, C. H.; Pae, K. D.; Scheinbeim, J. I., Piezoelectric activity and field-induced crystal structure transitions in poled poly(vinylidene fluoride) films. *Journal of Applied Physics* **1979,** 50, (10), 6095-6100.

29.Doll, W. W.; Lando, J. B., The polymorphism of poly(vinylidene fluoride) V. The effect of hydrostatic pressure on the melting behavior of copolymers of vinylidene fluoride. *Journal of Macromolecular Science, Part B* **1970,** 4, (4), 897-913.

30.Geiss, D.; Hofmann, D., Investigation of structural changes in PVDF by modified X-ray texture methods. *IEEE Transactions on Electrical Insulation* **1989,** 24, (6), 1177-1182.

31.Hasegawa, R.; Takahashi, Y.; Chatani, Y.; Tadokoro, H., Crystal Structures of Three Crystalline Forms of Poly(vinylidene fluoride). *Polymer Journal* **1972,** 3, (5), 600-610.

32.Lando, J. B.; Olf, H. G.; Peterlin, A., Nuclear magnetic resonance and x-ray determination of the structure of poly(vinylidene fluoride). *Journal of Polymer Science Part A-1: Polymer Chemistry* **1966,** 4, (4), 941-951.

33.Davis, G. T.; McKinney, J. E.; Broadhurst, M. G.; Roth, S. C., Electric-field-induced phase changes in poly(vinylidene fluoride). *Journal of Applied Physics* **1978,** 49, (10), 4998-5002.

34.Russell, K. E.; Hunter, B. K.; Heyding, R. D., Monoclinic polyethylene revisited. *Polymer* **1997,** 38, (6), 1409-1414.

35.Ince-Gunduz, B. S.; Alpern, R.; Amare, D.; Crawford, J.; Dolan, B.; Jones, S.; Kobylarz, R.; Reveley, M.; Cebe, P., Impact of nanosilicates on poly(vinylidene fluoride) crystal polymorphism: Part 1. Melt-crystallization at high supercooling. *Polymer* **2010,** 51, (6), 1485-1493.

36.Hoffman, J. D.; Lauritzen, J. I., Jr., Crystallization of Bulk Polymers With Chain Folding: Theory of Growth of Lamellar Spherulites. *Journal of research of the National Bureau of Standards. Section A, Physics and chemistry* **1961,** 65A, (4), 297-336.

37.Lorenzo, A. T.; Müller, A. J., Estimation of the nucleation and crystal growth contributions to the overall crystallization energy barrier. *Journal of Polymer Science Part B: Polymer Physics* **2008,** 46, (14), 1478-1487.

38.Avrami, M., Granulation, Phase Change, and Microstructure Kinetics of Phase Change. III. *The Journal of Chemical Physics* **1941,** 9, (2), 177-184.

39.Müller, A. J.; Michell, R. M.; Lorenzo, A. T., Isothermal Crystallization Kinetics of Polymers. *Polymer Morphology: Principles, Characterization, and Processing* **2016,** 714, 181-203.

40.Fillon, B.; Wittmann, J. C.; Lotz, B.; Thierry, A., Self-nucleation and recrystallization of isotactic polypropylene (α phase) investigated by differential scanning calorimetry. *Journal of Polymer Science Part B: Polymer Physics* **1993,** 31, (10), 1383-1393.

Chapter 7

$(PVDF)_2(PEO)_2$ miktoarm star block copolymers

7.1 Introduction

Even though PVDF is the second-most produced fluoropolymer,[1] only a limited number of non-linear macromolecular architectures incorporating PVDF blocks have been described.[2] The reason for this is the relative scarcity of controlled polymerization techniques applicable to vinylidene fluoride (VDF). For example, the reversible addition-fragmentation transfer (RAFT) polymerization, with carefully chosen chain transfer agents is compatible with VDF.[3-7] Several studies reported well-defined PVDF and its block-copolymers produced *via* iodine transfer polymerization (ITP).[8, 9] Very few PVDF-based branched architectures have been described, even though star polymers and brushes could be designed with a range of valuable and unique properties.[10, 11] In particular, PVDF miktoarm star polymers could give rise to complex self-assembly behaviors and structural diversity beyond that of simple block copolymers.[12-14]

Hadjichristidis *et al.* have developed different synthetic routes to obtain complex miktoarm star macromolecular architectures.[15-17] Even though many miktoarm star copolymers[18] have been prepared up to this day, 4-miktoarm star copolymers containing PVDF arms are novel materials whose properties are unexplored. In this chapter, we study the non-isothermal and the isothermal crystallization of the PVDF component within newly synthesized ($PVDF_2$)(PEO_2) 4-miktoarm star block copolymers. These materials are star block copolymers with 4 arms, where two of the arms are PEO chains and the other two PVDF chains, and all arms radiate from a common centre.

A recent work has reported the isothermal crystallization of a linear PVDF homopolymer using a flash DSC equipment, which uses a cooling rate of 3000 ºC/s to avoid any crystallization during cooling process to the crystallization temperature. At crystallization temperatures between 60-65 ºC, the formation of the β-phase was reported.[19] Isothermal crystallization experiments of PVDF films cast from solutions

have also been studied, where PVDF in DMA (dimethylacetamide) solutions are cast on glass substrates and crystallized isothermally at 60 ºC. In these films, the DMA helps the crystallization of PVDF in the polar β-phase.[20] This is unusual behaviour in linear PVDF, in which normally the stable α-phase is formed when the sample is isothermally crystallized, and only in some isolated cases when the crystallization temperature is quite high, the γ-phase can be achieved.[21]

The present chapter reports, apart from the study of the non-isothermal and isothermal crystallization, a brief summary of the synthesis of novel complex 4-miktoarm star copolymers. The application of different experimental techniques, such as Differential Scanning Calorimetry (DSC), Fourier Transform Infrared Spectroscopy **(**FTIR), and Polarized Light Optical Microscopy (PLOM), allow us to determine how these materials crystallize and which polymorphs can be formed. By determining nucleation, growth, and overall crystallization kinetics, we determine the parameters that affect the crystallization kinetics of the miktoarm star copolymers and evaluate the influence of chain topology and/or chain structure on polymorphic properties.

7.2 Materials and method

7.2.1 Materials

Reagents and solvents used during the synthesis part of the manuscript were purchased from different chemical companies and used as received without any further purification. Dimethyl carbonate (DMC) (Sigma-Aldrich, ≥99 %), dimethylformamide (DMF) (Sigma-Aldrich, 99.8%), acetonitrile (VWR, 99.8%), dichloromethane (VWR, 99.9%), tetrahydrofuran (THF) (Sigma-Aldrich, 99%), n-hexane (Alfa Aesar, 99.5%), ethyl acetate (VWR, 99%), triethylamine (Fisher Scientific, 99%), sodium iodide (Sigma-Aldrich, 99.5%), sodium azide (Sigma-Aldrich, 99.5%), 2,2-bis(bromomethyl)propane-1,3-diol (Sigma-Aldrich, 99%), tetrakis(acetonitrile) copper(I) hexafluorophosphate (Sigma-Aldrich, 99.9%) and bis(t-butyl peroxy)cyclohexane (Sigma-Aldrich, 80%). 1,1-vinylidene fluoride was purchased from Apollo Scientific (≥98%) and used as it is. 1-*tert*-Butyl-4,4,4-tris(dimethylamino)-2,2-bis[tris(dimethylamino) phosphoranyli -denamino]-2λ5,4λ5-catenadi-(phosphazene) (*t*-BuP4, 0.8 M in hexane) and propargyl alcohol were supplied by Sigma-Aldrich and rediluted by an appropriate solvent (hexane or tetrahydrofuran) in a specific glass apparatus. Ethylene oxide (EO) (Sigma-Aldrich, 99.5%) was successively dried over calcium hydride and *n*-butyllithium (n-BuLi) before the polymerization.

The molecular weights, polydispersity indexes ($Đ$) of all precursors and final products, characterized by NMR and size exclusion chromatography, are listed in Table 7.1. The three $(PVDF)_2(PEO)_2$ 4-miktoarm star block copolymers employed in this study have practically the same molecular weight and PVDF/PEO ratios of 0.15, 0.43, and 0.97. For comparison purposes, the 2-arm (linear) $(PVDF_{29}\text{-}N_3)_2$ (M_n = 3700, $Đ$ = 1.23), and PEO-alkylyne (M_n = 10000, $Đ$ = 1.13) precursors, as well as a commercial PVDF homopolymer (M_w = 180000 g/mol, M_n = 71000; purchased from Aldrich) are also used.

Table 7. 1. Molecular characteristics of the samples studied in this chapter.

Sample	Topology	PVDF/PEO ratio (wt%/wt%)[a]	M_n (g/mol)[b]	M_n PVDF (g/mol)[b]	M_n PEO (g/mol)[b]	$Đ^c$
$(PVDF_{29}\text{-}N_3)_2$	2-arm (linear)	1/0	3800	3800	-	1.23
PEO_{227}-Alkyne	1-arm (linear)	0/1	10000	-	10000	1.10
$(PVDF_{29})_2(PEO_{272})_2$	4-arm (miktoarm)	13/87	27800	3800	24000	1.11
$(PVDF_{66})_2(PEO_{227})_2$	4-arm (miktoarm)	29/71	28500	8500	20000	1.13
$(PVDF_{106})_2(PEO_{159})_2$	4-arm (miktoarm)	48/52	27900	13900	14000	1.13

[a] Based on PVDF and PEO M_n values. [b] Estimated from ^{1}H NMR integration. [c] Acquired from SEC analysis. Due to the non-linear baseline, these values are underestimated.

7.2.2 Methods

a) Differential Scanning Calorimetry (DSC)

All DSC experiments were performed with a Perkin Elmer DSC 8000 equipment with an Intracooler II as a cooling system. The calorimeter was calibrated with indium and tin. All experiments were performed employing ultra-high purity nitrogen as a purge gas.

Non-isothermal experiments at different cooling rates were done to study the different polymorphic phases that could exist in the PVDF arms crystals. For non-isothermal DSC scans, first, the samples were heated at 20 ºC/min to 200 ºC. The samples were kept at 200 ºC for 3 min to erase thermal history, and then, they were

cooled at different cooling rates (60, 20, 5, and 1 ºC/min) to room temperature (RT). Finally, they were heated at 20 ºC/min to 200 ºC.

The isothermal experimental protocol suggested by Lorenzo *et al.*[22] was used to determine the overall isothermal crystallization. First, the minimum isothermal crystallization temperature to be used was found. This was done by heating the sample to 200 ºC for 3 minutes to ensure that the sample was completely melted, then it was cooled down at 60 ºC/min to a chosen T_c and immediately heated up again to the molten state (at 20 ºC/min). The lowest T_c, which does not generate any latent heat of fusion during a subsequent DSC heating scan, was selected as the minimum T_c used.[22]

For the isothermal experiments, samples were melted (at 200 ºC during 3 min) to remove any crystalline thermal history. From that temperature, they were cooled at 60 ºC/min (at this cooling rate, the calorimeter has an excellent control of the temperature) to (as mentioned above) a previously chosen isothermal crystallization temperature, T_c. At this temperature, the samples were left to crystallize until saturation, around 40 min in all the samples. After the completed crystallization, a heating scan was carried out at 20 ºC/min until melting to study the polymorphic nature of the isothermally produced crystals.

For the 4-miktoarm star block copolymer samples, when the block of study was the PEO phase, a preliminary first step was carried out to crystallize the PVDF phase until saturation as it crystallizes at higher temperatures than PEO blocks. Once the PVDF blocks are crystallized, a second isothermal crystallization process is carried out at different chosen T_c values. Hence, during the PEO blocks overall isothermal crystallization process, the PVDF component is always semi-crystalline. All the kinetic calculations were performed with the complimentary Origin® plugin developed by Lorenzo *et al.*[22]

b) Fourier Transform Infrared Spectroscopy (FTIR)

A Nicolet 6700 Fourier Transform Infrared spectrometer equipped with an Attenuated Total Reflectance (ATR) Golden Gate MK II with a diamond crystal was employed. Film samples were previously melted and then crystallized at 60, 5, and 1 ºC/min in an external Linkam hot-stage, and after these thermal treatments, they were measured in the FTIR equipment. The measurements were carried out at room temperature after the cooling process. For the isothermal experiments film samples were prepared by first melting bulk samples at 200 ºC for 3 minutes and then cooled them down at 60 ºC/min to 150 ºC to allow their crystallization at this temperature for 2 hours. Finally, the samples were cooled down again at a controlled cooling rate of 20 ºC/min until room temperature, all this protocol was carried out in the same Linkam hot-stage system. FTIR experiments were performed at room temperature.

c) Small and Wide Angle X-Ray Scattering (SAXS/WAXS)

Small Angle X-ray Scattering (SAXS) and Wide Angle X-ray Scattering (WAXS) experiments were performed using synchrotron radiation at beamline BL11-NCD in the ALBA Synchrotron facility. By this technique, it is possible to observe the structural *in situ* evolution of the samples during cooling or heating at scan rates identical to those used in the DSC experiments, allowing a meaningful comparison between the data. Samples were measured in a Linkam hot-stage coupled to a liquid nitrogen cooling system. The samples were first cooled from the melt (200 ºC) at 60, 20, and 1 ºC/min until room temperature or close to room temperature, depending on the sample. Subsequently, the samples were heated to 200 ºC at 20 ºC/min in all cases.

The energy of the X-ray source was 12.4 keV (λ = 1.0 Å). In the WAXS configuration, a Rayonix LX255-HS sample detector with an active area of 230.4×76.8 mm was employed. A sample to detector distance of 15.5 mm with a tilt angle of 27.3° was employed, the resulting pixel size was 44 μm^2. In the case of the SAXS

configuration, the sample detector was a Pilatus 1M, which had an activated image area of 168.7×179.4 mm^2, a total number of pixels of 981×1043, 172×172 μm^2 pixels size, 25 frames/sec rate and the distance employed was 6463 mm.

For the neat PVDF sample, SAXS diffraction experiments were carried out by means of a Rigaku 3-pinhole PSAXS-L equipment operating at 45 kV and 0.88 mA. Cu-Kα transition photons of wavelength λ=1.54 Å were produced by a MicroMax-002+ X-Ray Generator System composed by a microfocus sealed tube source module and an integrated X-Ray generator unit. Flight path and sample chamber in the equipment were under vacuum. A two-dimensional multiwire X-Ray Detector (Gabriel design, 2D-200X) detected the scattered X-Rays.

d) Polarized Light Optical Microscopy (PLOM)

Polymer films were examined with an Olympus BX51 polarizing microscope fitted with a hot-stage (Linkam) and a liquid N_2 system to control the cooling rate and temperature. An Olympus SC50 camera was used to take images. The samples were prepared by the drop-casting method. Solutions (at 4 wt%) containing either the precursors or block copolymers in DMF solvent were drop cast on glass substrates and dried in a heater before observing them under the microscope. The isothermal crystallization experiments were carried out following the same protocol explained before for DSC experiments.

7.3 Results and discussion

7.3.1 Polymer synthesis

The synthesis of the bifunctional iodine transfer polymerization (ITP) agent containing the $N_3(C_3)N_3$ "clickable" moiety and the miktoarm star copolymers, are given in Figure 7.1. Polymerization of VDF using ITP as chain transfer agent and bis (*tert*-butyl peroxy) cyclohexane as initiator yielded the linear polymers PVDF-1, PVDF-2, and PVDF-3 with two 1,3-diazide groups at the middle of the PVDF chains. The molecular characterization data for these samples are given in Table 7.1.

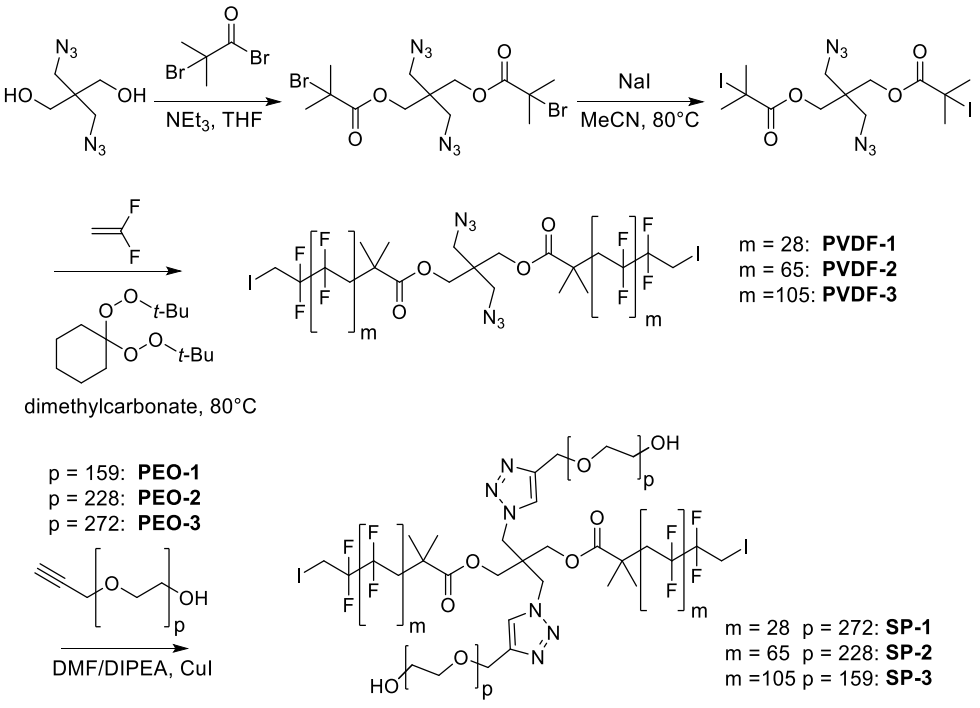

Figure 7. 1. Synthesis of $(PVDF)_2(PEO)_2$ miktoarm star copolymers.

The azide-functionalized PVDF-1, PVDF-2, and PVDF-3 were then reacted with complementary alkyne-functionalized poly(ethylene oxide) PEO-1, PEO-2, and PEO-3 to yield star polymers SP-1, SP-2 and SP-3. The molar masses of the PEO and PVDF blocks were varied. Because of the peculiar mechanism of CuAAC discovered by Finn et al.[23] both azides of the $N_3(C_3)N_3$ moiety react simultaneously,

with complete absence of mono-triazole intermediate. This property of CuAAC is most convenient, as it prevents the need for purification to separate the four-arm miktoarm star from the incompletely-reacted three-arm intermediate, as an excess of PEO-alkyne is not required.

In summary, the three $(PVDF)_2(PEO)_2$ star block copolymers studied here have similar molar masses, and PVDF/PEO ratios are 0.15, 0.41, and 0.92. To compare with the 4-miktoarm star block copolymers, the $(PVDF_{29}\text{-}N_3)_2$ (M_n = 3700, $Đ$ = 1.23), and PEO-alkyne (M_n = 10000, $Đ$ = 1.10) precursors were also analyzed.

7.3.2 Segregation studies in the molten state

SAXS experiments in the melt were performed to ascertain if the miktoarm star copolymer samples are phase segregated in the melt or not. Figure 7.2a shows SAXS curves (plots of intensity as a function of the scattering vector q) for each copolymer at 200 ºC, a temperature well above the melting point of the samples. The curves are mostly featureless, without any significant diffraction peaks. However, if the Lorentz correction is applied (multiplying the intensity (I) by q^2) to the data (Figure 7.2b), a broad scattering peak is observed for the $(PVDF_{29})_2(PEO_{272})_2$ sample, and a very weak broad maximum for the $(PVDF_{66})_2(PEO_{227})_2$ sample. In contrast, the sample $(PVDF_{106})_2(PEO_{159})_2$ still exhibits a featureless SAXS curve. The samples showing the weak SAXS signals in the melt could be either weakly segregated in the melt or melt mixed. It is known that many miscible block copolymers can still show broad peaks in SAXS experiments due to the so-called “hole correlation” effect caused by density fluctuation along the chains.[24]

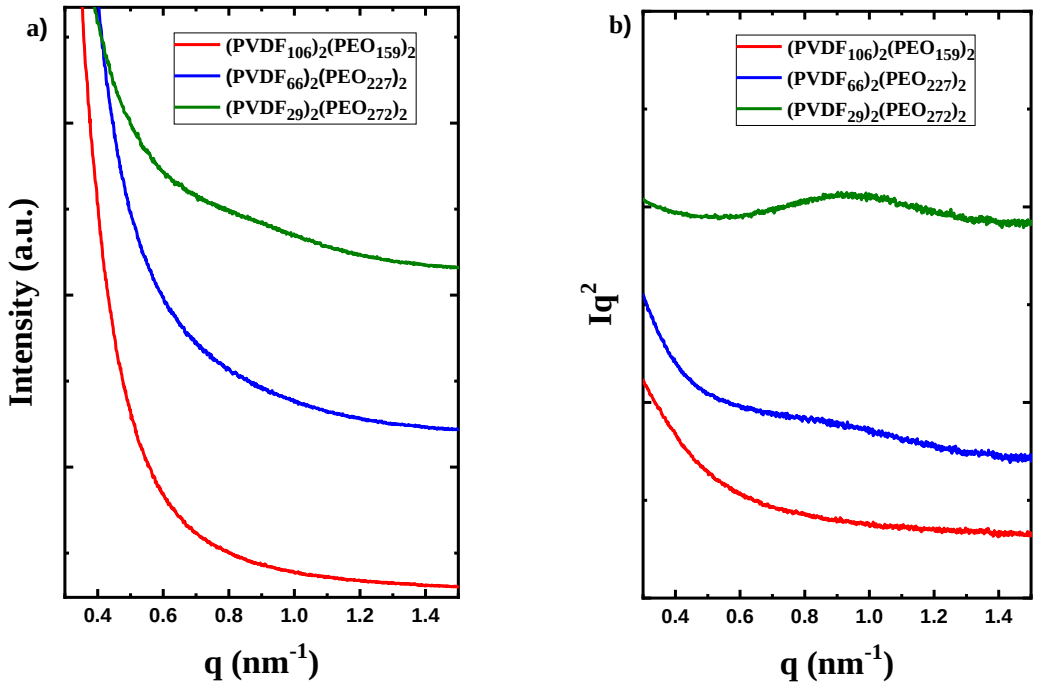

Figure 7. 2. Comparison of SAXS diffractograms for the 4-miktoarm star samples at different compositions at 200 ºC, and b) with Lorentz correction applied.

When block copolymers crystallize from a single phase in the melt, the crystallisable components can form superstructures (like axialites or spherulites) even when they are present in smaller concentrations. If weak phase segregation in the melt exists, crystallization can "break out" of the possible weakly segregated microdomains, and still superstructures like spherulites or axialites can be observed. In our case, as it will be explained and discussed below (Figure 7.3), PLOM experiments show that the PVDF arms can indeed form spherulites during crystallization process from the melt, indicating that the miktoarm star copolymers are either weakly segregated in the melt or even melt-mixed.

The Flory-Huggins theory can be used to estimate an approximate value for the PEO/PVDF interaction parameter, χ_{12}, by employing equation 7.1:[25]

$$\chi_{12} = 0.34 + \frac{V_1}{RT}(\delta_1 - \delta_2)^2 \qquad \text{eq. 7.1}$$

where V_1 is the molar volume of the PEO component (calculated from the molar mass of the repeating unit, M = 44 g/mol, and the density, ρ = 1.13 g/cm^3, and the obtained value is V_1 = 38.94 cm^3/mol), T is a temperature where both polymers are in the molten state, R has a value of 1.987 cal/K mol and δ_1 = 10.17 (cal/cm^3)$^{1/2}$ and δ_2 = 8.56 (cal/cm^3)$^{1/2}$. In our case, the value of χ_{12} calculated at 200 ºC is 0.44.

The segregation strength in a linear diblock copolymer is defined as $\chi_{12}N$, where N is the degree of polymerization. If the approximate value of the segregation strength is under about 10.5 the copolymer is miscible in the melt; if the value is between 10.5 and 30 the copolymer is weakly segregated; values between 30 and 50 indicate an intermediate segregation strength, and finally, with values above 50 there is strong segregation between both components. The values obtained for the samples employed here depend on the composition studied in each case. For the copolymer $(PVDF_{29})_2(PEO_{272})_2$, the value obtained is 25.5, indicating a weak to intermediate segregation strength. However, for $(PVDF_{66})_2(PEO_{227})_2$, the segregation strength is 58.1, and for $(PVDF_{106})_2(PEO_{159})_2$, the value is 93.3, indicating strong segregation strength.

The approximate calculations of the segregation strength seem to overestimate the segregation strength, as the experimental results obtained by SAXS indicate that the samples are either melt mixed or weakly segregated in the melt. Furthermore, PLOM evidence, presented in Figure 7.3, suggests that the PVDF arms can crystallize forming spherulites in the sample with 48% PVDF (i.e., $(PVDF_{106})_2(PEO_{159})_2$) and even in the sample with just 29% PVDF (i.e, $(PVDF_{66})_2(PEO_{227})_2$). In this last case, the only way that the PVDF arms can form spherulites or axialites observable by PLOM is either by crystallizing from a homogeneous melt or by a break-out mechanism in case the miktoarm star copolymer phase segregates in the melt.

The segregation strength in miktoarm star block copolymers is probably lower than that calculated for linear diblock copolymers, as the fact that the arms join in a

common centre possibly makes an additional contribution to lowering the mixing free energy. Previous comparisons between linear and miktoarm star copolymers have indicated that the microphase segregated morphologies in the melt change as a result of increased miscibility in the miktoarm case.[26, 27]

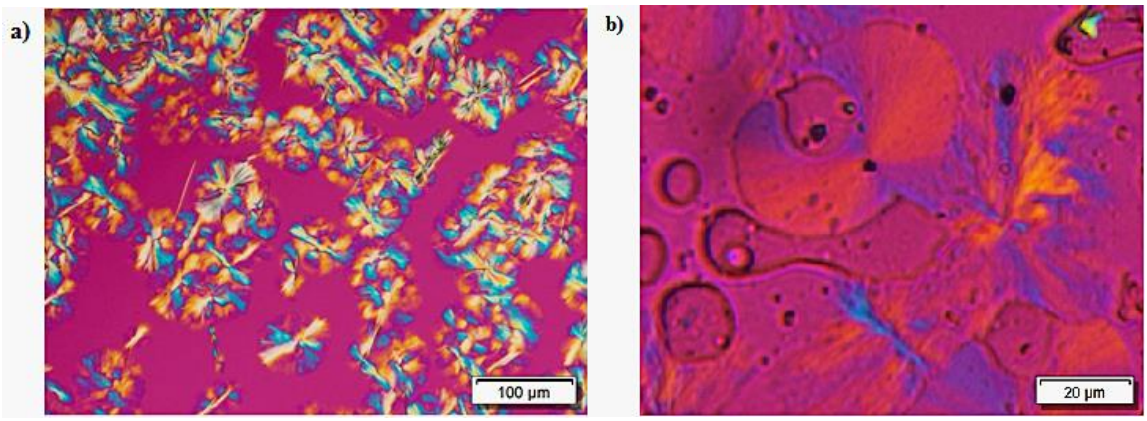

Figure 7. 3. PVDF arms spherulites observed during isothermal crystallization at temperatures above the melting point of the PEO arms in the following 4-miktoarm star copolymer samples: a) $(PVDF_{66})_2(PEO_{227})_2$ crystallized at 143 ºC and b) $(PVDF_{106})_2(PEO_{159})_2$ crystallized at 155 ºC.

7.3.3 Non-isothermal crystallization and melting processes

Figure 7.4 compares the crystallization and melting behaviour of a neat PVDF sample with the precursor $(PVDF_{29}\text{-}N_3)_2$ 2-arm (linear) sample, and Table 7.2 lists the calorimetric parameters extracted from the DSC data. The $(PVDF_{29}\text{-}N_3)_2$ sample crystallizes at higher temperatures than the neat PVDF sample, a result of its much lower molecular weight. Its crystallization enthalpy (ΔH_c = 61.0 J/g) is also higher than that of the neat PVDF sample (ΔH_c = 40.6 J/g). This result indicates that the non-isothermal crystallization kinetics in the $(PVDF_{29}\text{-}N_3)_2$ is also faster than that of the neat PVDF.

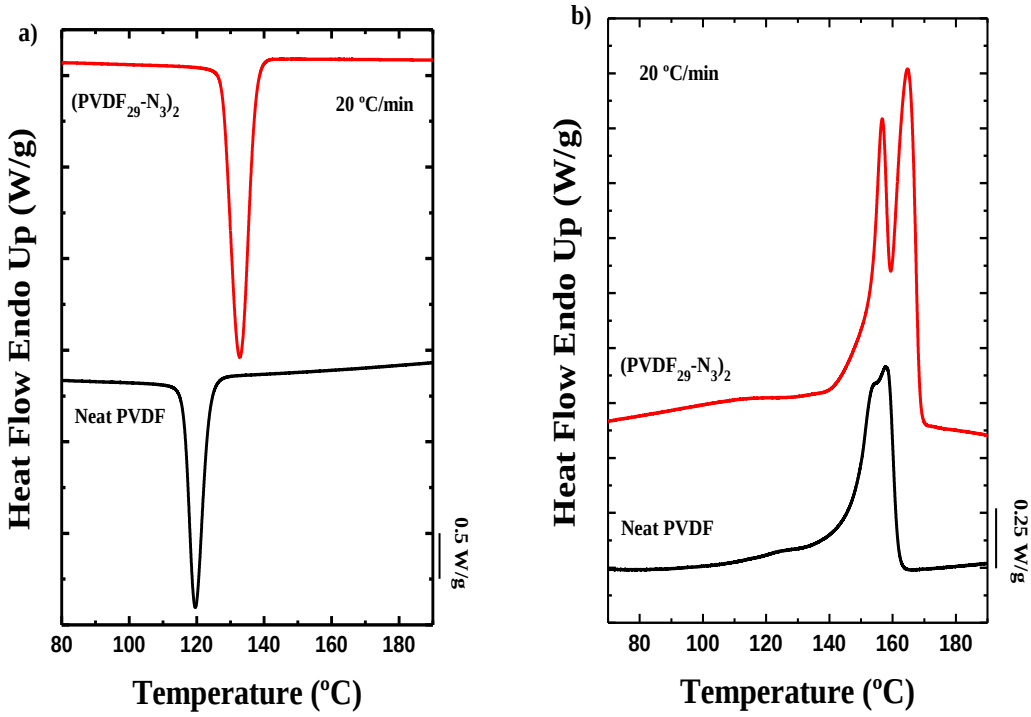

Figure 7. 4. a) Cooling and b) subsequent heating DSC scans at 20 ºC/min for neat PVDF homopolymer and $(PVDF_{29}\text{-}N_3)_2$.

Table 7. 2. Melting and crystallization temperatures and melting and crystallization enthalpies values for the employed samples. The melting and crystallization enthalpies reported have been normalized by the weight fraction of the crystallisable component.

Sample	Rate (ºC/min)	$T_{m\,PEO}$ (ºC)	$T_{m\beta}$ (ºC)	$T_{m\alpha}$ (ºC)	$T_{m\gamma}$ (ºC)	T_c (ºC)	ΔH_m (J/g)	ΔH_c (J/g)
Neat PVDF	20	-	-	158.1	-	119.6	43	41
$(PVDF_{29}\text{-}N_3)_2$	1	-	162.6	167.2	172.2	144.7	54	59
	5	-	159.8	166.0	-	139.9	52	61
	20	-	156.7	164.7	-	132.9	57	61

	60	-	156.2	164.8	-	126.3	57	60
PEO_{227}-Alkyne	1	61.8	-	-	-	41.9	131	126
	5	61.6	-	-	-	36.2	145	136
	20	61.5	-	-	-	29.7	152	143
	60	61.6	-	-	-	24.2	124	106
$(PVDF_{29})_2(PEO_{272})_2$ PVDF arms	1	-	172.2	-	-	150.5	25	22
	5	-	170.6	-	-	146.4	27	19
	20	-	168.4	173.1	-	140.4	25	21
	60	-	168.8	173.1	-	134.4	23	31
PEO arms	1	62.6	-	-	-	46.8	119	115
	5	61.6	-	-	-	43.3	117	113
	20	59.3	-	-	-	38.3	123	118
	60	61.4	-	-	-	32.6	116	95
$(PVDF_{66})_2(PEO_{227})_2$ PVDF arms	1	-	171.1	-	-	147.9	31	35
	5	-	168.9	-	-	144.4	34	36
	20	-	165.8	170.9	-	136.9	34	27
	60	-	166.1	172.2		129.1	34	35
PEO arms	1	61.2	-	-	-	45.1	107	102
	5	60.8	-	-	-	41.6	114	109
	20	58.2	-	-	-	37.3	132	126

	60	59.7	-	-	-	28.5	109	89
$(PVDF_{106})_2(PEO_{159})_2$ PVDF arms	1	-	171.9	-	-	149.9	32	33
	5	-	170.1	-	-	145.4	28	34
	20	-	167.1	171.8	-	137.5	31	30
	60	-	167.1	171.9		130.4	26	33
PEO arms	1	60.3	-	-	-	44.8	111	98
	5	58.9	-	-	-	40.8	117	109
	20	56.4	-	-	-	35.8	129	125
	60	59.0	-	-	-	31.1	110	85

The lower molecular weight has a determining influence in comparison with the change in chemical structure. It must be noted that the 2-arm (linear) sample has a complex chemical moiety in the middle of the chain (see Figure 7.1) that interrupts the linear crystallizable chain segments, dividing each molecule into two short length arms, each one with less than 2000 g/mol in number average molecular weight. This bulky chemical group in the middle of the chain is excluded to the amorphous regions and cannot enter inside the PVDF crystalline lattice, as indicated by the WAXS diffractograms shown in Figure 7.5. The WAXS pattern for the 2-arm (linear) sample shows the typical reflections attributed to the PVDF (see discussion below).

Figure 7.4b shows the subsequent heating DSC scans (after the cooling of Figure 7.4a). The melting temperatures (T_m) are in the same temperature range for both samples, but in $(PVDF_{29}\text{-}N_3)_2$, two well-differentiated melting peaks appear. This effect is probably due to the polymorphic structure of PVDF.[28, 29] The difference in melting points is not expected, as the low M_n sample should have a lower T_m value.

These results could be explained by the different chemical structure of the samples, but WAXS indicates (Figure 7.6) that the crystalline structure (apart from polymorphic phases) corresponds in both cases to that expected by PVDF. Another possibility could be a difference in the lamellar thickness of both samples. The SAXS patterns and the lamellar thickness values obtained for these samples are shown in the Figure 7.5 and Table 7.3. The increase in lamellar thickness of (PVDF$_{29}$-N$_3$)$_2$ sample explains the remarkable rise of the melting point exhibited by this sample when it is compared with the neat PVDF.

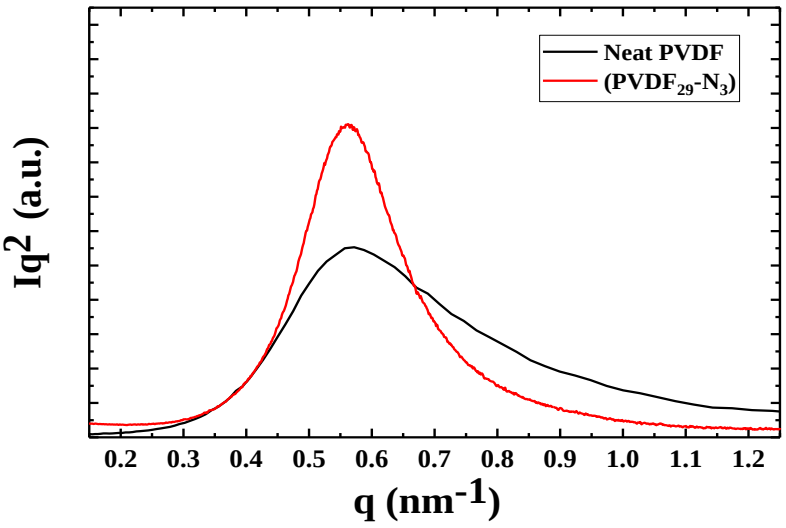

Figure 7. 5. Lorentz-corrected SAXS patterns for neat PVDF and (PVDF$_{29}$-N$_3$)$_2$ sample.

Table 7. 3. Comparison between DSC parameters related to the enthalpy (ΔH_m), crystallinity (X_c), and the SAXS parameters related to the long period (d^*) values and average lamellar thicknesses (l) obtained for the studied PVDF samples.

	DSC		**SAXS**	
Sample	ΔH_m (J/g)	X_c (%)	d^* (nm)	l (nm)
Neat PVDF	43	40	11.2	4.5
(PVDF$_{29}$-N$_3$)$_2$	57	53	11.2	6.0

Neat PVDF crystallizes upon cooling at 20 ºC/min preferentially in the paraelectric α-phase, as commonly reported in the literature,[30] and Figure 7.4b shows a melting endotherm for the neat PVDF sample with a small shoulder at lower temperatures, that probably indicates the melting of a small amount of crystals, followed by the melting of a majority of α-phase crystals.

Wide Angle X-ray Scattering (WAXS) analysis has been performed to detect the phases that can coexist in the different samples. Figure 7.6 shows WAXS diffractograms obtained at room temperature for $(PVDF_{29}\text{-}N_3)_2$ samples that were previously cooled from the melt at two different cooling rates, 20 ºC/min, and 1 ºC/min.[31] However, neat PVDF usually crystallizes in the paraelectric α-phase when the crystallization occurs from the melt,[32] regardless of the cooling rate employed to prepare the sample.[33] To promote the formation of the most interesting β-phase, the material needs to undergo special treatments like stretching, high-energy irradiation, or electric poling. Figure 7.6 shows a peculiar result, different from literature reports on neat PVDF. Slow cooling at 1 ºC/min induces the formation of a certain amount of β-phase in the $(PVDF_{29}\text{-}N_3)_2$ sample, while faster cooling (at 20 ºC/min) can only produce the paraelectric α-phase. This is probably due to the difference in the chemical structure between neat PVDF (i.e., 100% linear crystallisable chains) and $(PVDF_{29}\text{-}N_3)_2$ sample (i.e., each linear chain is divided into two crystallisable segments by the bulky $\text{-}N_3$ group).

Figure 7.6 shows that the $(PVDF_{29}\text{-}N_3)_2$ sample, cooled previously at 20 ºC/min, displays four main characteristic reflections at 25 ºC at the following *q*-values: 12.5; 13.0; 14.1 and 18.8 nm^{-1}. These reflections can be assigned to the following crystallographic planes: (100), (020), (110), (120/021) of the α-crystalline phase of PVDF.[34-37] The α-crystalline phase of PVDF is characterized by a pseudo-orthorhombic unit cell with a = 0.496 nm, b = 0.964 nm, c = 0.462 nm and β = 90º, with *P2/C* space group.[34, 37, 38] Table 7.4 reports the indexing of the WAXS patterns along with values reported in the literature.[39-41] For the sample cooled at 20 ºC/min, we

could not detect the presence of any β-phase PVDF crystals at room temperature by WAXS experiments.

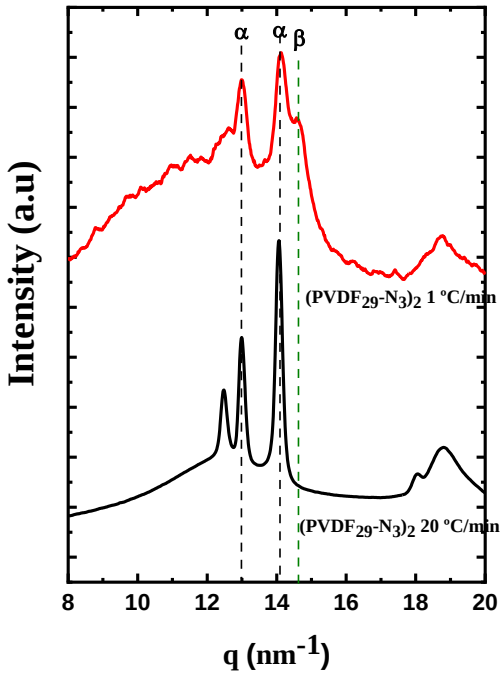

Figure 7. 6. WAXS diffraction patterns determined at 25 ºC in (PVDF$_{29}$-N$_3$)$_2$ samples previously crystallized from the melt by cooling them at 1 and 20 ºC/min.

On the other hand, Figure 7.6 also shows a WAXS pattern for the same (PVDF$_{29}$-N$_3$)$_2$ sample but cooled previously at 1 ºC/min. In this case, both α- and β-phases are presented in the scattering pattern displayed in Figure 7.6. The existence of these two phases at the same time is unusual but possible as observed before in the literature.[42-44] The β-phase of PVDF is characterized by an orthorhombic unit cell with *Cm2m* space group and dimensions a = 0.847 nm, b = 0.490 nm, and c = 0.256 nm.[39, 45] One characteristic reflection of PVDF β-phase is that corresponding to the (200/110) plane that appears in Figure 7.6 at a *q*-value of 14.3 nm^{-1}.[45, 46] This value is very close to that of the (110) plane corresponding to the α-phase, i.e., 14.1 nm^{-1}.

Due to the similar WAXS diffraction patterns, sometimes reflections for α- and β-phases can be overlapped.

Going back to Figure 7.4b, the $(PVDF_{29}\text{-}N_3)_2$ sample exhibits a clear and higher intensity low temperature melting peak in comparison to that of the neat PVDF sample, which possibly corresponds to the melting of β-phase crystals (see also evidences of β-phase presence by FTIR in Figure 7.12). At higher temperatures, the sample displays a very intense endothermic peak where α-phase crystals melt. The special chain topology of this precursor with a central bulky chemically different group is triggering the crystallization of some of the short PVDF arms into less stable crystalline β-phase crystals. The amount of β-phase formed is much larger than in the neat PVDF crystallized by a previous cooling process at 20 ºC/min (as judged by the intensity and area under the melting peaks in Figure 7.4b).

Table 7. 4. Values of q, crystalline planes d_{hkl} reported and d_{hkl} values of studied samples crystallized at 20 ºC/min.

Sample	q (nm^{-1})	d (nm)	d reported (nm)[39-41]	Crystalline planes
$(PVDF_{29}\text{-}N_3)_2$	12.5	0.50	0.49	(100) α
	13.0	0.48	0.48	(020) α
	14.1	0.44	0.44	(110) α
	18.8	0.33	0.33	(021) α
$(PVDF_{29})_2(PEO_{272})_2$	13.6	0.46	0.46	(120)
	14.3	0.43	0.44	(110) β
	16.5	0.38	0.38	(032)
$(PVDF_{66})_2(PEO_{227})_2$	13.6	0.46	0.46	(120)
	14.3	0.43	0.44	(110) β
	16.5	0.38	0.38	(032)
$(PVDF_{106})_2(PEO_{159})_2$	13.6	0.46	0.46	(120)
	14.3	0.43	0.44	(110) β
	16.5	0.38	0.38	(032)
PEO_{227}-Alkyne	13.6	0.46	0.46	(120)
	16.5	0.38	0.38	(032)

One of the advantages of performing *in situ* WAXS at the synchrotron is that diffractograms can be obtained in real-time as the samples are cooled or heated at 20 ºC/min. Hence, the collected data can be directly compared with DSC results. Figure 7.7 presents DSC data for all the synthesized samples in this work, while Figures 7.8 (synthesized homopolymers) and 7.10 (miktoarm stars copolymers)

show the corresponding WAXS patterns obtained under identical thermal history. Table 7.2 reports all relevant calorimetric data.

Figure 7.7a shows the cooling scans at 20 ºC/min for all synthesized samples. The low-temperature exotherms around 30 ºC are due to the crystallization of the PEO component in the samples and those at much higher temperatures, around 130 ºC correspond to the PVDF component. It can be observed that both phases can crystallize for all compositions, and in all cases, the arms within the 4-miktoarm samples crystallize at higher temperatures in comparison with the precursor reference materials (i.e., $(PVDF_{29}\text{-}N_3)_2$ and PEO_{227}-Alkyne). In the case of the PEO, this increase we have attributed to a probably nucleation effect that occurs due to the previously crystallized PVDF phase upon cooling from the melt. In the case of the PVDF phase, Figure 7.7a shows that 4-miktoarm star copolymer samples crystallize at higher temperatures than the $(PVDF_{29}\text{-}N_3)_2$ precursor. This is an unusual behaviour, as in block copolymers the crystallization temperature for the precursor homopolymer is normally higher than that of the same block within the copolymer.[47] This probably corresponds to a nucleation effect caused by catalytic remains, as in order to attach the PEO arms, a catalyst (CuAAC) has been added to the synthesis medium.

Figure 7.7b presents the subsequent DSC heating scans of samples cooled in Figure 7.7a. The melting peaks at low temperatures (~ 55 ºC) correspond to the melting of the PEO component and those at high temperatures (~ 150-170 ºC) to the melting of the PVDF crystalline phases. The PEO crystalline phase melting peak seems to be constant for both precursors and 4-miktoarm block copolymer samples. This suggests that after the PVDF arms crystallize, an important phase segregation is generated, as the amorphous regions of PVDF do not seem to alter the PEO melting behaviour.

On the other hand, Figure 7.7b shows that for PVDF some differences are observed between the precursor and the 4-miktoarm block copolymer samples. The first one is that the melting points for the PVDF arms crystals are higher in the 4-

miktoarm block copolymer samples, or when the PEO arms are present in the material. The M_n values of the PVDF arms increase upon increasing the fraction of PVDF in the 4-miktoarm copolymers from 13 to 29 to 48% (see Table 7.1), so an increase in T_m value between these samples would be expected, but it is not seen (the corresponding melting values are reported in Table 7.2 and are 142.0, 137.0 and 137.5 ^oC, respectively).

The second and significant difference observed in these heating scans of Figure 7.7b is referred to the PVDF phase melting peaks. The $(PVDF_{29}\text{-}N_3)_2$ precursor has two well-defined melting peaks, and the highest temperature one, is the most prominent. On the other hand, for the 4-miktoarm star block copolymers, independently of the composition, the first melting peak is the predominant one, which corresponds to lower temperatures. The most stable phase always melts at higher temperatures, which in our case could corresponds either to the paraelectric α-phase or to the ferroelectric γ-phase. The less stable one, the ferroelectric β-phase, melts at lower temperatures.

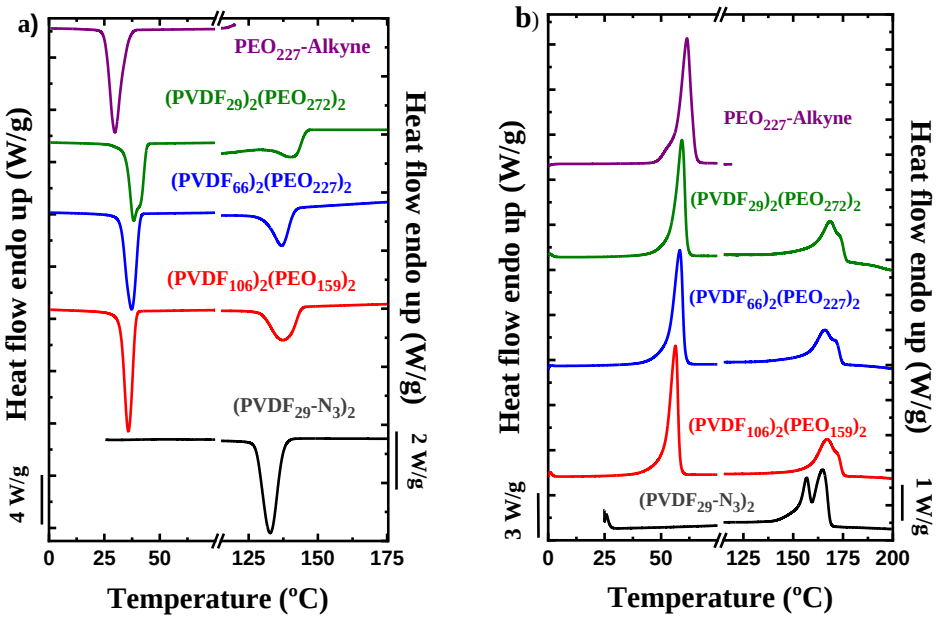

Figure 7. 7. a) DSC cooling scans from the melt at 20 ºC/min and b) subsequent heating scans at 20 ºC/min for the five samples synthesized.

Figure 7.8 shows WAXS diffractograms obtained during *in situ* heating at 20 ºC/min for the two samples that can be considered similar to homopolymers, i.e., $(PVDF_{29}\text{-}N_3)_2$ and PEO_{227}-Alkyne. The samples were previously crystallized from the melt by controlled cooling at 20 ºC/min. These WAXS patterns can be directly compared to the DSC heating scans in Figure 7.6b.

Figure 7.8a shows that $(PVDF_{29}\text{-}N_3)_2$ displays the four main α-phase characteristic reflections at 100 ºC (below its melting point). The WAXS patterns at temperatures between 25 and 100 ºC showed identical reflections than at 100ºC. These reflections can be assigned to the following crystallographic planes: (100), (020), (110), and (120/021), which correspond to the crystalline α-phase of PVDF. Upon increasing temperature from 100 to 160 ºC, these four main reflections remain qualitatively similar, although at 160 ºC their intensities are substantially reduced as the

material starts to melt. In fact, at 170 ºC only traces of crystallinity remain, and the patterns collected at 180-200 ºC only show the typical amorphous halo.

In Figure 7.8b, WAXS diffractograms corresponding to PEO$_{227}$-Alkyne diffraction pattern can be observed. PEO crystallizes in a monoclinic unit cell with dimensions a = 0.805 nm, b = 1.304 nm, c = 1.948 nm and β = 125.4º and P21/aC2h space group. Figure 7.4b shows that once the polymer crystallizes from the melt, two main reflections can be observed at 13.6 and 16.5 nm^{-1} which can be assigned to the (120) and (032) planes.[41, 48]

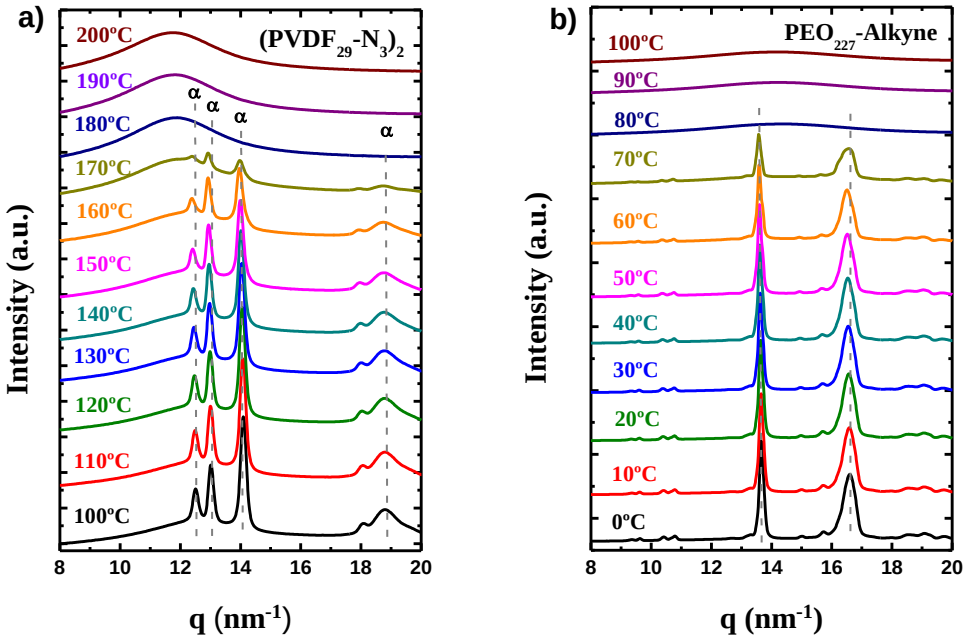

Figure 7. 8. WAXS diffraction patterns during heating at 20 ºC/min (the samples were previously cooled from the melt at 20 ºC/min) at the indicated temperatures for a) (PVDF$_{29}$-N$_3$)$_2$ and b) PEO$_{227}$-Alkyne.

Figure 7.8a does not show any clear signs of any other PVDF crystal phases. The characteristic reflection of PVDF β-phase corresponding to the (200/110) plane that should appear at a *q*-value of 14.3 nm^{-1} is apparently absent. However, its *q*-value is very close to that of the (110) plane corresponding to the α-phase, i.e., 14.1 nm^{-1}.

Therefore, it is also possible that in Figure 7.8a there could be some overlap between these two reflections. A close-up of the WAXS diffractograms in the region between 13.5 and 14.5 nm^{-1} can be observed in Figure 7.9a. Additionally, we have measured the intensity of the scattered X-rays at 14.1 nm^{-1} (corresponding to the α-phase) and that at 14.3 nm^{-1} (corresponding to the β-phase), and they are plotted as a function of temperature in Figure 7.9b. It can be observed that the intensity at 14.3 nm^{-1} is much smaller than that at 14.1 nm^{-1} and decreases gradually with temperature until it becomes zero at a temperature of 170 ºC. According to the DSC scans in Figure 7.7b, the melting of the β-phase occurs at 169 ºC in full agreement with WAXS data.

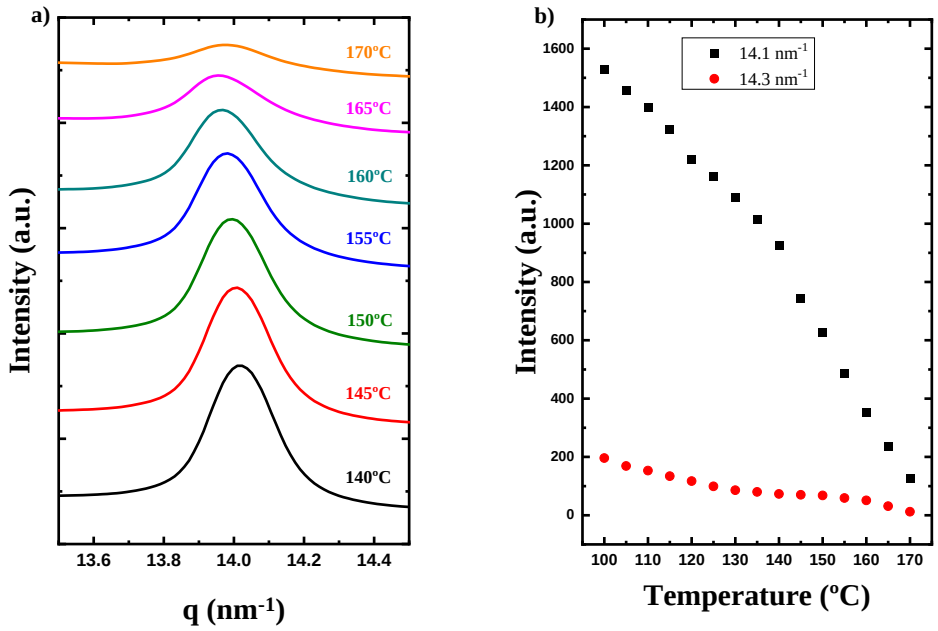

Figure 7. 9. a) Evolution of the peak at 14.1 nm^{-1}, between 140-170ºC, during the heating in WAXS diffraction of the $(PVDF_{29}\text{-}N_3)_2$ when the crystallization rate is 20ºC/min. b) Evolution of the intensity of the peak at 14.1 nm^{-1} and the tail of this peak at 14.3 nm^{-1} during the heating in the WAXS analysis of the $(PVDF_{29}\text{-}N_3)_2$ when the sample is cooled down at 20ºC/min.

In the case of the miktoarm star block copolymers, Figure 7.10 shows WAXS patterns during heating at 20 ºC/min that can be compared with the DSC heating

scans of Figure 7.7b. In the three studied copolymer samples, there is just one main peak for the PVDF component that corresponds to the (110) PVDF β-phase reflection centred around a *q*-value of approximately 14.3 nm^{-1} (see the vertical dashed line in Figures 7.10 a-c). When the PVDF content increases in the copolymers (from Figure 7.10a to 7.10c), the relative amount of PVDF β-phase also increases, and this is well appreciated in WAXS results. That is why in the 13/87 based copolymer (Figure 7.10a), the PVDF β-phase reflection is quite small in comparison with the PEO related ones.

According to the DSC heating scans shown in Figure 7.7b, the melting endotherms corresponding to the crystals of PVDF arms within the three miktoarm star copolymer samples are very similar and display an intense lower melting endotherm (most likely the melting of a β-phase according to the WAXS results in Figure 7.10) with a higher intensity and a much higher enthalpy of melting that the high-temperature shoulder (most likely the melting of the α-phase). The small amount of α-phase (as indicated by the DSC results of Figure 7.7b), is difficult to detect by WAXS, as its corresponding reflection appears around a *q*-value of 14.1 nm^{-1}, and it is overlap with the β-phase reflection at 14.3 nm^{-1} (dominant in Figure 7.10). A similar analysis of the intensities of the reflections performed in Figure 7.9a can be applied to the samples in Figure 7.10, and the detection of the overlapping reflections can be observed, although the signals are much noisier due to the presence of the PEO component in the samples.

Summarizing, both DSC and WAXS results clearly show that the PVDF component within the 4-miktoarm star block copolymers crystallize at 20 ºC/min with a predominant amount of β-phase, in comparison with the PVDF star precursor or to the neat PVDF. This is a very interesting result, as the β-phase is the most important phase for ferroelectric and piezoelectric properties.

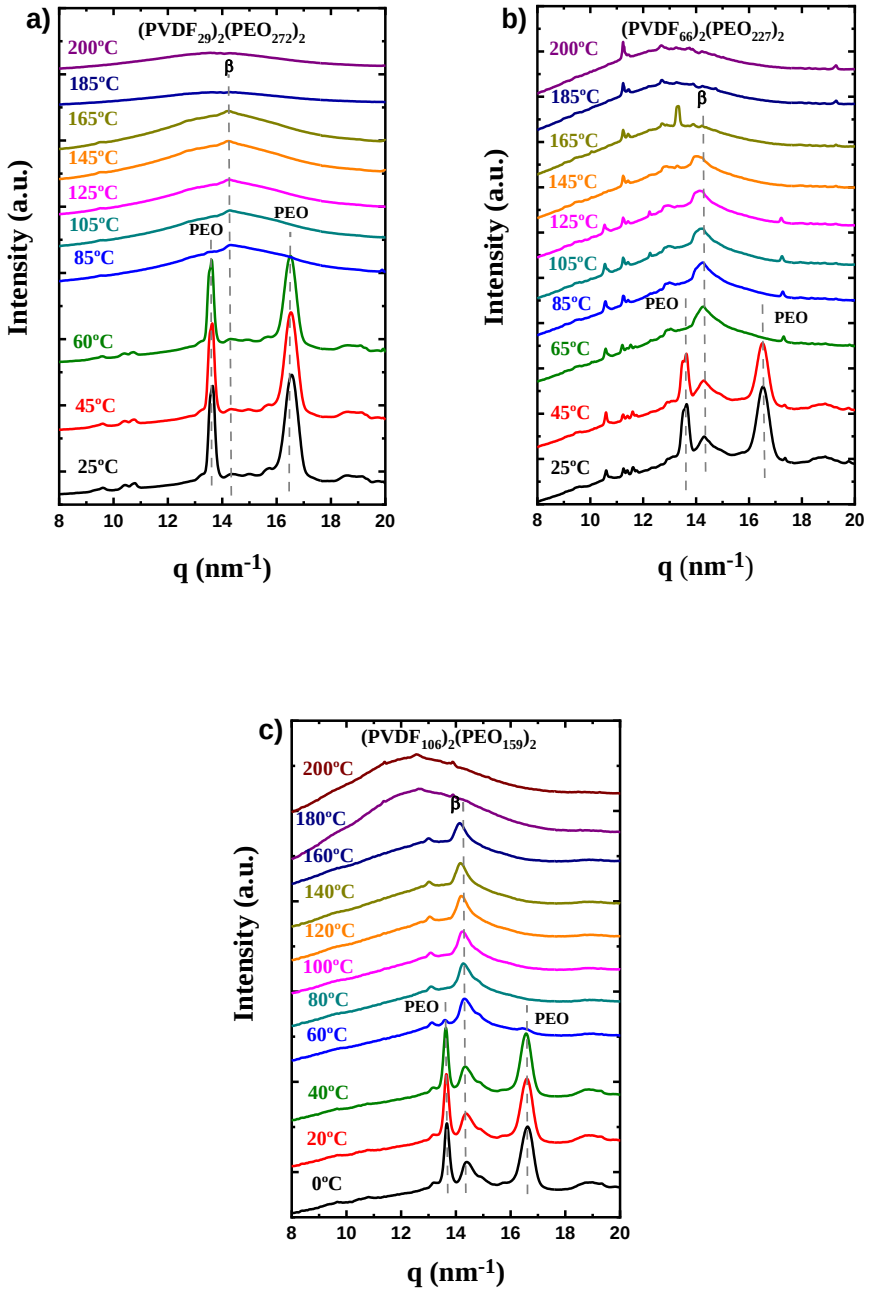

Figure 7. 10. WAXS diffraction patterns of 4-miktoarm star copolymers a) $(PVDF_{29})_2(PEO_{272})_2$, b) $(PVDF_{66})_2(PEO_{227})_2$, and c) $(PVDF_{106})_2(PEO_{159})_2$ all of them crystallized at 20ºC/min.

As the formation of the β-phase was promoted in our precursor $(PVDF_{29}\text{-}N_3)_2$ sample (see Figure 7.6) by slow cooling from the melt, we decided to explore the effects of different cooling rates by DSC. Samples were cooled from the melt at four

different cooling rates (60, 20, 5 and 1 ºC/min), and then heated at the same heating rate (20 ºC/min). The heating scans are plotted together in Figure 7.11 in the temperature range where the PVDF component melts, as this is the component of interest in this work.

Figure 7.11a shows that cooling at different rates, the polymorphic structure of $(PVDF_{29}\text{-}N_3)_2$ changes. Considering that the first melting peak at temperatures between 157 and 163 ºC is due to the melting of β-phase crystals, the second prominent peak at temperatures around 165 ºC is probably due to the melting of α-phase crystals. In fact, for the sample cooled at 20 ºC/min, Figure 7.10a demonstrated by WAXS that the sample preferentially crystallized in the crystalline α-phase (with a small amount of β-phase, as indicated in Figure 7.9a). Judging by the area under the melting peaks in Figure 7.11a, it is clear that the amount of β-phase formed increases as the cooling rate decreases, and this is unexpected behaviour.

Based on previous literature for neat PVDF samples, normally, the β-phase is promoted by quenching the sample at very high cooling rates, i.e., by immersing the sample in cold water after the PVDF sample has been previously annealed at 150 ºC for 1 hour using a laboratory press.[31] In the case of the precursor $(PVDF_{29}\text{-}N_3)_2$ sample cooled at 1 ºC/min, the melting endotherm shows a large low-temperature melting peak assigned to the melting of β-phase crystals, followed by a small shoulder at around 169 ºC, which is probably due to the melting of α-phase crystals. Finally, at a temperature of 171 ºC, a very small melting endotherm can be observed, which may correspond to a small amount of γ-phase.[49, 50]

In the case of the three 4-miktoarm star block copolymer samples (Figure 7.11b-d) the β-phase is dominant at 20 ºC/min (and 60 ºC/min), as previously demonstrated by WAXS (Figure 7.10). As the cooling rate is decreased to 5 or 1 ºC/min, a single melting exothermic peak can be observed in all samples that corresponds to the melting of PVDF β-phase crystals. This result is remarkable, as slow cooling of the three synthesized 4-miktoarm star block copolymers results in materials whose PVDF fraction crystallizes exclusively in the ferroelectric/piezoelectric β-phase.

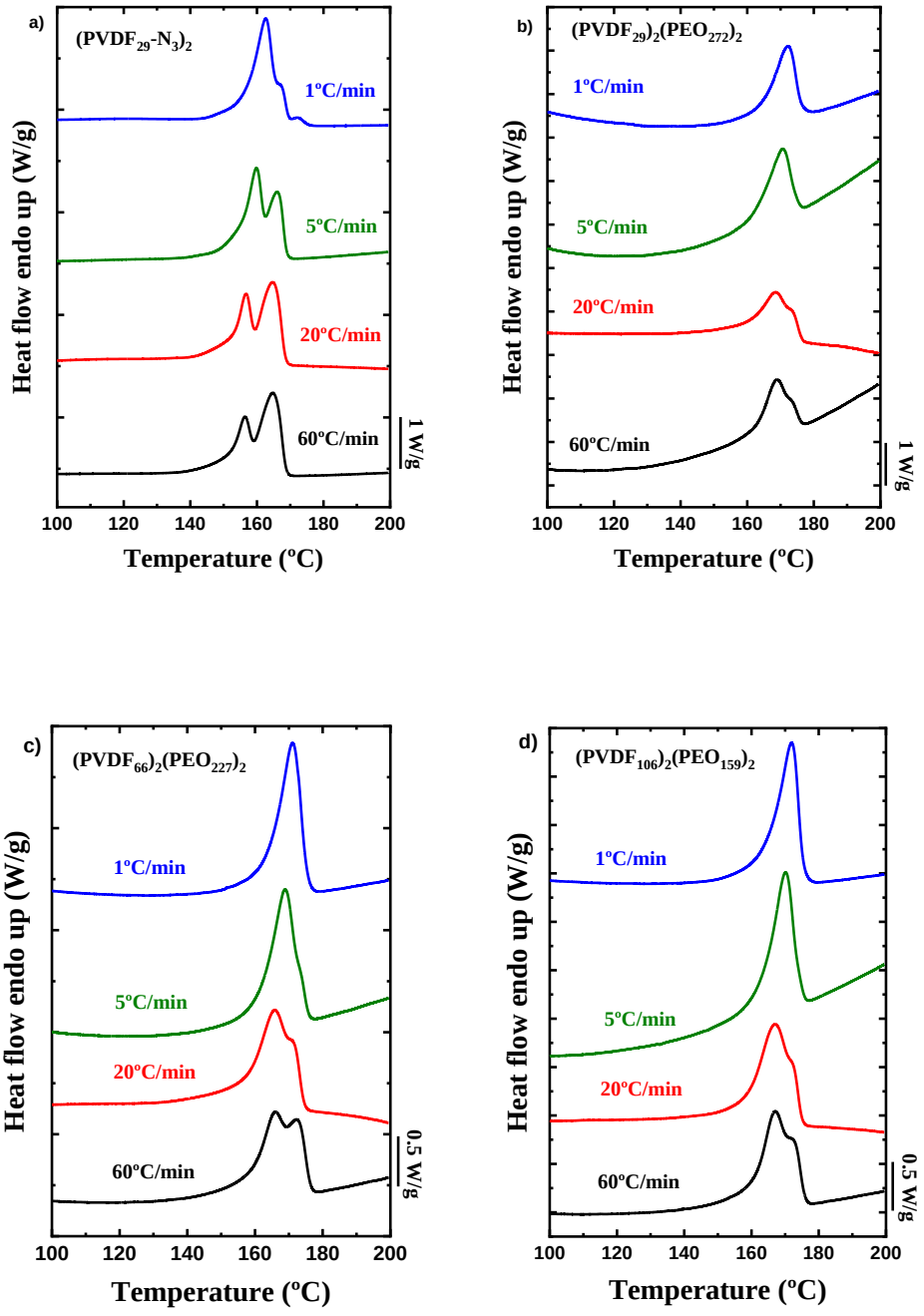

Figure 7. 11. Heating scans at 20 ºC/min after different cooling scans at 60, 20, 5, and 1 ºC/min for a) $(PVDF_{29}\text{-}N_3)_2$, b) $(PVDF_{29})_2(PEO_{272})_2$ sample, c) $(PVDF_{66})_2(PEO_{227})_2$ sample and d) $(PVDF_{106})_2(PEO_{159})_2$ sample.

7.3.4 Non-isothermal crystalline phase detection

FTIR spectroscopy is another important technique to identify PVDF polymorphism. However, as the 4-miktoarm star block copolymers contain both PEO and PVDF phases, band overlap can make difficult the identification tasks of the various phases in PVDF. We first show the results obtained by FTIR on the homopolymer samples (i.e., $(PVDF_{29}\text{-}N_3)_2$ and PEO_{227}-Alkyne) to identify the main bands of each polymer, and then we describe the results obtained in the copolymers. The samples were cooled at different cooling rates (1, 5 and 60 ºC/min), and then their FTIR spectra were recorded at room temperature.

Figure 7.12 presents the FTIR spectra for PEO_{227}-Alkyne and $(PVDF_{29}\text{-}N_3)_2$ samples. For PEO, the most characteristic IR bands are located at 841, 960 and 1100 cm^{-1}.[51] Table 7.5 shows all the main bands that appear in the FTIR analysis in Figures 7.12 and 7.13.

Table 7. 5. Values and description of main FTIR bands for α, β, γ-phases for PVDF and PEO.

Wavenumber (cm^{-1})	Phase	Description[52, 53]
764	α-PVDF	C-C in plane rocking vibration
796	α-PVDF	CH_2 rocking
833	γ-PVDF	-
840	β-PVDF	CH_2,CF_2 asymmetric stretching vibration
841	PEO	CH_2 wagging
960	PEO	CH_2-CH_2 rocking
976	α-PVDF	CH out of plane deformation
1100	PEO	C-O-C stretching
1232	γ-PVDF	CF out of plane deformation
1275	β-PVDF	CF out of plane deformation

In the case of polymorphic PVDF, each phase has its own characteristic bands. For the α-phase, the main bands are located at 764, 796 and 976 cm^{-1}; in the case of

the β-phase the main bands appear at 840 and 1275 cm^{-1},[52] and for the γ-phase the characteristic bands should be at 1232 cm^{-1}.[53, 54] Vertical dashed lines highlight the main bands observed in Figure 7.12.

For $(PVDF_{29}\text{-}N_3)_2$, previously cooled at 60 ºC/min, shown in Figure 7.12b, there are two small bands at 1275 cm^{-1} and 840 cm^{-1}, which indicate that there is a small amount of β-phase, while the presence of the other characteristic PVDF bands corresponds to the α-phase. When the cooling rate decreases, the bands corresponding to the β-phase increase their intensity (see the two vertical dashed red lines in Figure 7.12b), corroborating the results obtained by DSC. FTIR bands corresponding to the γ-phase cannot be observed in the sample cooled at 1 ºC/min, as the amount of γ-phase is probably too small for detection.

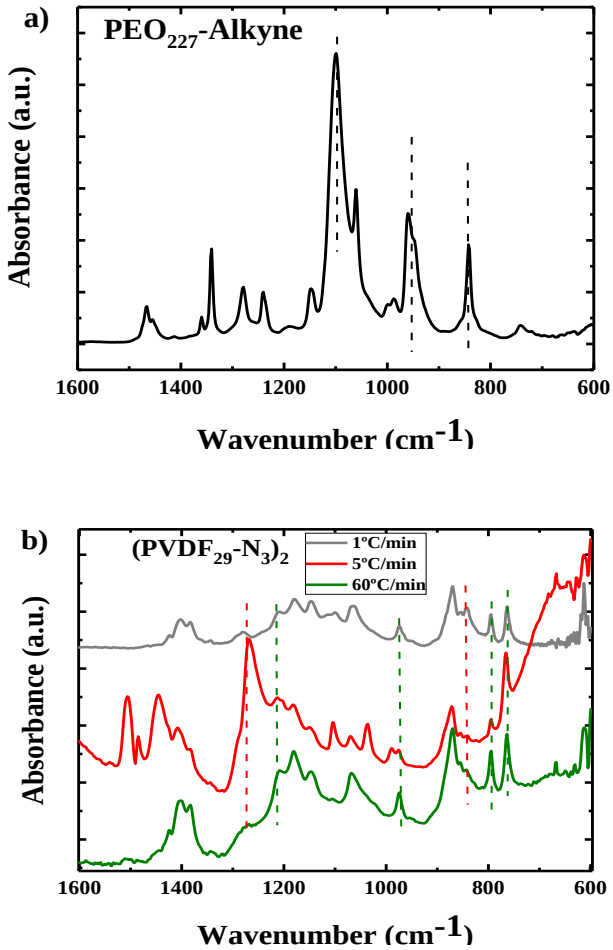

Figure 7. 12. FTIR spectra for a) PEO_{227}-Alkyne and b) $(PVDF_{29}\text{-}N_3)_2$, where for the PVDF, different cooling rates are applied. The different vertical dashed lines represent the different phases. PEO: black. PVDF α- phase: green and PVDF β-phase: red.

In the case of the 4-miktoarm samples, represented in Figure 7.13, the only characteristic band of the β-phase crystals that do not overlap with a characteristic band of PEO is that located at 1275 cm^{-1}. Figure 7.13 shows that the PVDF based 4-miktoarm star copolymers always crystallize with predominant β-phase crystals independently of the cooling rate applied and independently of the composition. The results are consistent with the DSC scans presented in Figure 7.11. Moreover, it is possible to observe how a small band at 976 cm^{-1}, which corresponds to the α-phase,

is very clear at high cooling rates. This band decreases in intensity when the cooling rate decreases, almost disappearing when the cooling rate is 1 ºC/min.

The results presented above by DSC, WAXS, and FTIR indicate that when the cooling rate decreases, the 4-miktoarm star copolymers crystallize preferentially in the β-phase. In the case of the 1 ºC/min cooling rate, the materials crystallize almost exclusively in the PVDF ferroelectric/piezoelectric β-phase modification. We speculate that the reason behind this remarkable behaviour is the peculiar chain packing of the PVDF arms in the star topology, as the arms radiate from a common centre. The centre of each star will not be able to crystallize and must remain in the amorphous regions of spherulites (interlamellar, interfibrillar and inter-spherulitic regions). The peculiar star chain topology probably prevents the PVDF arms to efficiently pack within the crystals in the lowest energy $TG^{+}TG^{-}TG^{+}TG^{-}$ chain conformation required to produce the α-phase, and as a result, the less stable β-phase can be formed even at low cooling rates. The exclusive formation of the β-phase at low cooling rates turns these 4-miktoarm copolymers into potentially very interesting candidates for energy harvesting applications.

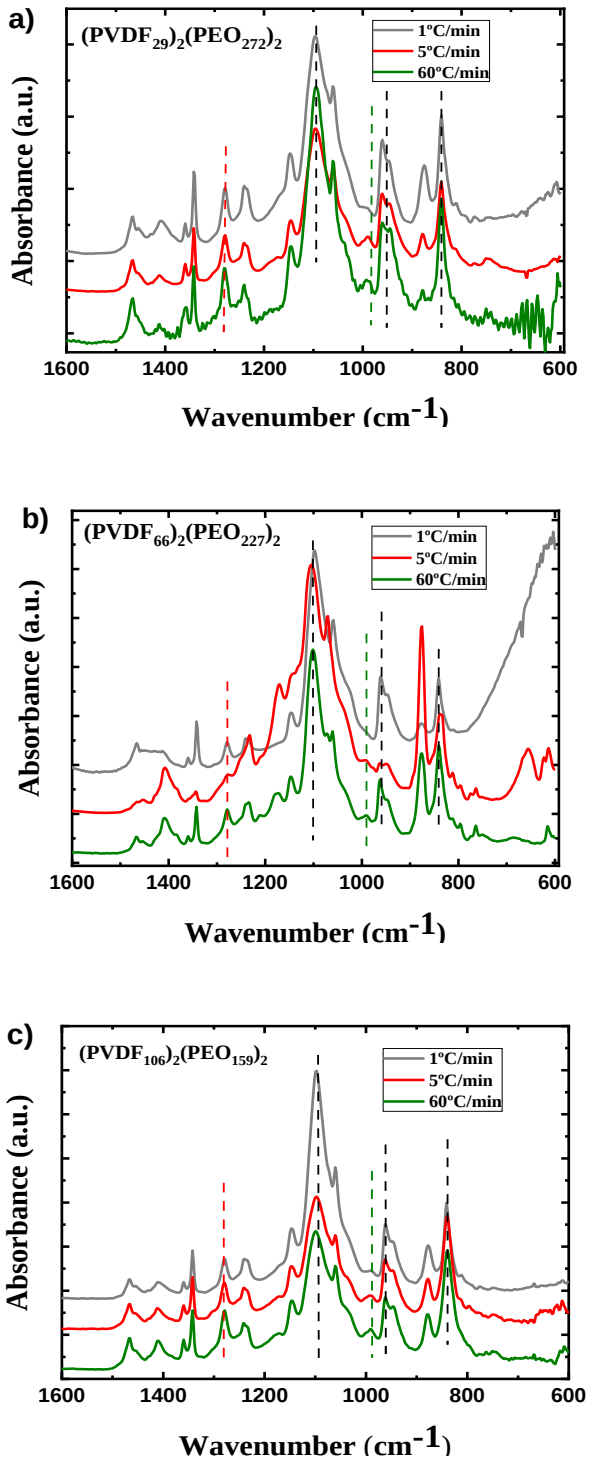

Figure 7. 13. FTIR spectra of the 4-miktoarm star copolymers a) $(PVDF_{29})_2(PEO_{272})_2$ sample, b) $(PVDF_{66})_2(PEO_{227})_2$ sample and c) $(PVDF_{106})_2(PEO_{159})_2$ sample cooled at different cooling rates. The different vertical dashed lines represent the different phases. PEO: black, PVDF α-phase: green and PVDF β-phase: red.

7.3.5 Isothermal crystallization kinetics

The determination of the crystallization kinetic parameters for PVDF and PEO blocks in every sample was carried out. When the PVDF blocks are crystallized, the PEO blocks are still in the molten state. On the other hand, to calculate the kinetic parameters of PEO blocks, first, the PVDF blocks are crystallized to saturation, and subsequently, the PEO blocks are crystallized.

Figures 7.14a and 7.14b show the inverse of the induction time (t_0), a quantity proportional to the primary nucleation rate before the crystallization process has started. This nucleation rate of the PVDF and PEO blocks is plotted for all samples as a function of the crystallization temperature (T_c) and the supercooling (T_m^0-T_c), respectively. The two PVDF arms of the 4-miktoarm star block copolymers have nucleation rates that are higher than that of the 2-arm linear PVDF precursor, a peculiar effect as the PEO arms in the stars are in the melt when the PVDF arms nucleate. We were not able to identify an unifying trend in the three different star copolymers with respect to their composition. Similarly, the PEO precursor shows a lower nucleation rate in comparison to the PEO arms within the stars.

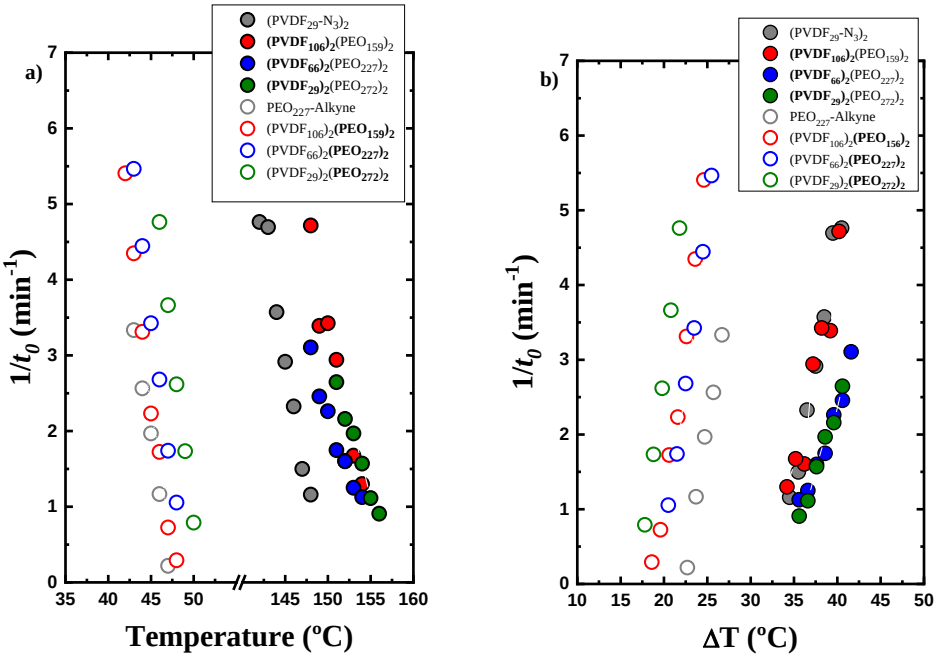

Figure 7. 14. Inverse of the induction time (t_0) obtained by DSC versus a) the crystallization temperature and b) the supercooling for PVDF precursor, PEO precursor, $(PVDF_{106})_2(PEO_{159})_2$, $(PVDF_{29})_2(PEO_{272})_2$ and $(PVDF_{66})_2(PEO_{227})_2$ samples.

The estimation of the equilibrium melting temperature (T_m^0) for each sample using the Hoffman-Week method is explained in the Figure 7.15. We have estimated the values of equilibrium melting temperature (T_m°) using the following procedure. To estimate the T_m°, first, we use the Hoffman-Weeks method,[55, 56] which consists in experimentally obtaining melting temperatures (T_m) of isothermally crystallized samples at different crystallization temperatures (T_c). Subsequently, these data are fitted to a straight line of positive slope in a graph of T_m versus T_c, where the line is extrapolated to its intersection with the line $T_m = T_c$. The temperature at this intersection is T_m°. With the procedure described, the values of T_m° were calculated for PEO, PVDF, and their copolymers, and the values for the T_m^0 are represented in Table 7.6.

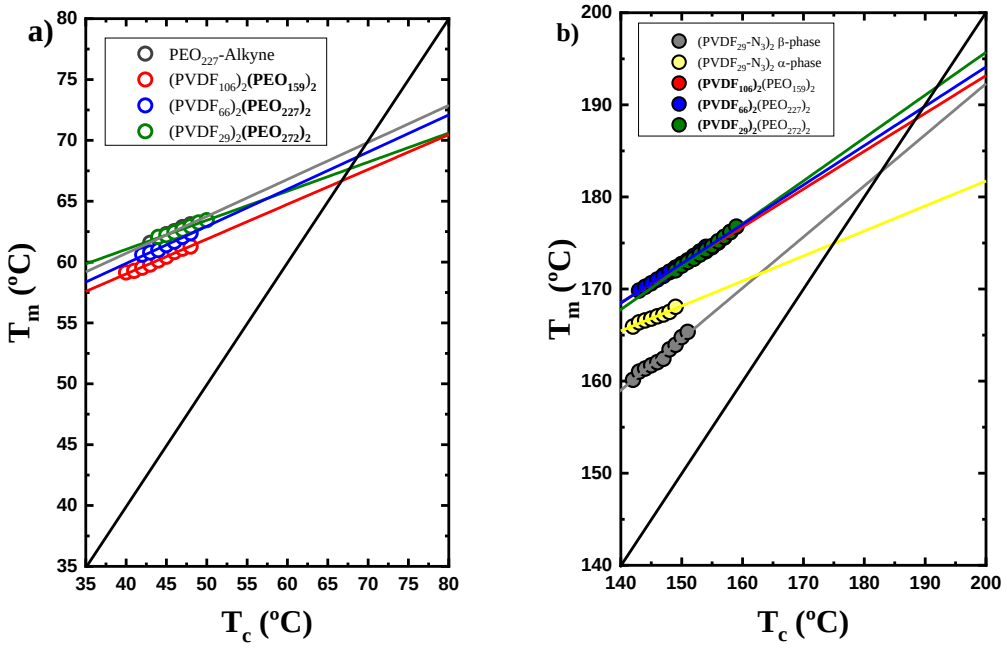

Figure 7. 15. Linear fit of melting temperature against crystallization temperature in a) PEO homopolymer and PEO blocks and b) PVDF homopolymer and PVDF blocks.

Table 7. 6. Equilibrium melting temperature values for each sample obtained by the Hoffman-Weeks method.

Sample	PEO_{227}-Alkyne	$(PVDF_{29}\text{-}N_3)_2$	$(PVDF_{106})_2$ $(PEO_{159})_2$	$(PVDF_{66})_2$ $(PEO_{227})_2$	$(PVDF_{29})_2$ $(PEO_{272})_2$
T_m^0 PVDF (ºC)	-	174.8 (α) 182.5 (β)	188.2	189.6	191.6
T_m^0 PEO (ºC)	69.7	-	66.6	68.5	67.8

These values extrapolated by the Hoffman-Weeks method are employed to fit the data presented in Figures 7.16a and 7.16b with the Lauritzen and Hoffman theory. Figures 7.16a and 7.16b plot overall crystallization rates (i.e., the inverse of the

half crystallization time ($1/\tau_{50\%}$)), versus T_c and the supercooling for all the materials examined. The curves plotted as a function of supercooling are closer to each other, but there is not a perfect superposition between copolymers and their homopolymers. This result indicates the predominance of kinetic factors over the thermodynamic normalization attempted by plotting the curves as a function of supercooling. The trends observed in Figure 7.16a and 7.16b are qualitatively similar to those observed in Figures 7.14a and 7.14b, indicating that nucleation is a dominant factor for the overall crystallization behavior of the materials (that includes nucleation and growth contributions). In summary, both the nucleation rate and the overall crystallization rates of the PVDF and PEO arms within the 4-miktoarm star block copolymers are higher than those of their precursors. The nucleation effects dominate the overall crystallization kinetics.

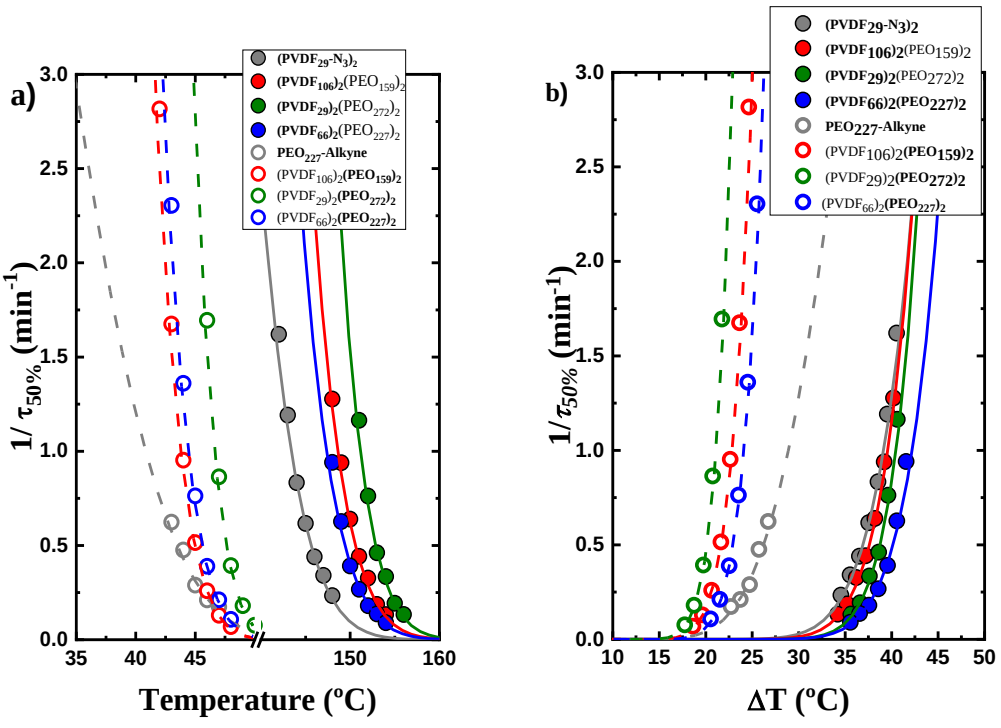

Figure 7. 16. Inverse of half crystallization time ($1/\tau_{50\%}$) as a function of a) isothermal crystallization temperature and b) the supercooling for PVDF precursor, PEO precursor, $(PVDF_{106})_2(PEO_{159})_2$, $(PVDF_{29})_2(PEO_{272})_2$ and $(PVDF_{66})_2(PEO_{227})_2$.

The Avrami equation describes well the primary crystallization in polymers (see Chapter 2).[57, 58] One of the possible ways to write the equation is:

$$1 - V_c(t - t_0) = exp(-k(t - t_0)^n) \qquad \text{eq. 7.2}$$

where V_c is the relative volumetric transformed fraction, t_0 is the induction time before any crystallization has started, t is the experimentally determined time, k is the overall crystallization rate constant, and n is the Avrami index. The Avrami index depends on the nucleation rate and crystal growth geometry.

Through the Avrami equation fit, the Avrami index (n) is calculated for every temperature chosen during the isothermal crystallization. The Avrami index values are plotted in Figure 7.17a against the crystallization temperature. The values of the Avrami index fluctuate between 2 and 3. If the studied block is PEO for the copolymers, the Avrami index is closer to 3 (instantaneous nucleated spherulites). On the other hand, if the studied block is PVDF, it is closer to 2 (instantaneous nucleated axialites) with the exception of the homopolymer, whose n values are closer to 3.

Figure 7.17b shows the crystallization temperature dependence of $k^{1/n}$ values. These values obtained by the Avrami fit for $k^{1/n}$ are proportional to the overall crystallization rate constant (whose excellent fit is given up to 25% relative conversion to the semicrystalline state by the free growth of spherulites or axialites) in normalized units of min^{-1} (thanks to elevating k to the power $1/n$, as the units of k are given as $time^{-n}$). This is a good way to compare the Avrami predictions (plotted as data points in Figure 7.17b with the experimental values obtained during the isothermal crystallization experiments (experimental values of $1/\tau_{50\%}$ in Figure 7.16a). In Figure 7.17b, the comparison between the experimental data and the Avrami fit predictions are made at 50% relative crystalline conversion. This means that in the experimental case, impingement between spherulites would have probably started, especially

when the nucleation is not perfectly instantaneous. This explains why there is a qualitative agreement between Figure 7.17b and Figure 7.16a, but there are some quantitative differences.

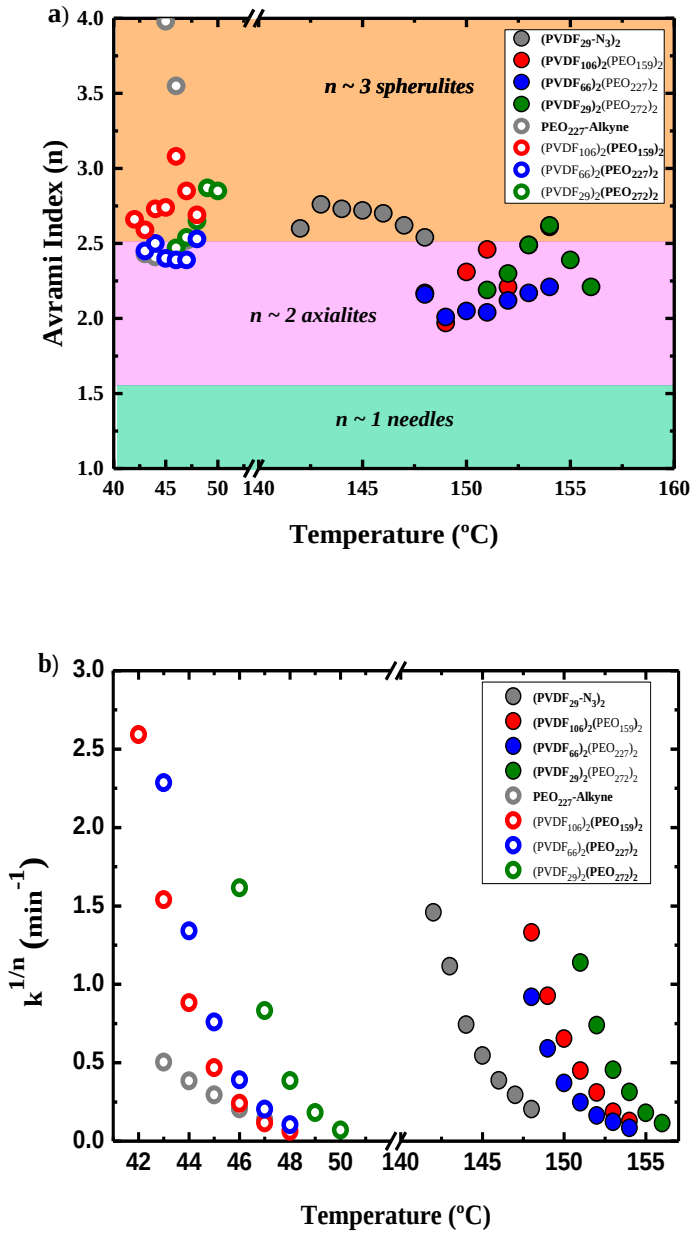

Figure 7. 17. a) Avrami index values as a function of the crystallization temperature and b) normalized isothermal crystallization rate constant of the Avrami model as a function of crystallization temperature for all the samples studied.

7.3.6 Melting process after the isothermal crystallization procedure

This section analyses the melting process after isothermally crystallized samples and heated in the DSC (starting at their corresponding T_c values), registering their melting behaviour. Figure 7.18 shows the DSC heating scans at 20 ºC/min after each isothermal crystallization process for the $(PVDF_{29}\text{-}N_3)_2$ and PEO_{227}-Alkyne samples. In the case of the $(PVDF_{29}\text{-}N_3)_2$ homopolymer (Figure 7.18a), the temperature range chosen for the isothermal crystallization study was 142-152 ºC, and for the PEO_{227}-Alkyne homopolymer (Figure 7.18b), the temperature range was 43-50 ºC.

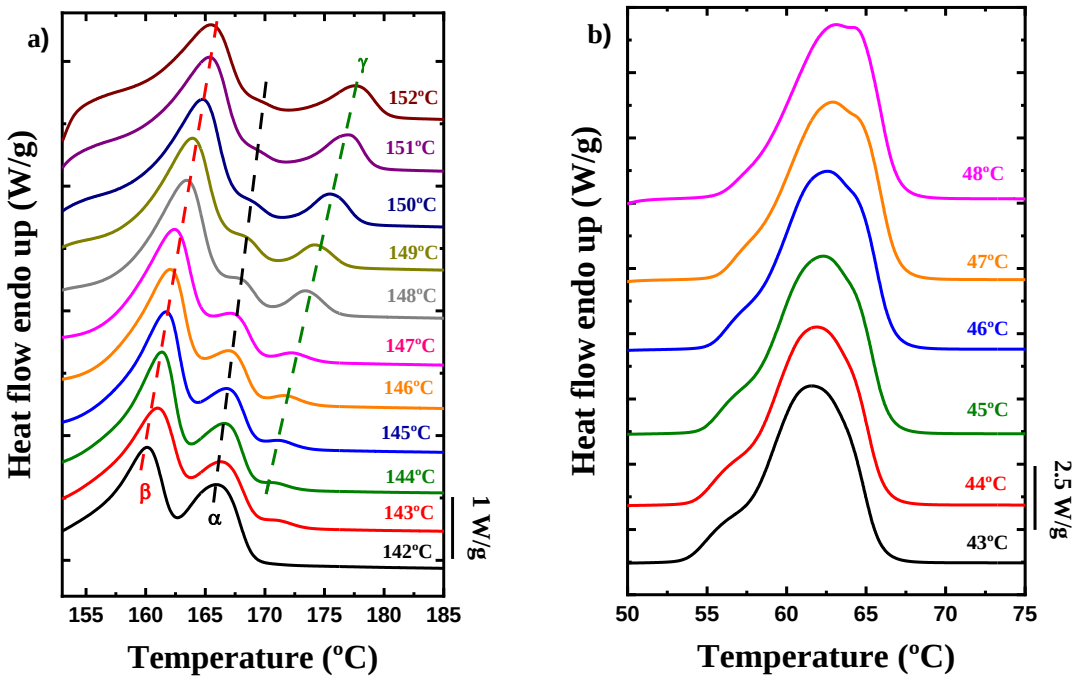

Figure 7. 18. DSC heating scans at 20 ºC/min after the samples were isothermally crystallized for 40 min at the indicated temperatures: a) $(PVDF_{29}\text{-}N_3)_2$ and b) PEO_{227}-Alkyne precursor samples.

In the case of PEO (Figure 7.18b), the main melting peak is observed at approximately 62 ºC, and this peak increases as the crystallization temperature increases.

We will not address the behaviour of the PEO precursor in detail, as the main objective of this work is to investigate the polymorphic behaviour of PVDF block. Figure 7.18a shows the melting behaviour of the (PVDF$_{29}$-N$_3$)$_2$ precursor (a linear 2-arm PVDF sample). Different melting peaks are observed due to the different polymorphic phases detected in PVDF. The isothermal crystallization peaks at the different crystallization temperatures are plotted in Figure 7.19 for both samples.

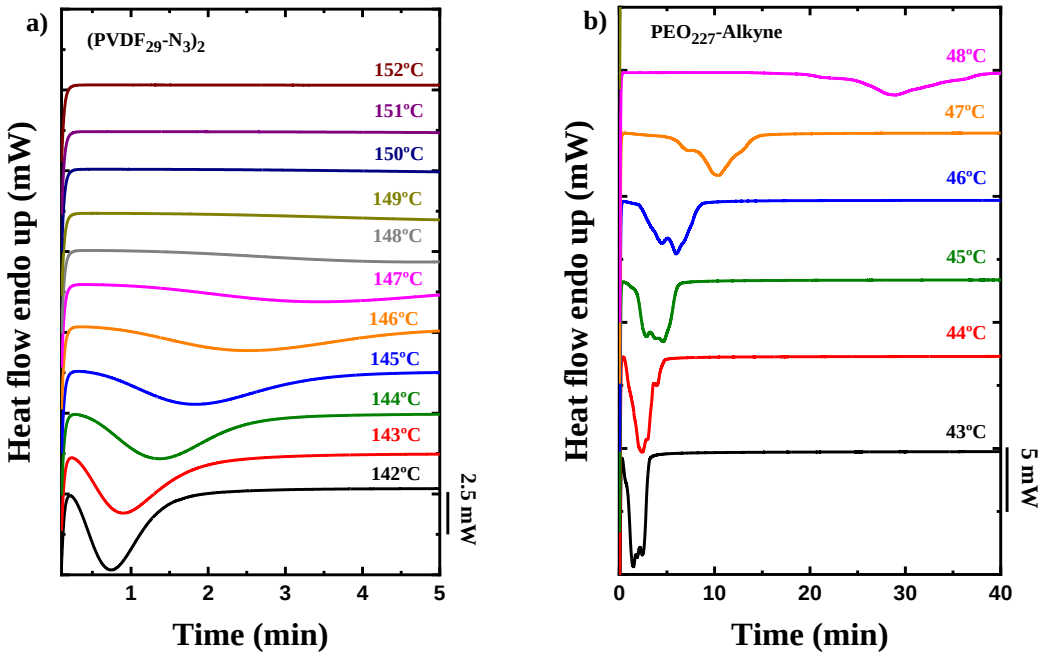

Figure 7. 19. DSC isothermal crystallization scans of a) (PVDF$_{29}$-N$_3$)$_2$ and b) PEO$_{227}$-Alkyne.

According to the literature, commercial PVDF homopolymers exhibit only one melting peak when are isothermally crystallized from the melt, specifically the α-non-polar phase.[59, 60] In our case, in the synthesized (PVDF$_{29}$-N$_3$)$_2$ precursor, at low isothermal crystallization temperatures (T_c = 142 ºC), two melting peaks can be distinguished. The first one appears at low temperatures, and can be assigned to the less stable crystalline β-phase. The second one, at higher temperatures, and corresponds

to the crystalline α-phase. When the isothermal crystallization temperature increases, the α-phase melting peak area decreases, and a new peak can be observed at higher temperatures. This peak corresponds to the melting of a new crystalline phase crystals, which can be assigned to the γ-phase. At the highest isothermal crystallization temperature (T_c = 152 ºC), the α-phase crystals have almost disappeared, and both β and γ-phases coexist. A possible explanation may be that a transition from the α-phase to the γ-phase occurs during the isothermal crystallization process, as it has been observed before in the literature when the isothermal crystallization temperature selected is high enough.[33, 61] These type of transitions have been previously reported for PVDF nanocomposite samples but has never been reported before for PVDF-based block copolymer samples.[62-64] It is important to remind that in the present chapter, the $(PVDF_{29}\text{-}N_3)_2$ homopolymer precursor is not equal to a commercial PVDF homopolymer, as it has a more complex structure being a 2-arm copolymer.

A morphological study was carried out by PLOM. Figure 7.20 shows micrographs of the $(PVDF_{29}\text{-}N_3)_2$ precursor taken at two different isothermal crystallization temperatures that complement the DSC results. Figure 7.20a presents some PVDF spherulites grown at 146 ºC after 3 minutes at this temperature, where the main phase observed by DSC was the β-phase. On the other hand, Figure 7.20b shows spherulites grown at 157 ºC during 10 minutes on the same sample where the main phase observed by DSC was the γ-phase. Differences in texture are detected in both cases, where the γ-phase crystals observed in Figure 7.20b are more compact and dense than the β-phase crystals observed in Figure 7.20a. Therefore, depending on the isothermal crystallization temperature employed, it is possible to observe two types of spherulites in the same sample. In the literature, some works have found with similar differences in the texture of PVDF spherulites depending on the crystalline phases that are being formed.[21, 65-67]

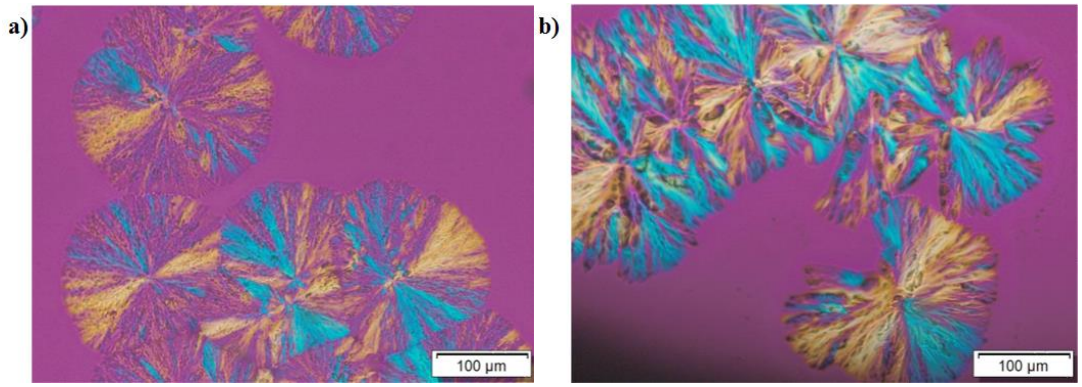

Figure 7. 20. PLOM micrographs of (PVDF$_{29}$-N$_3$)$_2$ spherulites isothermally crystallized a) at 146 ºC and b) at 157 ºC from the melt.

As explained before, the α- to γ-phase transition is a well-known process in the literature.[68-70] Normally, this conversion process requires long crystallization times, but in our case, as we have confirmed before, due to the topological effects of the 2-arm chain conformation in this PVDF precursor, this α-γ phase transition occurs with the increased of the crystallization temperature, even at short crystallization times. The chain topology influences the final properties of the sample, as we demonstrated in miktoarm star structures before.

To understand how the α-phase changes to γ-phase, different calculations were performed. Three different hypotheses will be discussed: (i) a direct transition from α-phase crystals to γ-phase crystals during the duration of the isothermal crystallization, (ii) the α-phase, that is first formed, melts (during isothermal crystallization) and the γ-phase forms from this melt state, as the crystallization temperature increases and (iii) the β-phase, that is first formed, melts, and then the γ-phase crystallizes from this molten state. To study these different possibilities, some calculations are carried out and are presented in Figure 7.21.

Figure 7.21 presents a plot of the degree of crystallinity of each Phase ($X_c^{\alpha,\beta,\gamma}$) divided by the total degree of crystallinity (X_c^{total}) for each isothermal crystallization temperature.

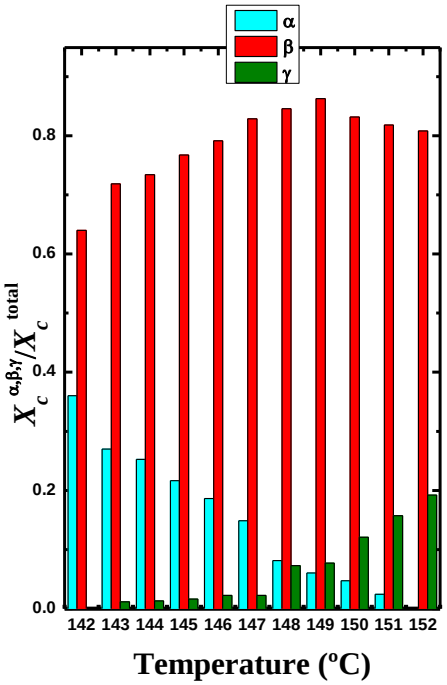

Figure 7. 21. Degree of crystallinity of each phase divided by the total degree of crystallinity at all the isothermal crystallization temperatures studied.

$X_c^{\alpha,\beta,\gamma}$ is calculated from the melting enthalpy data obtained by DSC analysis (equation 7.3), and X_c^{total} value is obtained by the sum of all the crystallinity degrees (equation 7.4):

$$X_c = \frac{\Delta H_m}{\Delta H_m^0 * \varphi} \qquad \text{eq. 7.3}$$

$$X_c^T(T) = X_c^\alpha(T) + X_c^\beta(T) + X_c^\gamma(T) \qquad \text{eq. 7.4}$$

where ΔH_m is the experimental latent heat of fusion measured in the DSC, ΔH_m^0 is the equilibrium melting enthalpy (i.e, for a 100% crystalline sample), and φ is the weight fraction of the polymer. For the PVDF we have employed a value of ΔH_m^0 = 104.7 J/g.[71]

To calculate the degree of crystallization for each phase in the $(PVDF_{29}\text{-}N_3)_2$ precursor, we need to divide the melting enthalpy measured for each individual

phase between the melting enthalpy when the polymer is completely crystalline, as is shown in Equation 7.3. To obtain the melting enthalpy of each phase, we used the Pyris manager software (Perkin Elmer, MA, USA). The enthalpies for each phase were calculated using the application of partial areas at the onset of the corresponding peaks (see Figure 7.22).

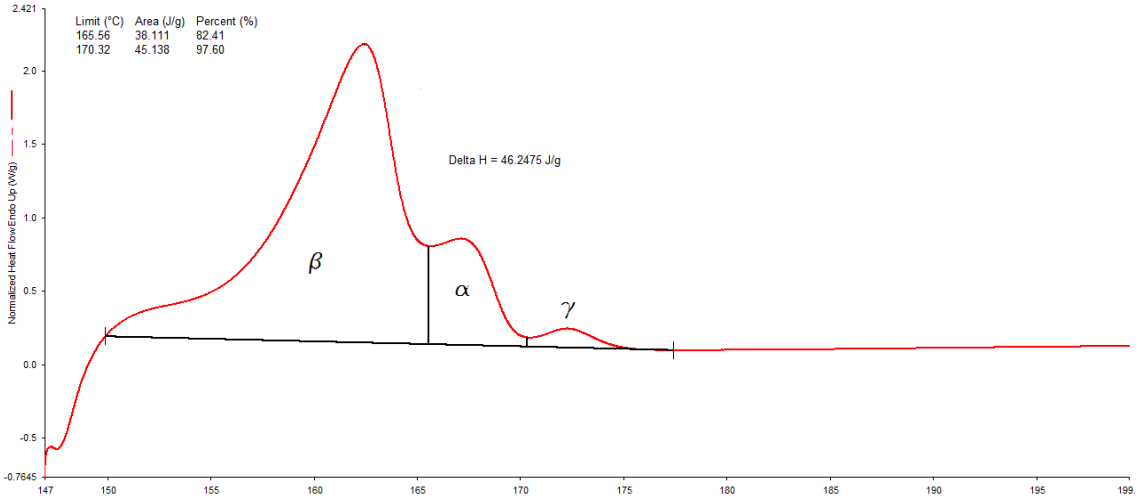

Figure 7. 22. Image taken from the Pyrys manager software that shows the curve of the $(PVDF_{29}\text{-}N_3)_2$ heating after an isothermal crystallization process at 147 ºC.

After all the melting enthalpies were calculated in each phase for every crystallization temperature, we calculated the degree of crystallization of each phase for all the crystallization temperatures using the Equation 7.3. The degrees of crystallization of each phase were summed up according to Equation 7.4 to obtain the total degree of crystallization. To obtain the data plotted in Figure 7.21 we divided the total degree of crystallization between the degrees of crystallization for each phase.

Figure 7.21 shows how the β-phase is almost constant in the whole range calculated; thus, we can estimate that the β-phase does not melt as the isothermal crystallization temperatures are increased and always remains crystalline, so hypothesis (iii) can be excluded. For the α-phase, the value of the degree of crystallinity decreases when the crystallization temperature increases, and at the same time, the degree of crystallinity for the γ-phase increases. In addition, the β-phase is not

changing with crystallization temperature, as the total crystallinity observed remains almost constant, so hypothesis (ii) can be also excluded. Figure 7.21 thus demonstrates that there is a direct crystalline phase transition from α- to γ-phase in the $(PVDF_{29}\text{-}N_3)_2$ sample during the isothermal crystallization process.

The melting of the PVDF arms crystals within the $(PVDF)_2(PEO)_2$ 4-miktoarm star block copolymers was also studied after isothermal crystallization by DSC. Figure 7.23 shows the DSC heating curves of the miktoarm star block copolymer samples at 20 ºC/min for the PVDF blocks after their isothermal crystallization for 40 min at different T_c values. The behaviour of the PVDF arms within the 4-miktoarm star block copolymers is remarkable. A single melting peak (this peak value increases as T_c increases as expected) can be observed in Figure 7.23 for all three samples. A single melting peak is observed in all samples regardless of the isothermal crystallization temperature employed or the miktoarm star copolymer composition selected. Compared to the PVDF precursor studied, this melting peak means that the copolymers, regardless of the sample studied, always crystallize in one crystalline phase.

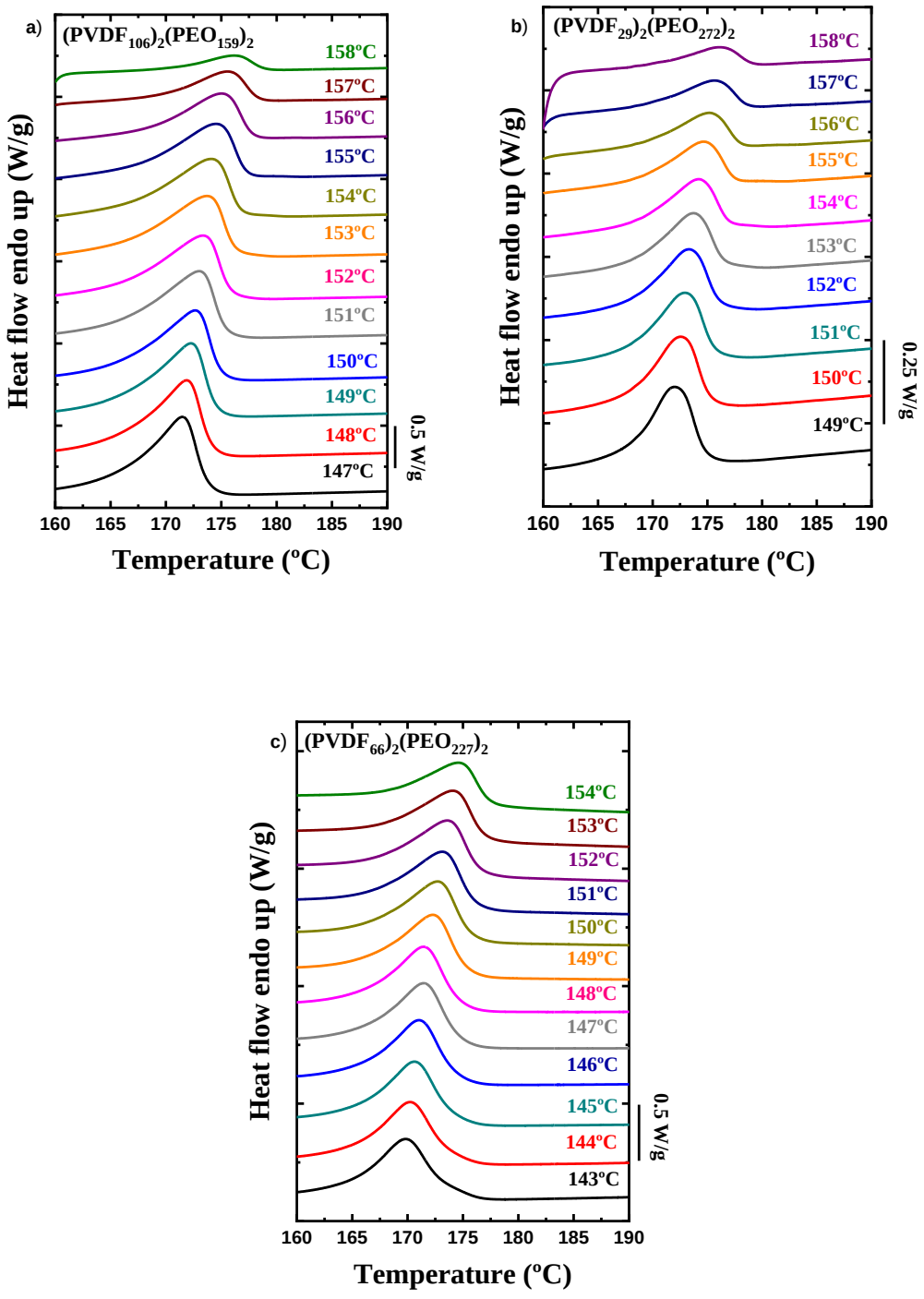

Figure 7. 23. DSC heating scans after 40 min isothermal crystallization at the indicated temperatures for the PVDF arms of the following samples: a) $(PVDF_{106})_2(PEO_{159})_2$, b) $(PVDF_{29})_2(PEO_{272})_2$ and c) $(PVDF_{66})_2(PEO_{227})_2$

The respective DSC cooling curves are displayed in Figure 7.24.

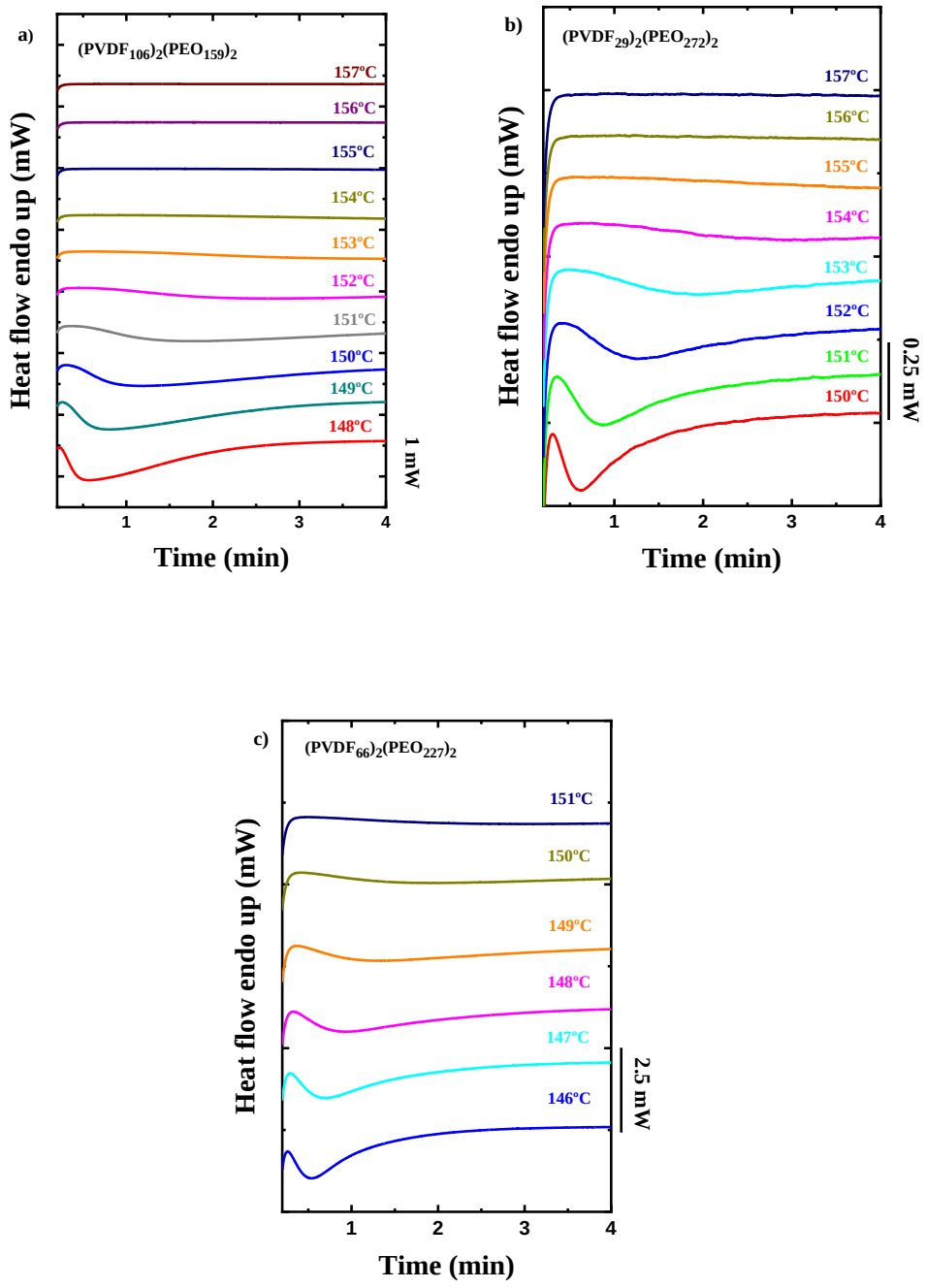

Figure 7. 24. Isothermal crystallization of the block copolymers a) $(PVDF_{106})_2(PEO_{159})_2$, b) $(PVDF_{29})_2(PEO_{272})_2$ and c) $(PVDF_{66})_2(PEO_{227})_2$.

When these block copolymers samples are observed in the PLOM during an isothermal crystallization at high temperatures, it is possible to follow the crystallization of the PVDF arms. For the $(PVDF_{29})_2(PEO_{272})_2$ sample, the small amount of PVDF prevents the observation of PVDF block crystals in the microscope. Figure 7.25 shows the PVDF arms crystals obtained for $(PVDF_{66})_2(PEO_{227})_2$ (Figure 7.25a) and $(PVDF_{106})_2(PEO_{159})_2$ (Figure 7.25b) respectively, at a crystallization temperature of 140 ºC. In micrograph 7.25a, the PVDF arms crystals have a morphology in between spherulites and axialites. However, when the amount of PVDF in the star copolymers is the highest, as shown in Figure 7.25b, the crystals formed by the PVDF arms are clear negative spherulites. In both cases, the crystals observed are consistent with PVDF β-phase morphology.

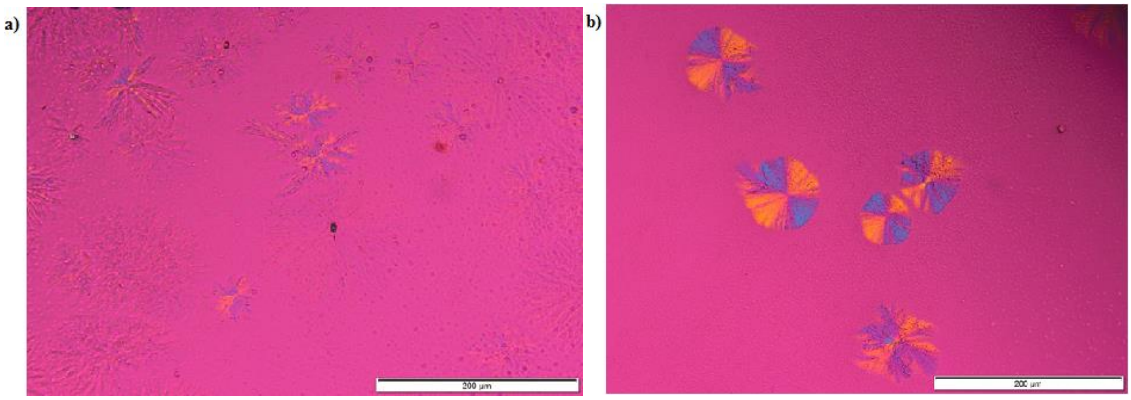

Figure 7. 25. a) $(PVDF_{66})_2(PEO_{227})_2$ and b) $(PVDF_{106})_2(PEO_{159})_2$ crystals during an isothermal crystallization at 140 ºC.

7.3.7 Isothermal crystalline phase detection

The three 4-miktoarm star block copolymers were isothermally crystallized at 150 ºC for 2 hours and finally cooled down at 20 ºC/min to room temperature before the FTIR spectra were measured. Figure 7.26 shows the FTIR results for the copolymers, crystallized all of them at the same temperature.

Figure 7.26 shows some characteristic bands for $(PVDF_{106})_2(PEO_{159})_2$, $(PVDF_{29})_2(PEO_{272})_2$, and $(PVDF_{66})_2(PEO_{227})_2$ samples. As expected, considering the melting temperature range observed by DSC, the bands detected in the FTIR spectra for the PVDF arms are related to the crystalline β-phase. The FTIR spectra shown here are just focused in the range of 1600-600 cm^{-1}, where all the PVDF characteristic bands appear. The bands located at 1238, 1101, and 961 cm^{-1} are the main bands detected for the PEO, as have been explained above.[51] In Figure 7.26 for the PVDF blocks, there is a single band located at 1275 cm^{-1}, this band is characteristic for the β-phase.[52] It is remarkable that after the isothermal crystallization of these miktoarm block copolymers only the β-phase was formed. In fact, all characteristic bands from the α-phase (764, 796, and 976 cm^{-1}) are absent. Moreover, the bands corresponding to the γ-phase (833 and 1232 cm^{-1}) are also not observed.

The results presented here prove that the PVDF arms within the 4-miktoarm star block copolymers crystallize only in the β-phase when the samples are isothermally crystallized from the melt.

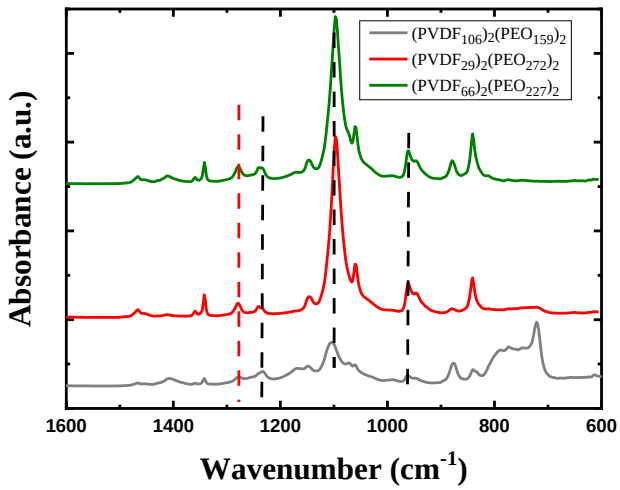

Figure 7. 26. FTIR spectra for $(PVDF_{106})_2(PEO_{159})_2$, $(PVDF_{29})_2(PEO_{272})_2$ and $(PVDF_{66})_2(PEO_{227})_2$ samples where PVDF was isothermally crystallized at 150 ºC during 2 h. The different vertical dashed lines indicate the bands for the PVDF and PEO. Black: PEO. Red: PVDF β-phase.

7.4 Conclusion

Novel A_2B_2 PVDF-based amphiphilic miktoarm star polymers are synthesized having fluoropolymer PVDF and hydrophilic PEO blocks via a combination of anionic ring-opening, ITP and CuAAC methodologies. The combination of ITP and CuAAC chemistries and selection of multi-functional precursors allows facile access to synthesize different complex macromolecular architectures based on PVDF.

The PVDF arms of the novel $(PVDF)_2(PEO)_2$ 4-miktoarm star copolymers synthesized in this chapter exhibit remarkable crystallization properties and polymorphism that depend on the cooling rate employed. By comparing their behaviour with one linear 2-arm precursor sample and a commercial PVDF, we have demonstrated that the 4-miktoarm star topology induces the exclusive formation of the ferroelectric crystalline β-phase when the samples are cooled slowly from the melt. This finding paves the way for the preparation of new ferroelectric and piezoelectric materials based on 4-miktoarm star copolymers with potential energy harvesting applications.

Moreover, we have shown how chain topology can significantly affect the isothermal crystal phase formation in PVDF. Contrary to the well-known behaviour of linear PVDF materials that crystallize in the α-phase when they are isothermally crystallized from the melt, a linear 2-arm block copolymer ($(PVDF_{29}\text{-}N_3)_2$) exhibits a polymorphic behaviour (with a predominant β-phase formation) during melting after isothermal crystallization that significantly depends on the temperature of crystallization. An analysis of the multiple melting behaviour indicates that the sample forms both α- and β-phases, where the α-phase transforms into the γ-phase during an isothermal crystallization process.

In the case of the more complex $(PVDF)_2(PEO)_2$ 4-miktoarm star block copolymers, we found a remarkable behaviour, as the PVDF arms only form the ferroelectric β-phase when all three materials were isothermally crystallized regardless of the crystallization temperature employed.

7.5 References

1. Voet, V. S. D.; ten Brinke, G.; Loos, K., Well-defined copolymers based on poly(vinylidene fluoride): From preparation and phase separation to application. *Journal of Polymer Science Part A: Polymer Chemistry* **2014,** 52, (20), 2861-2877.
2. Ameduri, B., Controlled Radical (Co)polymerization of Fluoromonomers. *Macromolecules* **2010,** 43, (24), 10163-10184.
3. Ameduri, B., From Vinylidene Fluoride (VDF) to the Applications of VDF-Containing Polymers and Copolymers: Recent Developments and Future Trends. *Chemical Reviews* **2009,** 109, (12), 6632-6686.
4. Guerre, M.; Campagne, B.; Gimello, O.; Parra, K.; Ameduri, B.; Ladmiral, V., Deeper Insight into the MADIX Polymerization of Vinylidene Fluoride. *Macromolecules* **2015,** 48, (21), 7810-7822.
5. Lopez, G.; Guerre, M.; Améduri, B.; Habas, J.-P.; Ladmiral, V., Photocrosslinked PVDF-based star polymer coatings: an all-in-one alternative to PVDF/PMMA blends for outdoor applications. *Polymer Chemistry* **2017,** 8, (20), 3045-3049.
6. Apostolides, D. E.; Patrickios, C. S.; Sakai, T.; Guerre, M.; Lopez, G.; Améduri, B.; Ladmiral, V.; Simon, M.; Gradzielski, M.; Clemens, D.; Krumm, C.; Tiller, J. C.; Ernould, B.; Gohy, J.-F., Near-Model Amphiphilic Polymer Conetworks Based on Four-Arm Stars of Poly(vinylidene fluoride) and Poly(ethylene glycol): Synthesis and Characterization. *Macromolecules* **2018,** 51, (7), 2476-2488.
7. Voet, V. S. D.; Alberda van Ekenstein, G. O. R.; Meereboer, N. L.; Hofman, A. H.; Brinke, G. t.; Loos, K., Double-crystalline PLLA-b-PVDF-b-PLLA triblock copolymers: preparation and crystallization. *Polymer Chemistry* **2014,** 5, (7), 2219-2230.
8. Boyer, C.; Valade, D.; Sauguet, L.; Ameduri, B.; Boutevin, B., Iodine Transfer Polymerization (ITP) of Vinylidene Fluoride (VDF). Influence of the Defect of VDF Chaining on the Control of ITP. *Macromolecules* **2005,** 38, (25), 10353-10362.
9. Boyer, C.; Valade, D.; Lacroix-Desmazes, P.; Ameduri, B.; Boutevin, B., Kinetics of the iodine transfer polymerization of vinylidene fluoride. *Journal of Polymer Science Part A: Polymer Chemistry* **2006,** 44, (19), 5763-5777.
10. Junnila, S.; Houbenov, N.; Hanski, S.; Iatrou, H.; Hirao, A.; Hadjichristidis, N.; Ikkala, O., Hierarchical Smectic Self-Assembly of an ABC Miktoarm Star Terpolymer with a Helical Polypeptide Arm. *Macromolecules* **2010,** 43, (21), 9071-9076.
11. Gao, H.; Matyjaszewski, K., Synthesis of Star Polymers by a Combination of ATRP and the "Click" Coupling Method. *Macromolecules* **2006,** 39, (15), 4960-4965.
12. Bates Frank, S., Polymer-Polymer Phase Behavior. *Science* **1991,** 251, (4996), 898-905.
13. Bates, F. S.; Fredrickson, G. H., Block copolymers-designer soft materials. *Physics today* **2000,** 52.
14. Mai, Y.; Eisenberg, A., Self-assembly of block copolymers. *Chemical Society Reviews* **2012,** 41, (18), 5969-5985.
15. Patil, Y.; Bilalis, P.; Polymeropoulos, G.; Almahdali, S.; Hadjichristidis, N.; Rodionov, V., A Novel Poly(vinylidene fluoride)-Based 4-Miktoarm Star Terpolymer: Synthesis and Self-Assembly. *Molecular Pharmaceutics* **2018,** 15, (8), 3005-3009.
16. Iatrou, H.; Hadjichristidis, N., Synthesis and characterization of model 4-miktoarm star co- and quaterpolymers. *Macromolecules* **1993,** 26, (10), 2479-2484.

17. Mavroudis, A.; Hadjichristidis, N., Synthesis of Well-Defined 4-Miktoarm Star Quarterpolymers (4μ-SIDV) with Four Incompatible Arms: Polystyrene (S), Polyisoprene-1,4 (I), Poly(dimethylsiloxane) (D), and Poly(2-vinylpyridine) (V). *Macromolecules* **2006,** 39, (2), 535-540.
18. Khanna, K.; Varshney, S.; Kakkar, A., Miktoarm star polymers: advances in synthesis, self-assembly, and applications. *Polymer Chemistry* **2010,** 1, (8), 1171-1185.
19. Pérez, E.; Angulo, I.; Blázquez-Blázquez, E.; Cerrada, M. L., Characteristics of the Non-Isothermal and Isothermal Crystallization for the β Polymorph in PVDF by Fast Scanning Calorimetry. *Polymers* **2020,** 12, (11).
20. Salimi, A.; Yousefi, A. A., Conformational changes and phase transformation mechanisms in PVDF solution-cast films. *Journal of Polymer Science Part B: Polymer Physics* **2004,** 42, (18), 3487-3495.
21. Silva, M. P.; Sencadas, V.; Botelho, G.; Machado, A. V.; Rolo, A. G.; Rocha, J. G.; Lanceros-Mendez, S., α- and γ-PVDF: Crystallization kinetics, microstructural variations and thermal behaviour. *Materials Chemistry and Physics* **2010,** 122, (1), 87-92.
22. Lorenzo, A. T.; Arnal, M. L.; Albuerne, J.; Müller, A. J., DSC isothermal polymer crystallization kinetics measurements and the use of the Avrami equation to fit the data: Guidelines to avoid common problems. *Polymer Testing* **2007,** 26, (2), 222-231.
23. Rodionov, V. O.; Fokin, V. V.; Finn, M. G., Mechanism of the Ligand-Free CuI-Catalyzed Azide–Alkyne Cycloaddition Reaction. *Angewandte Chemie International Edition* **2005,** 44, (15), 2210-2215.
24. Leibler, L., Theory of microphase separation in block copolymers. *Macromolecules* **1980,** 13, (6), 1602-1617.
25. Hiemenz, P. C. L., T.P., Polymer chemistry. *CRC Press* **2007,** 2nd edition.
26. Lorenzo, A. T.; Müller, A. J.; Lin, M.-C.; Chen, H.-L.; Jeng, U. S.; Priftis, D.; Pitsikalis, M.; Hadjichristidis, N., Influence of Macromolecular Architecture on the Crystallization of (PCL2)-b-(PS2) 4-Miktoarm Star Block Copolymers in Comparison to Linear PCL-b-PS Diblock Copolymer Analogues. *Macromolecules* **2009,** 42, (21), 8353-8364.
27. Müller, A. J.; Lorenzo, A. T.; Hirao, A., Crystallization behavior of polyethylene/polystyrene AmBn miktoarm star copolymers. *Polymers for Advanced Technologies* **2014,** 25, (11), 1257-1263.
28. Li, M.; Stingelin, N.; Michels, J. J.; Spijkman, M.-J.; Asadi, K.; Feldman, K.; Blom, P. W. M.; de Leeuw, D. M., Ferroelectric Phase Diagram of PVDF:PMMA. *Macromolecules* **2012,** 45, (18), 7477-7485.
29. Roerdink, E.; Challa, G., Influence of tacticity of poly(methyl methacrylate) on the compatibility with poly(vinylidene fluoride). *Polymer* **1978,** 19, (2), 173-178.
30. Lovinger, A. J., Crystallization and morphology of melt-solidified poly(vinylidene fluoride). *Journal of Polymer Science: Polymer Physics Edition* **1980,** 18, (4), 793-809.
31. Bormashenko, Y.; Pogreb, R.; Stanevsky, O.; Bormashenko, E., Vibrational spectrum of PVDF and its interpretation. *Polymer Testing* **2004,** 23, (7), 791-796.
32. Lovinger, A. J., Poly(Vinylidene Fluoride). In *Developments in Crystalline Polymers—1*, Bassett, D. C., Ed. Springer Netherlands: Dordrecht, 1982; pp 195-273.
33. Cui, Z.; Hassankiadeh, N. T.; Zhuang, Y.; Drioli, E.; Lee, Y. M., Crystalline polymorphism in poly(vinylidenefluoride) membranes. *Progress in Polymer Science* **2015,** 51, 94-126.
34. Bachmann, M. A.; Lando, J. B., A reexamination of the crystal structure of phase II of poly(vinylidene fluoride). *Macromolecules* **1981,** 14, (1), 40-46.

35. Newman, B. A.; Yoon, C. H.; Pae, K. D.; Scheinbeim, J. I., Piezoelectric activity and field-induced crystal structure transitions in poled poly(vinylidene fluoride) films. *Journal of Applied Physics* **1979,** 50, (10), 6095-6100.
36. Geiss, D.; Hofmann, D., Investigation of structural changes in PVDF by modified X-ray texture methods. *IEEE Transactions on Electrical Insulation* **1989,** 24, (6), 1177-1182.
37. Doll, W. W.; Lando, J. B., The polymorphism of poly(vinylidene fluoride) V. The effect of hydrostatic pressure on the melting behavior of copolymers of vinylidene fluoride. *Journal of Macromolecular Science, Part B* **1970,** 4, (4), 897-913.
38. Hasegawa, R.; Takahashi, Y.; Chatani, Y.; Tadokoro, H., Crystal Structures of Three Crystalline Forms of Poly(vinylidene fluoride). *Polymer Journal* **1972,** 3, (5), 600-610.
39. Lando, J. B.; Olf, H. G.; Peterlin, A., Nuclear magnetic resonance and x-ray determination of the structure of poly(vinylidene fluoride). *Journal of Polymer Science Part A-1: Polymer Chemistry* **1966,** 4, (4), 941-951.
40. Ince-Gunduz, B. S.; Alpern, R.; Amare, D.; Crawford, J.; Dolan, B.; Jones, S.; Kobylarz, R.; Reveley, M.; Cebe, P., Impact of nanosilicates on poly(vinylidene fluoride) crystal polymorphism: Part 1. Melt-crystallization at high supercooling. *Polymer* **2010,** 51, (6), 1485-1493.
41. Mihaylova, M. D.; Krestev, V. P.; Kresteva, M. N.; Amzil, A.; Berlinova, I. V., Amphiphilic graft copolymers with poly(oxy ethylene) side chains: supermolecular structure in solid state: I. WAXS studies. *European Polymer Journal* **2001,** 37, (2), 233-239.
42. Freire, E.; Bianchi, O.; Martins, J. N.; Monteiro, E. E. C.; Forte, M. M. C., Non-isothermal crystallization of PVDF/PMMA blends processed in low and high shear mixers. *Journal of Non-Crystalline Solids* **2012,** 358, (18), 2674-2681.
43. Lee, S., Crystal structure and thermal properties of poly(vinylidene fluoridehexafluoropropylene) films prepared by various processing conditions. *Fibers and Polymers* **2011,** 12, (8), 1030-1036.
44. De Neef, A.; Samuel, C.; Stoclet, G.; Rguiti, M.; Courtois, C.; Dubois, P.; Soulestin, J.; Raquez, J.-M., Processing of PVDF-based electroactive/ferroelectric films: importance of PMMA and cooling rate from the melt state on the crystallization of PVDF beta-crystals. *Soft Matter* **2018,** 14, (22), 4591-4602.
45. Lando, J. B.; Doll, W. W., The polymorphism of poly(vinylidene fluoride). I. The effect of head-to-head structure. *Journal of Macromolecular Science, Part B* **1968,** 2, (2), 205-218.
46. Davis, G. T.; McKinney, J. E.; Broadhurst, M. G.; Roth, S. C., Electric-field-induced phase changes in poly(vinylidene fluoride). *Journal of Applied Physics* **1978,** 49, (10), 4998-5002.
47. Meereboer, N. L.; Terzić, I.; Saidi, S.; Hermida Merino, D.; Loos, K., Nanoconfinement-Induced β-Phase Formation Inside Poly(vinylidene fluoride)-Based Block Copolymers. *ACS Macro Letters* **2018,** 7, (7), 863-867.
48. Zhu, L.; Huang, P.; Chen, W. Y.; Ge, Q.; Quirk, R. P.; Cheng, S. Z. D.; Thomas, E. L.; Lotz, B.; Hsiao, B. S.; Yeh, F.; Liu, L., Nanotailored Crystalline Morphology in Hexagonally Perforated Layers of a Self-Assembled PS-b-PEO Diblock Copolymer. *Macromolecules* **2002,** 35, (9), 3553-3562.
49. Soin, N.; Boyer, D.; Prashanthi, K.; Sharma, S.; Narasimulu, A. A.; Luo, J.; Shah, T. H.; Siores, E.; Thundat, T., Exclusive self-aligned β-phase PVDF films with abnormal piezoelectric coefficient prepared via phase inversion. *Chemical Communications* **2015,** 51, (39), 8257-8260.

50. Lovinger, A. J.; Keith, H. D., Electron Diffraction Investigation of a High-Temperature Form of Poly(vinylidene fluoride). *Macromolecules* **1979,** 12, (5), 919-924.
51. Yoshihara, T.; Tadokoro, H.; Murahashi, S., Normal Vibrations of the Polymer Molecules of Helical Conformation. IV. Polyethylene Oxide and Polyethylene-d4 Oxide. *The Journal of Chemical Physics* **1964,** 41, (9), 2902-2911.
52. Lanceros-Méndez, S.; Mano, J. F.; Costa, A. M.; Schmidt, V. H., FTIR AND DSC STUDIES OF MECHANICALLY DEFORMED β-PVDF FILMS. *Journal of Macromolecular Science, Part B* **2001,** 40, (3-4), 517-527.
53. Boccaccio, T.; Bottino, A.; Capannelli, G.; Piaggio, P., Characterization of PVDF membranes by vibrational spectroscopy. *Journal of Membrane Science* **2002,** 210, (2), 315-329.
54. Bachmann, M. A.; Gordon, W. L.; Koenig, J. L.; Lando, J. B., An infrared study of phase-III poly(vinylidene fluoride). *Journal of Applied Physics* **1979,** 50, (10), 6106-6112.
55. Hoffman, J. D.; Weeks, J. J., Melting process and the equilibrium melting temperature of polychlorotrifluoroethylene. *J. Res. Natl. Bur. Stand., Sect. A* **1962,** 66, (1), 13-28.
56. Marand, H.; Xu, J.; Srinivas, S., Determination of the Equilibrium Melting Temperature of Polymer Crystals: Linear and Nonlinear Hoffman−Weeks Extrapolations. *Macromolecules* **1998,** 31, (23), 8219-8229.
57. Reiter, G.; Strobl, G. R., *Progress in understanding of polymer crystallization*. Springer: 2007; Vol. 714.
58. Avrami, M., Kinetics of Phase Change. II Transformation-Time Relations for Random Distribution of Nuclei. *The Journal of Chemical Physics* **1940,** 8, (2), 212-224.
59. Miyazaki, T.; Takeda, Y.; Akasaka, M.; Sakai, M.; Hoshiko, A., Preparation of Isothermally Crystallized γ-Form Poly(vinylidene fluoride) Films by Adding a KBr Powder as a Nucleating Agent. *Macromolecules* **2008,** 41, (7), 2749-2753.
60. Sencadas, V.; Costa, C. M.; Gómez Ribelles, J. L.; Lanceros-Mendez, S., Isothermal crystallization kinetics of poly(vinylidene fluoride) in the α-phase in the scope of the Avrami equation. *Journal of Materials Science* **2010,** 45, (5), 1328-1335.
61. Martín, J.; Zhao, D.; Lenz, T.; Katsouras, I.; De Leeuw, D. M.; Stingelin, N., Solid-state-processing of δ-PVDF. *Materials Horizons* **2017,** 4, (3), 408-414.
62. Abolhasani, M. M.; Naebe, M.; Guo, Q., A new approach for mechanisms of ferroelectric crystalline phase formation in PVDF nanocomposites. *Physical Chemistry Chemical Physics* **2014,** 16, (22), 10679-10687.
63. Abolhasani, M. M.; Zarejousheghani, F.; Cheng, Z.; Naebe, M., A facile method to enhance ferroelectric properties in PVDF nanocomposites. *RSC Advances* **2015,** 5, (29), 22471-22479.
64. Asai, K.; Okamoto, M.; Tashiro, K., Crystallization behavior of nano-composite based on poly(vinylidene fluoride) and organically modified layered titanate. *Polymer* **2008,** 49, (19), 4298-4306.
65. Wang, H.; Yang, X.; Zhao, Y.; Yan, C.; Wang, S.; Yang, H.; Wang, X.; Schultz, J. M., Preparation of gamma-PVDF with controlled orientation and insight into phase transformation. *Polymer* **2017,** 123, 282-289.
66. Gregorio, R.; CapitãO, R. C., Morphology and phase transition of high melt temperature crystallized poly(vinylidene fluoride). *Journal of Materials Science* **2000,** 35, (2), 299-306.

67. Wang, M.; Wang, S.; Hu, J.; Li, H.; Ren, Z.; Sun, X.; Wang, H.; Yan, S., Taming the Phase Transition Ability of Poly(vinylidene fluoride) from α to γ′ Phase. *Macromolecules* **2020,** 53, (14), 5971-5979.
68. Prest, W. M.; Luca, D. J., The morphology and thermal response of high-temperature–crystallized poly(vinylidene fluoride). *Journal of Applied Physics* **1975,** 46, (10), 4136-4143.
69. Osaki, S.; Ishida, Y., Effects of annealing and isothermal crystallization upon crystalline forms of poly(vinylidene fluoride). *Journal of Polymer Science: Polymer Physics Edition* **1975,** 13, (6), 1071-1083.
70. Lovinger, A. J., Crystalline transformations in spherulites of poly(vinylidene fluoride). *Polymer* **1980,** 21, (11), 1317-1322.
71. Nakagawa, K.; Ishida, Y., Annealing effects in poly(vinylidene fluoride) as revealed by specific volume measurements, differential scanning calorimetry, and electron microscopy. *Journal of Polymer Science: Polymer Physics Edition* **1973,** 11, (11), 2153-2171.

Chapter 8

The effect of chain topology on the crystallization and polymorphism of PVDF: linear versus star molecules

---

8.1 Introduction

According to the chosen polymerization method and the adopted strategy, PVDF usually has regular head-to-tail sequences (HT) and a reversed monomeric addition, leading to head-to-head (HH) and tail-to-tail (TT) defects. Lovinger *et al.* reported that such head-to-head (HH) or tail-to-tail (TT) defects would affect the crystalline form of PVDF.[1] The crystalline phase transition from α- to β-phase is more prominent when the HHTT content is increased at room temperature.[1] The crystallinity of PVDF is also strongly influenced by the extent of head-to-head and tail-to-tail structures, and the crystallinity decreases when the HHTT defects increase.[2] The relationship between the increase of β-phase amount and the decrease in the crystallinity degree has been previously studied.[3]

In this chapter, we focus on the study of novel synthetic PVDF star homopolymers by RAFT polymerization technique (Reversible Addition-Fragmentation chain Transfer). Given this synthetic capability of designing star macromolecules of several complexity level, we have studied the polymorphic behavior of the PVDF at different cooling rates and how the number of arms affects the crystallization kinetics during an isothermal crystallization process.

8.2 Materials and methods

8.2.1 Materials

The synthesis of polyvinylidene fluoride (PVDF) homopolymers has been accomplished via reversible addition−fragmentation chain-transfer polymerization (RAFT) polymerization, which is a controlled/living radical polymerization applied especially for fluorinated polymers, leading to homo/copolymers with different architectures and low dispersity.[4] Xanthate CTAs are used to polymerize VDF due to the effective control over less activated monomers, e.g., vinyl monomers.[5] In the presence of 1,1-bis(tert- butylperoxy)cyclohexane (Luperox® 331P80) as initiator, the synthesized CTAs were used for the polymerization of VDF in dimethyl carbonate at 80 °C to produce the final linear and star-shaped homopolymers.

The final samples studied consist in four PVDF homopolymers synthetized by the group of Professor Nikos Hadjichristidis in KAUST, Saudi Arabia. The samples have a benzene ring as center and different number of PVDF arms, 1 (linear), 3, 4 and 6- arms. The samples structure and their schematic representation were shown in Figure 3.5 (Chapter 3). Their main characteristics are listed in Table 8.1.

Table 8.1. Molecular characteristics of the linear and star PVDF samples synthesized by RAFT polymerization.

Polymer[a]	M_n **(NMR)**[a] **(g mol^{-1}) Total**	M_n **(NMR)**[a] **(g mol^{-1}) Each arm**	***PDI***[b]
Linear PVDF	4,000	4,000	1.28
3-arm Star PVDF	9,600	3,200	1.56
4-arm Star PVDF	12,300	3,000	1.55
6-arm Star PVDF	11,200	1,800	1.48

[a] Degree of polymerization and M_n were determined by ^{1}HNMR. [b] Determined by GPC in DMF, calibrated with linear PS standards.

8.2.2 Methods

a) Differential Scanning Calorimetry (DSC)

The equipment employed to carry out the DSC experiments was a Perkin Elmer DSC 8000 employing an Intracooler II cooling system. Before the DSC scans were carried out, a calibration process with indium and tin was performed. Ultra-high purity nitrogen was used as purge gas.

For the non-isothermal experiments, the samples were heated to 200 °C and held there for 3 min to ensure that the thermal history of the samples was completely erased. Then, samples were cooled at different cooling rates (60, 10, and 1 °C/min) from the melt to 25 °C and then heated again, at 20 ºC/min, to the molten state.

For the isothermal experiments, first, it is necessary to find the minimum crystallization temperature ($T_{c,min}$). In order to obtain this temperature, the sample was heated to 200 ºC for 3 minutes to ensure that the sample was completely melted, after that, the

sample was cooled down at 60 ºC/min to a chosen T_c and immediately heated again to the molten state (at 20 ºC/min). This process was repeated again with another T_c. The lowest T_c, which did not generate any appreciable curve of fusion during the subsequent DSC heating scan, was chosen as the $T_{c,min}$.[6]

Once the $T_{c,min}$ is known, the protocol performed for the isothermal experiments is the following. First, samples were melted at 200 ºC for 3 minutes to remove any crystalline memory. Then, from the melt, they were cooled fast (at 60 ºC/min) to the previously chosen isothermal crystallization temperature, T_c. At this temperature, the samples were left to crystallize during 40 min to saturate the crystallization. Finally, after the isothermal crystallization process, a heating scan was carried out at 20 ºC/min to the molten state to study how the polymorphism of the PVDF is affected by the isothermal conditions. All the kinetic parameters were calculated with the complimentary Origin® software developed by Lorenzo *et al.*[6, 7]

b) Fourier Transform Infrared Spectroscopy (FTIR)

A Nicolet 6700 FTIR coupled with an ATR (Attenuated Total Reflectance) Golden Gate MK II system with a diamond crystal was employed to analyse the samples. Samples were prepared by first melting a bulk portion at 200 ºC for 3 minutes and then cooled them down at 1 and 10 ºC/min from the melt to 25 ºC. For the thermal protocol, an external Linkam hot-stage was employed. FTIR experiments were always performed at room temperature after the cooling process.

c) Polarized Light Optical Microscope (PLOM)

The samples were examined with an Olympus BX51 polarized microscope, using a hot-stage (Linkam) and liquid N_2 to control the cooling rate and the temperature. An Olympus SC50 camera was used to take all the images. The samples were prepared by drop-casting. Solutions in DMF solvent with a concentration of 5 wt%

were drop-casted on glass substrates and dried in an oven before observe them under the microscope. The samples were cooled fast (60 ºC/min) to 152 ºC and crystallized at this temperature until saturation.

8.3 Results and discussion

8.3.1 Non-isothermal crystallization

All the samples synthesized in this chapter were studied under non-isothermal conditions to explore the influence of topology and the number of arms in the polymorphism of the synthesized PVDF samples. Figure 8.1 shows the results obtained by non-isothermal DSC experiments. Figure 8.1a shows crystallization exotherms corresponding to PVDF. There are no large changes in the crystallization temperature (T_c between 135 and 137 ºC) when the number of arms increase. In Figure 8.1b, the melting process of the PVDF after the crystallization procedure at 10 ºC/min is presented. In all the samples, two melting endotherms are observed, being this behavior characteristic of polymorphic PVDF.[8] Attending to the T_m peak values, the crystalline phase melting at higher temperatures corresponds to the paraelectric α-phase due to its larger thermodynamic stability when the crystallization occurs from the melt.[9] The other melting peak observed at lower temperatures, the less stable phase, probably corresponds to the β-phase.[10] In the linear PVDF sample, the melting peaks are observed at lower temperatures compared to the other samples with a higher number of PVDF arms. This behavior is due to the low molecular weight associated with the linear PVDF sample (see Table 8.1).

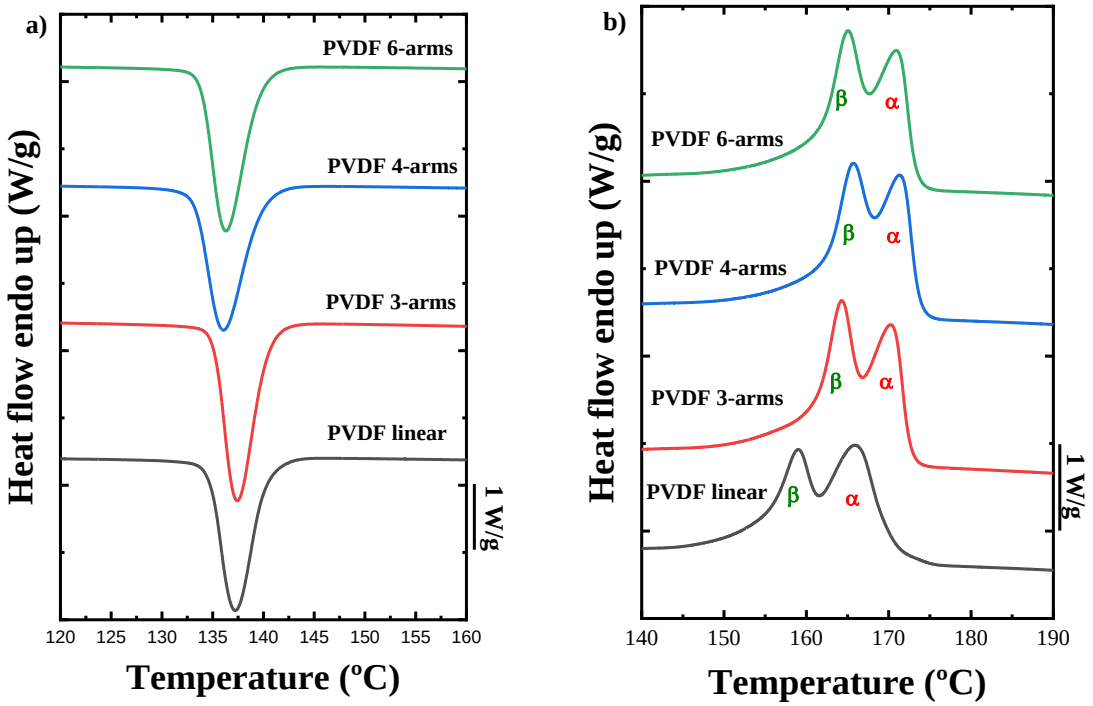

Figure 8.1. DSC scans for all the PVDF samples synthesized in this work. a) Cooling from the melt at 10 ºC/min and b) heating at 20 ºC/min after the cooling process shown in a).

The FTIR technique was employed to examine the crystalline phases of the PVDF after the cooling process at 10 ºC/min from the melt. In Figure 8.2 the FTIR results are plotted for each sample. All PVDF samples show the absorption bands at 764, 796, 976, and 1214 cm^{-1}, which indicate the presence of the α-phase.[11] In addition, other bands, related to the β-phase are also detected, e.g., the bands at 840 and 1278 cm^{-1}.[12] On the other hand, there are some missing bands due to the γ-phase at 833 and 1233 cm^{-1}, which confirm that the phases crystallizing in the samples when the cooling rate is 10 ºC/min are the β- and α-phases. The coexistence of these two crystalline phases of PVDF, as indicated by FTIR, correlate well with the DSC results shown in Figure 8.1.

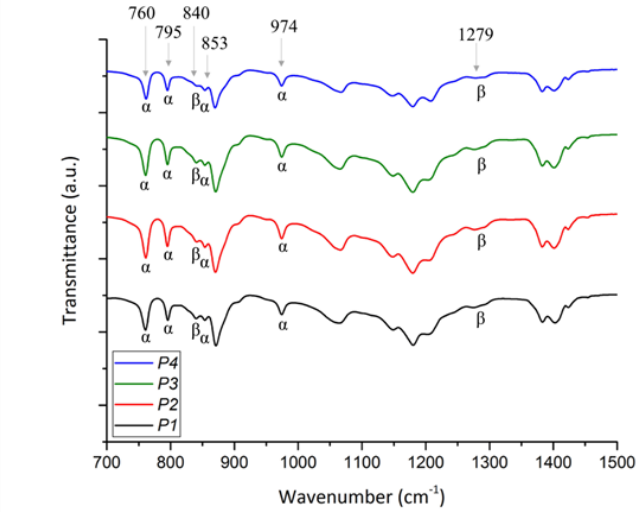

Figure 8.2. FTIR spectra of various crystalline phases for all PVDF homopolymers studied.

Once the phases observed by DSC are identified, it is also important to investigate how the number of arms affects the formation of the PVDF crystalline phases. Figure 8.3 shows the melting enthalpy of each phase for all the samples, and the results show that in the case of the linear PVDF the α-phase is the dominant one and when the number of arms increases, the amount of this α-phase decreases, hence the β-phase increases. Our results show that when the number of arms increases in the PVDF stars and the samples crystallized from the melt at 10 ºC/min, the amount of ferroelectric β-phase increases with respect to the paraelectric α-phase.

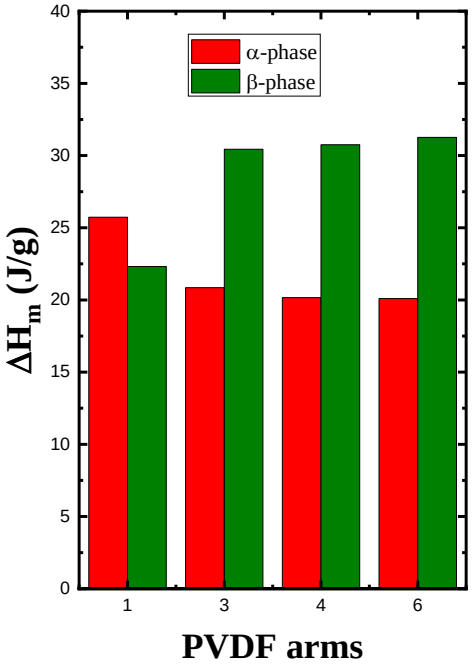

Figure 8.3. Melting enthalpy values for the α- (red) and β-phases (green) for all samples examined after crystallization process at 10 ºC/min.

In previous chapters, it has been demonstrated that the cooling rate affects the crystallization and the polymorphism of different PVDF systems. Therefore, we decided to consider or explore the cooling rate dependence of the PVDF stars by using a lower cooling rate (1 ºC/min) and a faster cooling rate (60 ºC/min). The melting curves of all the samples after the cooling procedure at 60 and 1 ºC/min are displayed in Figure 8.4. When the cooling rate is high, i.e., 60 ºC/min (Figure 8.4a), the α- and β-phases still coexist in all the samples, but in this case, this fast cooling process promotes the formation of the α-phase. On the other hand, when the cooling rate applied is low, i.e., 1 ºC/min (Figure 8.4b), the behavior of the samples changes completely. In the case of the PVDF samples with more than one arm, only one melting peak is observed and it can be associated with the α-phase. However, the linear PVDF shows three different melting peaks, which correspond to β-, α- and γ-phases, and these assignments are confirmed by

FTIR experiments, as it will be discussed below. This non-typical polymorphic behavior has been reported before, in the previous chapter, for low molecular weight PVDF systems. All the calorimetric data extracted from the DSC experiments are reported in Table 8.2.

FTIR experiments were carried out to identify the PVDF crystalline phases obtained in the different PVDF samples, after they were cooled at 1 ºC/min. The results are shown in Figure 8.4c. The PVDF samples with more than one arm show only the common bands of the α-crystalline phase at 764, 796, 976, and 1214 cm^{-1}, corroborating the DSC results. In the case of the linear PVDF, there is no evidence of the α-phase, probably due to its small amount in this sample (in the DSC curve this phase has the lowest melting enthalpy). The two characteristic bands with high intensity at 1275 and 833 cm^{-1} correspond to the γ-phase.[13] Due to their high intensity observed in this range, the bands corresponding to the β-phase are overlapped with those of the γ-phase. It is worth noting that the bands related to the β-phase appear at 840 and 1278 cm^{-1}, in the same range as those observed for the γ-phase. In summary, the presence of a ferroelectric β-phase is promoted for the linear PVDF at low cooling rates, whereas in the case of the PVDF stars with more than one arm, higher cooling rates are needed to partially crystallize the samples in the β-phase.

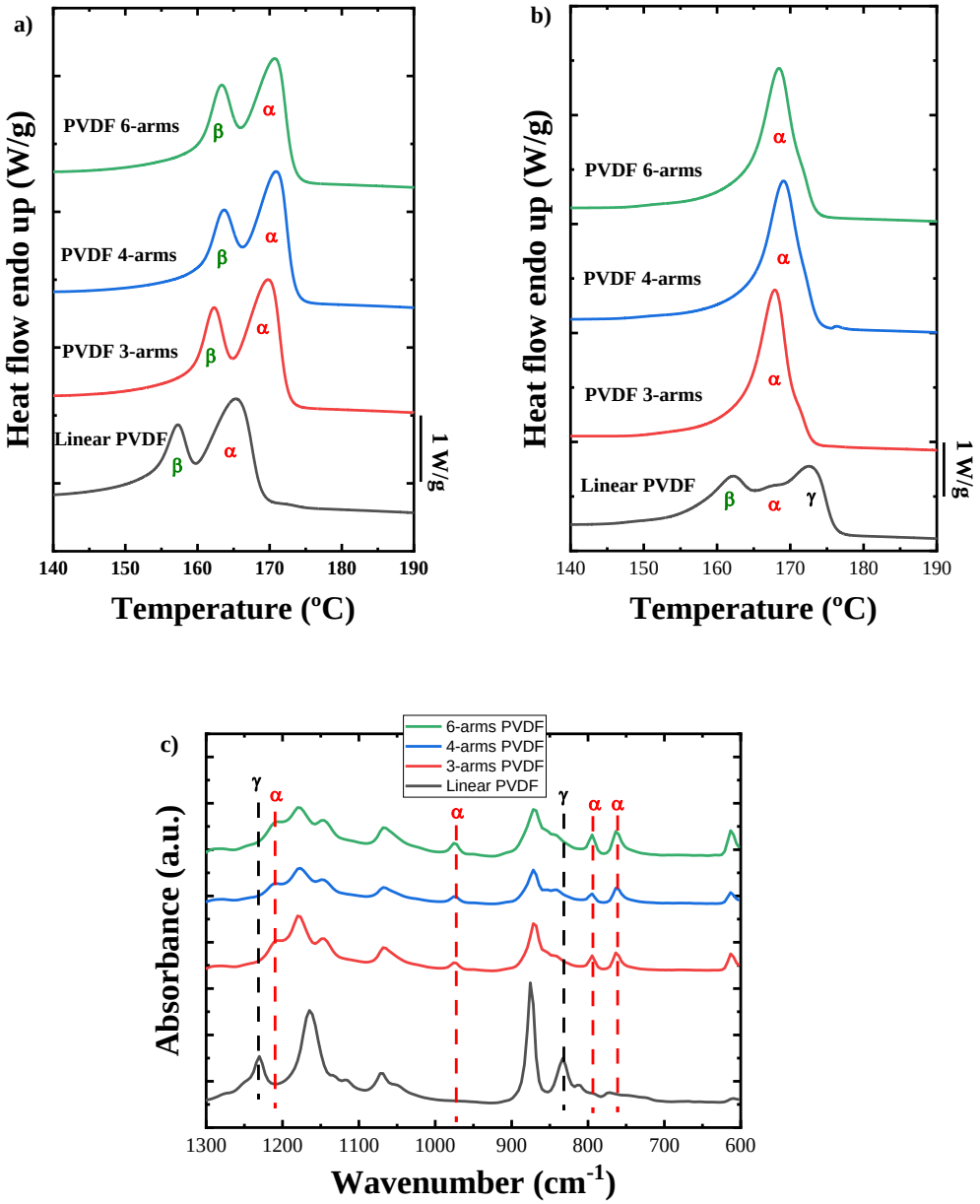

Figure 8.4. DSC heating scans at 20 ºC/min after cooling process a) at 60 ºC/min, b) at 1 ºC/min, and c) FTIR spectra at room temperature after a cooling process at 1 ºC/min.

Table 8.2. Calorimetric data extracted from the DSC experiments for all the samples studied.

Sample	Cooling rate (ºC/min)	$T_{m,\beta}$ (ºC)	$T_{m,\alpha}$ (ºC)	$T_{m,\gamma}$ (ºC)	T_c (ºC)	ΔH_m (J/g)	ΔH_c (J/g)
Linear	1	162.1	167.7	172.6	145.2	54.7	49.8
PVDF	10	159.0	165.9	-	137.2	50.1	51.0
	60	157.3	165.3	-	127.2	48.2	53.6
PVDF 3-	1	-	167.9	-	147.3	52.8	51.6
arms	10	164.3	170.2	-	137.4	51.9	55.8
	60	162.3	169.8	-	126.1	53.3	57.4
PVDF 4-	1	-	169.1	-	145.7	54.9	53.0
arms	10	165.7	171.3	-	136.1	52.4	57.1
	60	163.6	170.9	-	124.3	54.1	56.5
PVDF 6-	1	-	168.5	-	146.0	54.5	53.0
arms	10	165.1	170.9	-	136.3	51.4	57.7
	60	163.3	170.7	-	124.9	54.6	56.4

8.3.2 Isothermal Crystallization

The overall isothermal crystallization study (comprising both nucleation and growth) was performed by DSC to ascertain if the sample topology could affect the kinetics of crystallization. The primary nucleation rate is proportional to the inverse of the induction time (t_0) needed for crystallization to start, and it can be obtained during the isothermal crystallization procedure. Figure 8.5a shows the inverse of the induction time against the isothermal crystallization temperature employed. In the case of the linear PVDF, the primary nucleation rate values are the lowest compared to the samples with more than one arm. The nucleation rate in the PVDF stars is higher compared to the linear PVDF, but there is not a clear trend when the number of arms increases.

The inverse of the half crystallization time ($\tau_{50\%}$) is proportional to the overall crystallization rate, including the nucleation process and the growth of the crystals.[6] In Figure 8.5b, the inverse of the half crystallization time as a function of the isother-

mal crystallization temperature is shown. The results obtained are qualitatively similar to the ones obtained for the nucleation rate in Figure 8.5a. For linear PVDF, the overall crystallization rate is lower compared to the PVDF stars. All PVDF star samples show a higher overall crystallization rate than the linear sample, but the results are independent of the number of arms in the stars. These results indicate that the nucleation is controlling the overall crystallization process. The results have been fitted by solid lines using the Lauritzen and Hoffman theory.[14] We postulate that the higher nucleation rate in the PVDF stars (in comparison with the linear PVDF) results from the topological constraints provided by the covalent bonds between the arms that must radiate from the central benzene ring moiety that connects them.

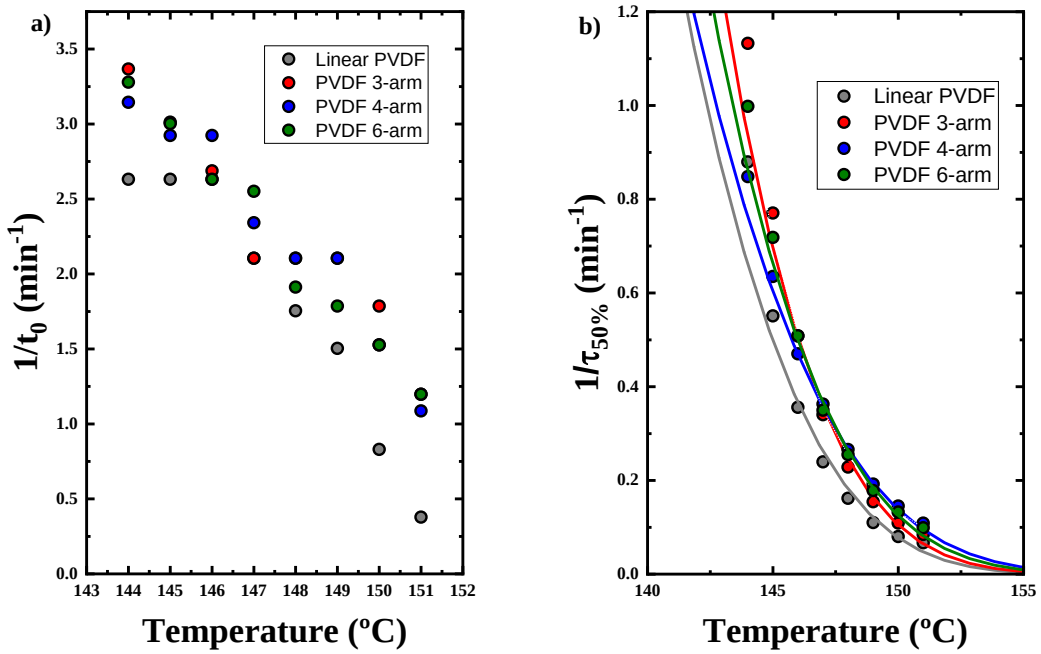

Figure 8.5. a) Inverse of the induction time (t_0) against the crystallization temperature, b) Inverse of the half crystallization time ($\tau_{50\%}$) against the crystallization temperature.

The Avrami theory can predict the kinetics of the primary crystallization process (before spherulite impingement) and the morphology of the crystals formed during isothermal crystallization.[6, 15] The Avrami equation can be written as:[6, 16, 17]

$$1 - V_c(t - t_0) = exp(-k(t - t_0)^n) \qquad \text{eq. 8.1}$$

where V_c is the relative volumetric transformed fraction, t_0 is the induction time, t is the experimentally determined time, k is the overall crystallization rate constant, and n is the Avrami index (which depends on the nucleation rate and the growth dimensionality).

Figure 8.6a shows the values of the Avrami index for each sample at different experimental isothermal crystallization temperatures. The Avrami index can predict the morphology of the crystals; the Avrami index has a range of values between 1 and 4. When the value is between 1 and 1.4 the morphology expected is needle-like (1D), which is not common in polymers. If the *n* value is between 1.5 and 2.4 the crystals should grow as axialites (2D lamellar aggregates), and if the Avrami index is in the range of 2.5 and 4, the crystal morphology in polymers is usually spherulitic (note than an Avrami index of 3 could also be caused by sporadically nucleated axialites). If the morphology corresponds to spherulites, $n = 3$ corresponds to instantaneously nucleated spherulites and $n = 4$ to sporadically nucleated spherulites.[6] The Avrami index for these PVDF samples were always within the range of the spherulitic morphology. In fact, they can all be approximated to $n = 3$, which corresponds to instantaneously nucleated spherulites. PLOM observations (see below) also corroborated the typical spherulitic morphology for all samples.

The overall crystallization rate constant elevated to the inverse of the Avrami index ($k^{1/n}$) is proportional to the overall crystallization rate. Figure 8.6b represents the overall crystallization rate predicted by the Avrami theory at each isothermal temperature used. As in the previous cases, the linear PVDF has the lowest crystallization rate. In contrast, in the case of the PVDF stars with more than one arm, the crystallization rate is faster and very similar among all star samples, with the exception of the isothermal crystallization that happened at low temperatures (144 ºC). If these theoretical data are compared with the experimental data obtained in Figure 8.5b, the similarity between them is a good example of how the Avrami theory has an accurate prediction regarding the experimental data obtained by DSC.

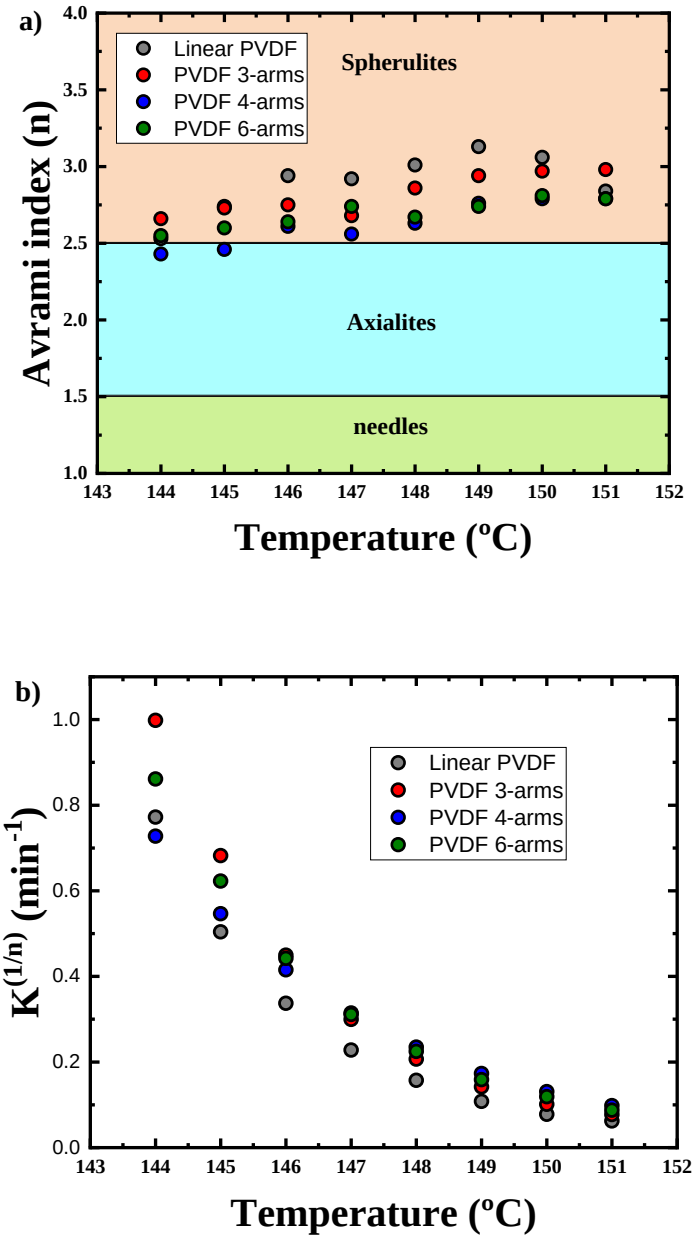

Figure 8.6. a) Representation of the Avrami index at every isothermal temperature employed in the experiments and b) representation of the overall crystallization constant elevated to the inverse of the Avrami index against the crystallization temperature.

The samples were also analysed by microscopy under isothermal conditions in order to check the accuracy of the Avrami prediction in this system. All the samples shown in Figure 8.7 were crystallized isothermally at 152 ºC. All PVDF samples

crystallize in spherulites as the Avrami theory predicts, moreover is possible to observe how the PVDF linear (Figure 8.7a) sample has a lower number of nuclei than the rest of PVDF stars samples with more than one arm. This result is according to the $1/t_0$ results obtained by DSC presented above (Figure 8.5a), where the nucleation rate of the linear PVDF was the lowest one.

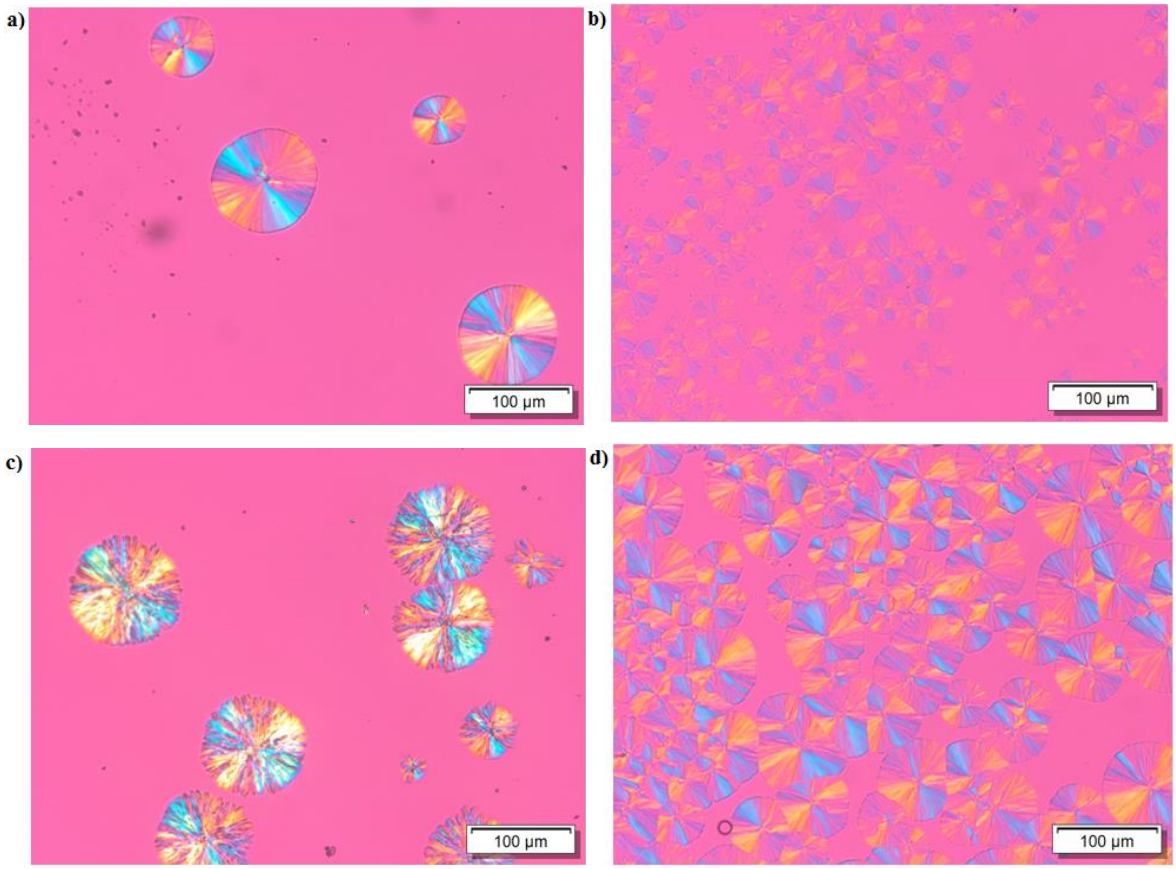

Figure 8.7. PLOM images taken at 152 ºC for a) Linear PVDF after 3 minutes, b) PVDF 3-arms after 2 minutes, c) 4-arms PVDF after 3 minutes and d) 6-arms PVDF after 1 minute and 30 seconds.

After the isothermal crystallization procedure, a study of the subsequent heating scans was performed to know how the isothermal crystallization process affects the polymorphism in these PVDF samples. Figure 8.8 shows the melting curves at 20 ºC/min after the isothermal crystallization process for all the samples analysed in this work. The linear PVDF shows different melting peaks, whereas in the case of the PVDF stars, only

one melting peak is observed, which means that the sample topology (linear versus star) controls the polymorphism of PVDF during the isothermal crystallization process.

Linear PVDF (Figure 8.8a) shows three melting peaks at low isothermal crystallization temperatures where the first one (and the biggest) corresponds to the ferroelectric β-phase (see labels in the figure), the next one corresponds to the melting of the paraelectric α-phase and the third one, at higher temperatures, corresponds to the ferroelectric γ-phase. When the isothermal crystallization temperature is increased, the melting peak of the α-phase decreases in size (and eventually disappears), and the peak of the γ-phase increases. At high isothermal crystallization temperatures, only two crystalline phases are formed, the β- and the γ-phases, both ferroelectrics. That means that when the isothermal crystallization temperature is increased, there is a transition from the paraelectric α-phase to the ferroelectric γ-phase. This behaviour has also been observed before in PVDF block copolymers with low molecular weight and it was presented before in a previous chapter.

In the case of PVDF stars (Figures 8.8b, c and d), the behaviour is very similar between them. All the samples show only one melting peak that corresponds to the α-phase, where at low isothermal crystallization temperatures, the melting peak shows a shoulder at higher temperatures that corresponds to the reorganization of the crystals during the heating process. In this case, the ferroelectric phase is not promoted, independently of the number of arms and isothermal crystallization temperatures studied.

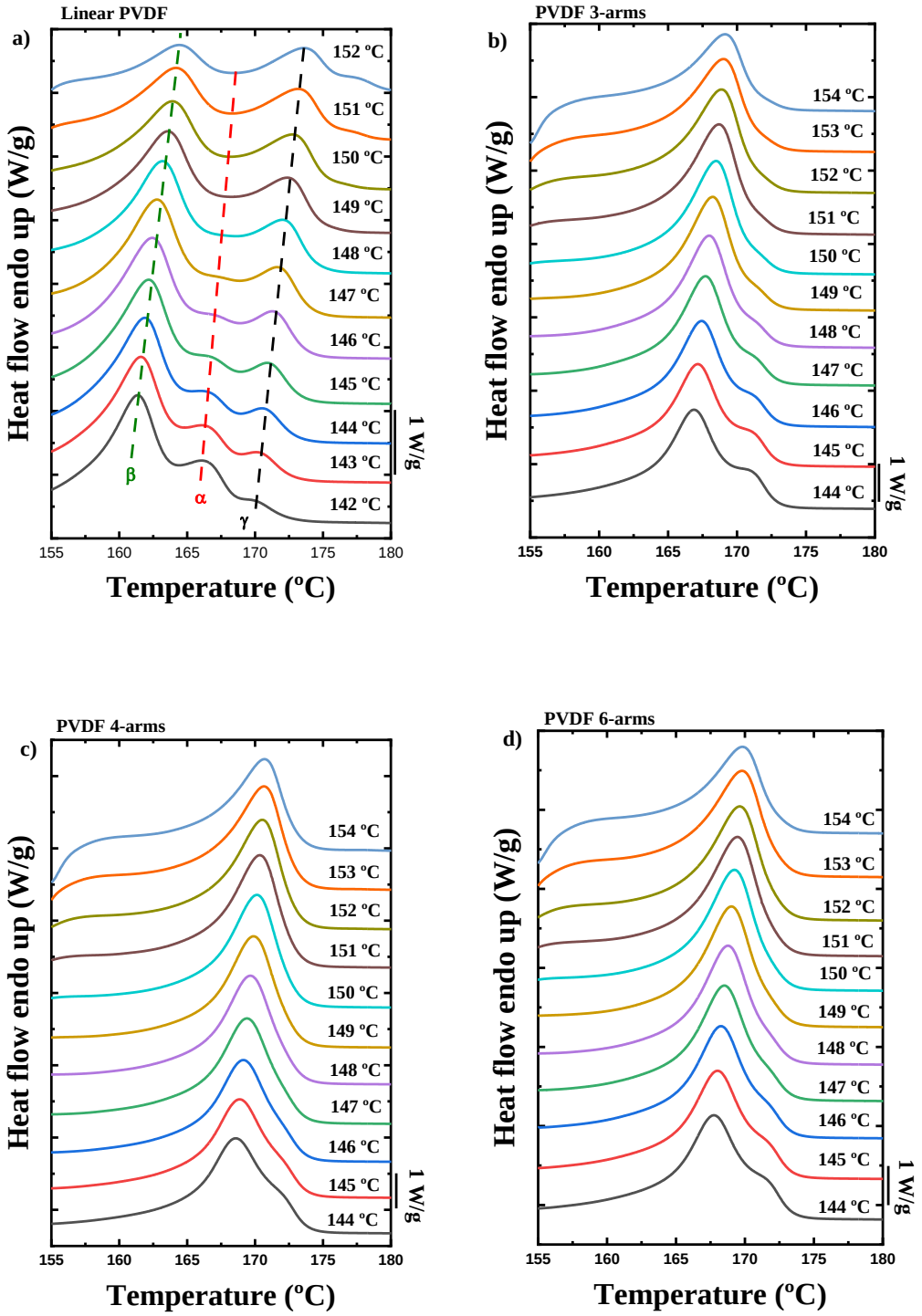

Figure 8.8. DSC heating curves after the isothermal crystallization procedure at different temperatures for all the samples studied in this work.

8.4 Conclusions

The effect of the PVDF architecture by increasing the arms number on the induced crystalline phases of well-defined linear 3-, 4- and 6-arm PVDF was investigated. At least two different crystalline phases, α- and β-phase, were produced during non-isothermal cooling from the melt. When the cooling rate was 10 ºC/min, the content of the ferroelectric β-phase increased in comparison to the paraelectric α-phase, as the number of arms also increased in the PVDF stars. This behavior is probably due to the increased topological complexity in the stars leading to the preferential formation of the less thermodynamically stable ferroelectric β-phase. On the other hand, when the cooling rate applied was 1 ºC/min, polymorphism was absent in the PVDF stars, which only formed the *α*-phase. However, paraelectric (α-phase) and ferroelectric phases (β- and γ-phases) were detected in the linear PVDF sample.

Linear PVDF presents a slower nucleation and crystallization rate under isothermal conditions than PVDF stars. This enhanced nucleation in the stars is probably related to the chain topology, as the arms must radiate from a common center. The number of arms did not affect the overall crystallization kinetics of the PVDF stars, which was always dominated by nucleation. The melting behavior of the isothermally crystallized samples was also examined in detail. The linear PVDF sample shows a polymorphic behavior with a phase transition from α- to γ-phase, but in the PVDF stars, the polymorphism disappeared, and only the α-phase was produced. Both slow cooling (at 1 ºC/min) and isothermal crystallization yielded similar results, as all PVDF star samples examined crystallized in the most stable α-phase. Only when the cooling rate is 10 ºC/min or higher rates (60 ºC/min) are the star samples able to form both α- and β-phases. The differences encountered between linear and star PVDF show that chain topology is a determining factor for its crystallization and polymorphism.

8.5 References

1. Lovinger, A. J., Ferroelectric Polymers. *Science* **1983,** 220, (4602), 1115.

2. Nandi, A. K.; Mandelkern, L., The influence of chain structure on the equilibrium melting temperature of poly(vinylidene fluoride). *Journal of Polymer Science Part B: Polymer Physics* **1991,** 29, (10), 1287-1297.

3. Gomes, J.; Serrado Nunes, J.; Sencadas, V.; Lanceros-Mendez, S., Influence of the β-phase content and degree of crystallinity on the piezo- and ferroelectric properties of poly(vinylidene fluoride). *Smart Materials and Structures* **2010,** 19, (6), 065010.

4. Tian, X.; Ding, J.; Zhang, B.; Qiu, F.; Zhuang, X.; Chen, Y., Recent Advances in RAFT Polymerization: Novel Initiation Mechanisms and Optoelectronic Applications. *Polymers* **2018,** 10, (3).

5. Moad, G., RAFT Polymerization – Then and Now. In *Controlled Radical Polymerization: Mechanisms*, American Chemical Society: 2015; Vol. 1187, pp 211-246.

6. Lorenzo, A. T.; Arnal, M. L.; Albuerne, J.; Müller, A. J., DSC isothermal polymer crystallization kinetics measurements and the use of the Avrami equation to fit the data: Guidelines to avoid common problems. *Polymer Testing* **2007,** 26, (2), 222-231.

7. Pérez-Camargo, R. A.; Liu, G.-M.; Wang, D.-J.; Müller, A. J., Experimental and Data Fitting Guidelines for the Determination of Polymer Crystallization Kinetics. *Chinese Journal of Polymer Science* **2022,** 40, (6), 658-691.

8. Roerdink, E.; Challa, G., Influence of tacticity of poly(methyl methacrylate) on the compatibility with poly(vinylidene fluoride). *Polymer* **1978,** 19, (2), 173-178.

9. Cortili, G.; Zerbi, G., Further infra-red data on polyvinylidene fluoride. *Spectrochimica Acta Part A: Molecular Spectroscopy* **1967,** 23, (7), 2216-2218.

10. Li, M.; Stingelin, N.; Michels, J. J.; Spijkman, M.-J.; Asadi, K.; Feldman, K.; Blom, P. W. M.; de Leeuw, D. M., Ferroelectric Phase Diagram of PVDF:PMMA. *Macromolecules* **2012,** 45, (18), 7477-7485.

11. Lanceros-Méndez, S.; Mano, J. F.; Costa, A. M.; Schmidt, V. H., FTIR AND DSC STUDIES OF MECHANICALLY DEFORMED β-PVDF FILMS. *Journal of Macromolecular Science, Part B* **2001,** 40, (3-4), 517-527.

12. Boccaccio, T.; Bottino, A.; Capannelli, G.; Piaggio, P., Characterization of PVDF membranes by vibrational spectroscopy. *Journal of Membrane Science* **2002,** 210, (2), 315-329.

13. Bachmann, M. A.; Gordon, W. L.; Koenig, J. L.; Lando, J. B., An infrared study of phase-III poly(vinylidene fluoride). *Journal of Applied Physics* **1979,** 50, (10), 6106-6112.

14. Hoffman, J. D.; Lauritzen, J. I., Jr., Crystallization of Bulk Polymers With Chain Folding: Theory of Growth of Lamellar Spherulites. *Journal of research of the National Bureau of Standards. Section A, Physics and chemistry* **1961,** 65A, (4), 297-336.

15. Reiter, G.; Strobl, G. R., *Progress in understanding of polymer crystallization*. Springer: 2007; Vol. 714.

16. Avrami, M., Kinetics of Phase Change. I General Theory. *The Journal of Chemical Physics* **1939,** 7, (12), 1103-1112.

17. Avrami, M., Granulation, Phase Change, and Microstructure Kinetics of Phase Change. III. *The Journal of Chemical Physics* **1941,** 9, (2), 177-184.

Resumen

Resumen

Actualmente, con el grado de desarrollo y globalización del planeta cada vez hay más avances tecnológicos en diferentes campos. Estos avances tecnológicos están siempre acompañados de nuevas tecnologías en equipos o maquinaria electrónica, los cuales están cada vez más desarrollados para tener un mejor rendimiento y capacidad. Para el desarrollo y construcción de estos aparatos electrónicos hacen falta complejos circuitos eléctricos, los cuales están constituidos de ciertos compuestos inorgánicos y metales pesados difíciles de encontrar en la naturaleza. A parte de ese inconveniente, la extracción de estos materiales también genera un alto impacto medioambiental y un alto grado de contaminación en las zonas de extracción. Evitar el uso de este tipo de materiales sin perder la eficacia ni el rendimiento de los aparatos constituidos por ellos es una de las temáticas de investigación más importantes. Es en este punto donde los polímeros con propiedades ferroeléctricas o piezoeléctricas juegan un papel importante a la hora de poder sustituir a los compuestos inorgánicos que tanto perjudican al medio ambiente. Los polímeros son mucho más baratos de sintetizar y pueden tener un rendimiento incluso mejor que los compuestos inorgánicos, por lo que su estudio para este tipo de aplicaciones es esencial.

El fluoruro de polivinilideno (PVDF según sus siglas en inglés) es un polímero semicristalino con unas buenas propiedades físicas y químicas, como por ejemplo

un alto grado de flexibilidad, un bajo coste, una alta compatibilidad con otros materiales y una alta resistencia química. Más allá de estas propiedades, el PVDF tiene otras dos importantes características, es un material polimórfico y puede tener capacidad ferroeléctrica/piezoeléctrica. El PVDF puede cristalizar en al menos cuatro fases diferentes dependiendo de las condiciones de cristalización. La fase más común y estable cuando la cristalización se produce desde el estado fundido es la fase α, pero esta fase tiene propiedades paraeléctricas, por lo que no es útil para su aplicación en aparatos electrónicos. Por lo tanto, si se quiere utilizar el PVDF en aparatos electrónicos, es necesario intentar evitar obtener la cristalización en dicha fase. Otra posible fase en la que se puede obtener el PVDF es la fase β, esta fase es la más deseada debido que es la fase que posee las mayores propiedades ferroeléctricas y piezoeléctricas debido a la conformación de las cadenas y a su máxima capacidad de polarización. El problema que tiene esta fase es la alta dificultad que existe a la hora de obtenerla. Las otras dos fases que se pueden obtener son la fase γ y la fase δ, ambas también tienen propiedades ferroeléctricas y piezoeléctricas, pero en bastante menor medida que la fase β.

La obtención de la fase β en el PVDF es uno de los grandes objetivos en la investigación de este material. Existen diversas maneras de obtener esta fase, desde el estiramiento de films de PVDF, a mezclas de PVDF con otros tipos de polímeros (como por ejemplo el PMMA, polimetil metacrilato), a la copolimerización del PVDF con otros polímeros (como el TrFE, trifluoroetileno) o la síntesis de nuevos materiales como los copolímeros de bloque que contienen PVDF.

En esta tesis se ha realizado un estudio sobre la caracterización y las cinéticas de cristalización de diferentes tipos de sistemas que contienen PVDF para intentar obtener la fase β y conocer cómo las diferentes topologías afectan a la cristalización.

El primer sistema estudiado son unos copolímeros al azar comerciales de PVDF con TrFE (Trifluoroetileno). Se estudiaron, un homopolímero (también comercial) de PVDF y tres copolímeros con diferentes composiciones de PVDF/TrFE (80/20, 75/25 y 70/30) y similar peso molecular. En este sistema se sabe, según la literatura previa, que el PVDF cristaliza en la fase β, pero no se han estudiado las cinéticas de cristalización ni como este proceso es afectado por la cantidad de TrFE en el copolímero. Se realizó un estudio isotérmico con un microscopio óptico de luz polarizada (PLOM) y con el equipo DSC (calorimetria de barrido diferencial) para conocer las cinéticas de cristalización, a parte también se realizó un estudio de autonucleación y de fraccionamiento térmico (SSA) de las muestras para ver cómo afecta el TrFE en la cristalización del PVDF. A partir de los resultados obtenidos se determinó que el TrFE actúa como agente nucleante del PVDF, acelerando las cinéticas de cristalización con respecto al homopolímero de PVDF. Además, se obtuvo que estos copolímeros son incapaces de autonuclear, probablemente debido al efecto nucleante del TrFE, y tampoco pueden fraccionarse, en este caso seguramente por la inclusión del TrFE en los cristales de PVDF.

El segundo sistema estudiado ha sido un conjunto de dos copolímeros de bloque PM-*b*-PVDF con distintas composiciones, (PM: polimetileno) dos mezclas de PM y

PVDF en la misma proporción que los copolímeros de bloque y los respectivos homopolímeros. Todas estas muestras fueron analizadas con el DSC a diferentes velocidades de enfriamiento de barrido para ver cómo afecta la velocidad de enfriamiento al polimorfismo del PVDF. Para saber que fases cristalizan en el PVDF se usaron las técnicas de FTIR (espectroscopía infrarroja con transformada de Fourier) y WAXS (rayos X de ángulo amplio). También se realizó un estudio de la miscibilidad en el fundido de las mezclas y de los copolímeros de bloque usando las técnicas de SAXS (rayos X de ángulo pequeño) y TEM (microscopía de transmisión de electrones). Las muestras de este sistema fueron analizadas isotérmicamente por DSC y PLOM para estudiar las cinéticas de cristalización y cómo afecta la cristalización isotérmica en el PVDF. Por ultimo también se caracterizaron los copolímeros de bloque con la técnica BDS (espectroscopia dieléctrica). Los resultados demostraron que en el caso de las mezclas el PM y el PVDF se segregaban en el fundido, pero cuando se trata de los copolímeros de bloque estos polímeros eran miscibles en el fundido. En este sistema se consiguió la cristalizacion de la fase β y α al mismo tiempo, además variando la velocidad de enfriamiento se pude conseguir la promoción de la fase β, aunque depende de la proporción de PM del compuesto.

El tercer sistema bajo estudio consiste en dos terpolímeros tribloque de PM-*b*-PS-*b*-PVDF (PS: poliestireno) con distintas composiciones, un precursor de PM-*b*-PS-Br y el respectivo homopolímero de PVDF. Primero las muestras fueron estudiadas en el fundido, para estudiar la miscibilidad en este estado, usando la técnica de SAXS. Las muestras fueron estudiadas con el DSC a diferentes velocidades de enfriamiento desde el fundido para ver cómo afecta al proceso de cristalización del

PVDF. La caracterización de las fases se realizó a través de las técnicas de FTIR y WAXS. También se realizó un estudio isotérmico y de las cinéticas de cristalización y de autonucleación y fraccionamiento. En este caso se consiguió obtener la cristalización de la fase β a velocidades bajas de enfriamiento desde el estado fundido. Como novedad con respecto a los anteriores sistemas cabe mencionar que en una de las muestras de los copolímeros de tres bloques se cristalizó la fase γ bajo condiciones de cristalización isotérmica a altas temperaturas, tal y como se demostró con el análisis de infrarrojos.

El cuarto sistema son unos novedosos copolímeros dibloque de PVDF-*b*-PEO (PEO: polióxido de etileno) con una topología con forma de estrella. Las muestras consisten en tres copolímeros de bloque, con dos brazos de PVDF en un mismo plano y dos brazos de PEO en el plano perpendicular y un centro en común para todos los brazos, un precursor de PVDF que consiste en dos brazos de PVDF con un centro en común y un precursor de PEO, el cual solo tiene un brazo. Al igual que en el resto de los casos se realizó un estudio de la miscibilidad en el fundido, un estudio del polimorfismo del PVDF a diferentes velocidades de enfriamiento, se caracterizaron las fases del PVDF con espectroscopía FTIR y WAXS y se realizó un estudio de las cinéticas de cristalización bajo condiciones isotérmicas. El objetivo en este caso es ver como la topología de estrella afecta al PVDF. Como en los anteriores casos la velocidad de cristalización afecta al polimorfismo del PVDF, gracias a la topología de estrella el PVDF cristaliza exclusivamente en fase β cuando se usan

velocidades de cristalización bajas o la cristalización es isotérmica. Además, se comprobó que en la cristalización isotérmica del precursor de PVDF (con dos brazos) cuando se aumenta la temperatura hay una transición de fases, de la fase paraeléctrica (α) a una ferroeléctrica (γ).

Por último se estudió un sistema de PVDF con un centro cíclico en el que hay diferentes números de brazos de PVDF (1, 3, 4 y 6) a diferentes velocidades de enfriamiento y en condiciones isotérmicas con el DSC, para la caracterización de las fases en este caso solo se usó el FTIR. En este caso se pudo comprobar como las cinéticas de nucleación y de cristalización se ven alteradas cuando hay más de un brazo de PVDF, pero no por el número de brazos. En cuanto el número de brazos es mayor de uno ambas cinéticas aumentan en comparación con el de un brazo. En cuanto a las fases cristalizadas en el PVDF, en el caso de las muestras con más de un solo brazo, a velocidades altas de cristalización se obtiene cristalización de las fases α y β, mientras que a velocidades baja solo cristalizan en la fase α. En cambio, en el caso del PVDF con un solo brazo a bajas velocidades de cristalización se obtienen hasta tres fases, siendo la fase γ la mayor de todas, e incluso en la cristalización isotérmica es posible observar de nuevo una transición de fases desde la α hacia la γ cuando la temperatura de cristalización isotérmica aumenta.

De manera general, este trabajo de tesis ha demostrado que la cristalización del PVDF y su carácter polimórfico se ven fuertemente influenciados por la constitución y topología de la cadena polimérica, pudiéndose obtener la deseada fase β solo bajo condiciones específicas de composición, cristalización y topología de la cadena.

Resumen

Resumen

Actualmente, con el grado de desarrollo y globalización del planeta cada vez hay más avances tecnológicos en diferentes campos. Estos avances tecnológicos están siempre acompañados de nuevas tecnologías en equipos o maquinaria electrónica, los cuales están cada vez más desarrollados para tener un mejor rendimiento y capacidad. Para el desarrollo y construcción de estos aparatos electrónicos hacen falta complejos circuitos eléctricos, los cuales están constituidos de ciertos compuestos inorgánicos y metales pesados difíciles de encontrar en la naturaleza. A parte de ese inconveniente, la extracción de estos materiales también genera un alto impacto medioambiental y un alto grado de contaminación en las zonas de extracción. Evitar el uso de este tipo de materiales sin perder la eficacia ni el rendimiento de los aparatos constituidos por ellos es una de las temáticas de investigación más importantes. Es en este punto donde los polímeros con propiedades ferroeléctricas o piezoeléctricas juegan un papel importante a la hora de poder sustituir a los compuestos inorgánicos que tanto perjudican al medio ambiente. Los polímeros son mucho más baratos de sintetizar y pueden tener un rendimiento incluso mejor que los compuestos inorgánicos, por lo que su estudio para este tipo de aplicaciones es esencial.

El fluoruro de polivinilideno (PVDF según sus siglas en inglés) es un polímero semicristalino con unas buenas propiedades físicas y químicas, como por ejemplo

un alto grado de flexibilidad, un bajo coste, una alta compatibilidad con otros materiales y una alta resistencia química. Más allá de estas propiedades, el PVDF tiene otras dos importantes características, es un material polimórfico y puede tener capacidad ferroeléctrica/piezoeléctrica. El PVDF puede cristalizar en al menos cuatro fases diferentes dependiendo de las condiciones de cristalización. La fase más común y estable cuando la cristalización se produce desde el estado fundido es la fase α, pero esta fase tiene propiedades paraeléctricas, por lo que no es útil para su aplicación en aparatos electrónicos. Por lo tanto, si se quiere utilizar el PVDF en aparatos electrónicos, es necesario intentar evitar obtener la cristalización en dicha fase. Otra posible fase en la que se puede obtener el PVDF es la fase β, esta fase es la más deseada debido que es la fase que posee las mayores propiedades ferroeléctricas y piezoeléctricas debido a la conformación de las cadenas y a su máxima capacidad de polarización. El problema que tiene esta fase es la alta dificultad que existe a la hora de obtenerla. Las otras dos fases que se pueden obtener son la fase γ y la fase δ, ambas también tienen propiedades ferroeléctricas y piezoeléctricas, pero en bastante menor medida que la fase β.

La obtención de la fase β en el PVDF es uno de los grandes objetivos en la investigación de este material. Existen diversas maneras de obtener esta fase, desde el estiramiento de films de PVDF, a mezclas de PVDF con otros tipos de polímeros (como por ejemplo el PMMA, polimetil metacrilato), a la copolimerización del PVDF con otros polímeros (como el TrFE, trifluoroetileno) o la síntesis de nuevos materiales como los copolímeros de bloque que contienen PVDF.

En esta tesis se ha realizado un estudio sobre la caracterización y las cinéticas de cristalización de diferentes tipos de sistemas que contienen PVDF para intentar obtener la fase β y conocer cómo las diferentes topologías afectan a la cristalización.

El primer sistema estudiado son unos copolímeros al azar comerciales de PVDF con TrFE (Trifluoroetileno). Se estudiaron, un homopolímero (también comercial) de PVDF y tres copolímeros con diferentes composiciones de PVDF/TrFE (80/20, 75/25 y 70/30) y similar peso molecular. En este sistema se sabe, según la literatura previa, que el PVDF cristaliza en la fase β, pero no se han estudiado las cinéticas de cristalización ni como este proceso es afectado por la cantidad de TrFE en el copolímero. Se realizó un estudio isotérmico con un microscopio óptico de luz polarizada (PLOM) y con el equipo DSC (calorimetria de barrido diferencial) para conocer las cinéticas de cristalización, a parte también se realizó un estudio de autonucleación y de fraccionamiento térmico (SSA) de las muestras para ver cómo afecta el TrFE en la cristalización del PVDF. A partir de los resultados obtenidos se determinó que el TrFE actúa como agente nucleante del PVDF, acelerando las cinéticas de cristalización con respecto al homopolímero de PVDF. Además, se obtuvo que estos copolímeros son incapaces de autonuclear, probablemente debido al efecto nucleante del TrFE, y tampoco pueden fraccionarse, en este caso seguramente por la inclusión del TrFE en los cristales de PVDF.

El segundo sistema estudiado ha sido un conjunto de dos copolímeros de bloque PM-*b*-PVDF con distintas composiciones, (PM: polimetileno) dos mezclas de PM y

PVDF en la misma proporción que los copolímeros de bloque y los respectivos homopolímeros. Todas estas muestras fueron analizadas con el DSC a diferentes velocidades de enfriamiento de barrido para ver cómo afecta la velocidad de enfriamiento al polimorfismo del PVDF. Para saber que fases cristalizan en el PVDF se usaron las técnicas de FTIR (espectroscopía infrarroja con transformada de Fourier) y WAXS (rayos X de ángulo amplio). También se realizó un estudio de la miscibilidad en el fundido de las mezclas y de los copolímeros de bloque usando las técnicas de SAXS (rayos X de ángulo pequeño) y TEM (microscopía de transmisión de electrones). Las muestras de este sistema fueron analizadas isotérmicamente por DSC y PLOM para estudiar las cinéticas de cristalización y cómo afecta la cristalización isotérmica en el PVDF. Por ultimo también se caracterizaron los copolímeros de bloque con la técnica BDS (espectroscopia dieléctrica). Los resultados demostraron que en el caso de las mezclas el PM y el PVDF se segregaban en el fundido, pero cuando se trata de los copolímeros de bloque estos polímeros eran miscibles en el fundido. En este sistema se consiguió la cristalizacion de la fase β y α al mismo tiempo, además variando la velocidad de enfriamiento se pude conseguir la promoción de la fase β, aunque depende de la proporción de PM del compuesto.

El tercer sistema bajo estudio consiste en dos terpolímeros tribloque de PM-*b*-PS-*b*-PVDF (PS: poliestireno) con distintas composiciones, un precursor de PM-*b*-PS-Br y el respectivo homopolímero de PVDF. Primero las muestras fueron estudiadas en el fundido, para estudiar la miscibilidad en este estado, usando la técnica de SAXS. Las muestras fueron estudiadas con el DSC a diferentes velocidades de enfriamiento desde el fundido para ver cómo afecta al proceso de cristalización del

PVDF. La caracterización de las fases se realizó a través de las técnicas de FTIR y WAXS. También se realizó un estudio isotérmico y de las cinéticas de cristalización y de autonucleación y fraccionamiento. En este caso se consiguió obtener la cristalización de la fase β a velocidades bajas de enfriamiento desde el estado fundido. Como novedad con respecto a los anteriores sistemas cabe mencionar que en una de las muestras de los copolímeros de tres bloques se cristalizó la fase γ bajo condiciones de cristalización isotérmica a altas temperaturas, tal y como se demostró con el análisis de infrarrojos.

El cuarto sistema son unos novedosos copolímeros dibloque de PVDF-*b*-PEO (PEO: polióxido de etileno) con una topología con forma de estrella. Las muestras consisten en tres copolímeros de bloque, con dos brazos de PVDF en un mismo plano y dos brazos de PEO en el plano perpendicular y un centro en común para todos los brazos, un precursor de PVDF que consiste en dos brazos de PVDF con un centro en común y un precursor de PEO, el cual solo tiene un brazo. Al igual que en el resto de los casos se realizó un estudio de la miscibilidad en el fundido, un estudio del polimorfismo del PVDF a diferentes velocidades de enfriamiento, se caracterizaron las fases del PVDF con espectroscopía FTIR y WAXS y se realizó un estudio de las cinéticas de cristalización bajo condiciones isotérmicas. El objetivo en este caso es ver como la topología de estrella afecta al PVDF. Como en los anteriores casos la velocidad de cristalización afecta al polimorfismo del PVDF, gracias a la topología de estrella el PVDF cristaliza exclusivamente en fase β cuando se usan

velocidades de cristalización bajas o la cristalización es isotérmica. Además, se comprobó que en la cristalización isotérmica del precursor de PVDF (con dos brazos) cuando se aumenta la temperatura hay una transición de fases, de la fase paraeléctrica (α) a una ferroeléctrica (γ).

Por último se estudió un sistema de PVDF con un centro cíclico en el que hay diferentes números de brazos de PVDF (1, 3, 4 y 6) a diferentes velocidades de enfriamiento y en condiciones isotérmicas con el DSC, para la caracterización de las fases en este caso solo se usó el FTIR. En este caso se pudo comprobar como las cinéticas de nucleación y de cristalización se ven alteradas cuando hay más de un brazo de PVDF, pero no por el número de brazos. En cuanto el número de brazos es mayor de uno ambas cinéticas aumentan en comparación con el de un brazo. En cuanto a las fases cristalizadas en el PVDF, en el caso de las muestras con más de un solo brazo, a velocidades altas de cristalización se obtiene cristalización de las fases α y β, mientras que a velocidades baja solo cristalizan en la fase α. En cambio, en el caso del PVDF con un solo brazo a bajas velocidades de cristalización se obtienen hasta tres fases, siendo la fase γ la mayor de todas, e incluso en la cristalización isotérmica es posible observar de nuevo una transición de fases desde la α hacia la γ cuando la temperatura de cristalización isotérmica aumenta.

De manera general, este trabajo de tesis ha demostrado que la cristalización del PVDF y su carácter polimórfico se ven fuertemente influenciados por la constitución y topología de la cadena polimérica, pudiéndose obtener la deseada fase β solo bajo condiciones específicas de composición, cristalización y topología de la cadena.

Summary

Summary

Nowadays there is a great development in the field of new technologies for its application in electronic devices and new equipment with the aim to have a better yield and capacity with a lower cost. For the construction of these novel devices it is necessary to employ inorganic compounds and heavy metals, which are very difficult to find in nature and their extraction generates a high impact on the environment apart from a high level of pollution in the extraction zones. In order to avoid these types of materials without efficiency loss and yield in the devices, the study of new materials is one of the most important topics in science. Polymers with ferroelectric and piezoelectric properties can play an important role at the time to substitute the inorganic compounds that cause many problems in the environment. The main advantage of the polymers against the inorganic compounds is their low cost needed in their synthesis and the good yield that they have, therefore their study for the application in electronic devices has a big relevance.

Poly vinylidenefluoride (PVDF) is a semicrystalline polymer with good mechanical and chemical properties, as for instance high flexibility, low cost, great compatibility with other materials and high chemical resistance. Apart from these properties, PVDF has two other important characteristics: polymorphism and ferroelectricity and piezoelectricity. PVDF has the capacity to crystallize in at least 4 different phases depending on the crystallization conditions. The most common and the most stable phase, when the crystallization is from the melt, is the α-phase, but

this phase is paraelectric, so it is not useful in electronic applications. Another phase in which PVDF can crystallize is the β-phase, this phase is the most desired phase for electronic applications due to its highest ferroelectric and piezoelectric properties, and thanks to its chain conformation, this phase has the highest polarization capacity. The inconvenience of the β-phase is the great difficulty of obtaining it in neat PVDF. The other two phases in which PVDF can crystallize are the γ- and δ-phases, both of them are also ferroelectric and piezoelectric but less than the β-phase.

The obtainment of the β-phase in the PVDF is one of the most important research topics in this polymer. There are several methods to crystallize it, from the stretching of thin films of PVDF, blends with other polymers, such as for instance PMMA (poly methyl methacrylate), copolymerization with other polymers such as for example TrFE (Trifluoroethylene), or the synthesis of new materials as block copolymers which contain PVDF.

In this thesis work, a study of crystallization kinetics in different systems containing PVDF has been performed. The main topics are the crystallization of the β-phase under different crystallization conditions and the study of how PVDF topology influences crystallization and polymorphism.

The first system studied are three commercial random copolymers with TrFE with different compositions PVDF/TrFE (80/20, 75/25 and 70/30) and a commercial PVDF homopolymer, all of them with similar molecular weights. This type of copolymers always crystallizes in the ferroelectric β-phase, but the kinetics of crystallization and the influence of TrFE content on it, has never been studied for these copolymers. An isothermal study employing polarized light optical microscopy

(PLOM) and Differential Scanning Calorimetry (DSC) techniques was carried out, moreover, a self-nucleation and successive self-nucleation study were done to know how TrFE comonomer affects the crystallization of PVDF. The results show that TrFE is acting as a nucleating agent in the PVDF, increasing the nucleation and crystallization rate in comparison to the PVDF homopolymer. Moreover, the PVDF within the random copolymers cannot self-nucleate, probably due to the already large nucleating effect of the TrFE, and also, it cannot be fractionated, in this last case, that is probably due to the inclusion of TrFE in the PVDF crystals.

The second system analysed consists in two diblock copolymes of PM-*b*-PVDF with different compositions (PM: polymethylene), two blends of PM and PVDF with the same composition than the diblock copolymers and the respective PM and PVDF homopolymers. All these samples were analysed by DSC at different cooling rates in order to observe how the crystallization rate and polymorphism of PVDF is affected. To identify the phases that crystallize, FTIR and in-situ WAXS analysis were done. MoreovAdditionally, a study of the miscibility in the molten state was done employing TEM and SAXS techniques. Isothermal studies were performed using PLOM and DSC techniques to explore the crystallization kinetics and observe the difference in polymorphism in PVDF between the crystallization during the cooling and isothermal crystallization. The outcome shows that in the case of the blends, there is a strong segregation between PM and PVDF in the molten state, but for the diblock copolymers, the situation changes and the polymers are miscible in the melt. In this system, PVDF crystallize in the β- and α-phase at the same time

during a cooling scan. Changing the cooling rate, it is possible to promote the crystallization of the β-phase, but only for one diblock copolymer, so the proportion of PM is an important factor.

The third system characterized consists of two triblock terpolymers of PM-*b*-PS-*b*-PVDF (PS: polystyrene) with different compositions, a diblock precursor PM-*b*-PS-Br and the respective PVDF homopolymer. First, the miscibility of the samples was studied in the molten state by SAXS. Different cooling rates from the melt were employed in the DSC to observe how the crystallization process of the PVDF is affected. The polymorphism of the PVDF was characterized by FTIR and WAXS techniques. Apart from the mentioned protocols, a self-nucleation and successive self-nucleation and annealing (SSA) study was done to see how PVDF topology can influence the thermal properties. For this system, low cooling rates yield PVDF crystallization in the β-phase. A difference regarding to the previously mentioned system is that in the triblock terpolymers, it was possible to crystallize the γ-phase for one of the triblock terpolymer samples, this phase was crystallized during an isothermal crystallization at high temperatures and could be demonstrated by FTIR analysis.

The following system consists of novel PVDF-*b*-PEO (PEO: poly ethylene oxide) miktoarm star diblock copolymers with two arms of PVDF in the same plane and two PEO arms in a perpendicular plane. The samples are constituted by three miktoarm star block copolymers with different compositions and similar molecular weights, a PVDF precursor which is formed by two PVDF arms, and a linear PEO precursor. As in the previous systems, a study of the miscibility, polymorphism at different cooling rates, characterization of the phases obtained by DSC and a study

of the kinetic of crystallization under isothermal conditions were carried out. In this case, the objective was to observe how the miktoarm star topology affects PVDF crystallization. Thanks to the topology, it is possible to crystallize PVDF exclusively in the β-phase when the cooling rate is low or the crystallization is provoked isothermally. Moreover, in the case of the 2-arm PVDF precursor during the isothermal crystallization, a phase transition was observed when the isothermal crystallization temperature increases. The phase transition occurs from the paraelectric α-phase to the ferroelectric γ-phase.

The last system studied consists of four samples with a common cyclic centre and different numbers of PVDF arms (1, 3, 4 and 6). This system was studied at different cooling rates from the melt and under isothermal conditions by DSC, the characterization of the phases was done employing FTIR technique. The nucleation and crystallization rate are affected by the number of arms, when the number of arms is more than one, both kinetics are increased, but there is not any dependence on the number of arms when there are more than one. Regarding the phases that crystallized, when there are more than one arm of PVDF, the α- and β-phases co-exist at high cooling rates but at low cooling rates only the α-phase is obtained. However, in the case of the sample with only one arm at low cooling rates, three phases were obtained being the γ-phase the majority of all of them. Also in this sample, during the isothermal crystallization, a phase transition from the α- to the γ-phase is observed when the isothermal crystallization temperature increases.

In general, this thesis work has shown that the crystallization of PVDF and its polymorphic character are strongly influenced by the constitution and topology of the polymer chain. The desired β-phase can only be obtained under specific conditions of composition, crystallization, and chain topology.